

NASA TECHNICAL  
MEMORANDUM



NASA TM X-301

Declassified by authority of NASA  
Classification Change Notices No. 50  
Dated 2/24/66

NASA

REF ID: A6570

00000000000000000000000000000000

00000000000000000000000000000000

00000000000000000000000000000000

00000000000000000000000000000000

00000000000000000000000000000000

N66-22925

FACILITY NUMBER		(CHRU)
167		1
TMX-1092 (AREA OR CH TMX OR AD NUMBER)		(CATE BORN)
01		

LONGITUDINAL AND LATERAL  
STABILITY CHARACTERISTICS OF  
TWO FOUR-JET VTOL MODELS IN  
THE TRANSITION SPEED RANGE

by Raymond D. Vogler and Richard E. Kubn

Langley Research Center

Langley Station, Hampton, Va.

NATIONAL AERONAUTICS AND SPACE ADMINISTRATION • WASHINGTON, D. C. • MAY 1965

~~Declassified by authority of NASA~~  
Classification Change Notices No. ~~50~~  
Dated \*\*~~2/6/66~~

LONGITUDINAL AND LATERAL STABILITY CHARACTERISTICS  
OF TWO FOUR-JET VTOL MODELS IN THE  
TRANSITION SPEED RANGE

By Raymond D. Vogler and Richard E. Kuhn

Langley Research Center  
Langley Station, Hampton, Va.

GROUP 4  
Downgraded at 3 year intervals;  
declassified after 12 years

CLASSIFIED DOCUMENT-TITLE UNCLASSIFIED

This material contains information affecting the national defense of the United States within the meaning of the espionage laws, Title 18, U.S.C., Secs. 793 and 794, the transmission or revelation of which in any manner to an unauthorized person is prohibited by law.

NOTICE

This document should not be returned after it has satisfied your requirements. It may be disposed of in accordance with your local security regulations or the appropriate provisions of the Industrial Security Manual for Safe-Guarding Classified Information.

~~DECLASSIFIED~~

LONGITUDINAL AND LATERAL STABILITY CHARACTERISTICS  
OF TWO FOUR-JET VTOL MODELS IN THE  
TRANSITION SPEED RANGE\*

By Raymond D. Vogler and Richard E. Kuhn  
Langley Research Center

SUMMARY

N66-22925

The investigation of the longitudinal and lateral stability characteristics of two four-jet vectored-thrust-type VTOL models in the transition speed range indicated significant effects of both the inlet and exit flow. The basic model experienced the expected induced nose-up pitching moments and loss in lift in the transition speed range. Removing the area of the delta wing rearward of the jets reduced the direct jet-induced interference effects for the tail-off configuration. Adding a conventional horizontal tail to this modified model, however, revealed high jet-induced downwash angles in the region of the horizontal tail that produced a severe tail-on pitch-up for this model.

The inlet effects for the basic model, which had the inlet far ahead of the center of gravity, were reasonably well predicted by simple calculations based on the inlet mass flow. The effective dihedral of the basic model at transition speeds with the jets deflected downward was greatly increased by the induced effects of the exiting jets. These jet-induced rolling moments arise from the same jet-induced pressure reduction on the lower surface that produced the jet-induced nose-up pitching moments.

*Author*

INTRODUCTION

Considerable research is currently being done by industry and the National Aeronautics and Space Administration toward the development of vertical take-off and landing (VTOL) aircraft that combine the utility of the helicopter with the higher speed and longer range capabilities of conventional aircraft. Jet-supported VTOL configurations are of obvious interest for missions requiring high subsonic or supersonic cruise performance. Investigations of the aerodynamic characteristics of jet VTOL aircraft in the transition speed range have been restricted largely to studies of the jet-induced effects of the exiting jets on the longitudinal characteristics. (See refs. 1 to 5.) As a consequence, an investigation has been conducted in the 17-foot test section of the Langley 300-MPH 7- by 10-foot tunnel to include the study of the effects of

---

\*Title, Unclassified.

inlet and exit flow on the static longitudinal and lateral aerodynamic characteristics of two models representing a VTOL airplane with a vectored-thrust-type engine.

The basic model investigated had a low-aspect-ratio delta wing with variable-sweep auxiliary wings, twin inlets, and four adjustable exit nozzles. An axial-flow fan was located in the duct system to provide variable jet-exit velocities. Elevators were located at the trailing edge of the delta wing and flaps were on the variable-sweep wings. The modified model was obtained by removing the delta-wing area rearward of the jet exits of the basic model and adding a conventional horizontal tail. Both models were investigated through an angle-of-attack range from  $-10^\circ$  to  $25^\circ$  at dynamic pressures from 0.21 to 10 pounds per square foot. The jet-deflection range was from  $4^\circ$  to  $78^\circ$ . Longitudinal data were obtained on the basic model with power at elevator deflections of  $0^\circ$  and  $10^\circ$  and without power at deflections from  $0^\circ$  to  $25^\circ$ . Longitudinal data were obtained on the modified model with horizontal tail off and with tail incidence angles of  $0^\circ$  and  $9^\circ$ . Lateral data with the flaps deflected and undeflected were obtained on the basic model only. The transonic and supersonic static aerodynamic characteristics of models very similar to the basic model but without powered jets are reported in references 6 and 7.

#### SYMBOLS AND COEFFICIENTS

The data are presented about the stability axes (fig. 1) with the origin of the axes with respect to the model located at the moment center as shown in figure 2. The reference area, span, and mean aerodynamic chord are based on the auxiliary wing in the  $15^\circ$  sweep position with the leading and trailing edges projected to the fuselage center line.

b span (auxiliary wing swept  $15^\circ$ ), 5.75 ft

c̄ mean aerodynamic chord of  $15^\circ$  swept auxiliary wing with leading and trailing edges extended to vertical plane of symmetry, 0.81 ft

$C_D$  drag coefficient,  $\frac{\text{Drag}}{q_\infty S}$

$C_l$  rolling-moment coefficient,  $\frac{M_X}{q_\infty S b}$

$C_{l\beta}$  effective dihedral parameter,  $\frac{\partial C_l}{\partial \beta}$

$C_L$  lift coefficient,  $\frac{\text{Lift}}{q_\infty S}$

~~SECRET~~ UNCLASSIFIED

$C_m$	pitching-moment coefficient, $\frac{M_Y}{q_\infty S \bar{c}}$
$\frac{\Delta C_m}{\Delta t}, \frac{\Delta C_m}{\Delta \delta_e}$	pitching-moment coefficient per degree of control-surface deflection
$\frac{\partial C_m}{\partial \alpha}$	slope of pitching-moment curve between $\alpha = -5^\circ$ and $\alpha = 5^\circ$
$C_n$	yawing-moment coefficient, $\frac{M_Z}{q_\infty S b}$
$C_{n\beta}$	directional stability parameter, $\frac{\partial C_n}{\partial \beta}$
$c_T$	thrust coefficient, $\frac{T}{q_\infty S}$
$C_Y$	side-force coefficient, $\frac{\text{Side force}}{q_\infty S}$
$D$	drag, lb
$D_e$	effective diameter, diameter of a circle equivalent in area to total jet-exit area of configuration
$i_t$	incidence of horizontal tail (positive when trailing edge is down), deg
$l$	distance from inlet to moment center, 37.0 in.
$L$	lift, lb
$\Delta L$	interference increment of lift, lb
$m$	mass flow, slugs/sec
$M$	Mach number
$\Delta M$	interference increment of pitching moment, ft-lb
$M_X$	rolling moment, ft-lb
$M_Y$	pitching moment, ft-lb
$(M_Y)_{\delta_j, T}$	pitching moment for a given jet deflection and given thrust at zero tunnel velocity, ft-lb

$M_Z$	yawing moment, ft-lb
$q_\infty$	free-stream dynamic pressure, lb/sq ft
R	Reynolds number
S	area of $15^\circ$ swept auxiliary wing with leading and trailing edges extended to vertical plane of symmetry, 4.55 sq ft
T	gross thrust, determined from $\sqrt{L^2 + D^2}$ at $\alpha = 0$ and $q_\infty = 0$ , lb
$V_j$	jet-exit velocity based on effective jet exit area, mass flow, and measured thrust, fps
$V_k$	free-stream velocity, knots
$V_\infty$	free-stream velocity, fps
W	assumed weight of hypothetical airplane (30,000 lb)
$\alpha$	angle of attack of fuselage (wing incidence $1.5^\circ$ ), deg
$\beta$	angle of sideslip, deg
$\delta_e$	elevator deflection (positive when trailing edge is down), deg
$\delta_f$	flap deflection (positive when trailing edge is down), deg
$\delta_j$	jet-deflection angle measured with respect to a horizontal plane parallel to fuselage center line, deg
$\rho_j$	mass density of air in jet exit, slugs/cu ft
$\rho_\infty$	mass density of free-stream air, slugs/cu ft
$\Lambda$	leading-edge sweep angle of auxiliary wing, deg

#### MODELS AND APPARATUS

The basic model (fig. 2) used in the present investigation represented a VTOL airplane configuration employing a fixed delta wing with  $81^\circ$  of sweep and an auxiliary variable-sweep outboard panel. The modified model (fig. 3) was obtained from the basic model by removing that part of the fixed delta wing rearward of the pivot area of the variable-sweep panel and adding a horizontal-tail. Photographs of various views of the two models are given in figures 4 and 5. Ailerons and landing gear are shown on the drawings and photographs of

the models but no tests were made with the ailerons deflected or with the landing gear on the model.

The models were powered with a 34.5-horsepower electric motor that drove an axial-flow fan 10 inches in diameter. (See fig. 6.) This power package was located in the fuselage just upstream of the front exit nozzles. Each of the four exit nozzles had separate ducts connecting them to the kidney-shaped exits of the power package. The air inlets to the fan consisted of two large ducts, an opening on top of the model at the apex of the delta wing to represent the "blow-in door" needed on a full-scale airplane for static operation, and a small rectangular inlet on the upper right-hand side of the fuselage near the wing apex. This rectangular inlet was added to correct for unequal mass flow at the kidney-shaped exits caused by nonuniform flow separation at the duct inlets.

The mass flow of the fan was determined by means of 17 total-pressure and 4 static-pressure orifices in each kidney-shaped exit behind the fan. (See fig. 6.) The pressure tubes were connected to a manometer for visual observation and the pressures were recorded on machine-punched cards for each data point. Jet deflection was accomplished by rotating the nozzle to which the deflection vanes were attached.

The auxiliary wing was the upper half of an NACA 65A012 airfoil with a flat lower surface. The basic model was very similar to one used in the high-speed investigations (refs. 6 and 7) except that in the present investigation the auxiliary wing was moved rearward a distance equal to 9.2 percent of the distance from the fuselage nose to the moment center, and the size of the 4-percent-thick vertical tail was increased. The horizontal tail of the modified model was made of 1/8-inch-thick flat plate. The hinge line of the plain flap was on the 72-percent wing-chord line.

A six-component strain-gage balance located within the fuselage was used for determining the forces and moments on the sting-supported model.

#### TESTS AND CORRECTIONS

Both models were tested through an angle-of-attack range from  $-10^\circ$  to  $25^\circ$  and dynamic pressures from 0.21 to 10 pounds per square foot in the 17-foot test section of the Langley 300-MPH 7- by 10-foot tunnel. The jet-deflection range was from  $4^\circ$  to  $78^\circ$  and the total thrust of the four jets varied from about 10 to 46 pounds. Most of the tests were made with the auxiliary wing swept  $15^\circ$ . With power off, data were obtained on the basic model with elevator deflections from  $0^\circ$  to  $25^\circ$  and with power on at  $0^\circ$  and  $10^\circ$ . Flaps were deflected  $40^\circ$  on the basic model only. Lateral data were obtained on the basic model only through an angle-of-sideslip range from  $-30^\circ$  to  $10^\circ$  with flaps undeflected and through a sideslip range from  $-70^\circ$  to  $10^\circ$  with the flaps deflected.

Longitudinal data for various power conditions were obtained on the modified model with tail off and with tail incidence angles of  $0^\circ$  and  $9^\circ$ .

The model jet thrust coefficient was varied by changing the model fan speed or the tunnel velocity. At static conditions, a relationship was established between fan speed, total pressure, and measured mass flow through the kidney-shaped exits at the rear of the power package (fig. 6) and the static jet thrust on the model as measured by the strain gage. For any test at forward velocity, the nominal jet thrust was set with fan speed and the more precise thrust was determined from the measured mass flow and the calibration between the total pressure, mass flow, and static jet thrust.

Corrections to the free-stream velocity for blockage for models of the size of the present model have been found to be negligible hence no correction for blockage has been applied. No jet-boundary corrections were applied inasmuch as reference 8 indicates that the jet-boundary corrections are negligible for models with ratios of jet-exit area to tunnel cross-sectional area as small ( $\approx 0.001$ ) as was the case in this investigation.

#### PRESENTATION OF RESULTS

Inasmuch as the investigation covered the transition speed range from hovering to conventional flight, it is not desirable to present all the data, particularly that at very low speeds, in terms of conventional coefficients. At the very low speed, therefore, the data are presented in terms of force-thrust ratios, for example,  $L/T$ ,  $D/T$ , and  $M_y/T\bar{c}$ , and so forth. At intermediate speeds some data are presented in both forms to provide an overlap. Data can be converted from one form to the other by appropriate application of the thrust coefficient  $C_T$  which is presented on each figure; for example,

$$C_L = \frac{L}{T} C_T, \quad C_m = \frac{M_y}{T\bar{c}} C_T, \text{ and so forth.}$$

The results of the investigation are presented in the following figures:

Figure

#### Basic model:

##### Longitudinal characteristics:

Effect of Reynolds number, power off, $\Lambda = 15^\circ$ . . . . .	7
Effect of elevator deflection, power off, $\Lambda = 15^\circ$ . . . . .	8
Effect of Reynolds number and elevator deflection, flaps deflected, power off, $\Lambda = 15^\circ$ . . . . .	9
Effect of power and jet deflection, $\Lambda = 15^\circ$ . . . . .	10
Effect of power and jet deflection, flaps deflected $40^\circ$ , $\Lambda = 15^\circ$ . . .	11
Effect of auxiliary wing sweep angle . . . . .	12
Effect of power, outboard panel retracted, $\Lambda = 81^\circ$ . . . . .	13
Effect of jet-deflection angle, $\Lambda = 81^\circ$ . . . . .	14
Effect of differential jet deflection, $\Lambda = 15^\circ$ . . . . .	15

##### Lateral characteristics:

Power off, tail on, $\Lambda = 15^\circ$ . . . . .	16
Power on, tail off, $\Lambda = 15^\circ$ . . . . .	17

Power on, flaps undeflected, $\Lambda = 15^\circ$	18
Power on, flaps deflected, $\Lambda = 15^\circ$	19

## Modified model:

## Longitudinal characteristics:

Horizontal-tail effectiveness, power on, $\delta_j = 4^\circ$ , $\Lambda = 15^\circ$	20
Effect of power, $\delta_j = 4^\circ$ , $\Lambda = 15^\circ$	21
Horizontal-tail effectiveness, $\delta_j = 31^\circ$ , $\Lambda = 15^\circ$	22
Effect of power, $\delta_j = 31^\circ$ , $\Lambda = 15^\circ$	23
Horizontal-tail effectiveness, $\delta_j = 60^\circ$ , $\Lambda = 15^\circ$	24
Effect of power, $\delta_j = 60^\circ$ , $\Lambda = 15^\circ$	25
Effect of power, $\delta_j = 68^\circ$ , $\Lambda = 15^\circ$	26

## Summary figures:

Drag-thrust breakdown	27
Velocity ratios and thrust coefficient relationship	28
Interference increments, basic model	29
Static thrust and pitching moments	30
Inlet effect on stability and pitching moments	31
Interference increments, modified model	32
Comparison of interference increments on four configurations	33
Longitudinal stability and pitch-up	34, 35
Tail and elevator effectiveness	36
Transition characteristic of airplane	37 to 39
Lateral characteristics	40, 41
Effect of 30-knot cross wind on basic airplane	42

The data of references 1 to 5 have used the ratio of free-stream velocity to jet velocity as the correlating speed parameter. This ratio is probably a satisfactory parameter for comparing the results of experiments with cold jets, that is, those in which the jet and free-stream densities do not vary greatly. It will probably not be satisfactory, however, for application to hot-jet configurations. Inductive reasoning and experience with jet flaps indicate that the induced pressures responsible for the interference increments of lift and pitching moment are more apt to be a function of the jet momentum than of the jet velocity. Therefore, a momentum coefficient would be more appropriate to use than the velocity ratio. However, a simple momentum coefficient, such as

$C_\mu = \frac{mV_j}{q_\infty S}$  which has been used in jet-flap work, cannot be used because reference 1 has clearly shown that the ratio of jet area to surrounding surface area is an important parameter. It appears logical therefore that a momentum ratio, that is, the ratio of free-stream momentum per unit area to jet momentum per

unit area or effective speed ratio  $\sqrt{\frac{\rho_\infty V_\infty^2}{\rho_j V_j^2}}$  will most likely become the proper correlating parameter. This correlating parameter is also suggested in

0313020000  
reference 9. The data in this report are plotted against  $\frac{V_\infty}{V_j}$ , which for this model powered by a low pressure fan, is simply the square root of  $\frac{\rho_\infty V_\infty^2}{\rho_j V_j^2}$ . When these results are applied to an airplane with a hot jet, however, it is suggested that the momentum ratio parameter be used.

## RESULTS AND DISCUSSION

### Effect of Reynolds Number

In order to cover the range of thrust coefficients appropriate to the entire transition speed range, it was necessary to vary the free-stream velocity over a fairly wide range and to test at free-stream velocities as low as 14 feet per second. Higher speeds could not be used at the high thrust coefficients because of the limited power available in the model. The aerodynamic surfaces of the model therefore were operating at different Reynolds numbers for each thrust coefficient. In order to determine the possible effects of Reynolds number on the basic aerodynamic characteristics of the model, power-off tests were run at various tunnel speeds and the results are shown in figures 7 and 9. As can be seen no significant effects of Reynolds number are apparent in the range studied. Power-on tests were run at lower speeds than those shown in figures 7 and 9, but accurate power-off data at these speeds could not be obtained because of the low forces involved. At these very low speeds the effects of Reynolds number would not be very important because the ratio of the contribution of the power-off aerodynamics of the configuration to the total model forces at these conditions is very small.

### Determination of Model Thrust

One of the most important and most difficult problems in the investigation of the jet-induced effects on VTOL configurations is the accurate determination of the exit momentum or gross thrust of the jets. As indicated in the section on "Tests and Corrections" the gross thrust of the model jets in this investigation was determined from the total pressure and mass flow measured in the ducts between the electric-motor-driven fan and the jet exits. The thrust, however, could not be calculated accurately from the mass flow and total pressure at the measuring station because there was an insufficient number of total- and static-pressure probes (and in a practical installation it is probably not possible to obtain a sufficient number of pressure measurements) to obtain an accurate measure of the mass flow through the ducts because of the distortion of the flow. Also there are pressure losses between the total pressure at the measuring station and that at the jet exit. It was necessary therefore to make appropriate calibrations of the thrust as determined from the measurements by correlating the measured mass flow with the actual thrust measured under static conditions on the thrust stand with the wing removed.

A check on the validity of the gross thrust so determined can be made in the cruise configuration by comparing the thrust determined from the calibrated flowmeter readings against the model power-on drag as shown in figure 27. The thrust determined from the flowmeter calibration is the gross thrust or total exit momentum. It is necessary to subtract both the inlet drag and the power-off aerodynamic drag of the model from this gross thrust to obtain a comparison with the measured power-on drag of the model. The inlet drag is given by

$$D_{\text{inlet}} = mV_{\infty}$$

Since the inlet and exit mass flows are the same for this model and since

$$T = mV_j$$

the inlet drag can be expressed in terms of the thrust as

$$D_{\text{inlet}} = T \frac{V_{\infty}}{V_j}$$

or in coefficient form

$$C_{D,\text{inlet}} = C_T \frac{V_{\infty}}{V_j}$$

The power-off drag shown in figure 27 ( $C_D = 0.046$ ) was determined from reference 6 because, in the present investigation, the windmilling drag of the internal fan added an increment to the power-off drag level. Note that the reference area used in nondimensionalizing the data in reference 6 is different than that used in the present report, and this difference has been accounted for in presenting the data in figure 27.

In general, the agreement between the net power-on drag as measured and as determined from these calculations is considered good except for a thrust coefficient of about 0.2. The difference between the other data points and the computed curves is considered to be within the accuracy of the drag data. The drag data, however, were not as good as would be desired because the balance was chosen to accept the component of the model weight measured by the drag beams of the balance with the model at high angles of attack. As a result, the accuracy of the drag measurements at low lift coefficients will not permit reliable assessment of the cruise performance of the present configuration.

The apparent inaccuracies in thrust coefficients at  $C_T = 0.2$  are also apparent in figure 28 which gives the variation of  $C_T \frac{V_{\infty}}{V_j}$  and  $\frac{\rho_{\infty} V_{\infty}^2}{\rho_j V_j^2}$  with

0317 [REDACTED] 30  
thrust coefficient. The quantity  $C_T \frac{V_\infty}{V_j}$  is important in calculating the inlet effects,

and the ratio of the free-stream pressure to the exit dynamic pressure as a function of  $C_T$  is of interest in connection with the exit effects. The line through the data points was calculated for a jet area of 0.257 square foot which is the apparent effective area of the jet exit. This area is about 80 percent of the projected open area between the exit vanes in the nozzles. The difference of approximately 20 percent is probably due to the boundary-layer losses on the exit vanes and, in particular, to the large losses in the very sharp corners between some of the vanes and the wall of the duct exit.

#### Longitudinal Characteristics

Power effects, basic configuration. - In the cruise configuration  $\delta_j = 4^\circ$ , the longitudinal stability of the configuration decreases with increasing thrust coefficient. (See figs. 10(a) and 11(a).) This effect was determined in some preliminary tests and because of it the auxiliary variable-sweep wing was moved rearward a distance equal to 9.2 percent of the distance from the fuselage nose to the moment center, from the position used in reference 6, in order to improve the stability at high thrust coefficients. All the data presented in this report are for the wing in the rearward position. This reduction in stability at high thrust coefficients is partly due to the inlet flow. The inlet flow contribution in reducing the stability, the effects of the wing-induced upwash at the inlet and fuselage cross flow being neglected and the assumption being made that all the flow enters the forward inlet, is given by

the equation  $\frac{\partial C_m}{\partial \alpha} = \frac{1}{57.3} C_T \frac{V_\infty}{V_j} \frac{l}{c}$ . Figure 31(a) shows the calculated effect of inlet flow compared with the measured reduction in stability.

With large jet deflections appropriate to the transition from hovering to forward flight, the expected induced nose-up moments and induced loss in lift (refs. 1 to 5) were encountered as shown in figure 29. At the smaller jet deflections and higher velocity ratios, the induced effects are reduced. The jet-induced increments of lift and pitching moment shown in figure 29 were determined in the same manner as those in reference 3. The direct thrust effects and the aerodynamic forces calculated from the power-off data were subtracted from the measured power-on data to leave only the jet-induced interference increments including the inlet effects.

Thus,

$$\frac{\Delta L}{T} = \frac{L}{T} - \sin(\alpha + \delta_j) - \frac{C_L q_\infty S}{T} \quad (1)$$

Similarly,

$$\frac{\Delta M}{Tc} = \frac{M_Y}{Tc} - \frac{(M_Y)_{\delta_j, T}}{Tc} - \frac{C_m q_\infty S \bar{c}}{Tc} \quad (2)$$

~~RECORDED~~

The second term of equation (2) accounts for the fact that in the present investigation the thrust line did not always pass through the center of gravity. With the jets in the cruise position the thrust line was below the center of gravity and produced a nose-up pitching moment. At the highest deflection appropriate to VTOL operation, the thrust line was behind the center of gravity and produced a slight nose-down moment. The measured variation of the pitching moment with jet deflection at zero speed is presented in figure 30 along with the static thrust for selected fan speeds.

The data for an angle of attack of  $10^\circ$  with the flaps retracted and with the flap deflected  $40^\circ$  are shown in figures 29(b) and 29(c), respectively. As can be seen by comparison of these figures with figure 29(a), there is a small effect of angle of attack and of flap deflection on the lift increments. The nose-up pitching moments are increased appreciably in going from an angle of attack of  $0^\circ$  to  $10^\circ$ . This increase due to angle of attack is considerably larger than increases shown in references 3 and 4. However, the results presented in these references did not include the effect of inlet flow. In the present case the inlet is a considerable distance ahead of the center of gravity, and a  $10^\circ$  increase in angle of attack results in the inlet momentum drag being applied appreciably higher with respect to the center of gravity and thus contributes a nose-up moment. In figure 31(b) the difference between the induced moments at angles of attack of  $10^\circ$  and  $0^\circ$  are compared with the calculated inlet contribution and shows that the inlet accounts for a large part of the increment in nose-up moment due to a  $10^\circ$  angle-of-attack change. However, some of the increment results from reduced pressures on the lower surface area behind the jets as indicated in reference 2.

Power effects, modified configuration. - In an attempt to alleviate the large nose-up moments induced by the deflected jets in transition on the original configuration which were partly due to the suction pressures induced on the lower surface of that part of the delta wing rearward of the jets the model was modified by removing the area of the delta wing rearward of the jets. For the tail-off configuration the jet-induced increments (figs. 32 and 33(a)) were greatly reduced, as expected. A further comparison of the effects of configuration is shown in figure 33(b) where the tail-off configuration of the present investigation is compared with the configurations of references 3 and 5. The configuration sketches in figure 33 are all drawn to scale such that the jet areas are identical. The model of reference 3 had a broad flat-bottom fuselage and a low-aspect-ratio wing providing considerable area behind and outboard of the jets and therefore it experienced the highest induced negative lift and nose-up moments. Both the model of reference 5 and the modified model of the present investigation had less area behind the jets and therefore show smaller induced effects. The investigations of references 3 and 5 were made at jet pressure ratios approaching those of actual jet engines whereas the present model was powered by a fan and therefore had a pressure ratio of less than 1.05.

With the addition of a horizontal tail set at zero incidence, the jet-induced loss in lift and the nose-up moments were greater than those for the basic model. (See fig. 33(a).) These additional increments are due to the high downwash angles induced at the tail by the jets. These additional increments were reduced with the tail set at an incidence of  $9^\circ$  and might be reduced further with higher incidence settings.

001785000000000000000000

The jet-induced downwash at the tail which produces the large nose-up moment increments in figure 33(a) also causes large changes in the tail-on stability of the configuration and at high jet deflections it causes a severe pitch up as shown in figure 34 where the pitching-moment curves, with controls neutral, for the modified and the basic configuration are compared for selected jet deflections and thrust coefficients. At low jet deflection  $\delta_j = 4^\circ$ , the modified configuration shows better characteristics in that it exhibits a pitch down at high lift coefficients, whereas the basic configuration shows a slight reduction in stability or a mild pitch-up at the high lifts.

At the higher thrust coefficients with the jets deflected, the modified configuration shows a violent pitch-up due to the jet-induced downwash field at the horizontal tail. This effect is illustrated in figure 35 where the tail-on data for two stabilizer settings and the tail-off data are compared. With the tail removed, the model is unstable and exhibits an increasing instability at high lift coefficients. This increasing instability with lift coefficient is common to variable-sweep wing configurations and is due to the fact that the highly swept fixed inboard section of the wing has a nonlinear lift-curve slope and continues to lift at angles of attack where the variable-sweep portion of the wing is beginning to experience stall and therefore a reduction in lift. In the present configuration, this effect is probably aggravated by the lift on the inlets which act as very low-aspect-ratio wings with the attendant nonlinear lift-curve slope and therefore nonlinear variation of pitching moment with angles of attack.

In power-off tests of variable-sweep wing configurations, it has been found that the unstable characteristics of these wings coupled with the downwash field from them will produce a pitch-up when the tail is located above the wing-chord plane. (See ref. 10.) It has been found from unpowered tests of these configurations that a stable pitching-moment curve with a stable break at the stall can be achieved by placing the horizontal tail below the wing-chord plane. This characteristic is shown also for the present model with the jets in the cruise position,  $\delta_j = 4^\circ$ . (See fig. 35.)

However, with the jets deflected  $\delta_j = 31^\circ$  or  $60^\circ$ , a pitch-up is encountered for both stabilizer settings. This pitch-up is apparently due to the action of the jets in deflecting the flow field from the wing downward so that the horizontal tail is no longer low with respect to the flow field, but is in the same type of flow encountered in a power-off condition with the tail in a high position. Note that for  $\delta_j = 31^\circ$ , the pitching-moment data for a horizontal-tail setting of  $\delta_t = 9^\circ$  is almost identical to that for the tail-off configuration. For this condition the downwash angle at the tail is apparently increasing at the same rate as the angle of attack; thus the horizontal tail stays at the same angle of attack relative to the local wind up to a lift coefficient of about  $C_L = 2.0$  and does not contribute to the stability.

Longitudinal control effectiveness. - The control effectiveness for both the basic and modified configurations is presented in figure 36 in terms of the pitching-moment coefficient per degree of surface deflection and as a function of thrust coefficient. The power-off estimate of tail effectiveness was made with the aid of reference 11. For all conditions except a jet deflection of  $4^\circ$

~~DECLASSIFIED~~

for the modified configuration, the control effectiveness is essentially independent of thrust coefficient. This condition indicates that the controls on both configurations are operating at essentially free-stream dynamic-pressure conditions. On the basic model with the delta wing, the jet-induced effects alter the basic pressure distribution on the wing but they do not modify the additional distribution due to control-surface deflection. On the modified model the jet-induced effects change the downwash at the horizontal tail but they do not change the dynamic pressure at the tail.

The only exception to this analysis is for the modified model with the jets deflected only  $40^\circ$  at two thrust coefficients,  $C_T = 0$  and  $C_T = 0.75$ . This behavior probably results from the placement of the horizontal tail essentially behind the large fuselage and in line with the jets. (See fig. 3.) The dynamic pressure at the tail would be reduced by the fuselage blockage at zero jet thrust and increased by the jet at high thrust conditions for this jet deflection.

Calculations for airplane of fixed weight. - The thrust and jet deflection required, and the resulting pitching moment encountered in a steady level flight transition for a 30,000-pound airplane were calculated by assuming the model to be 1/8 scale. The results are shown in figures 37 to 39. The effect of angle of attack is shown in figure 37. At  $\alpha = 0$  the jet-induced loss in lift results in a required thrust 20 percent greater than the weight of the airplane for flight at about 100 knots. The effects of wing lift in overcoming these induced losses are shown by the greatly reduced thrust requirements at the higher angles of attack.

The effects of deflecting the elevators  $10^\circ$  and the flaps  $40^\circ$  are shown in figure 38 for an angle of attack of  $10^\circ$ . The flaps on this model were plain flaps of relatively short span set far out on the auxiliary wing because of the presence of the fixed delta configuration. As a result they were not very effective and produced only small increments in lift coefficient, and did not produce as large a reduction in the thrust required in transition as could be achieved by a more effective flap system.

The nose-up moments encountered in transition are due largely to the jet-induced effects. As can be seen in figure 38, the basic configuration can be trimmed by the elevator down to about 100 knots. Below this speed the control would, of course, have to be augmented by jet-reaction-type controls.

The transition characteristics of the modified model are compared with the basic configuration in figure 39 for an angle of attack of  $10^\circ$ . Although the jet-induced interference effects were reduced for the tail-off configuration, the basic instability of the configuration resulted in large nose-up moments at the  $10^\circ$  angle-of-attack case chosen here for comparison. The jet-induced downwash and the associated pitch-up also are indicated by the high nose-up moments encountered with the tail on.

For both the basic and the modified models, deflection of the longitudinal control surface to trim out the jet-induced nose-up moments (figs. 38 and 39) produces lift increments that tend to offset the jet-induced losses in lift

and result in a reduction in thrust required at the high-speed end of the transition.

### Lateral Characteristics

The lateral-directional stability characteristics were investigated on only the basic configuration and are presented in figures 16 to 19. The directional stability  $C_{n\beta}$  and the dihedral effects  $C_{l\beta}$  are summarized in figure 40 for small sideslip angles at  $\alpha = 0^\circ$  and with flaps undeflected. The directional instability with the vertical tail removed increased with thrust coefficient as would be expected because of the flow into the inlet. The destabilizing contribution of the inlet can be calculated from the inlet mass flow to obtain a yawing moment due to sideslip angles  $\Delta M_Z = mV_\infty l \sin \beta$  which for small sideslip angles and in coefficient form yields an expression for the yawing moment per degree of sideslip angle as

$$(\Delta C_{n\beta})_{\text{inlet}} = -C_T \frac{V_\infty}{V_j} \frac{l}{b} \frac{1}{57.3}$$

For the present model this estimate is in excellent agreement with the measured data for the tail-off case (fig. 40). With the tail-on, however, the data for low jet deflections ( $\delta_j = 4^\circ$ ) do not show a decrease in directional stability as would be expected and predicted by these calculations. The increment shown as the tail contribution in figure 40 was calculated from the tail length and the lift-curve slope of the vertical tail from reference 11 by assuming that the vertical tail extended to the fuselage center line and had no other endplating effect from the fuselage. This estimate is in good agreement

with the power-off data  $C_T \frac{V_\infty}{V_j} = 0$ . The power-on tail contribution as determined from the experimental data, however, exceeds the power-off tail contribution.

The expected reduction in directional stability with power due to the inlet flow does not occur until jet deflections of  $60^\circ$  and values of

$C_T \frac{V_\infty}{V_j} = 0.6$  are reached. The reason for this result is not presently understood; however, the data suggest that there may be a favorable sidewash at the vertical tail created by the interaction of the jet flow on the free stream.

The effective dihedral parameter  $C_{l\beta}$  increases with power contrary to the slight decrease shown for the calculation. This estimate was made, however, by assuming that all the inlet flow entered the main inlets which are below the center of gravity for zero angle of attack. Flow entering the "blow-in door" inlet would produce the opposite trend, however, because this inlet is above the center of gravity. Unfortunately measurements of the division of air entering the main inlets and the blow-in-door inlet were not made and a proper estimate of the effects of inlet flow on  $C_{l\beta}$  cannot be made. In any event,

~~DECLASSIFIED~~

the effect of inlet flow on the dihedral effect for this model would appear to be small.

There is a large increase in the effective dihedral parameter  $C_{l\beta}$  with jet deflection. This increase is due to the same jet-induced effects that cause the nose-up pitching moment. With the model at a sideslip angle, the pattern of induced suction pressures behind the jets moves around to the downstream side so as to induce a rolling moment tending to raise the leading wing. This effect is also shown in figure 41 where the rolling moment, yawing moment, and induced negative lift experienced at a sideslip angle of  $70^\circ$  are summarized. The data points are taken from figure 19(g). The rolling moment experienced at a sideslip angle of  $70^\circ$  is compared with the induced pitching moments from figure 29(a). The data points represent total model moments. Unfortunately, the power-off data necessary to reduce the data to the form of increments, as was done in figure 29, were not measured. These increments, however, would be small at these high-thrust-low-speed conditions. Although there are configuration differences between figures 19(g) and 29, the comparison shown indicates that the same factors that induced the nose-up pitching moments also induced similar rolling moments with sideslip angle. Similarly, the losses in lift induced by the jets at a sideslip angle of  $70^\circ$  are comparable in magnitude to the losses in lift induced at zero sideslip.

The yawing moment is due almost entirely to the inlet flow, as shown by the close agreement between the measured data and that calculated from the inlet mass flow.

The yawing moment and rolling moments that would be encountered by the assumed 30,000-pound airplane in transition from hovering to forward flight in a 30-knot crosswind are shown in figure 42. At zero forward speed, of course, a crosswind produces a  $90^\circ$  sideslip angle, and it was necessary to extrapolate the data of figure 19(g) to the  $90^\circ$  case. At zero speed there is a large yawing moment from the inlet tending to turn the airplane "out of the wind." As the airplane gains forward speed, the sideslip angle decreases rapidly, the tail eventually becomes effective, and the airplane tends to turn into the wind. The rolling moment increases with speed because of the increase in free-stream dynamic pressure. The jet reaction controls used for roll and yaw will have to be made powerful enough to cope with the moments shown in figure 42 and with sufficient margin to provide the desired level of controllability.

#### CONCLUDING REMARKS

The investigation of the longitudinal and lateral stability characteristics of two four-jet vectored-thrust-type VTOL models in the transition speed range indicated significant effects of both the inlet and exit flow.

The basic model experienced the expected induced nose-up pitching moments and loss in lift in the transition speed range. Removing the area of the delta wing rearward of the jets reduced the direct jet-induced interference

001700000000  
effects for the tail-off configuration. Adding a conventional horizontal tail to this modified model, however, revealed high jet-induced downwash angles in the region of the horizontal tail that produced a severe tail-on pitch-up for this model.

The inlet effects for the basic model, which had the inlet far ahead of the center of gravity, were reasonably well predicted by simple calculations based on the inlet mass flow. The effective dihedral of the basic model at transition speeds with the jet deflected downward was greatly increased by the induced effects of the exiting jets. These jet-induced rolling moments arise from the same jet-induced pressure reduction on the lower surface that produced the jet-induced nose-up pitching moments.

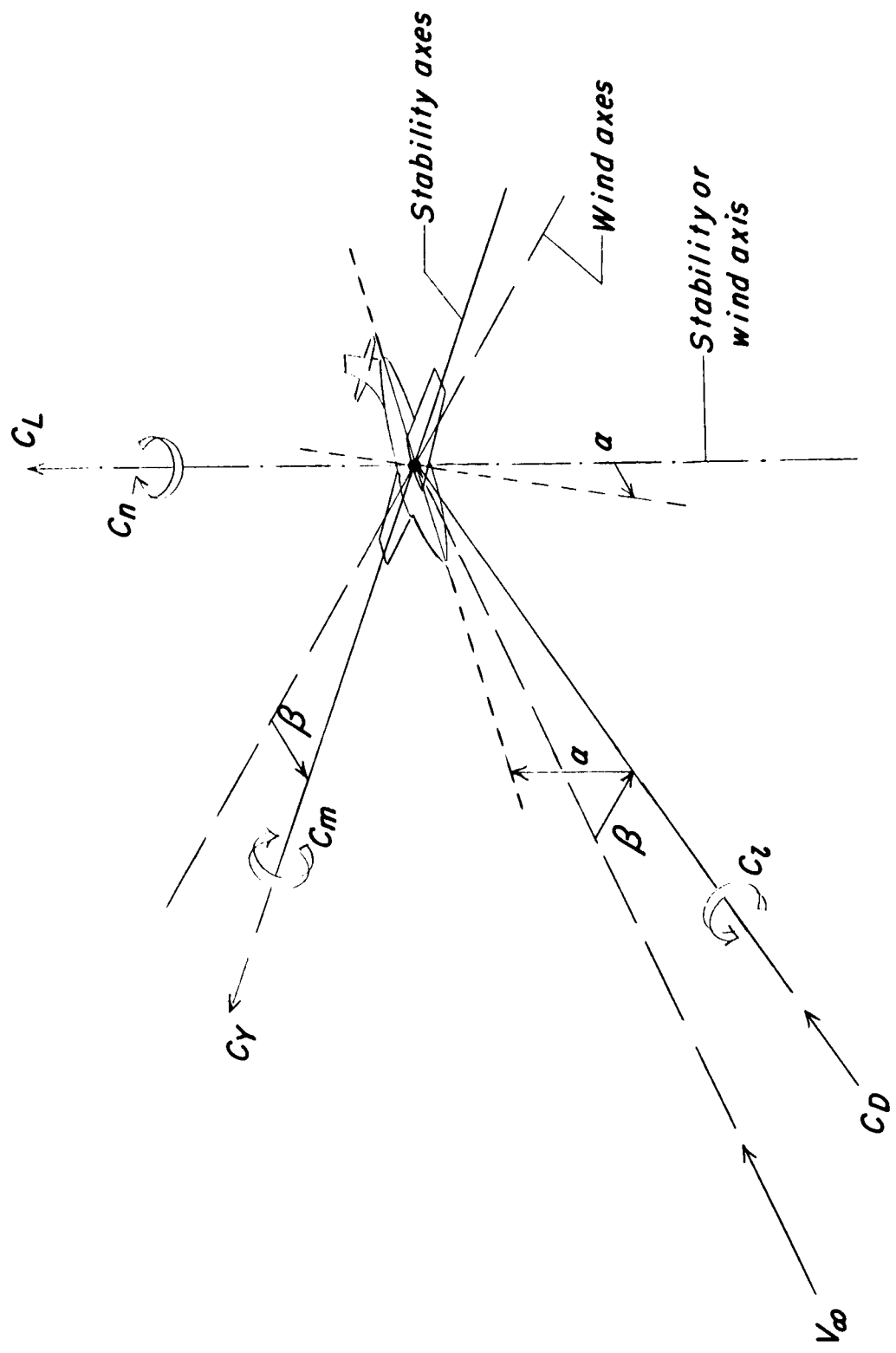
Langley Research Center,  
National Aeronautics and Space Administration,  
Langley Station, Hampton, Va., December 16, 1964.

~~DECLASSIFIED~~

REFERENCES

1. Williams, John: Some British Research on the Basic Aerodynamics of Powered Lift Systems. Jour. R.A.S., vol. 64, no. 595, July 1960, pp. 413-437.
2. Vogler, Raymond D.: Surface Pressure Distributions Induced on a Flat Plate by a Cold Air Jet Issuing Perpendicularly From the Plate and Normal to a Low-Speed Free-Stream Flow. NASA TN D-1629, 1963.
3. Vogler, Raymond D.: Interference Effects of Single and Multiple Round or Slotted Jets on a VTOL Model in Transition. NASA TN D-2380, 1964.
4. Spreemann, Kenneth P.: Investigation of Interference of a Deflected Jet With Free Stream and Ground on Aerodynamic Characteristics of a Semispan Delta-Wing VTOL Model. NASA TN D-915, 1961.
5. Otis, James H., Jr.: Induced Interference Effects on a Four-Jet VTOL Configuration With Various Wing Planforms in the Transition Speed Range. NASA TN D-1400, 1962.
6. Luoma, Arvo A.: Longitudinal Aerodynamic Characteristics at Transonic Speeds of a V/STOL Airplane Configuration With a Fixed Delta Wing Having Auxiliary Variable-Sweep Outboard Panels. NASA TM X-661, 1961.
7. Spearman, M. Leroy; and Foster, Gerald V.: Static Longitudinal and Lateral Aerodynamic Characteristics at a Mach Number of 2.01 of a Tailless Delta V/STOL Configuration Having Variable-Sweep Wing Panels. NASA TM X-634, 1961.
8. Staff of Powered-Lift Aerodynamics Section, NASA Langley Res. Center: Wall Effects and Scale Effects in V/STOL Model Testing. AIAA Aerodynamic Testing Conf., Mar. 1964, pp. 8-16.
9. Williams, John; and Butler, Sidney, F. J.: Further Developments in Low-Speed Wind-Tunnel Techniques for VSTOL and High-Lift Model Testing. AIAA Aerodynamic Testing Conf., Mar. 1964, pp. 17-32.
10. Alford, William J., Jr.; Lockwood, Vernard E.; McKinney, Linwood W.; and Grief, Richard K.: Stability and High-Lift Studies Applicable to Variable-Sweep Supersonic-Transport Configurations. Proc. NASA Conference on Supersonic-Transport Feasibility Studies and Supporting Research. NASA TM X-905, 1963, pp. 223-255.
11. Lowry, John G.; and Polhamus, Edward C.: A Method for Predicting Lift Increments Due to Flap Deflection at Low Angles of Attack in Incompressible Flow. NACA TN 3911, 1957.

Figure 1.- Conventions used to define positive forces, moments, and angles.



DECLASSIFIED

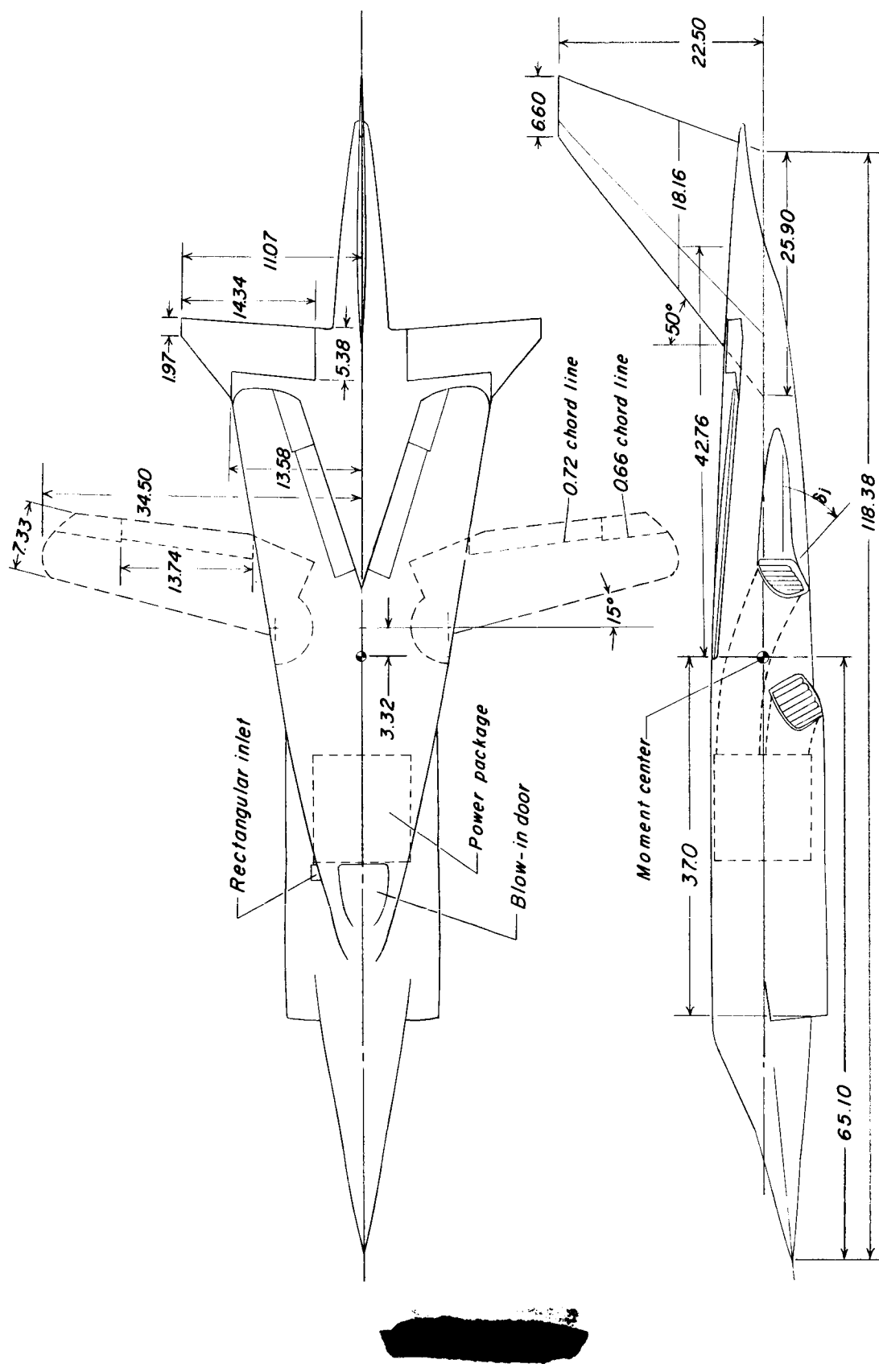


Figure 2. - Two-view drawing of the basic model. All dimensions are in inches.

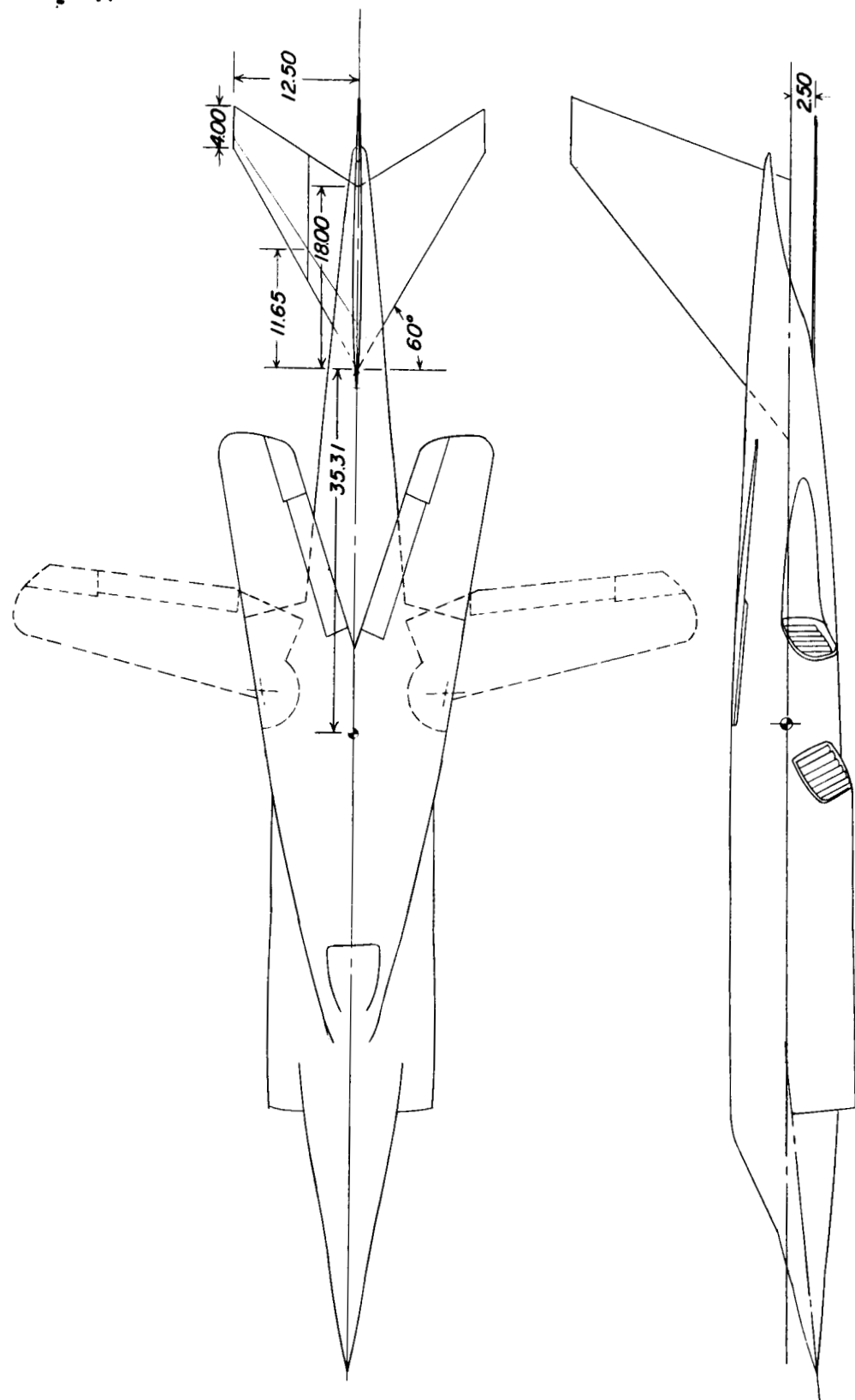
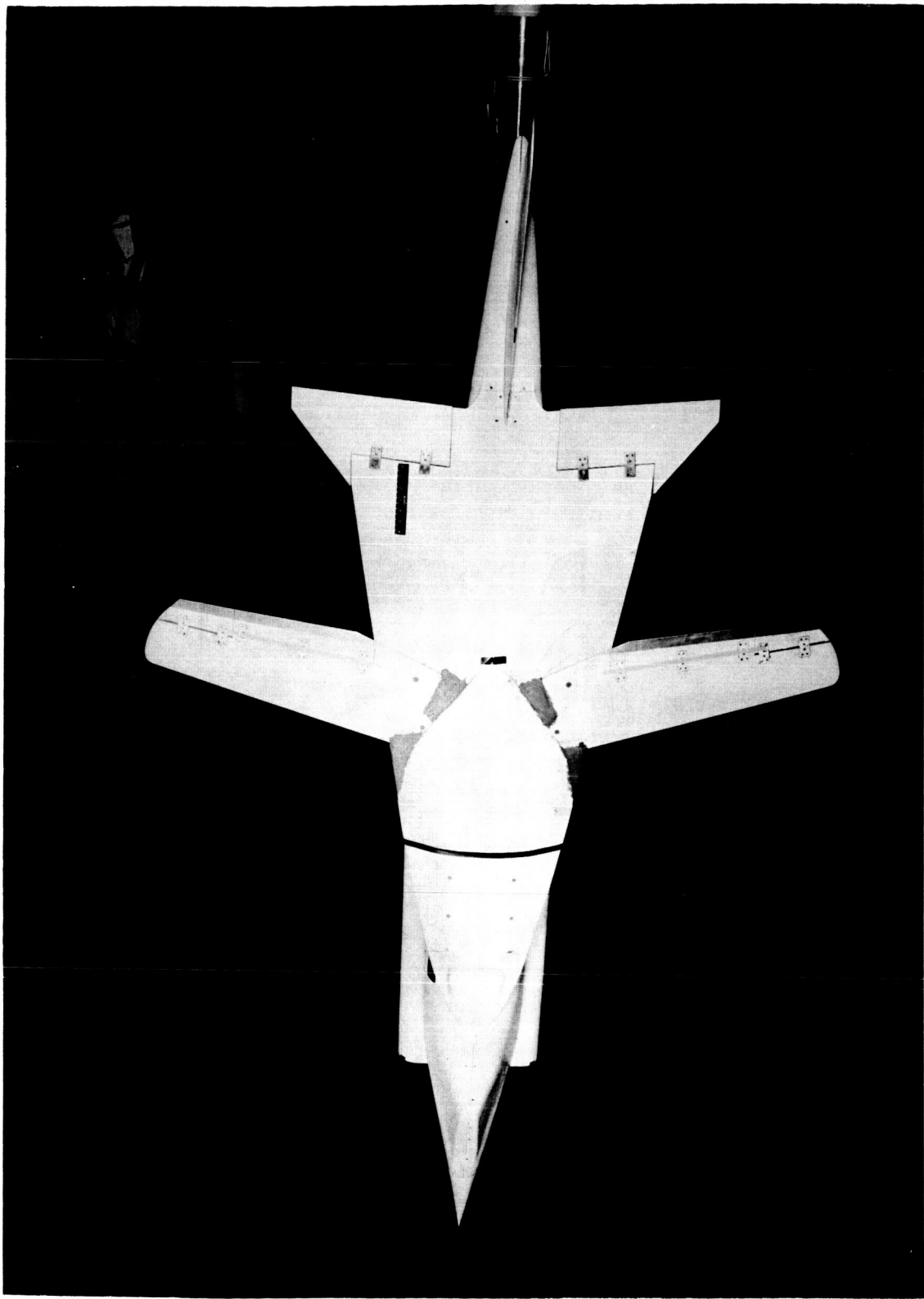


Figure 3.- Two-view drawing of the modified model. All dimensions are in inches.

DECLASSIFIED

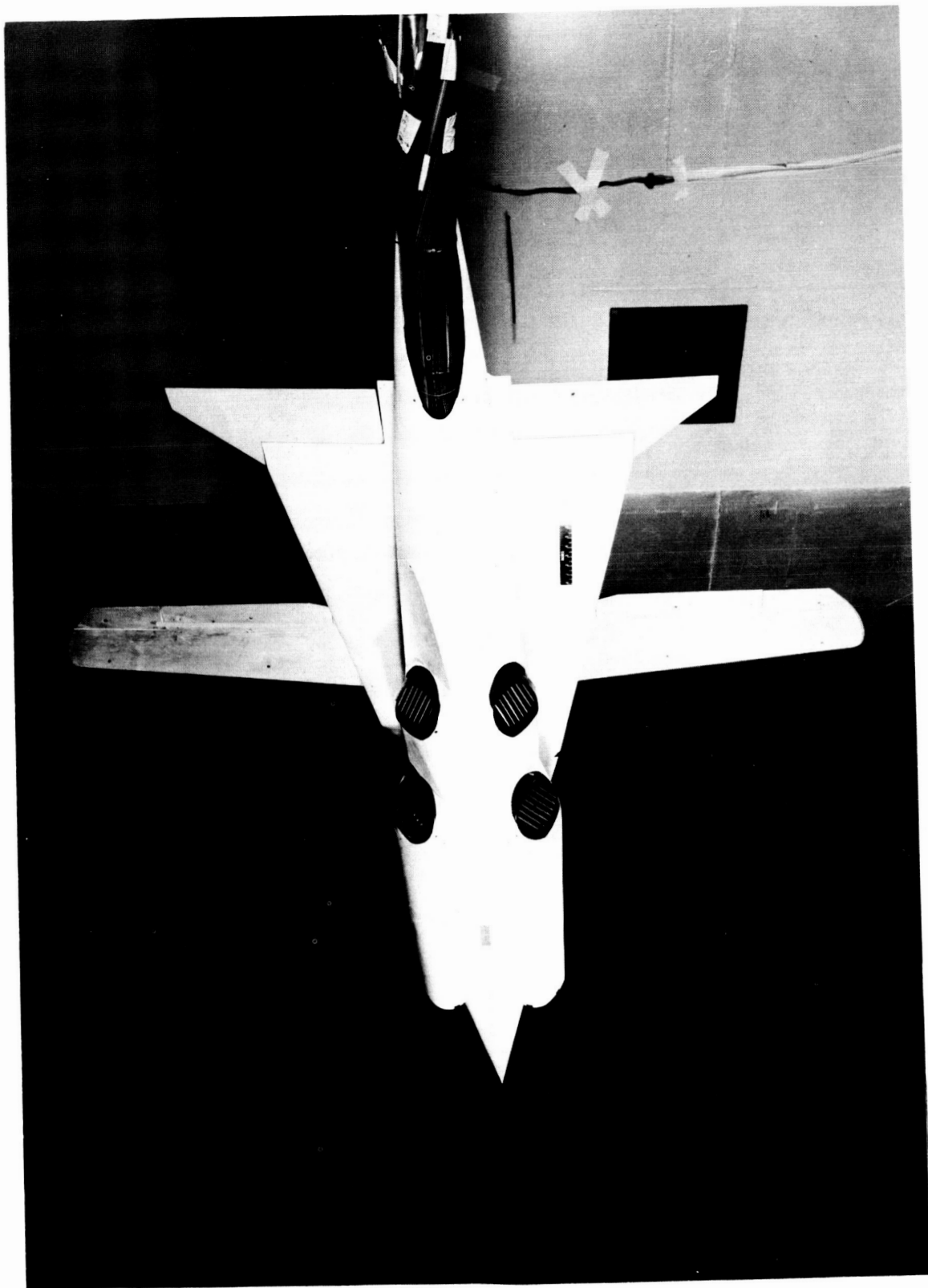


(a) Top view.

Figure 4.- Photographs of basic model.

L-61-7788

031703.00 1030

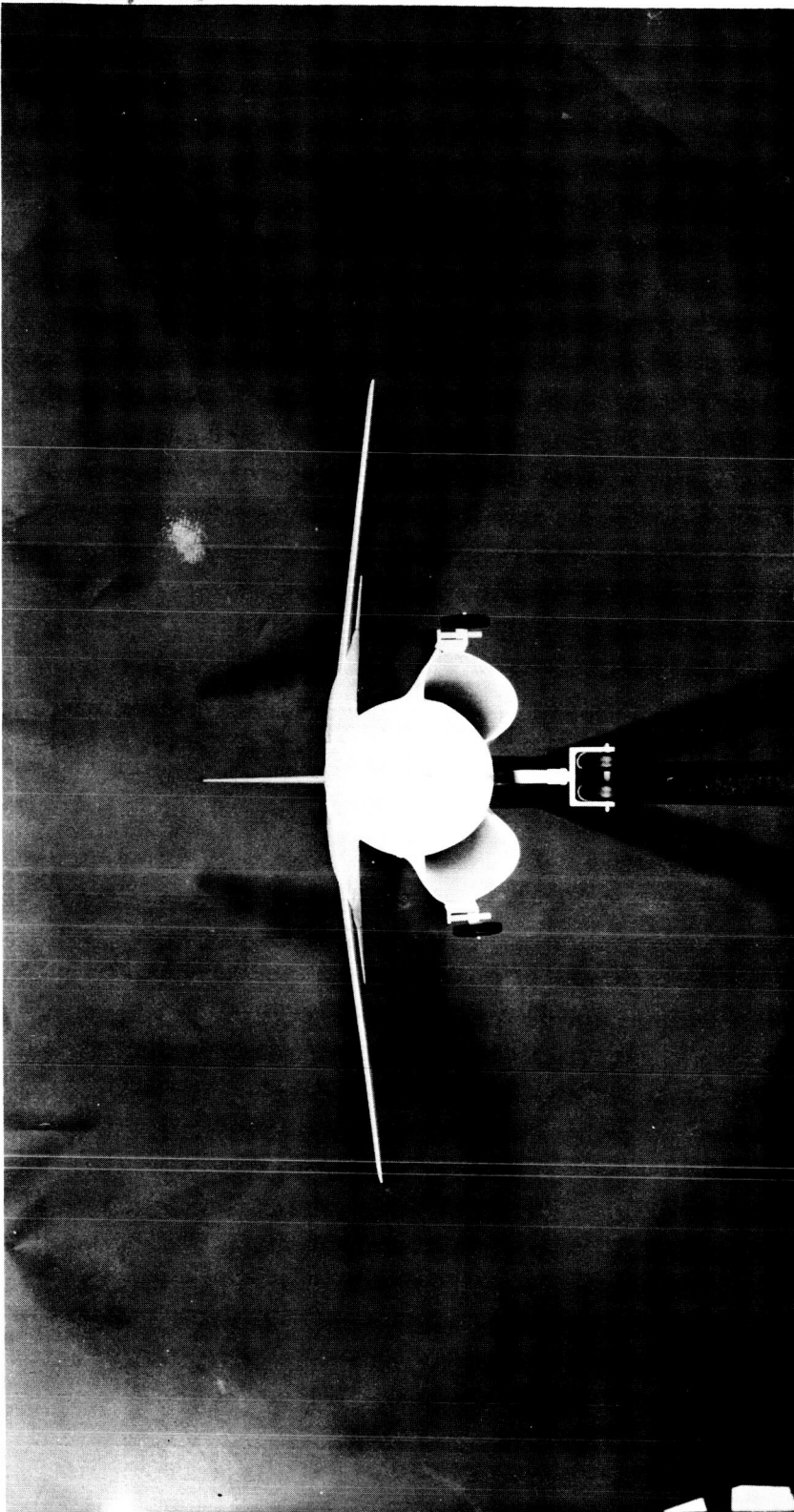


L-61-7787

(b) Bottom view with jet deflected  $78^\circ$ .

Figure 4.- Continued.

DECLASSIFIED



(c) Front view.

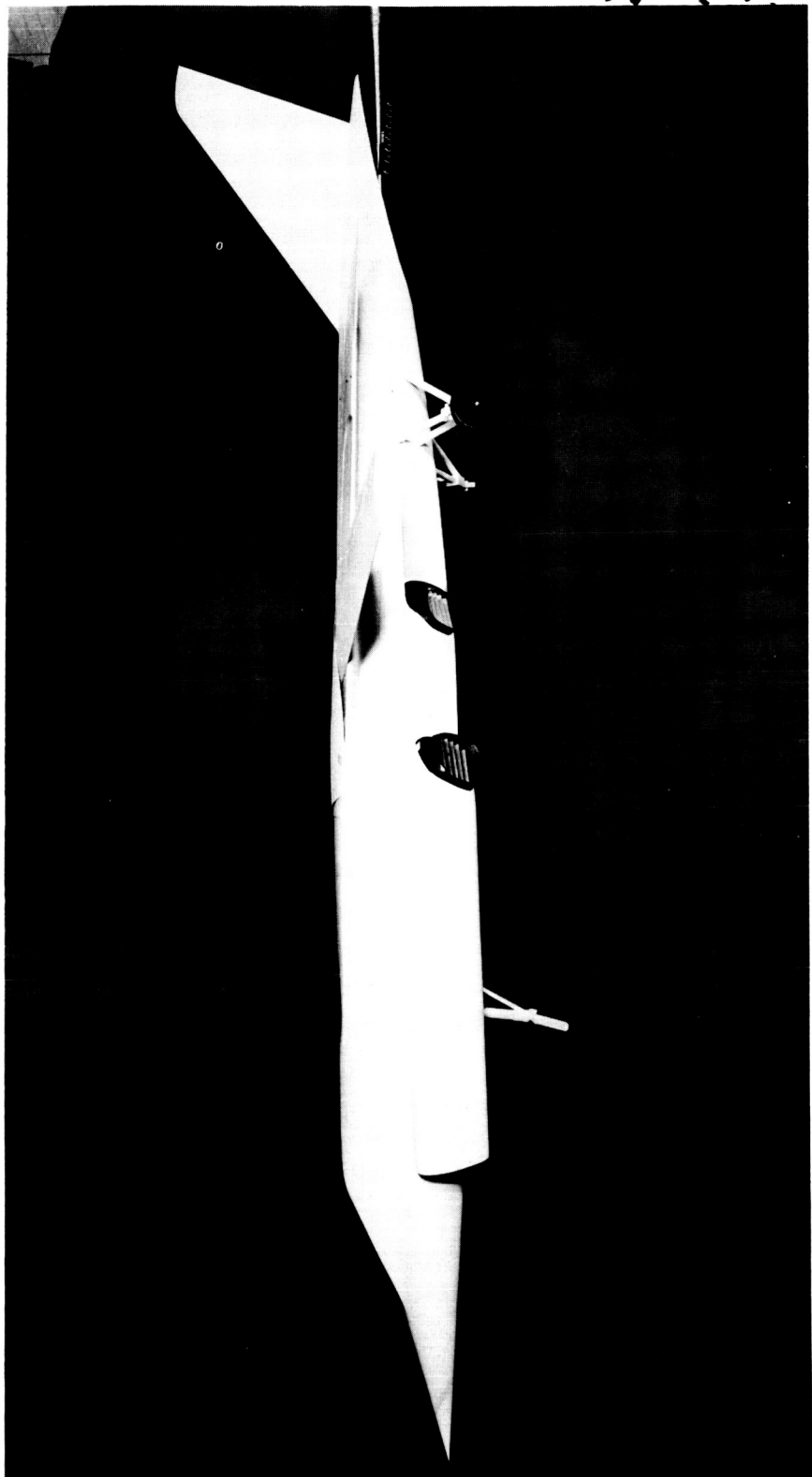
Figure 4.- Continued.

I-62-2641

L-62-2646

(d) Side view with jet deflected  $78^{\circ}$ .

Figure 4.- Concluded.



DECLASSIFIED

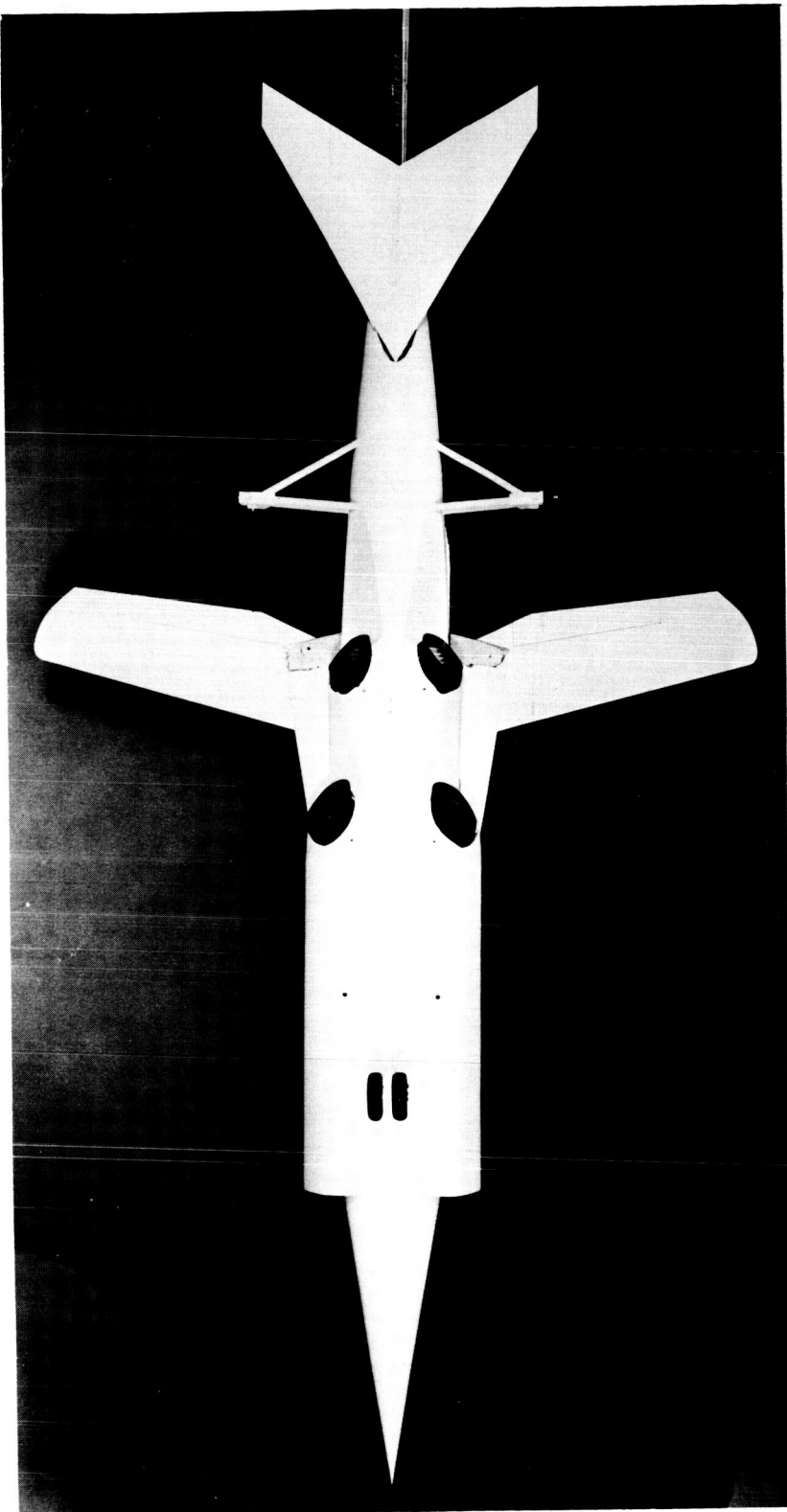


Figure 5.- Bottom view of modified model with jet in cruising position ( $\delta_j = 4^\circ$ ).

L-62-2647

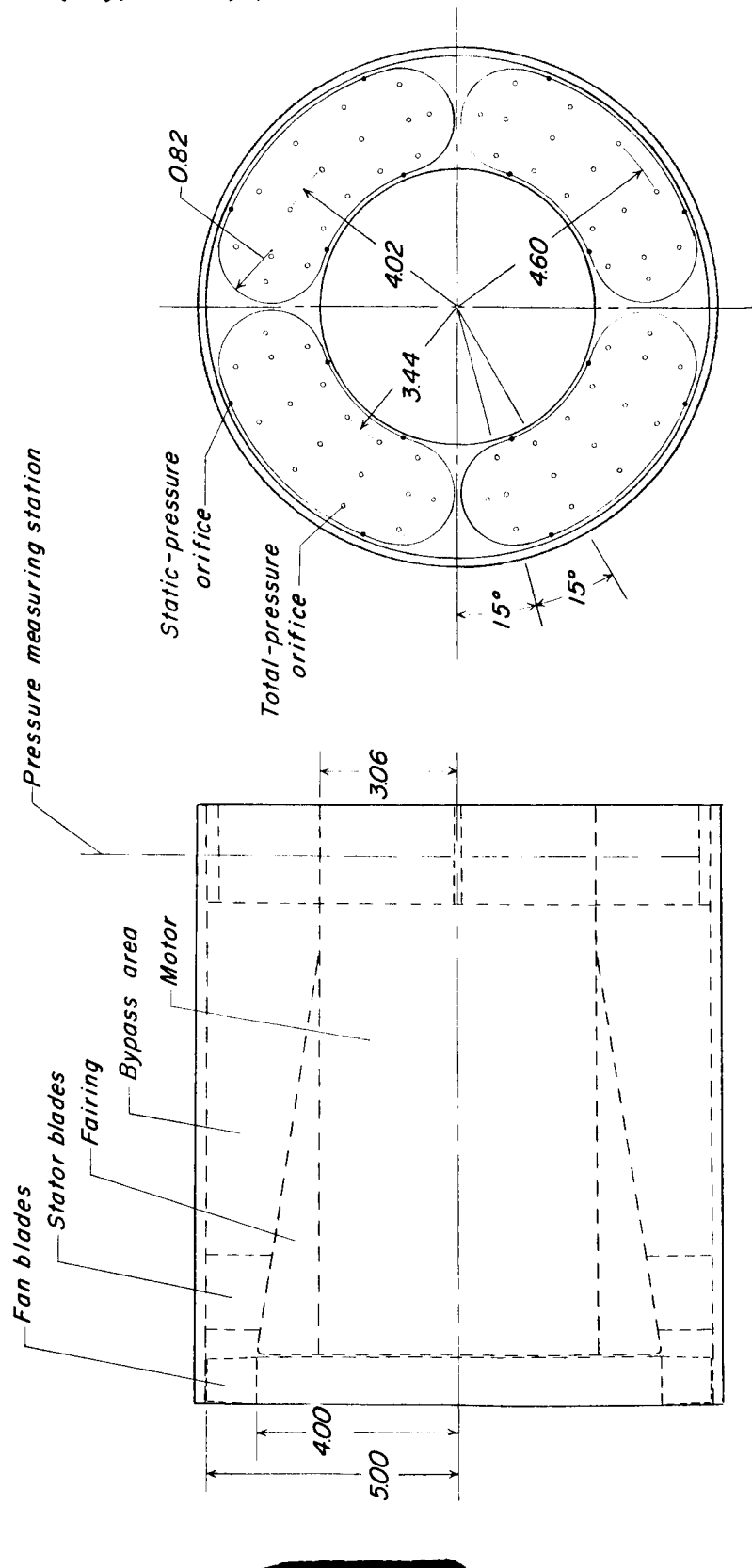


Figure 6.- The internal power package for operating the jets and the pressure tube layout at the rear of the motor.

DECLASSIFIED

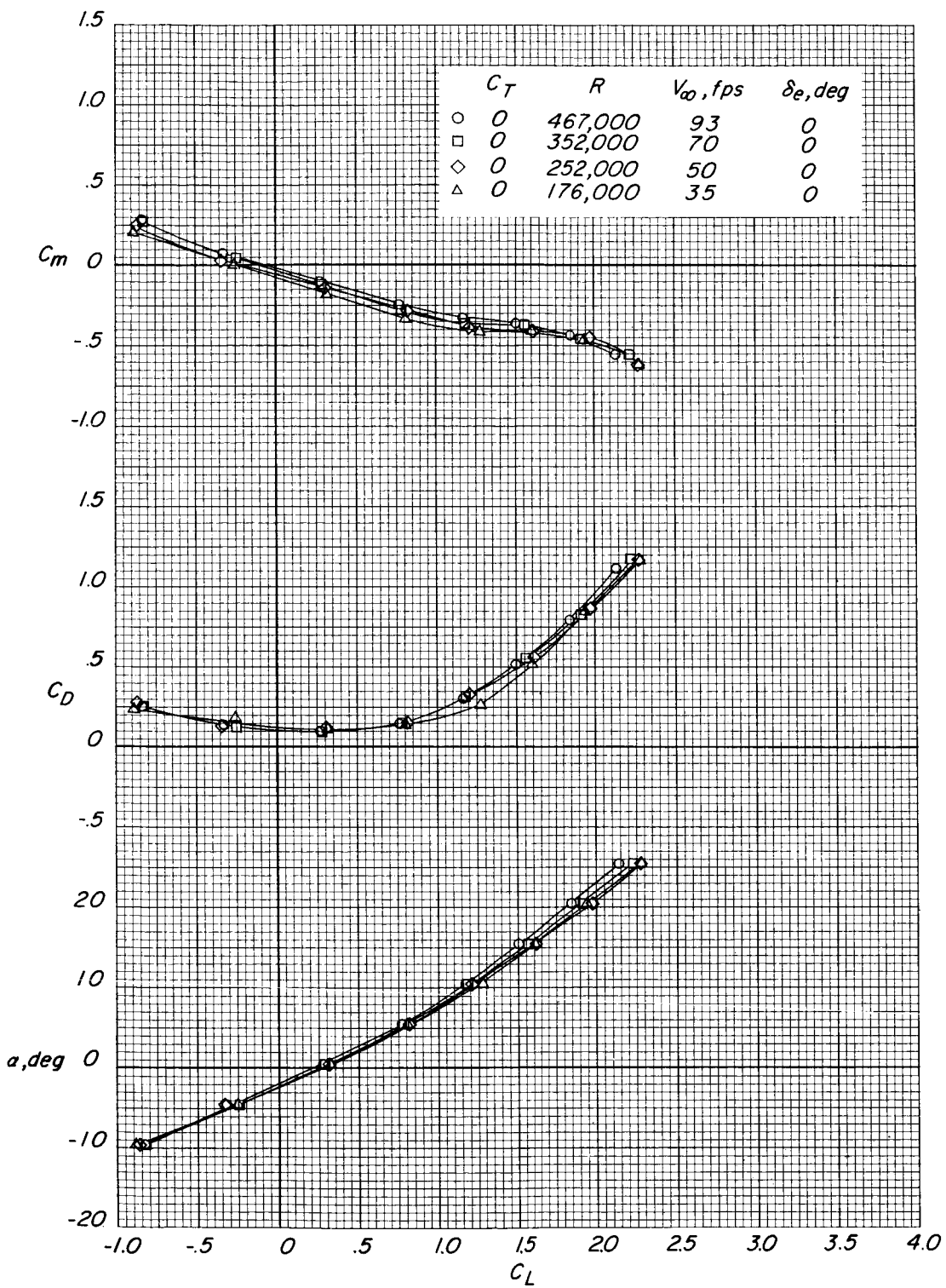


Figure 7.- Effect of Reynolds number on the power-off aerodynamic characteristics of the basic model.  $\Delta = 15^\circ$ .

# DATA FOR 1030

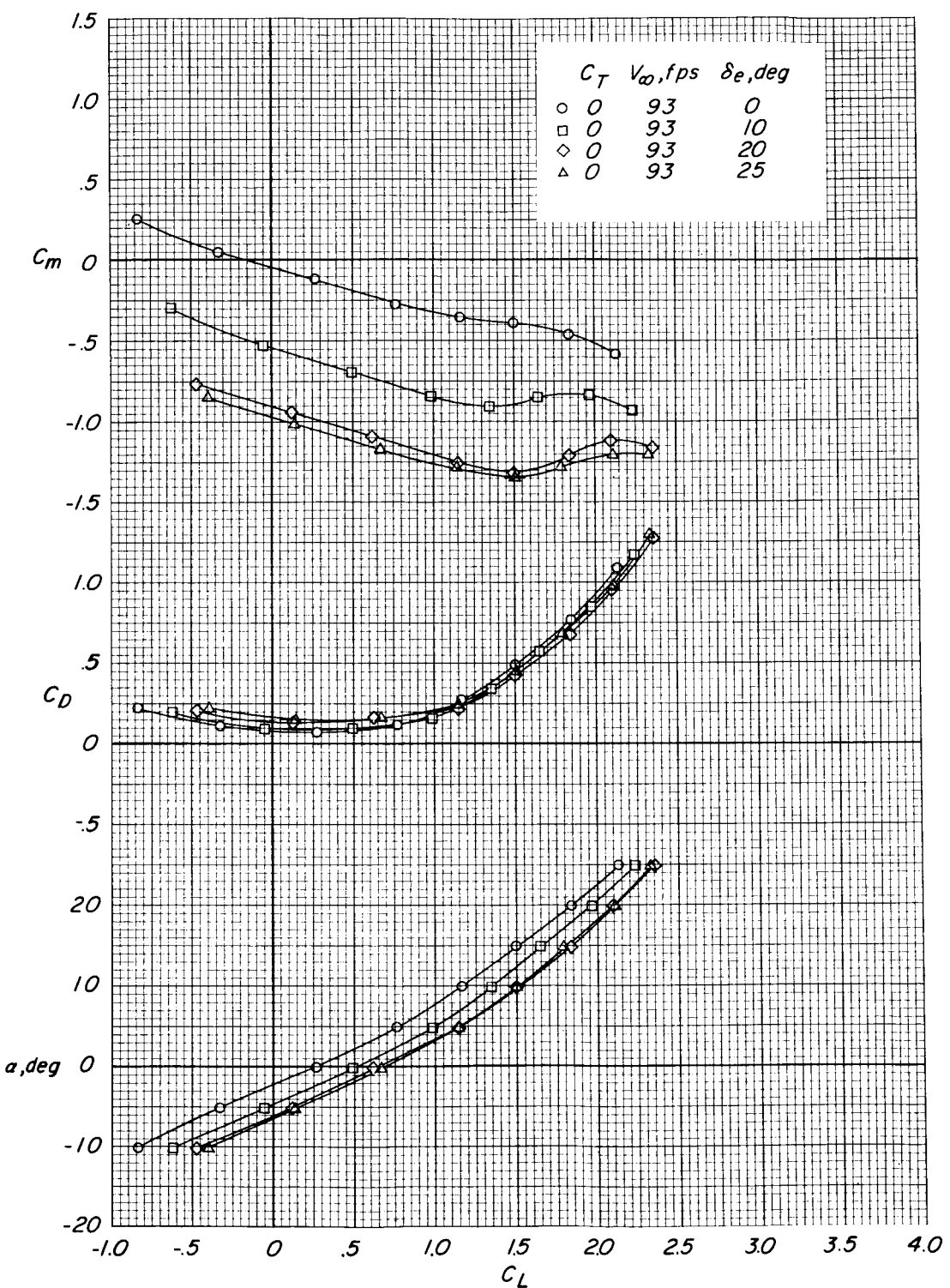


Figure 8.- Effect of elevator deflection on the power-off aerodynamic characteristics of the basic model.  $\Lambda = 15^\circ$ .

DECLASSIFIED

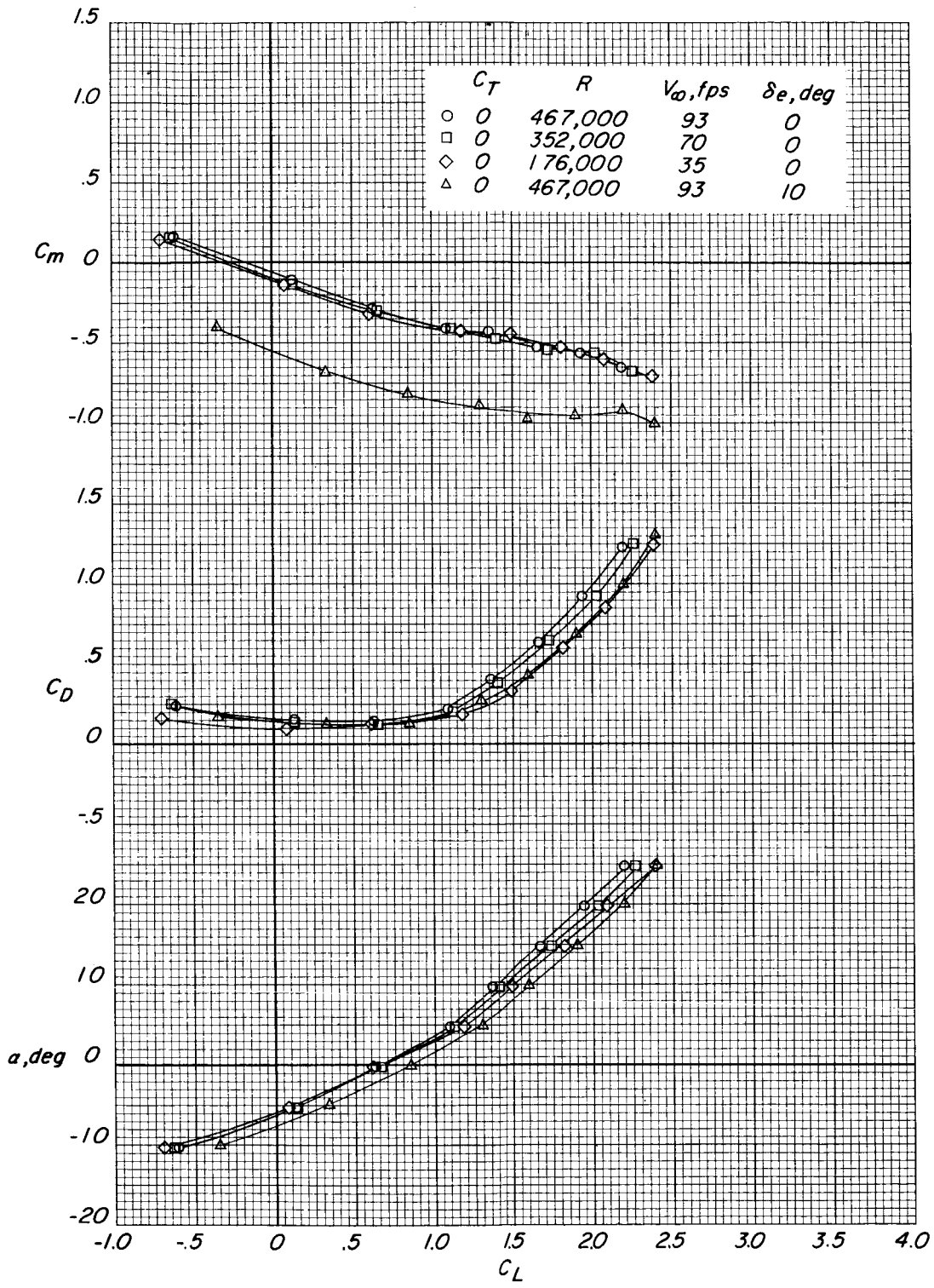
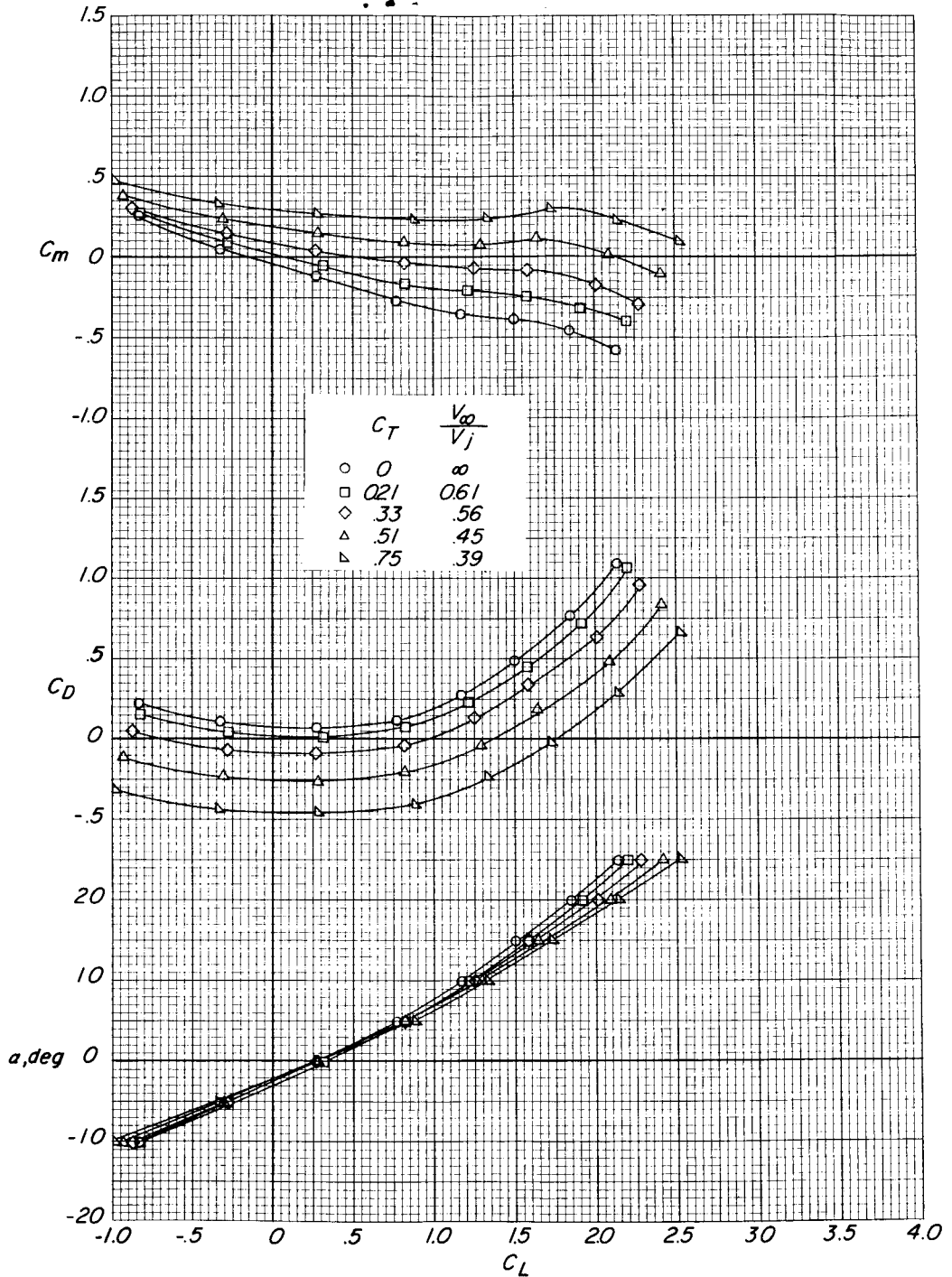


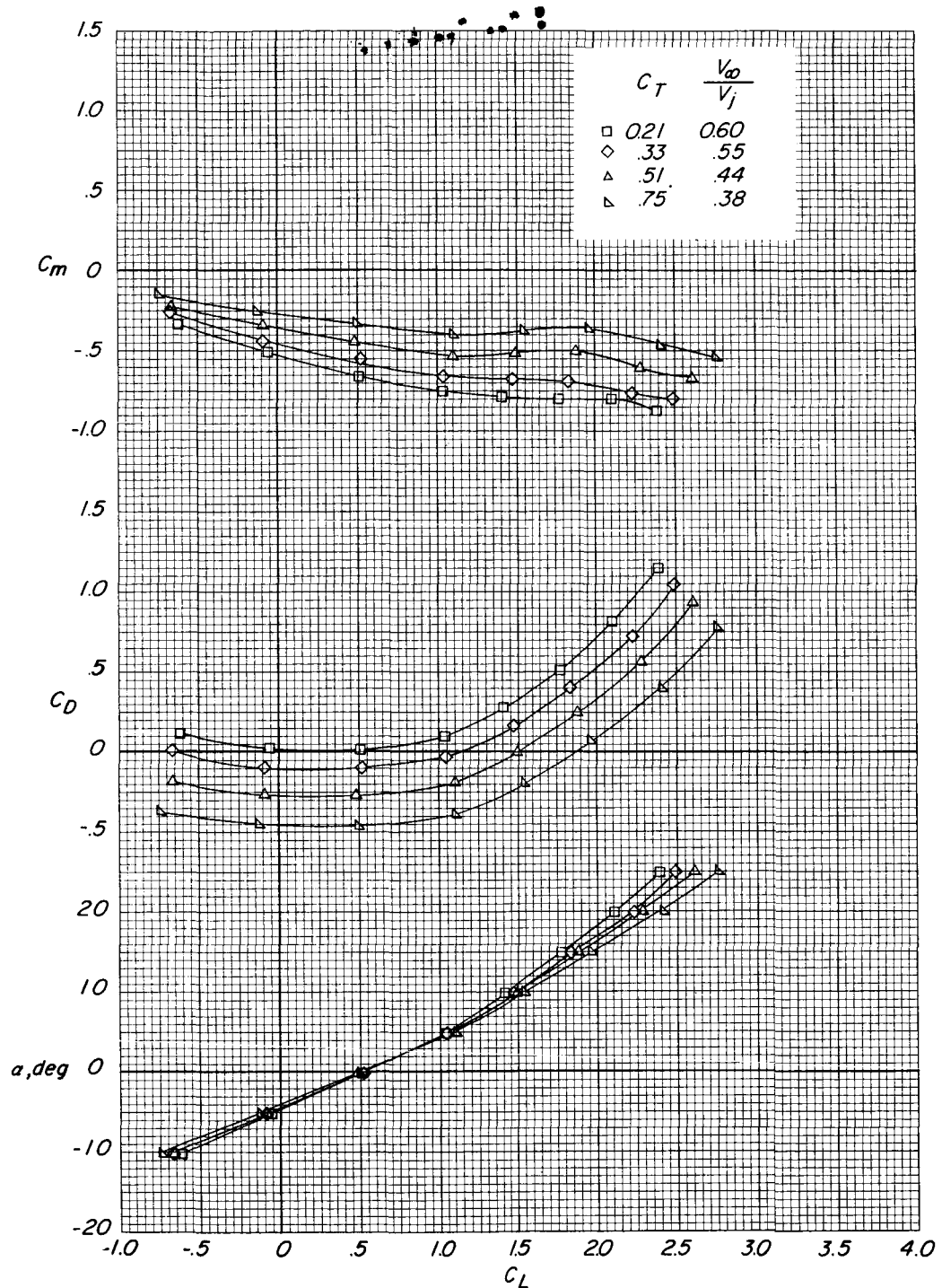
Figure 9.- Effect of Reynolds number and elevator deflection with flaps deflected  $40^\circ$  on the power-off aerodynamic characteristics of the basic model.  $\Delta = 15^\circ$ .



(a)  $\delta_j = 4^\circ$ ;  $\delta_e = 0^\circ$ .

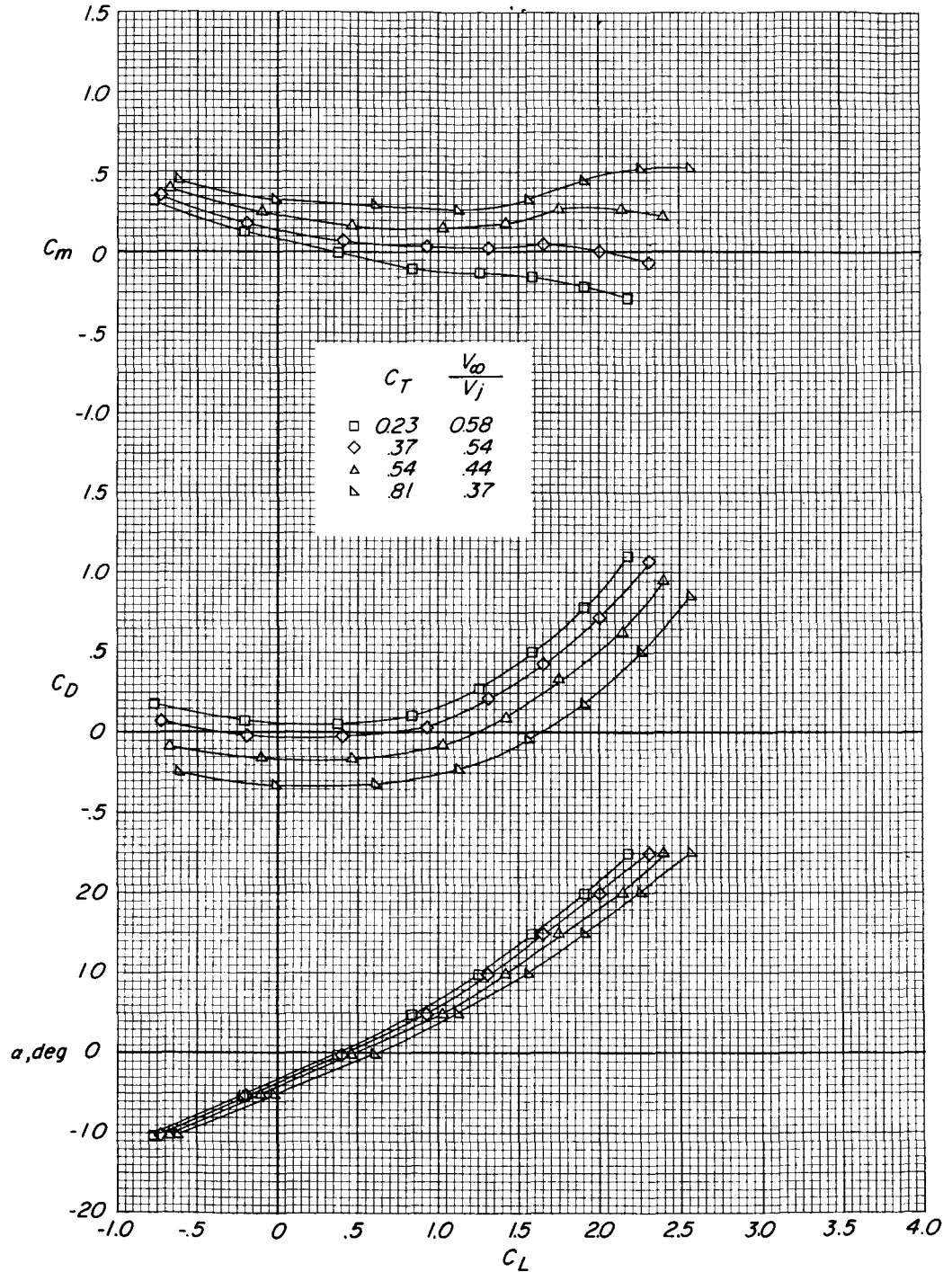
Figure 10.- Effect of power on the longitudinal aerodynamic characteristics of the basic model with flaps undeflected.  $\Lambda = 15^\circ$ .

# DECCELERATED



(b)  $\delta_j = 4^\circ$ ;  $\delta_e = 10^\circ$ .

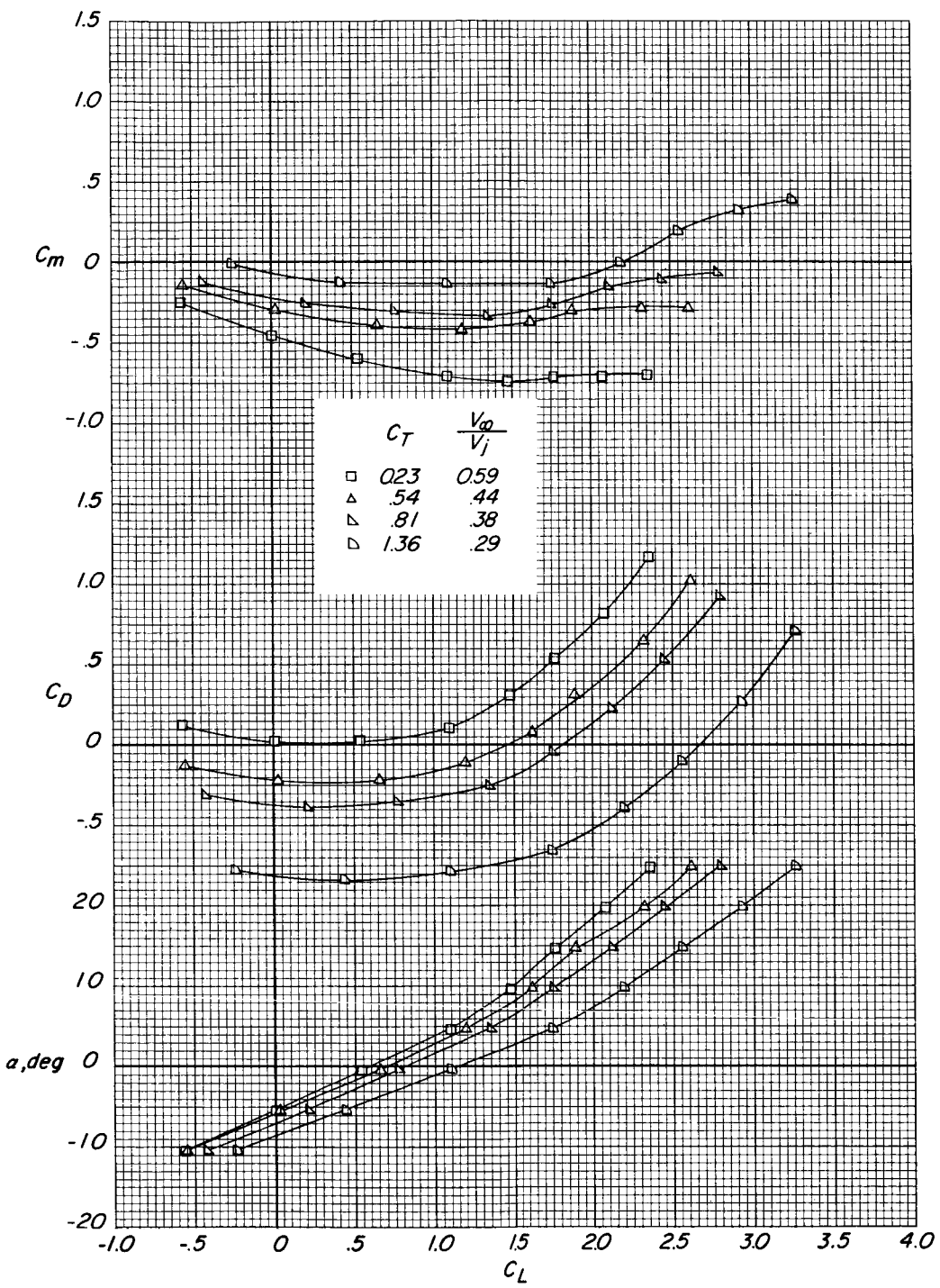
Figure 10.- Continued.



(c)  $\delta_j = 31^\circ$ ;  $\delta_e = 0^\circ$ .

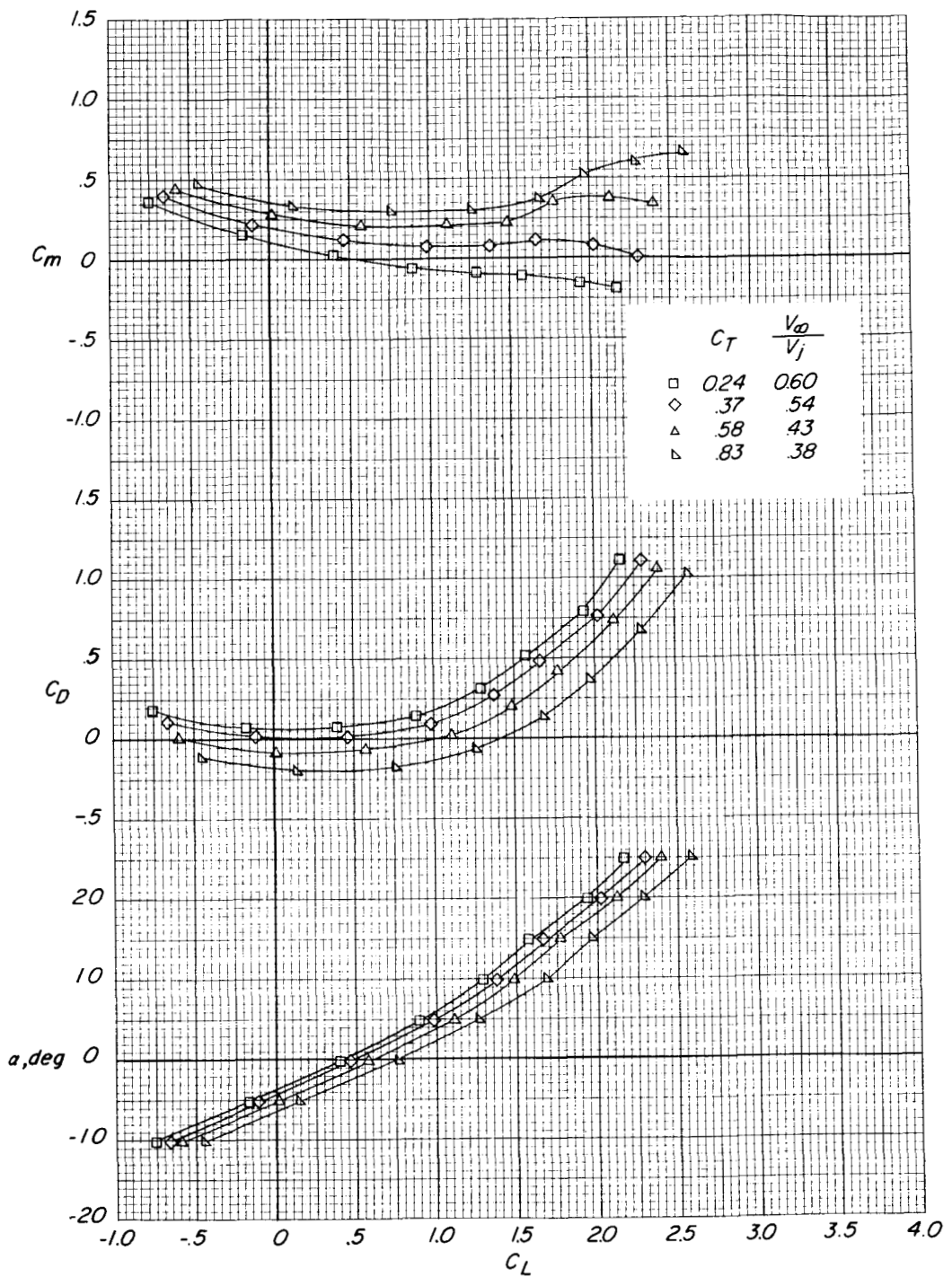
Figure 10.- Continued.

# DECORATED



(d)  $\delta_j = 31^\circ$ ;  $\delta_e = 10^\circ$ .

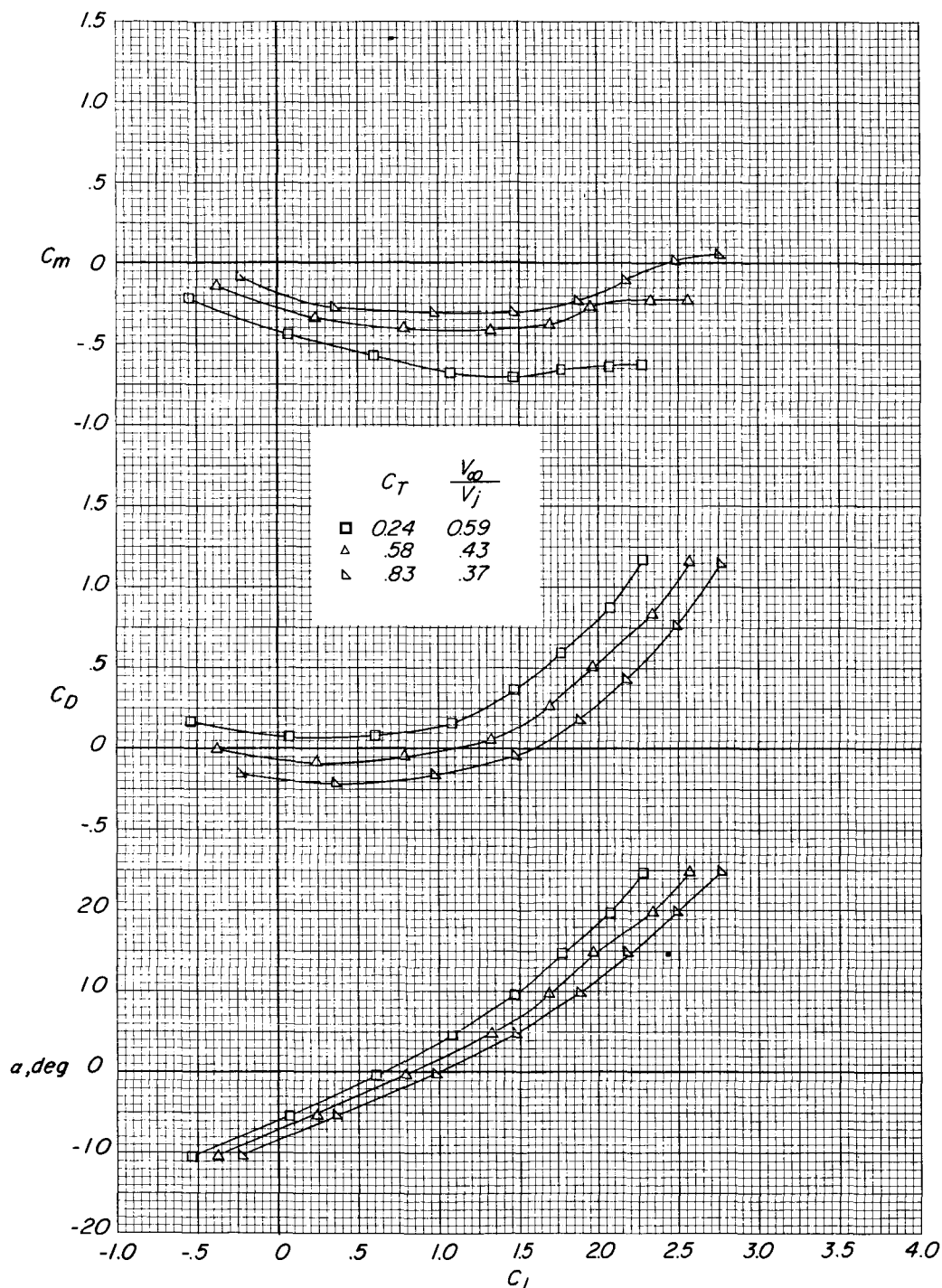
Figure 10.- Continued.



(e)  $\delta_j = 49^\circ$ ;  $\delta_e = 0^\circ$ .

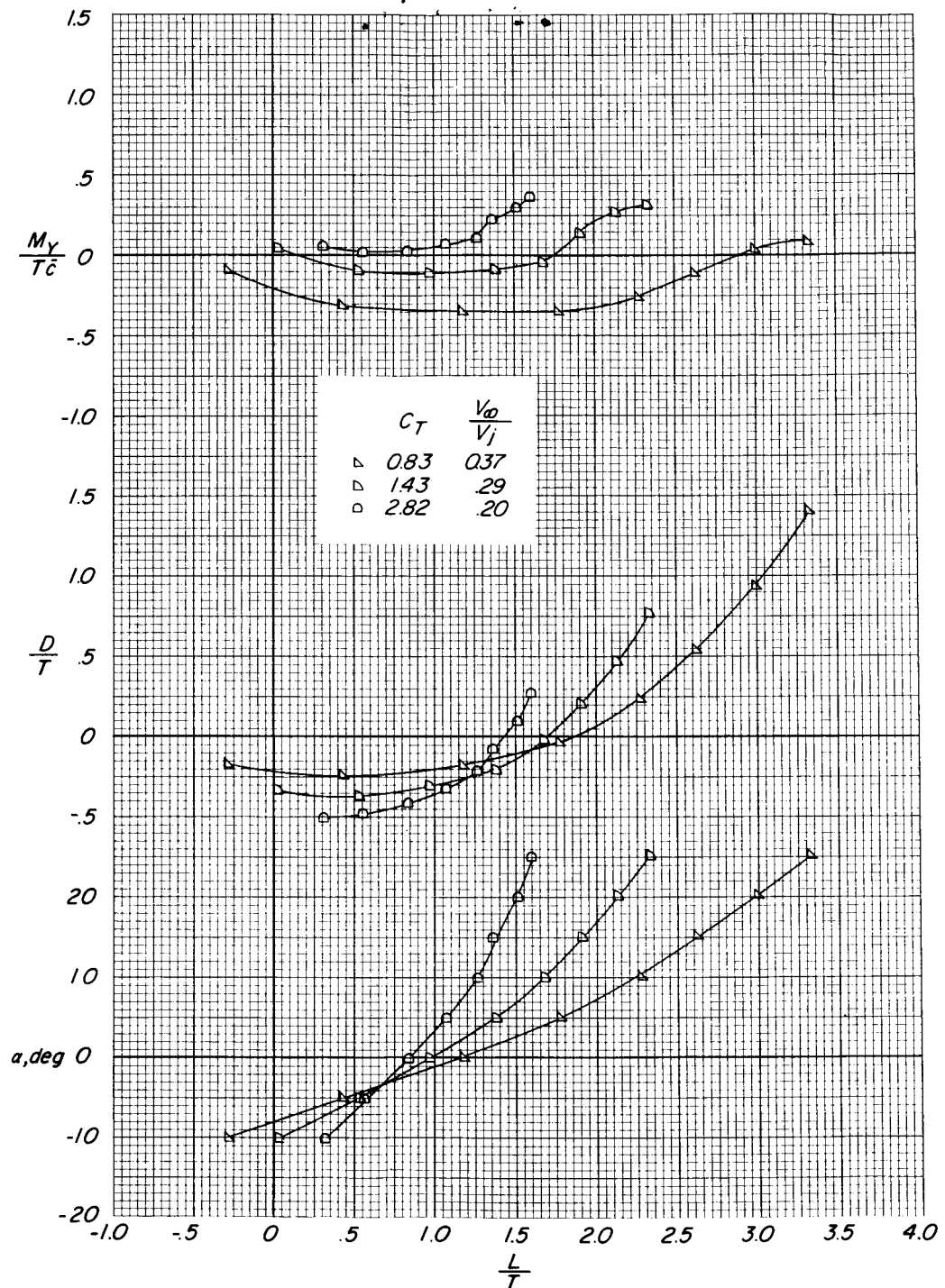
Figure 10.- Continued.

DECLASSIFIED



(f)  $\delta_j = 49^\circ$ ;  $\delta_e = 10^\circ$ .

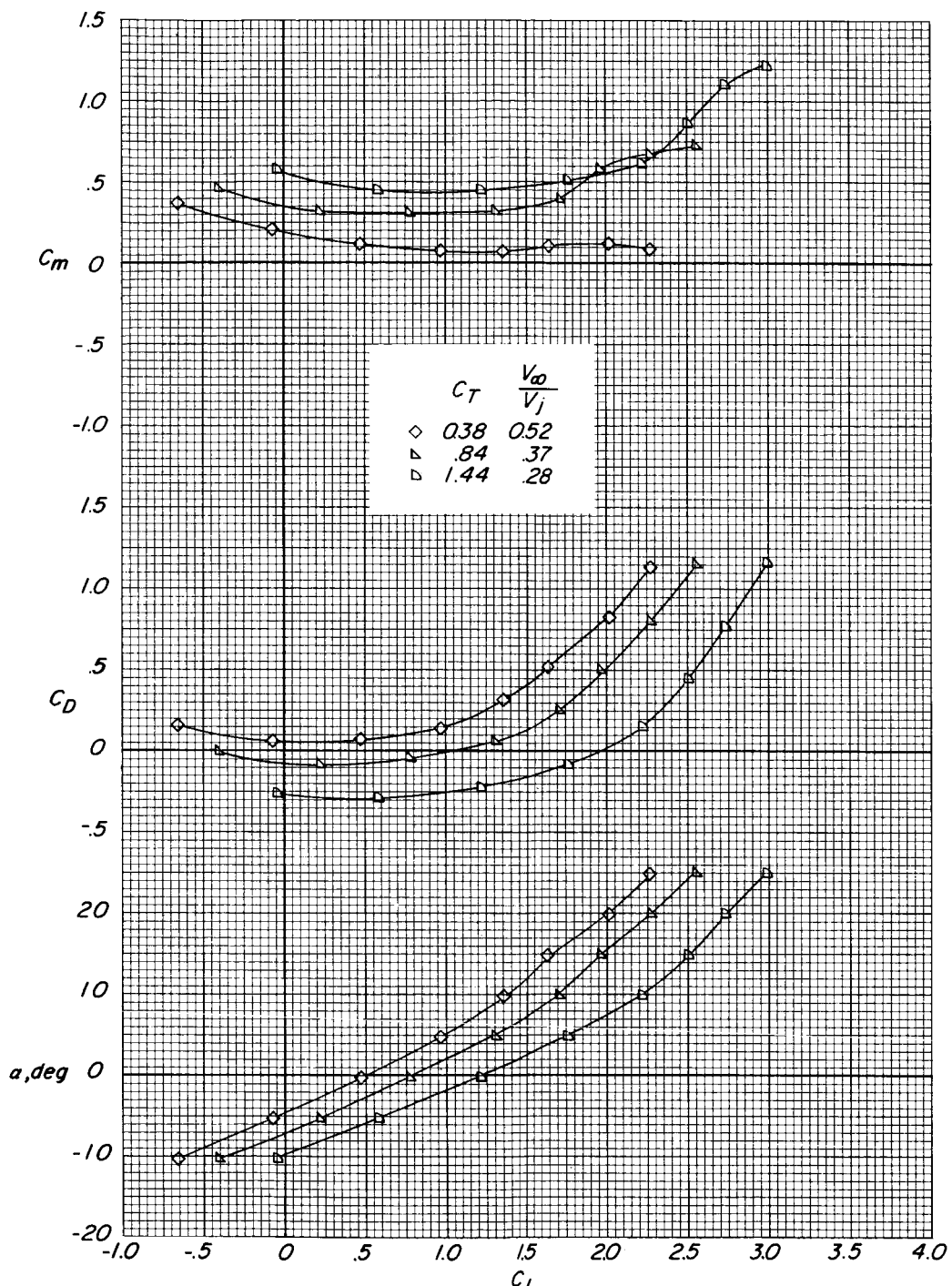
Figure 10.- Continued.



(f)  $\delta_J = 49^\circ$ ;  $\delta_e = 10^\circ$ . Concluded.

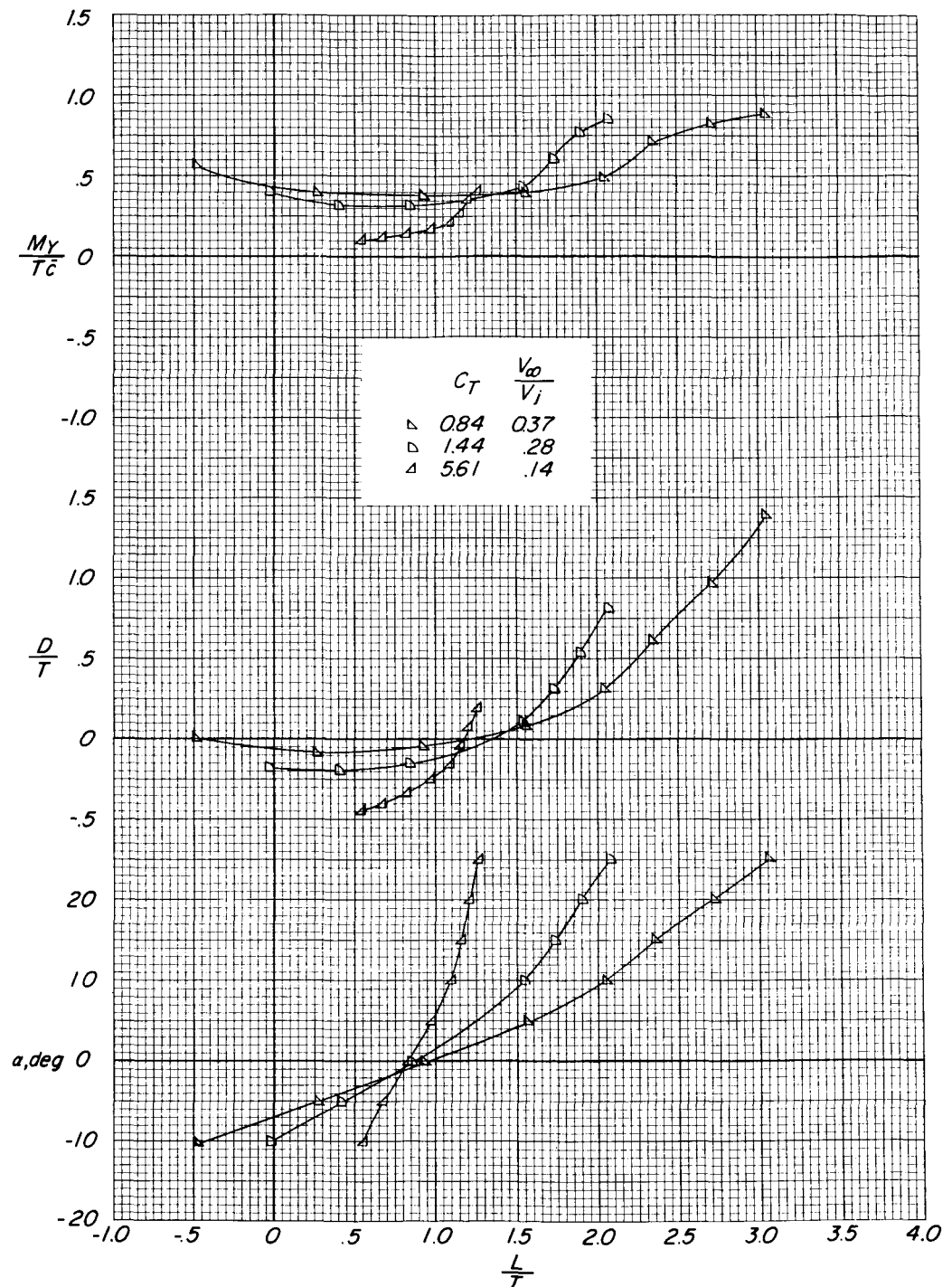
Figure 10.- Continued.

DECLASSIFIED



(g)  $\delta_j = 60^\circ$ ;  $\delta_e = 0^\circ$ .

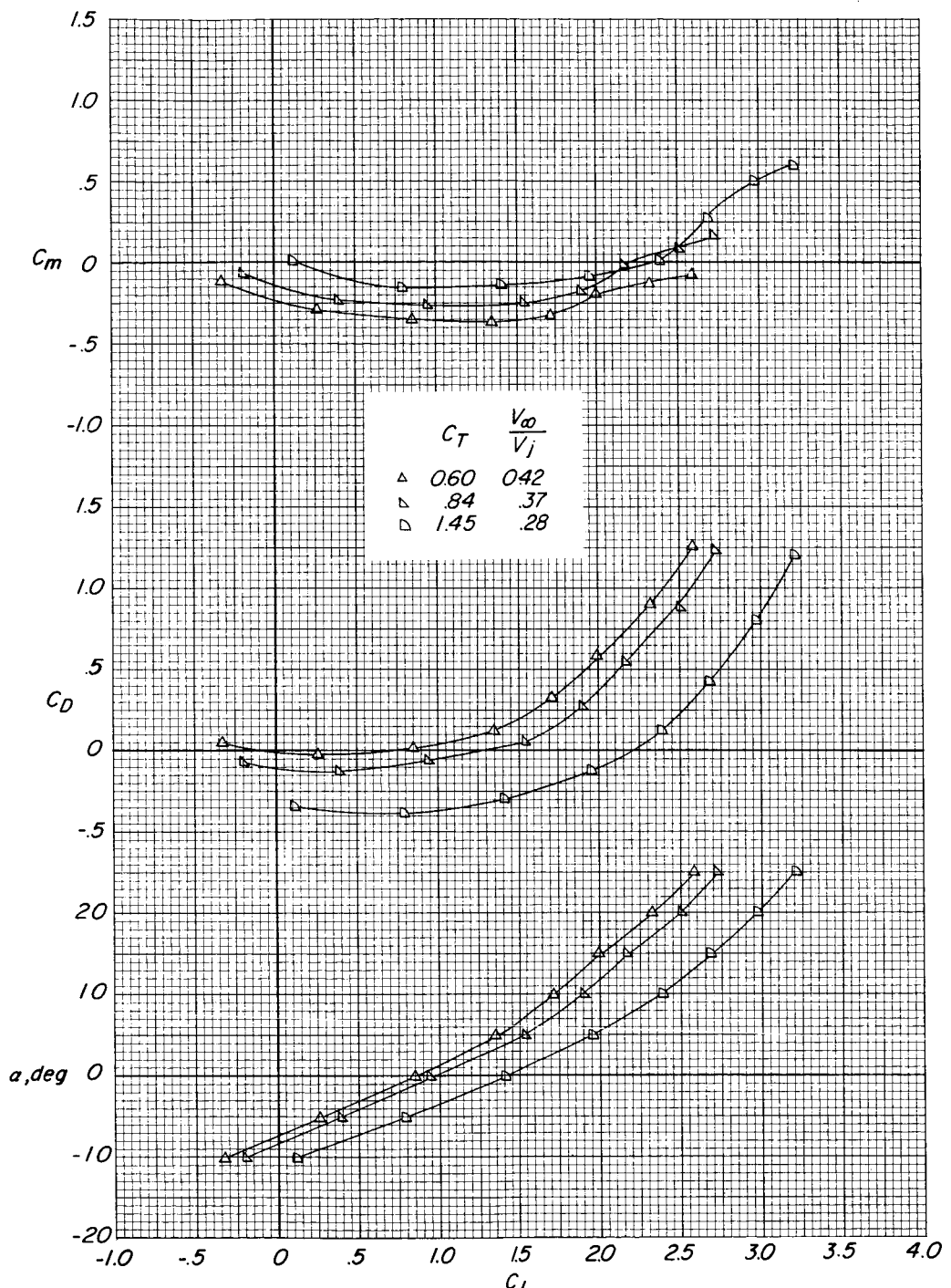
Figure 10.- Continued.



(g)  $\delta_j = 60^\circ$ ;  $\delta_e = 0^\circ$ . Concluded.

Figure 10.- Continued.

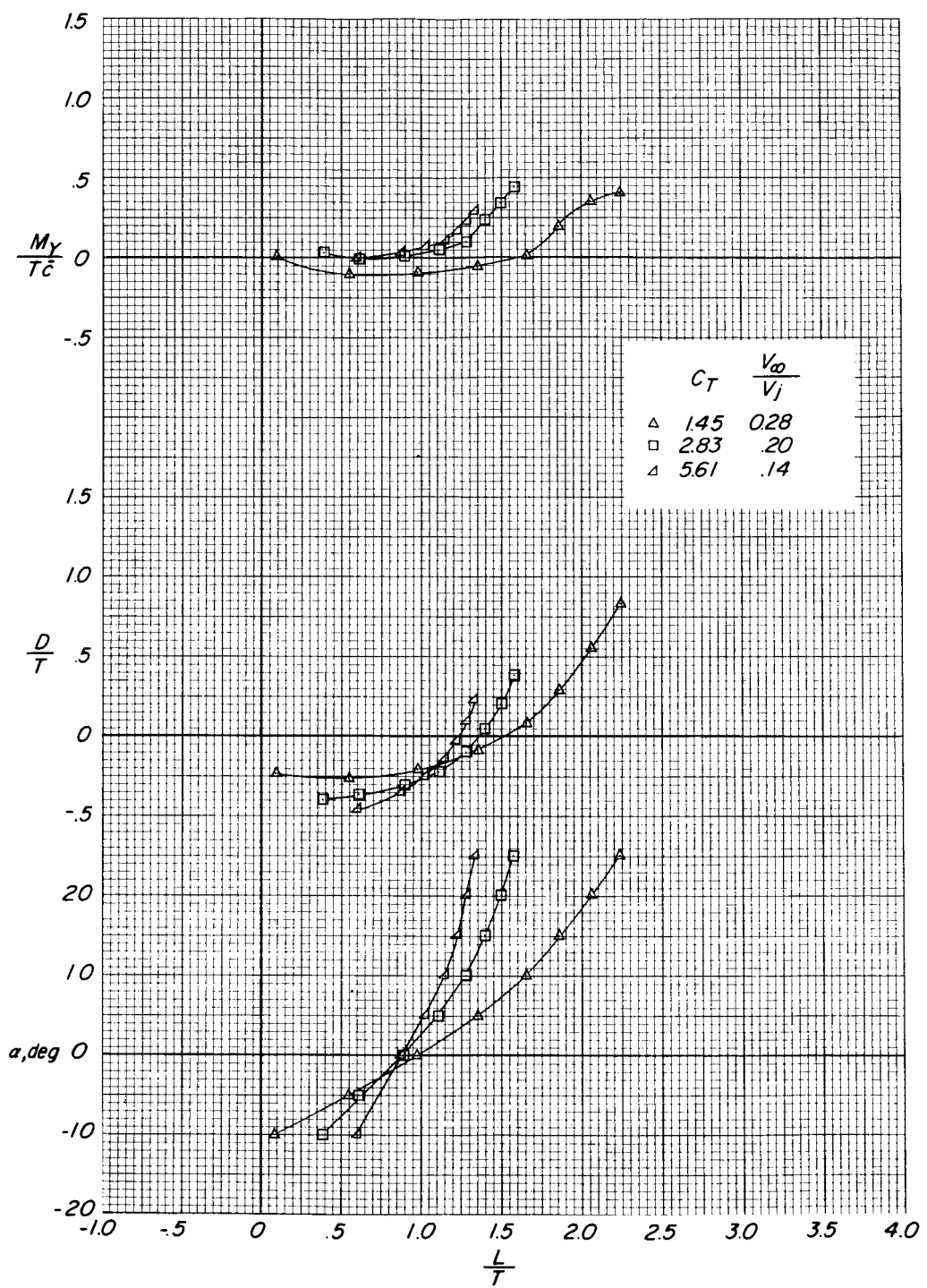
~~DECLASSIFIED~~



(h)  $\delta_j = 60^\circ$ ;  $\delta_e = 10^\circ$ .

Figure 10.- Continued.

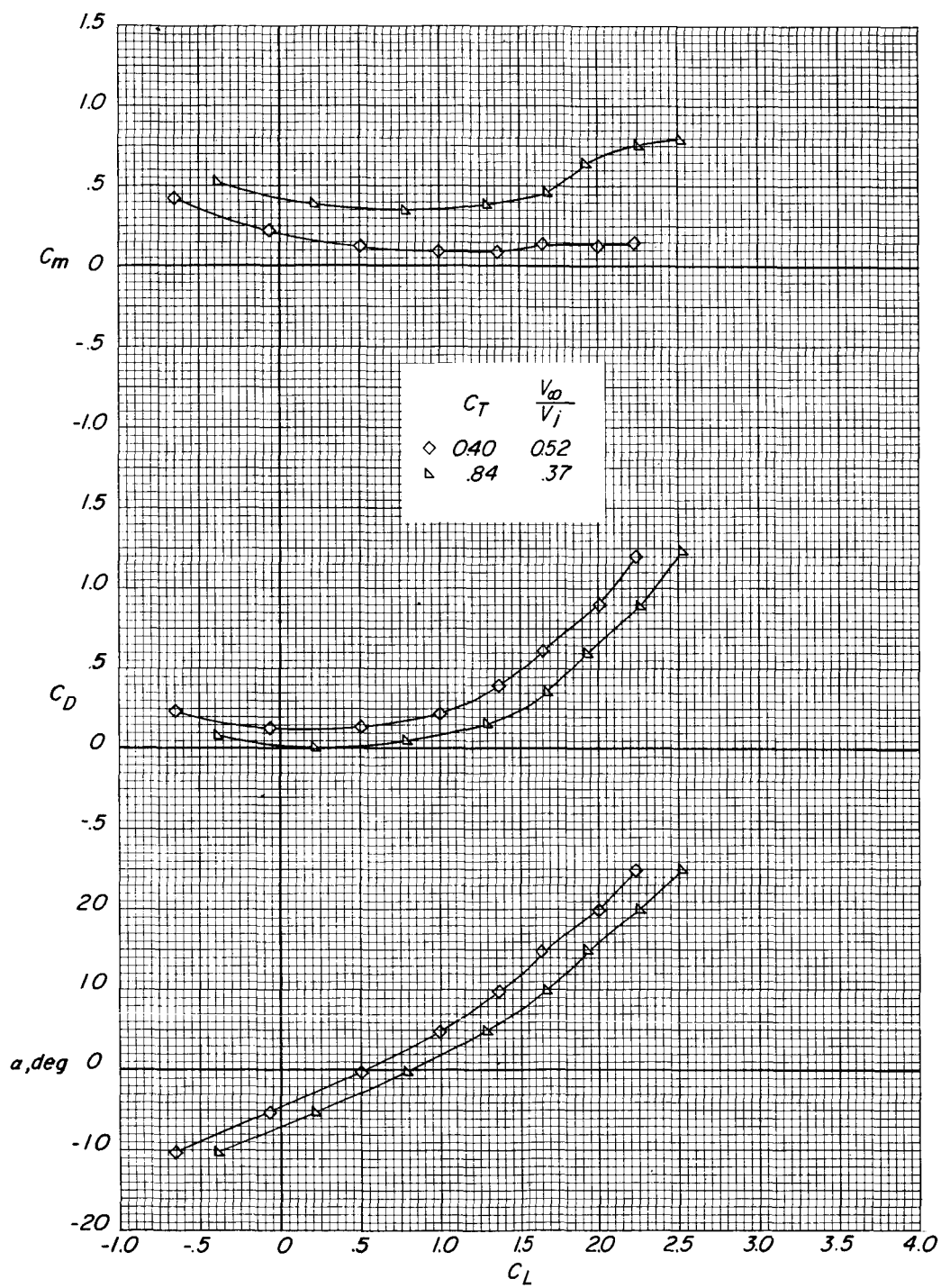
00120000 1030



(h)  $\delta_j = 60^\circ$ ;  $\delta_e = 10^\circ$ . Concluded.

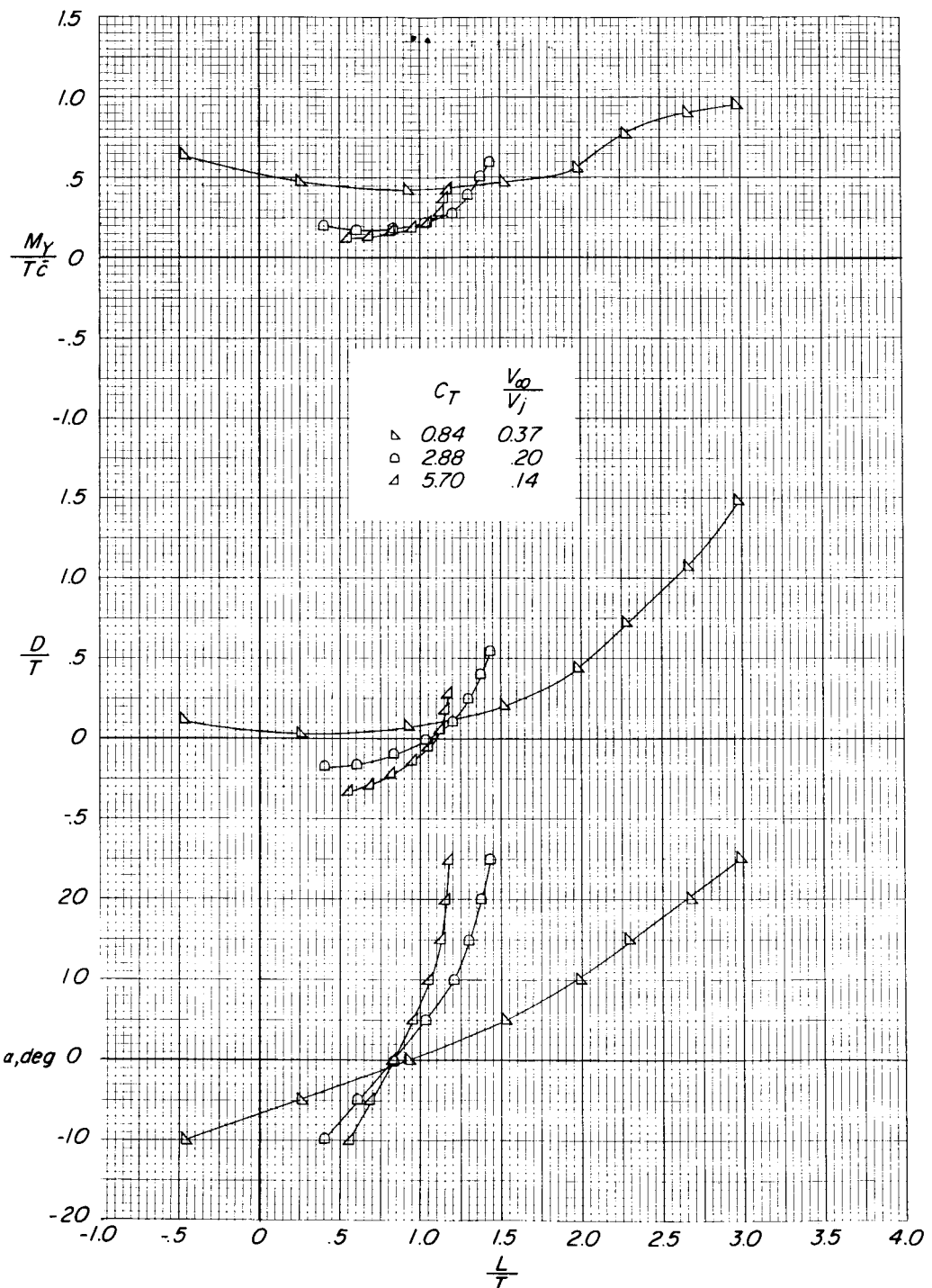
Figure 10.- Continued.

DECLASSIFIED



(i)  $\delta_j = 68^\circ$ ;  $\delta_e = 0^\circ$ .

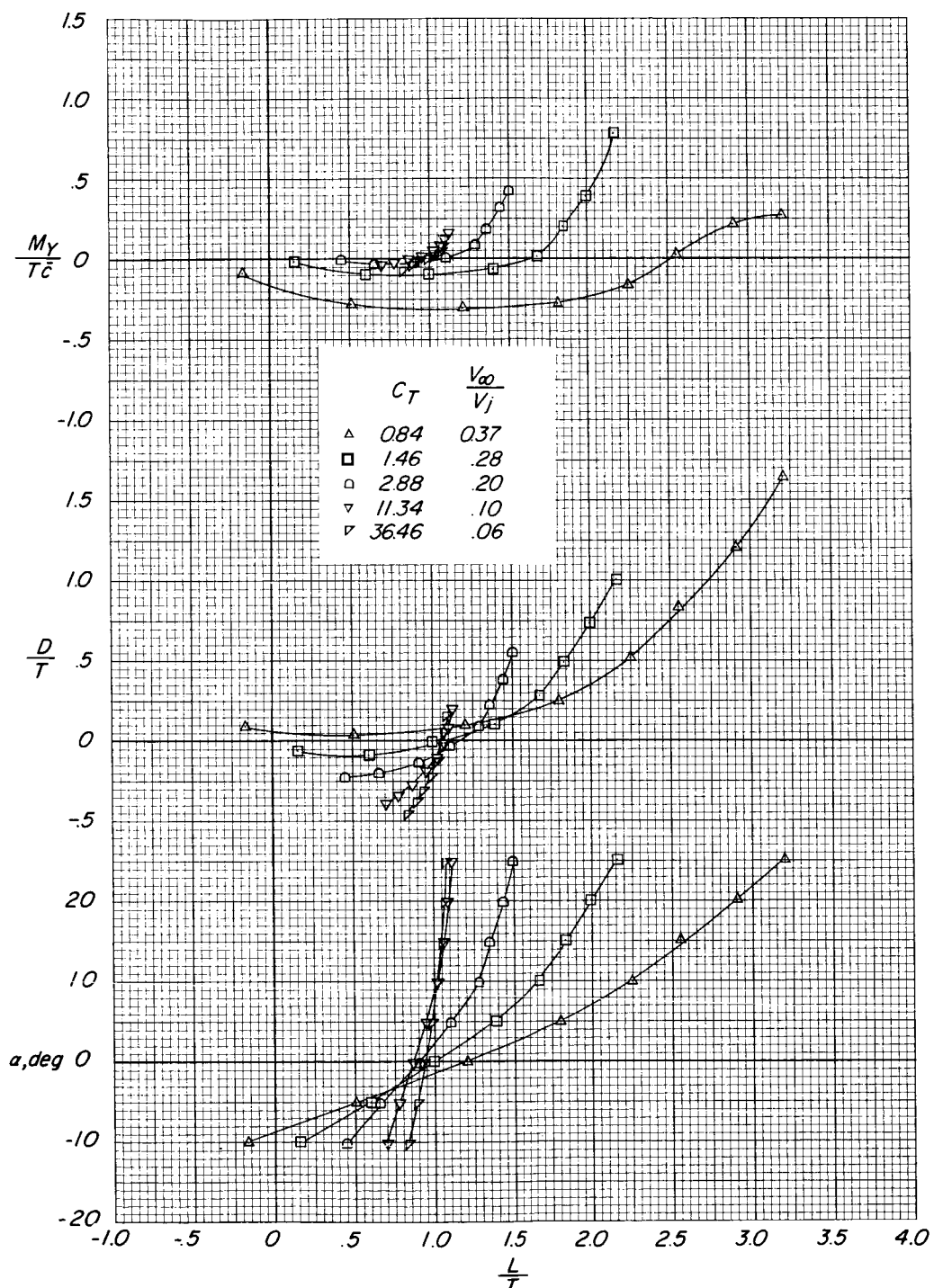
Figure 10.- Continued.



(i)  $\delta_j = 68^\circ$ ;  $\delta_e = 0^\circ$ . Concluded.

Figure 10.- Continued.

DECLASSIFIED



(j)  $\delta_j = 68^\circ$ ;  $\delta_e = 10^\circ$ .

Figure 10.- Continued.

0317102000 1030

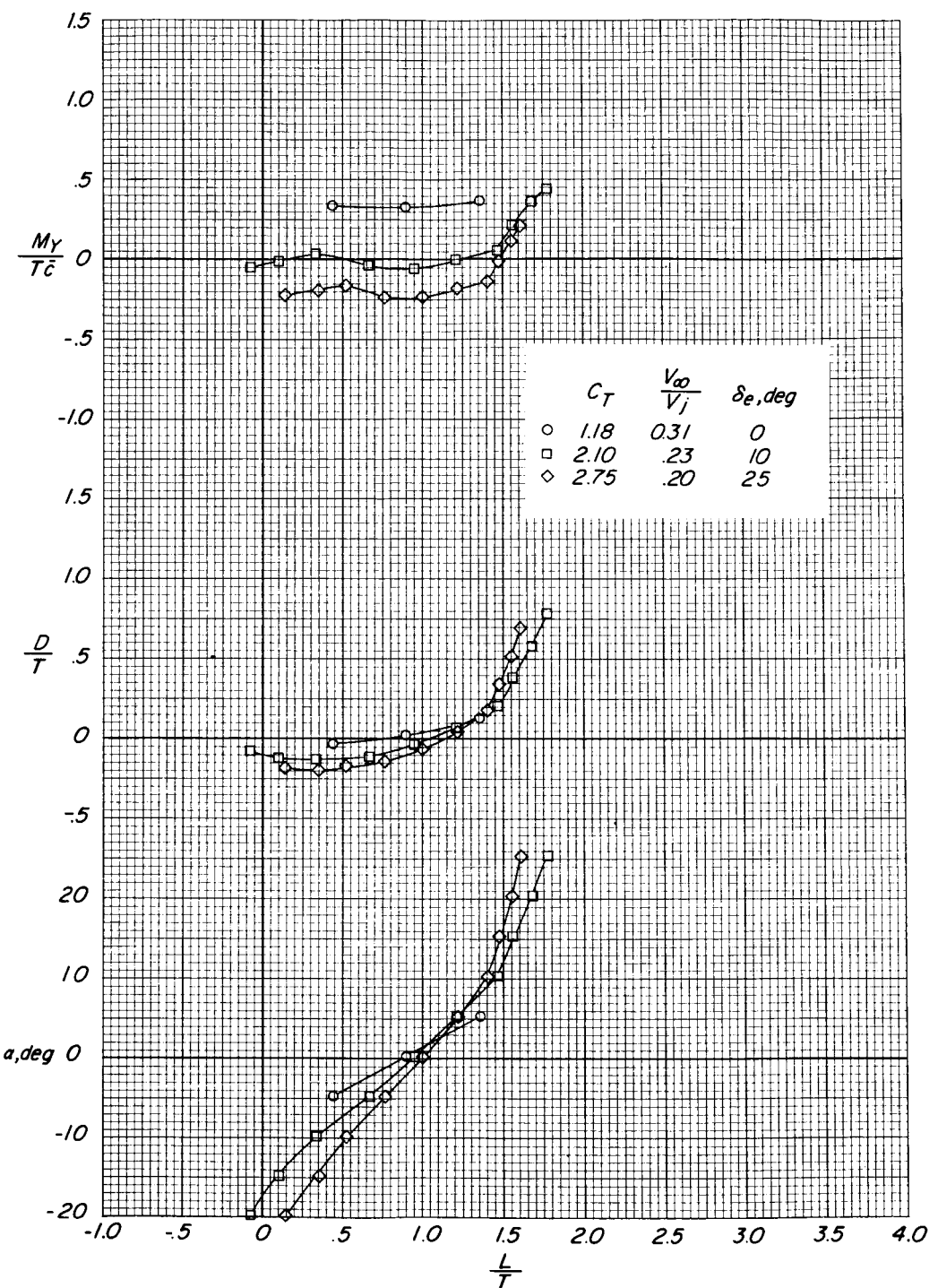
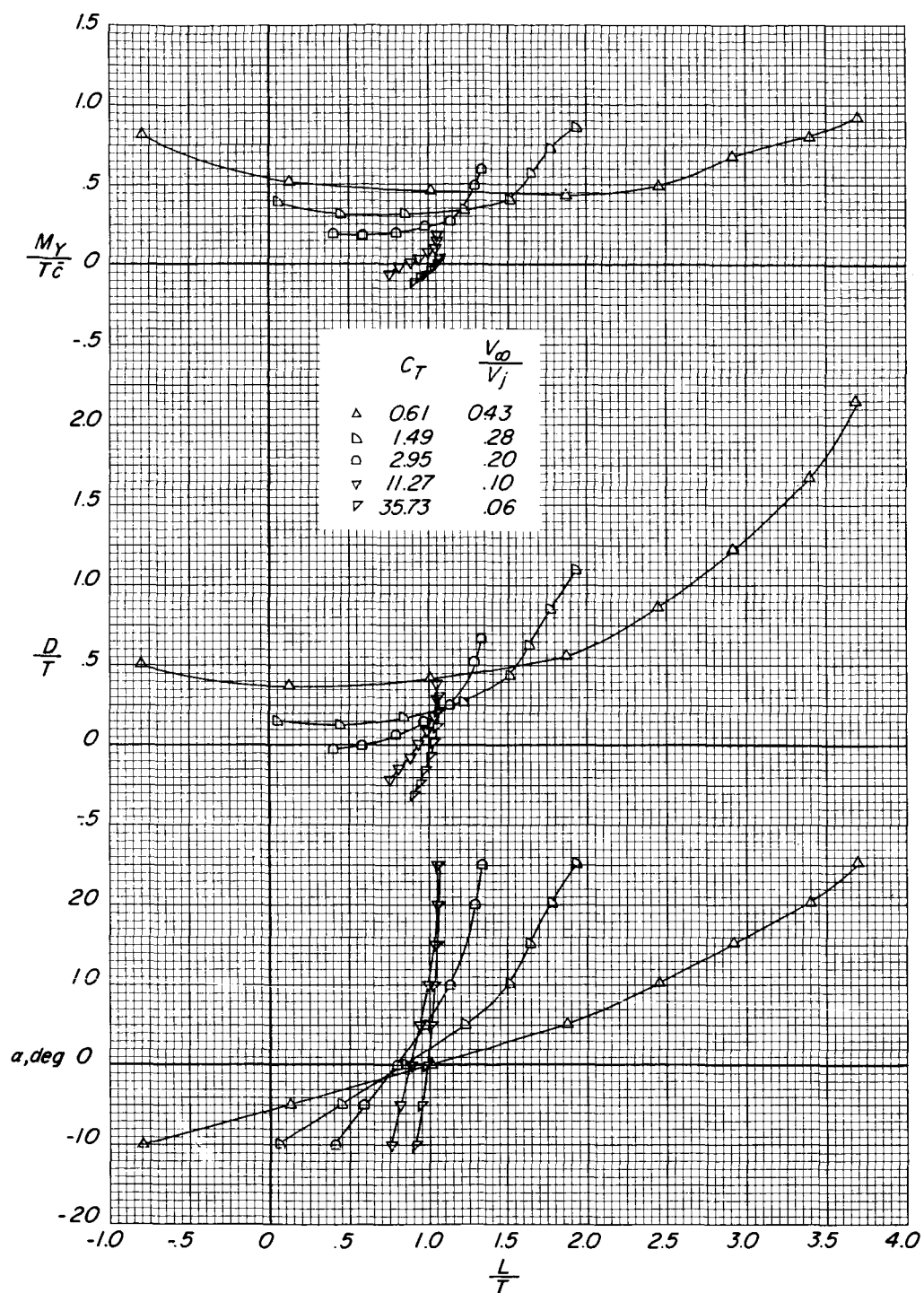
(k)  $\delta_j = 68^\circ$ ;  $\delta_e$  varies.

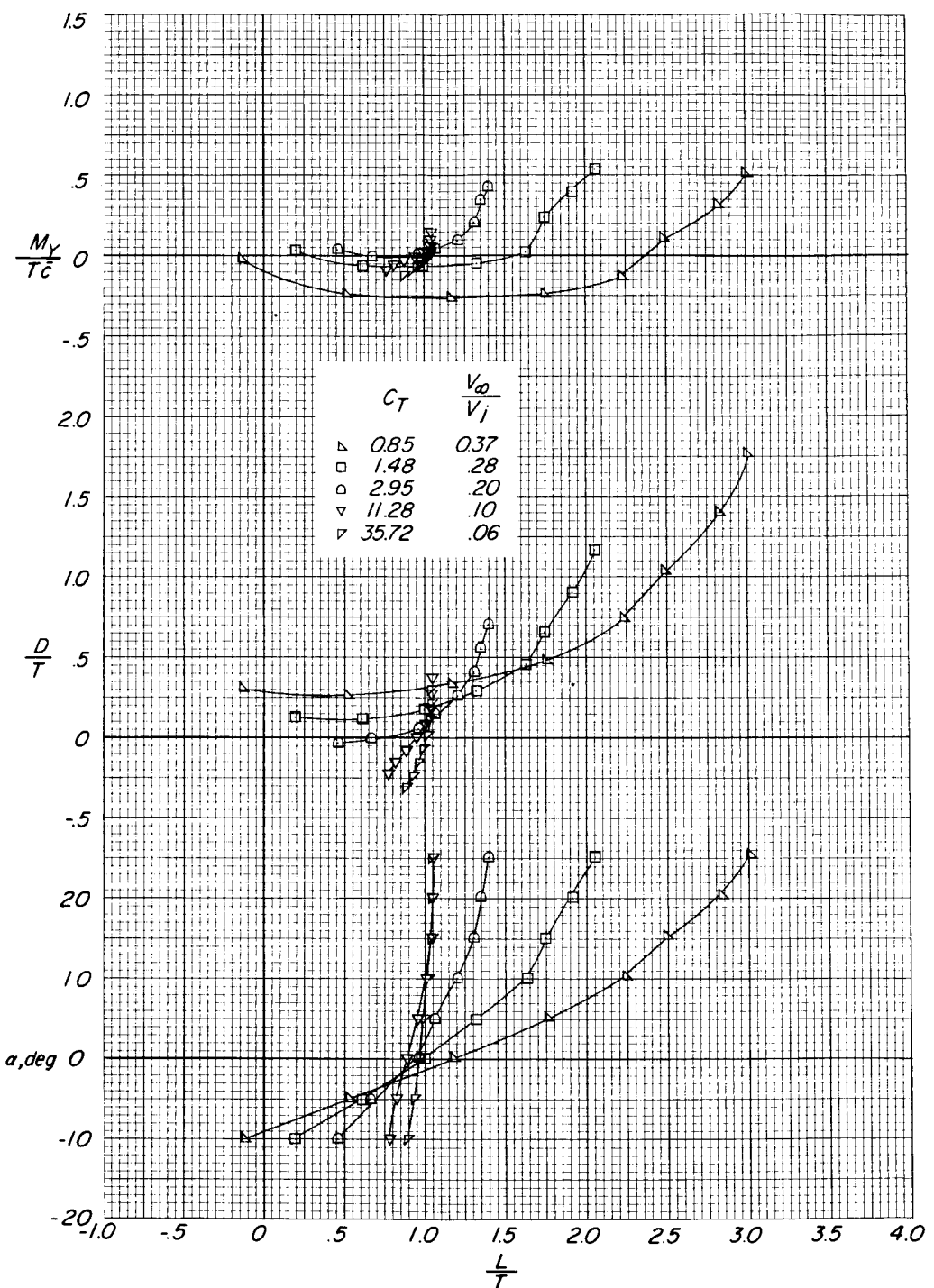
Figure 10.- Continued.

DECLASSIFIED



(i)  $\delta_j = 78^\circ$ ;  $\delta_e = 0^\circ$ .

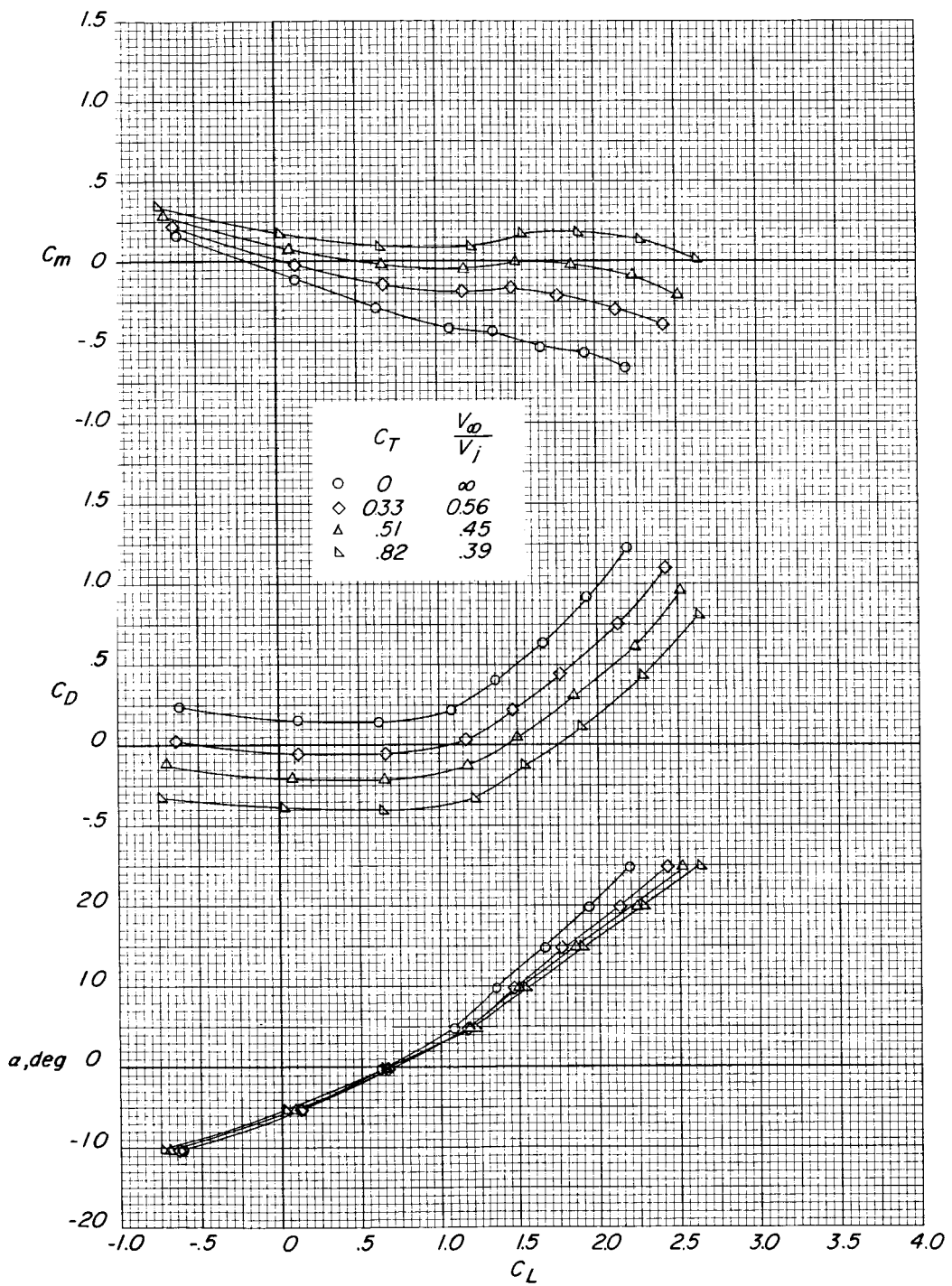
Figure 10.- Continued.



(m)  $\delta_j = 78^\circ$ ;  $\delta_e = 10^\circ$ .

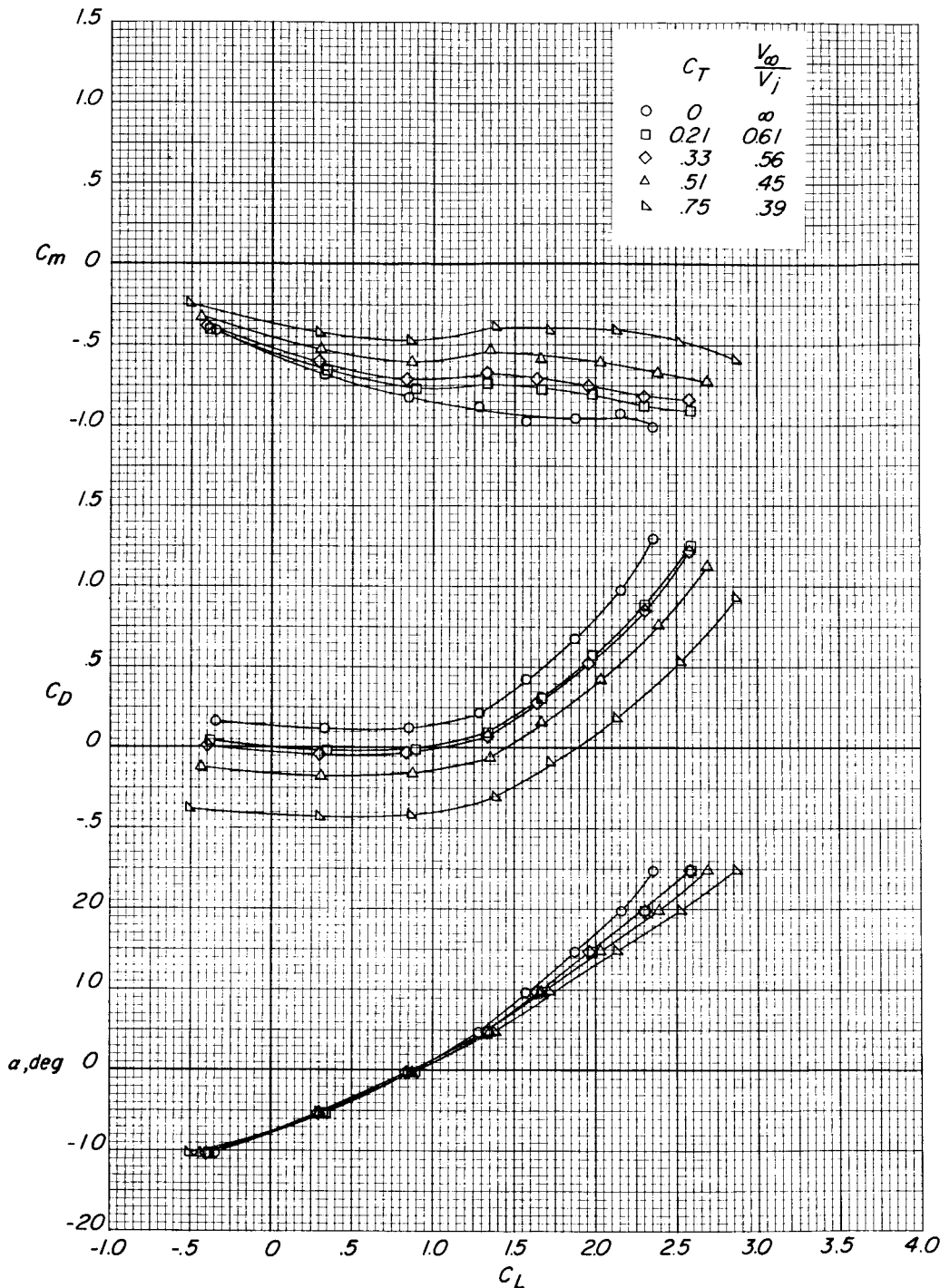
Figure 10.- Concluded.

DECLASSIFIED



(a)  $\delta_j = 4^\circ$ ;  $\delta_e = 0^\circ$ .

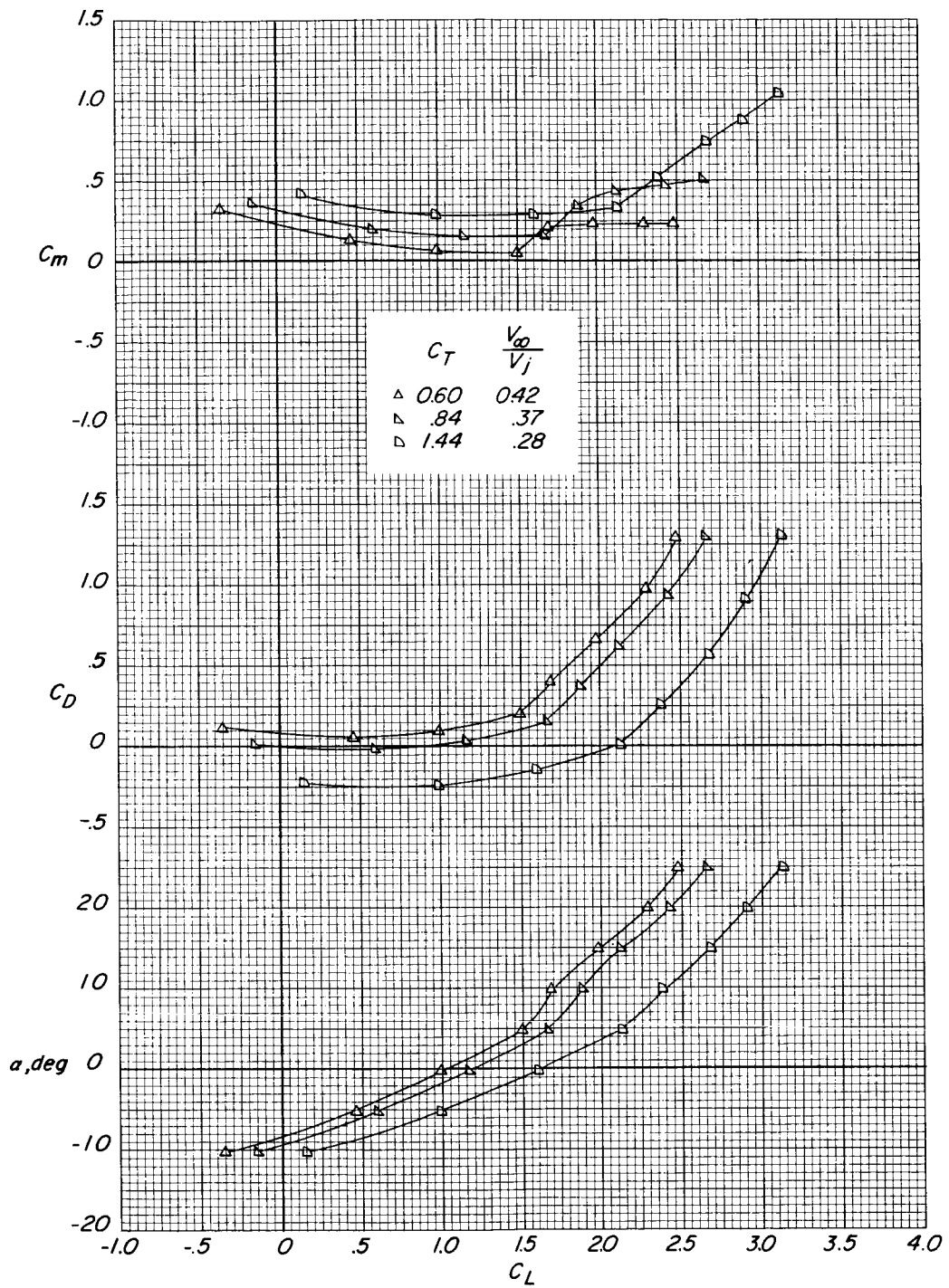
Figure 11.- Effect of power on the longitudinal aerodynamic characteristics of the basic model with flaps deflected  $40^\circ$ .  $\Lambda = 15^\circ$ .



(b)  $\delta_j = 4^\circ$ ;  $\delta_e = 10^\circ$ .

Figure 11.- Continued.

DECLASSIFIED



(c)  $\delta_j = 60^\circ$ ;  $\delta_e = 0^\circ$ .

Figure 11.- Continued.

03131030

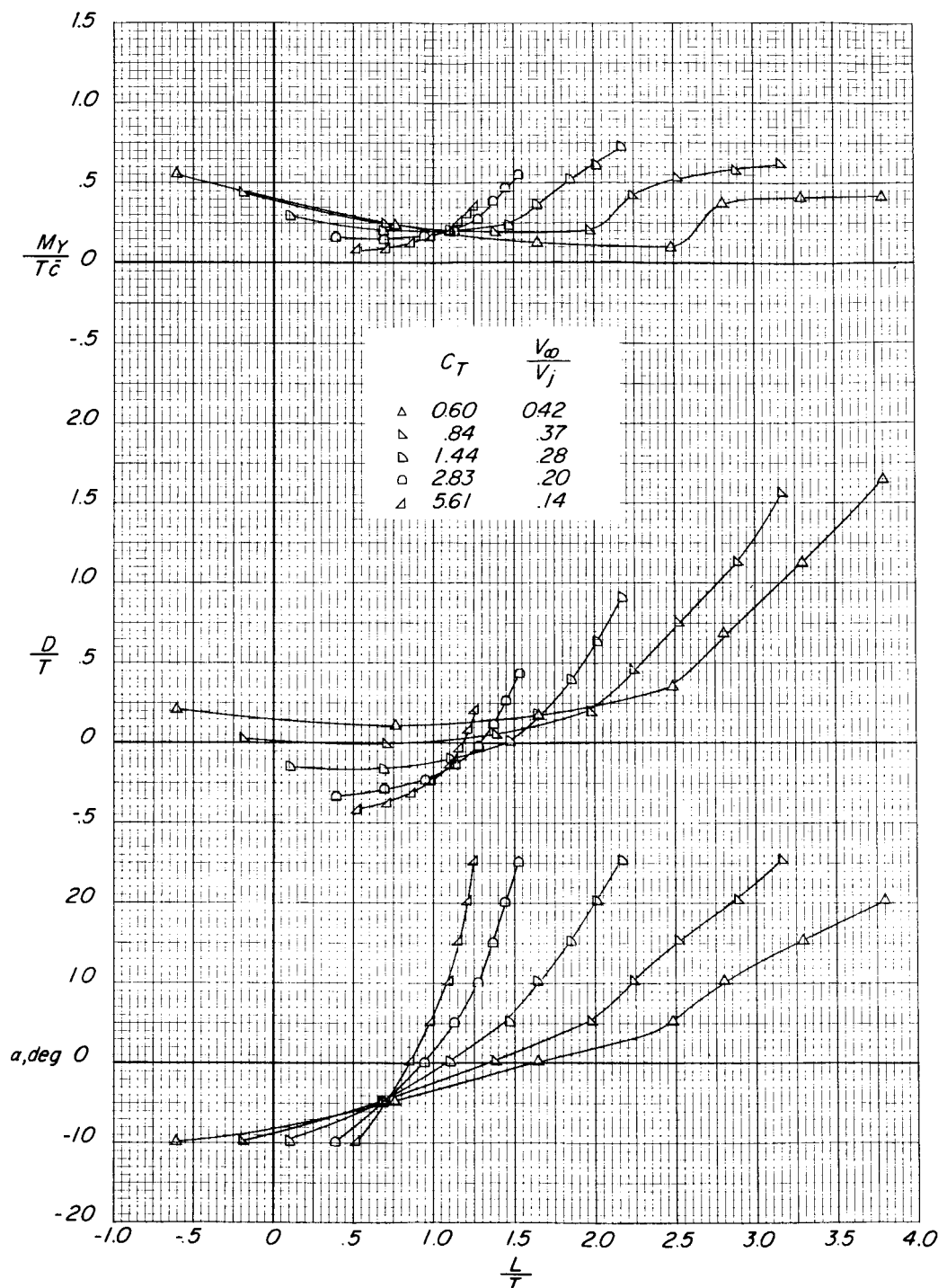
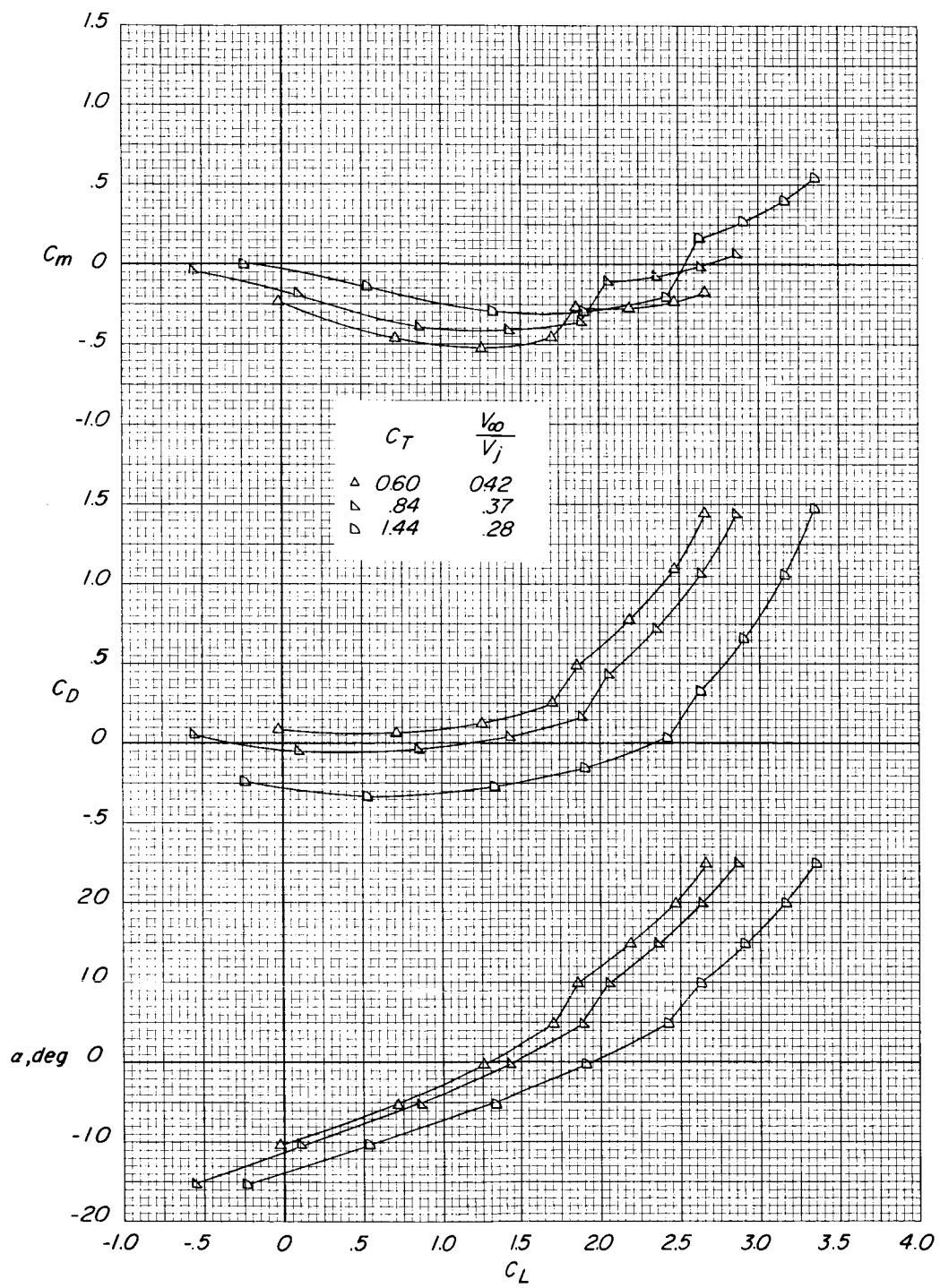
(c)  $\delta_j = 60^\circ$ ;  $\delta_e = 0^\circ$ . Concluded.

Figure 11. - Continued.

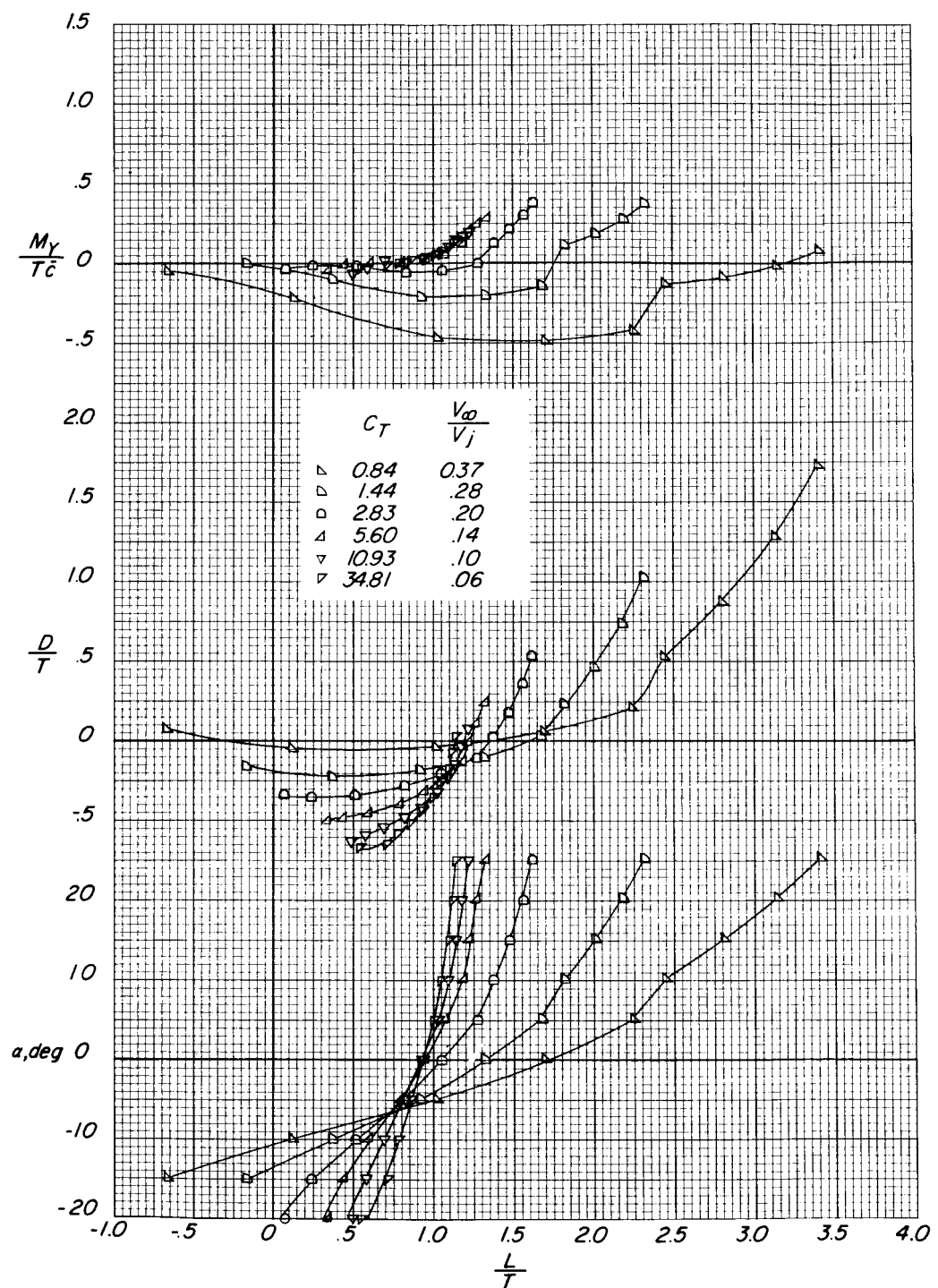
DECLASSIFIED



(d)  $\delta_j = 60^\circ$ ;  $\delta_e = 10^\circ$ .

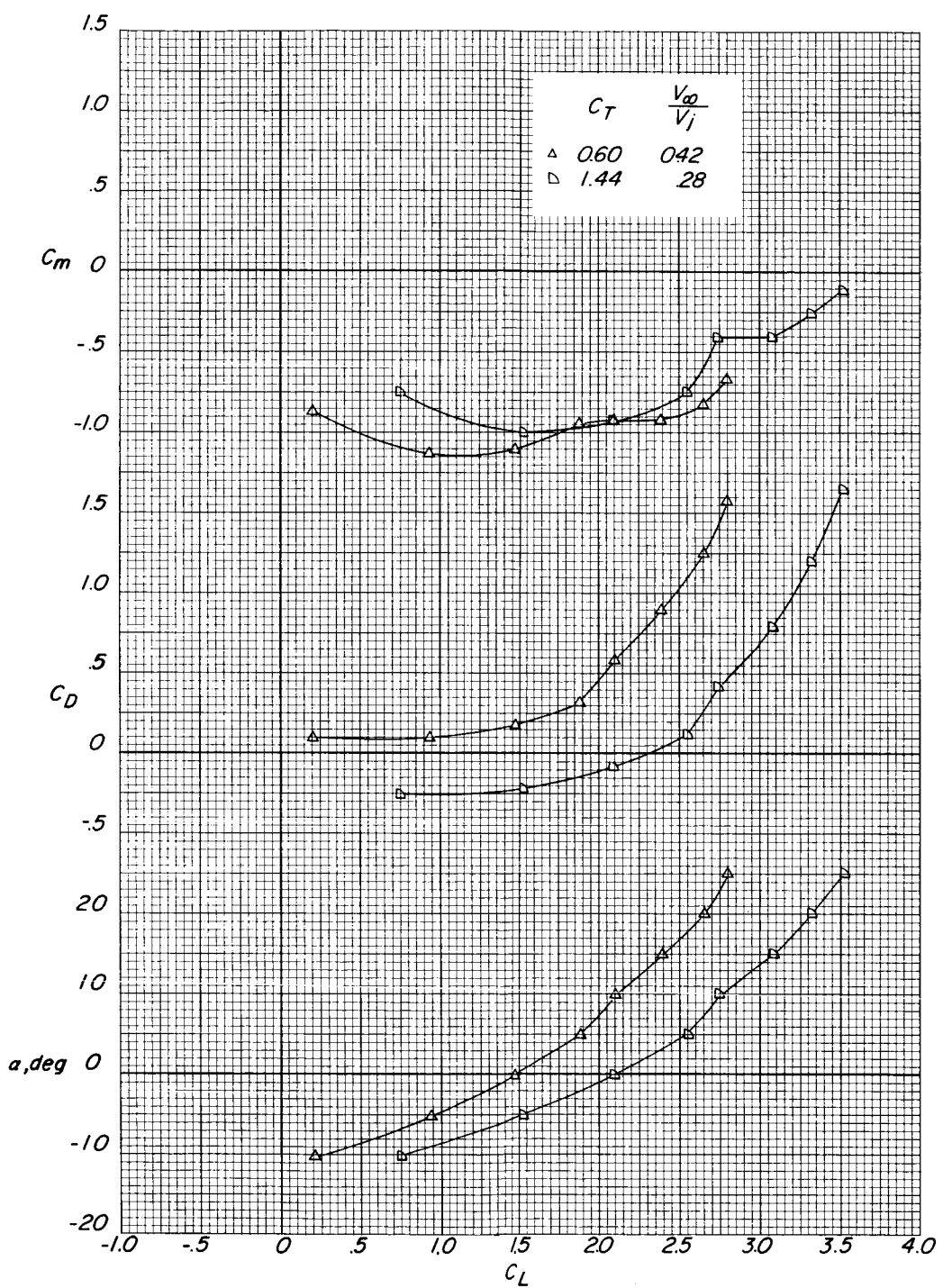
Figure 11. - Continued.

05/12/2010 30



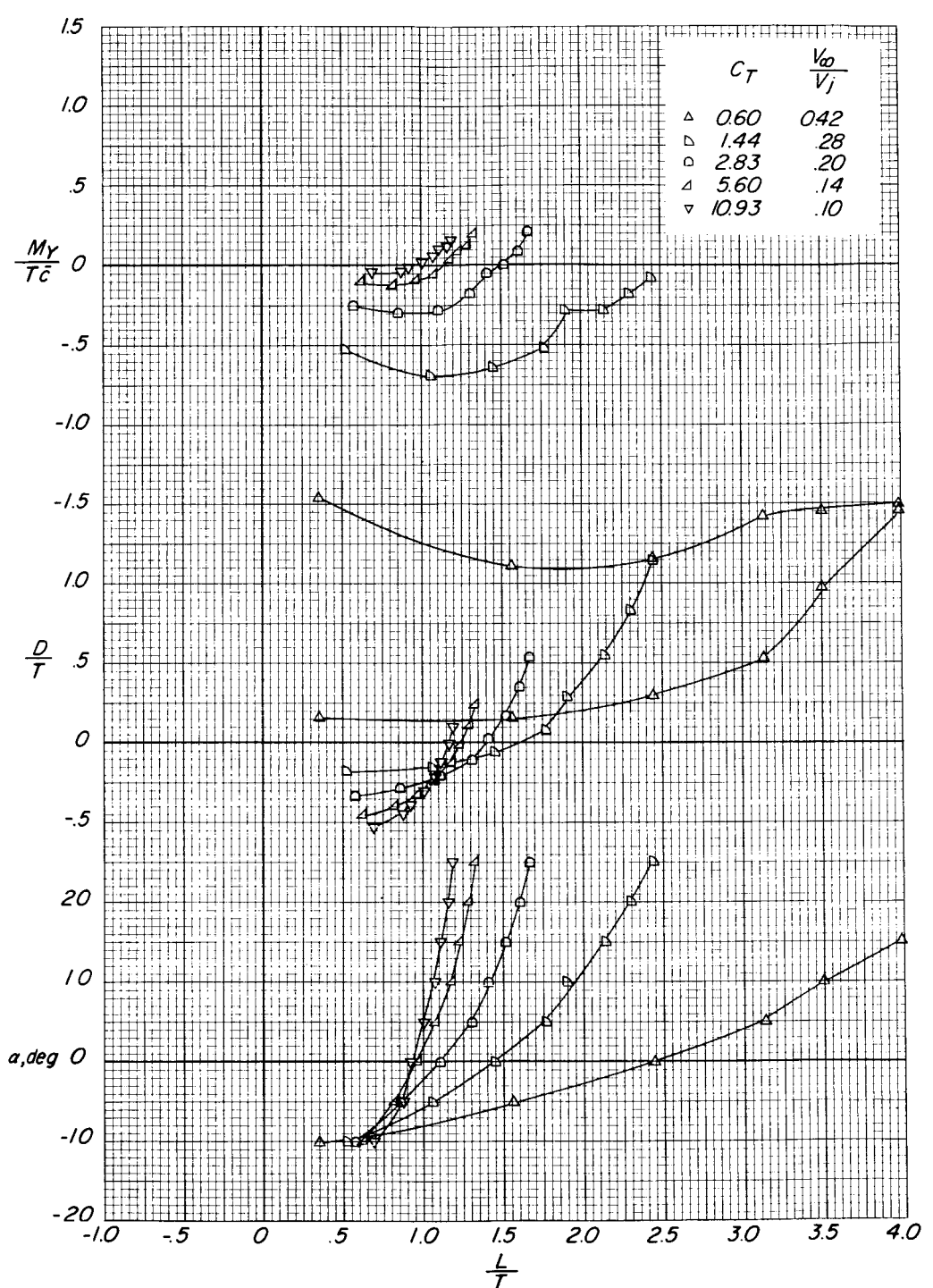
(d)  $\delta_j = 60^\circ$ ;  $\delta_e = 10^\circ$ . Concluded.

Figure 11.- Continued.



(e)  $\delta_j = 60^\circ$ ;  $\delta_e = 25^\circ$ .

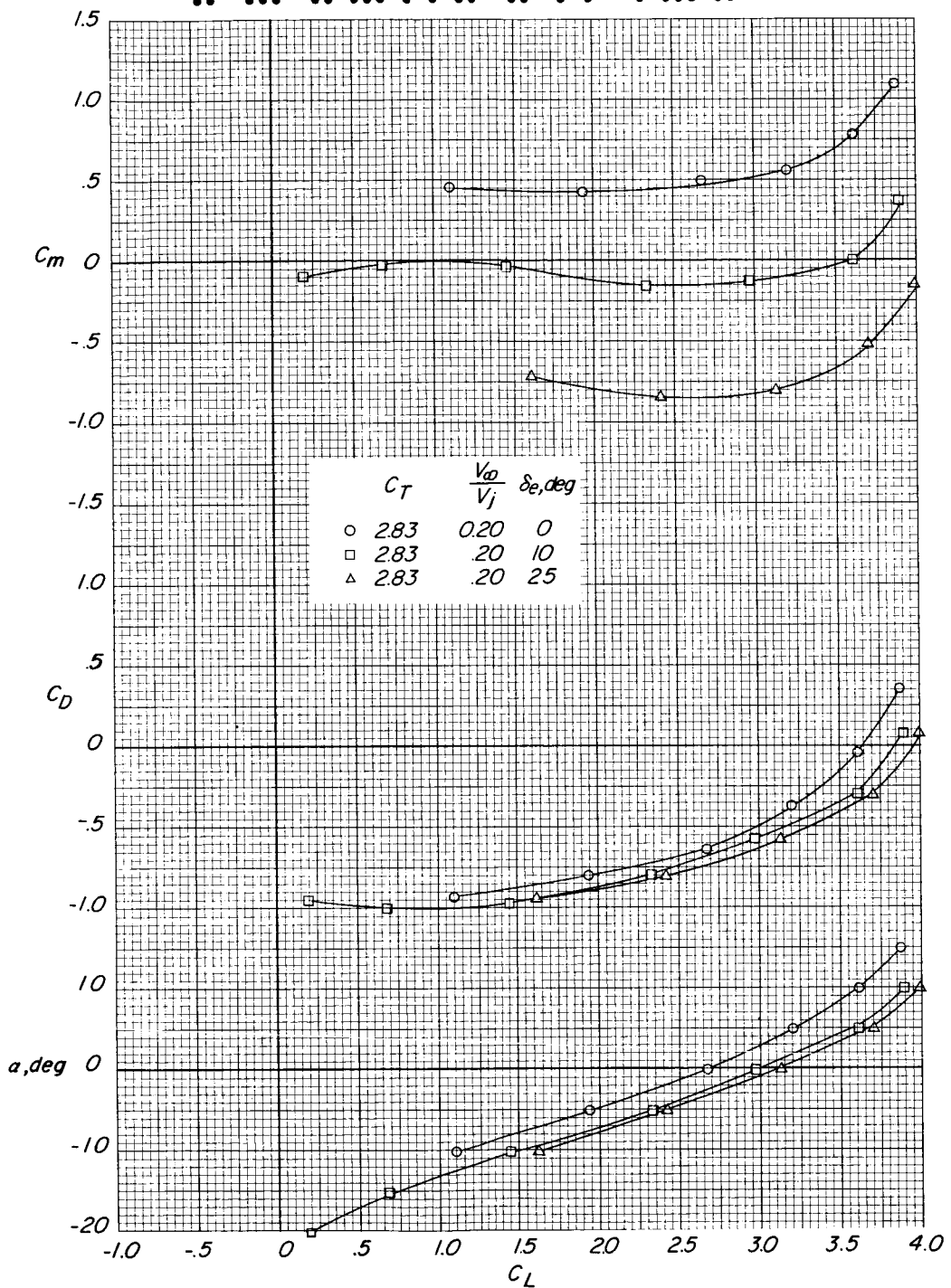
Figure 11.- Continued.



(e)  $\delta_j = 60^\circ$ ;  $\delta_e = 25^\circ$ . Concluded.

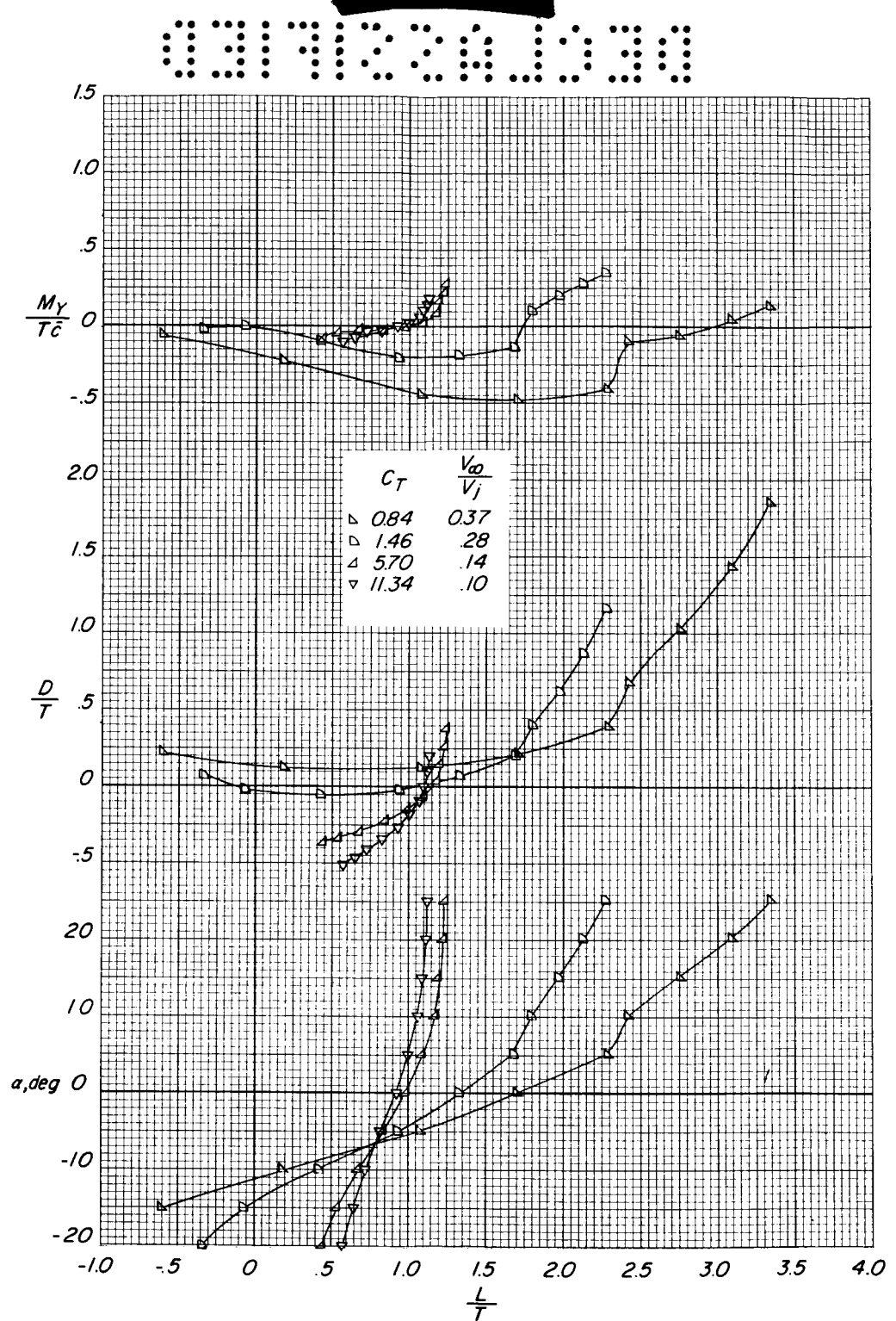
Figure 11.- Continued.

DECLASSIFIED



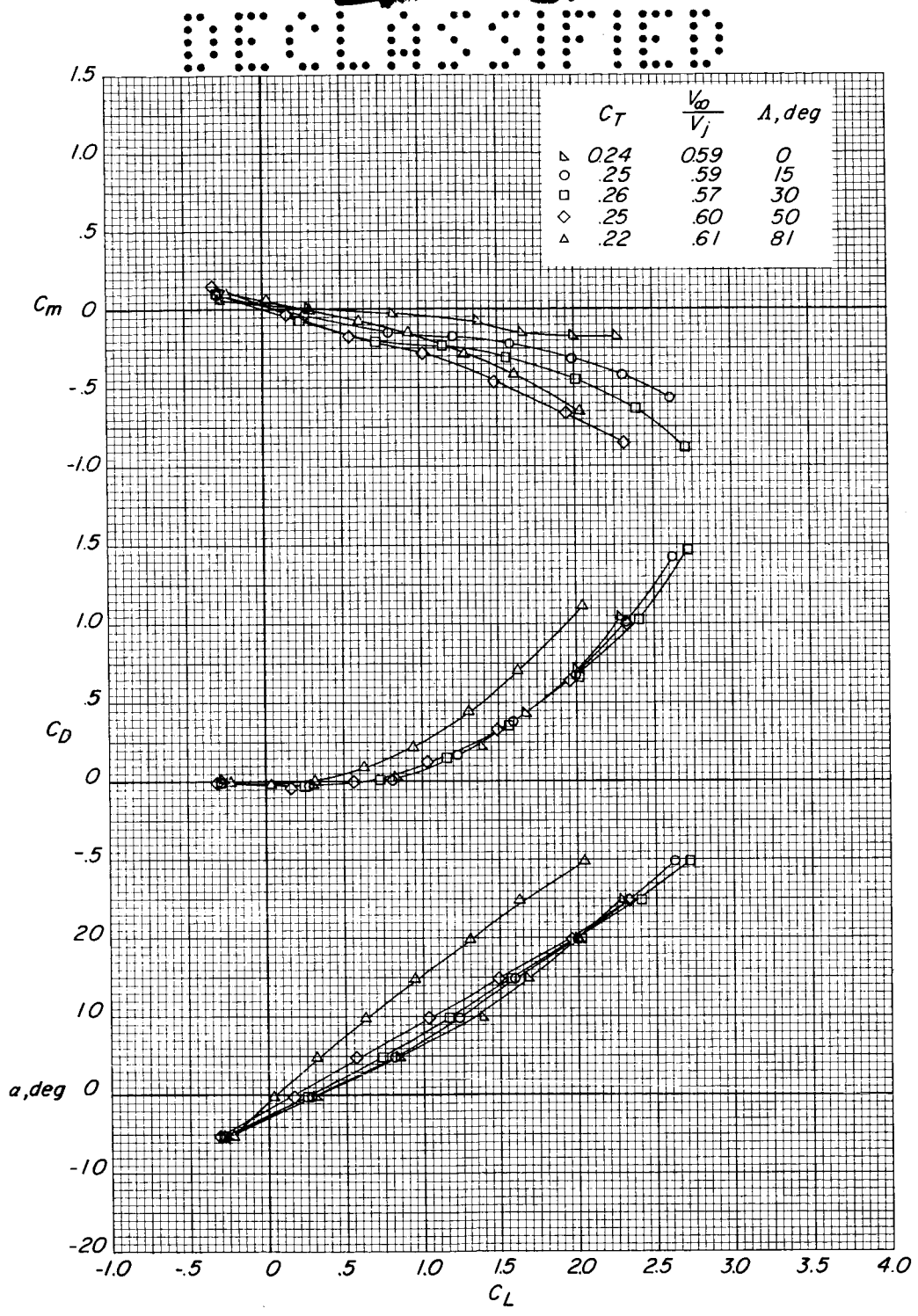
(f)  $\delta_j = 60^\circ$ ;  $\delta_e$  varies.

Figure 11.- Continued.



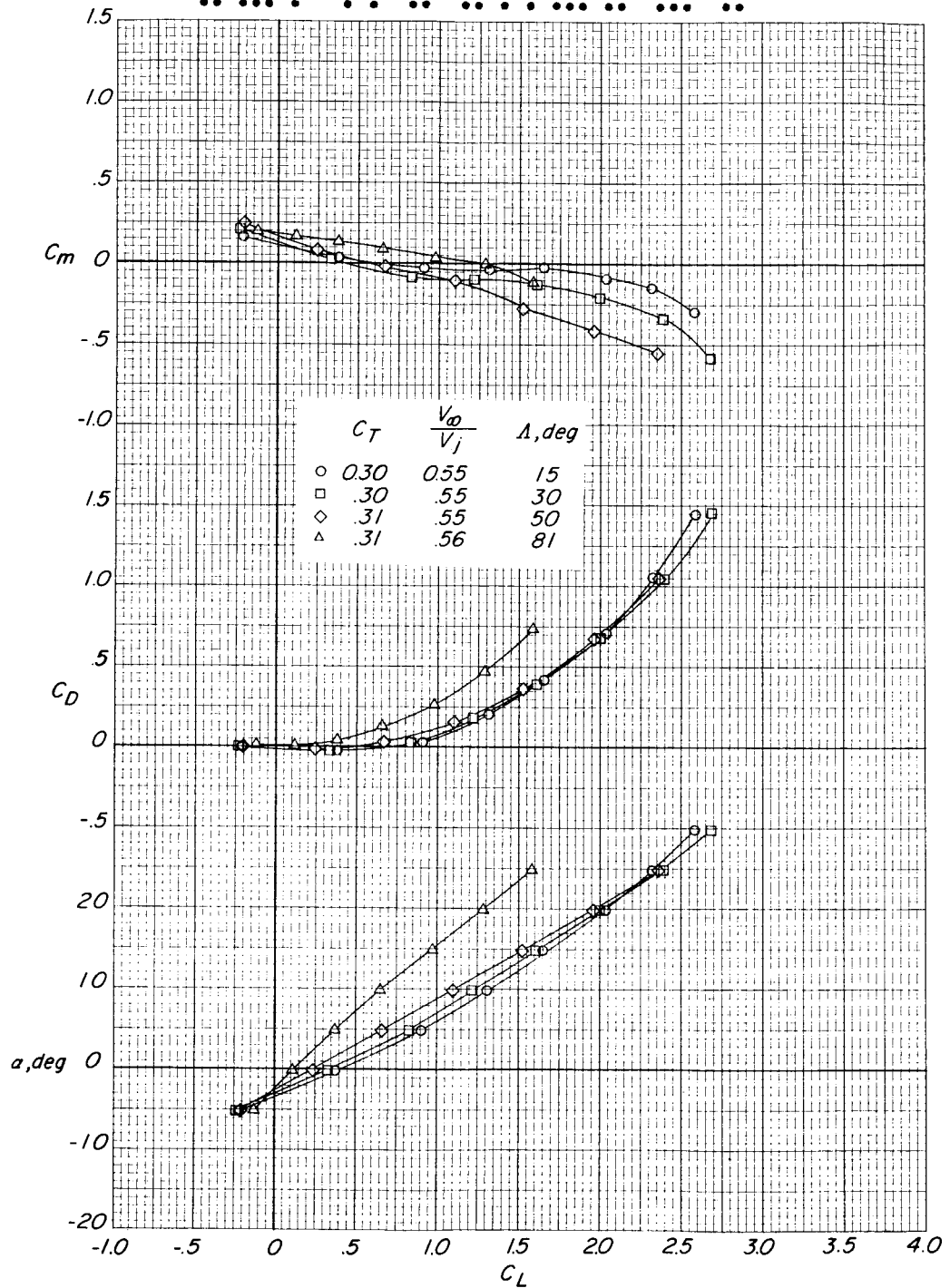
(g)  $\delta_j = 68^\circ$ ;  $\delta_e = 10^\circ$ .

Figure 11.- Concluded.



(a)  $\delta_j = 4^\circ$ .

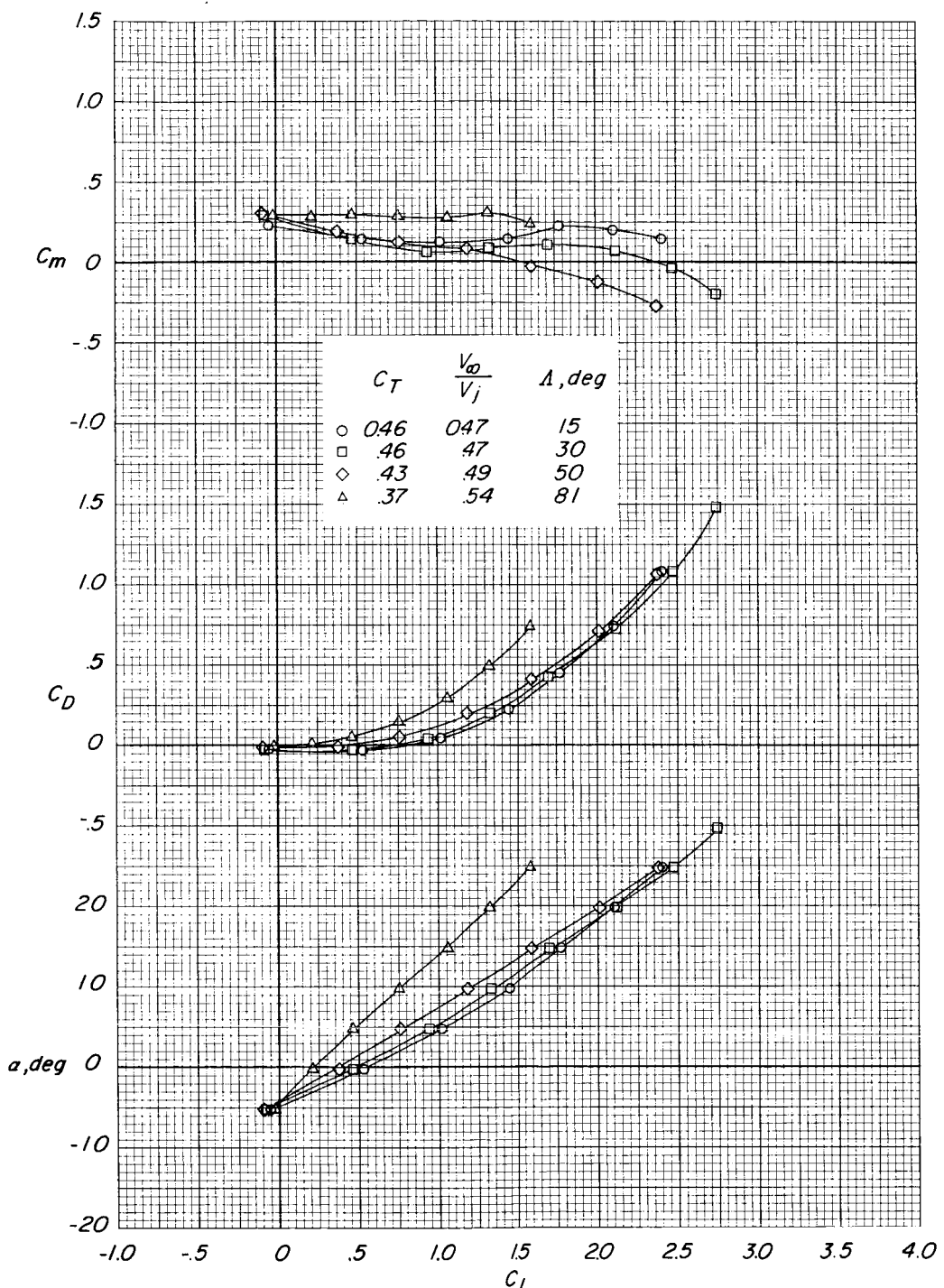
Figure 12.- Effect of sweep of the leading edge of the pivotal wing of the basic model with power on and jets deflected at various angles. Flaps and elevator undeflected.



(b)  $\delta_j = 31^\circ$ .

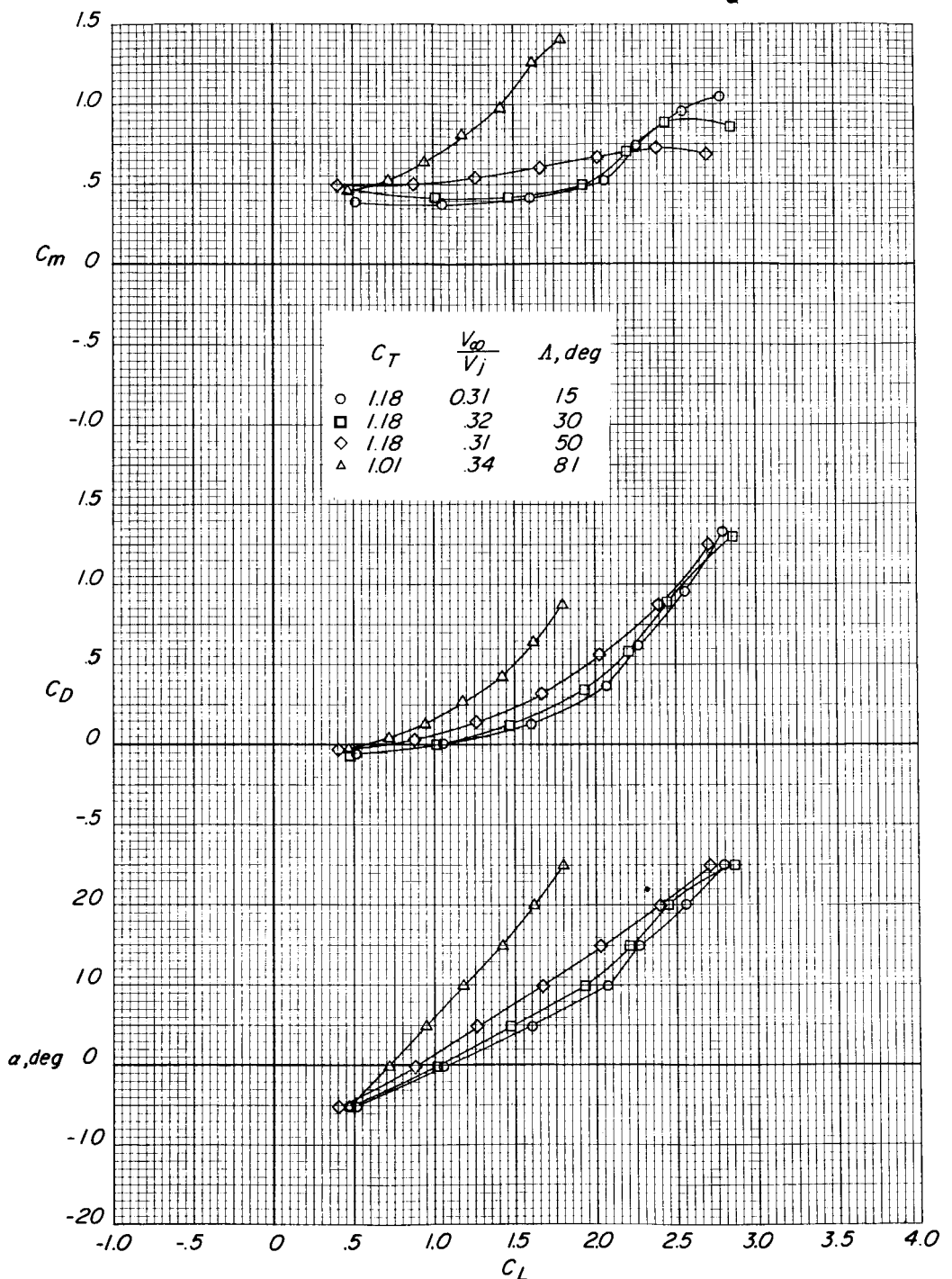
Figure 12.- Continued.

# DATA FOR UNSTEADY FLIGHT



(c)  $\delta_j = 49^\circ$ .

Figure 12.- Continued.



(a)  $\delta_j = 68^\circ$ .

Figure 12.- Concluded.

# DECODED

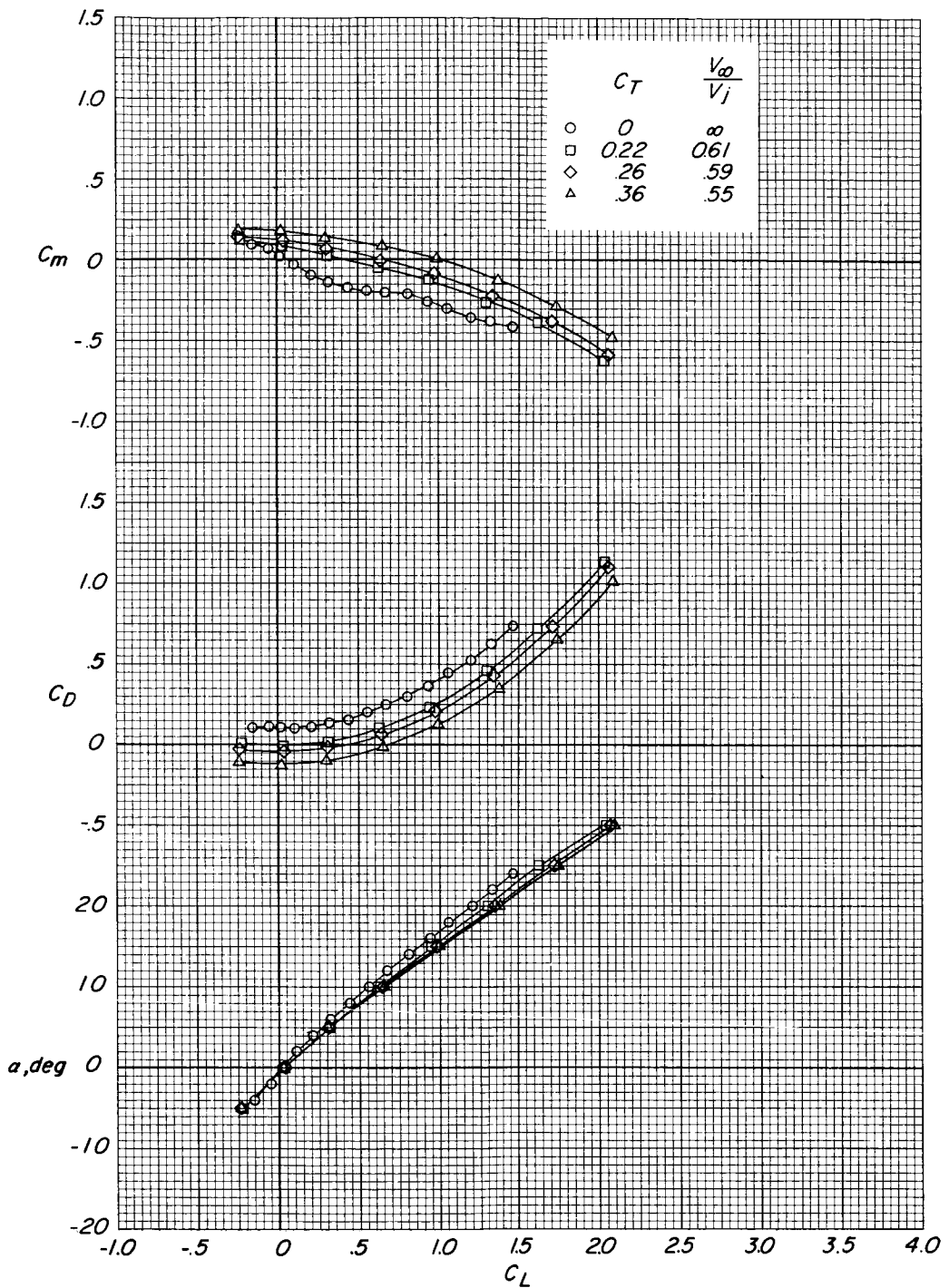


Figure 13.- Effect of power on the longitudinal aerodynamic characteristics of the basic model with the pivotal wing retracted (swept 81°). Flaps and elevator undeflected.  $\delta_j = 40^\circ$ .

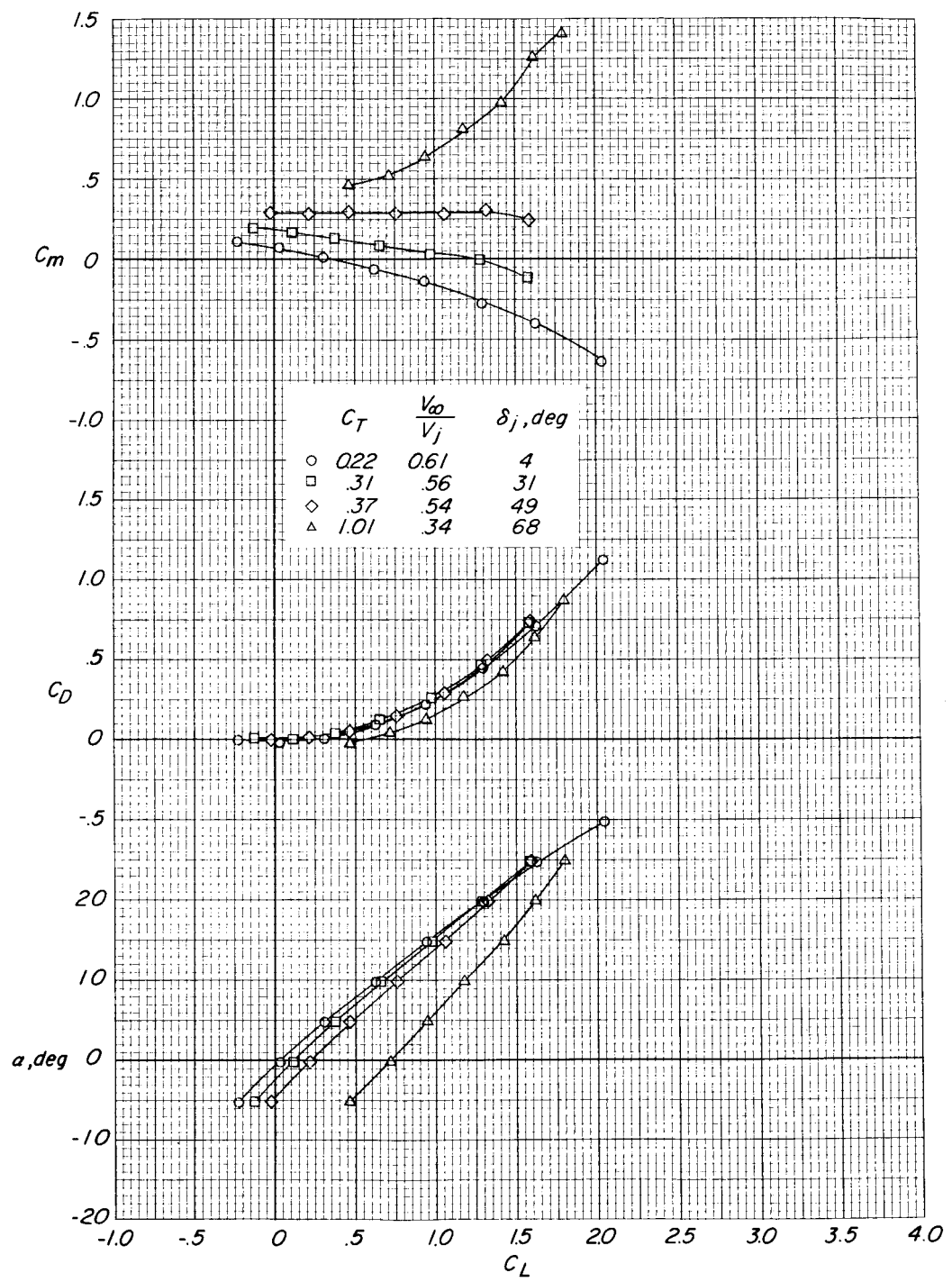
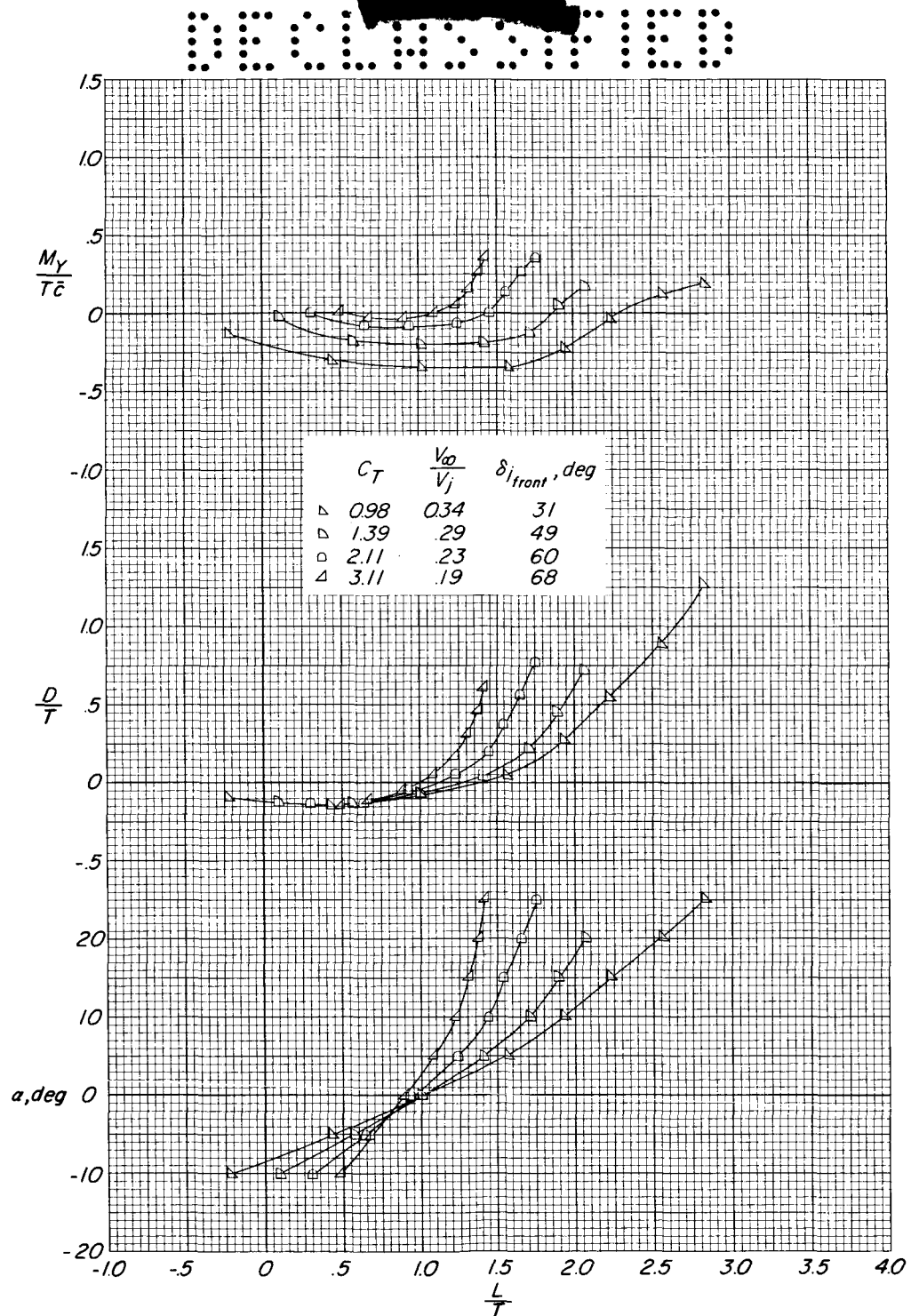
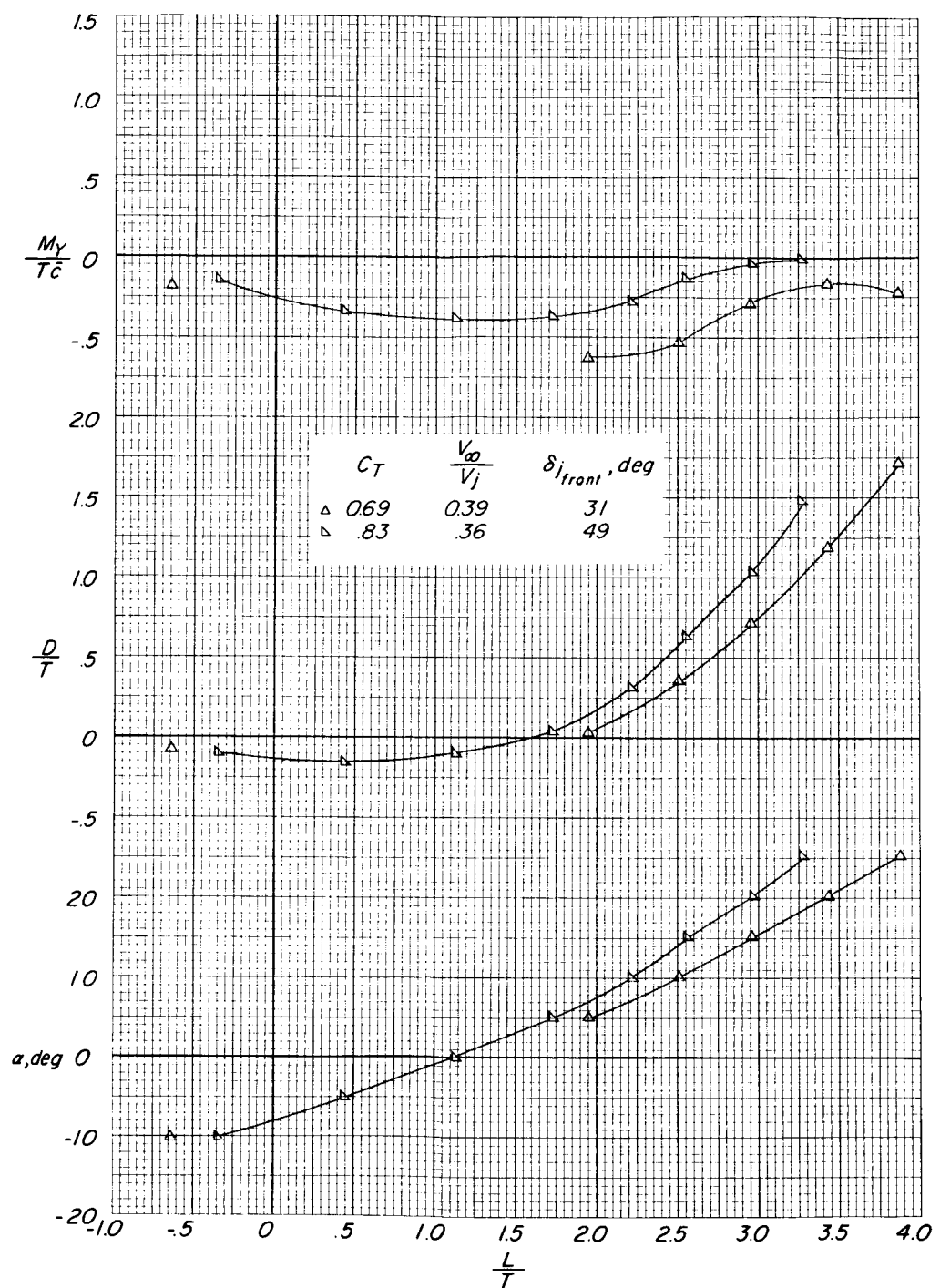


Figure 14.- Effect of jet deflection on the longitudinal aerodynamic characteristics of the basic model with the pivotal wing retracted (swept 81°). Flaps and elevator undeflected.



(a)  $\delta_{j,rear} = 78^\circ$ .

Figure 15.- Effect of differential jet deflection on the longitudinal aerodynamic characteristics of the basic model with flaps undeflected.  $\delta_e = 10^\circ$ ;  $\Lambda = 15^\circ$ .



(b)  $\delta_{j,\text{rear}} = 60^\circ$ .

Figure 15.- Concluded.

DECLASSIFIED

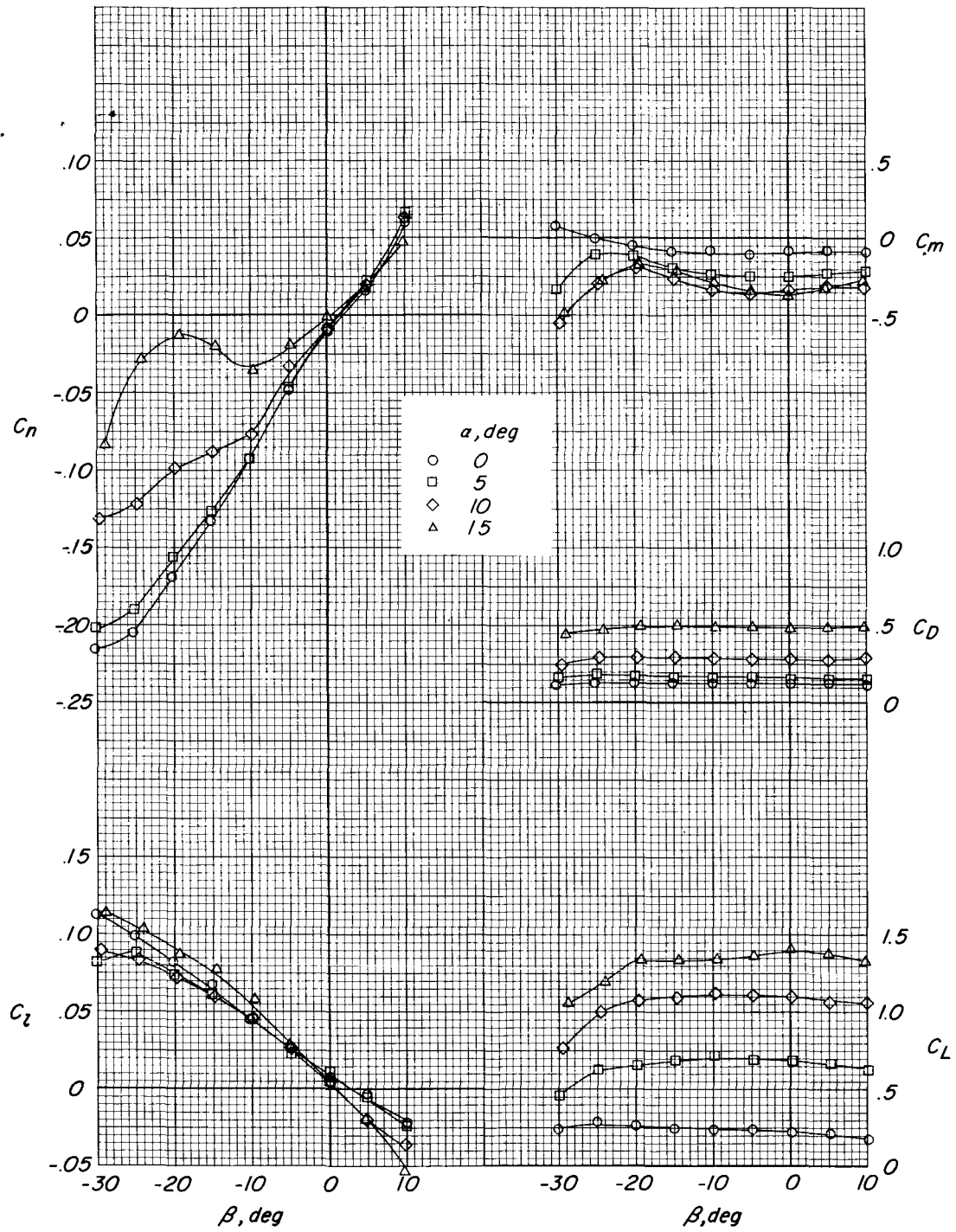


Figure 16.- Power-off lateral characteristics of the basic model with vertical tail on.  
 $\delta_j = 4^\circ$ ;  $\delta_f = 0^\circ$ ;  $\delta_e = 0^\circ$ ;  $\Lambda = 15^\circ$ .

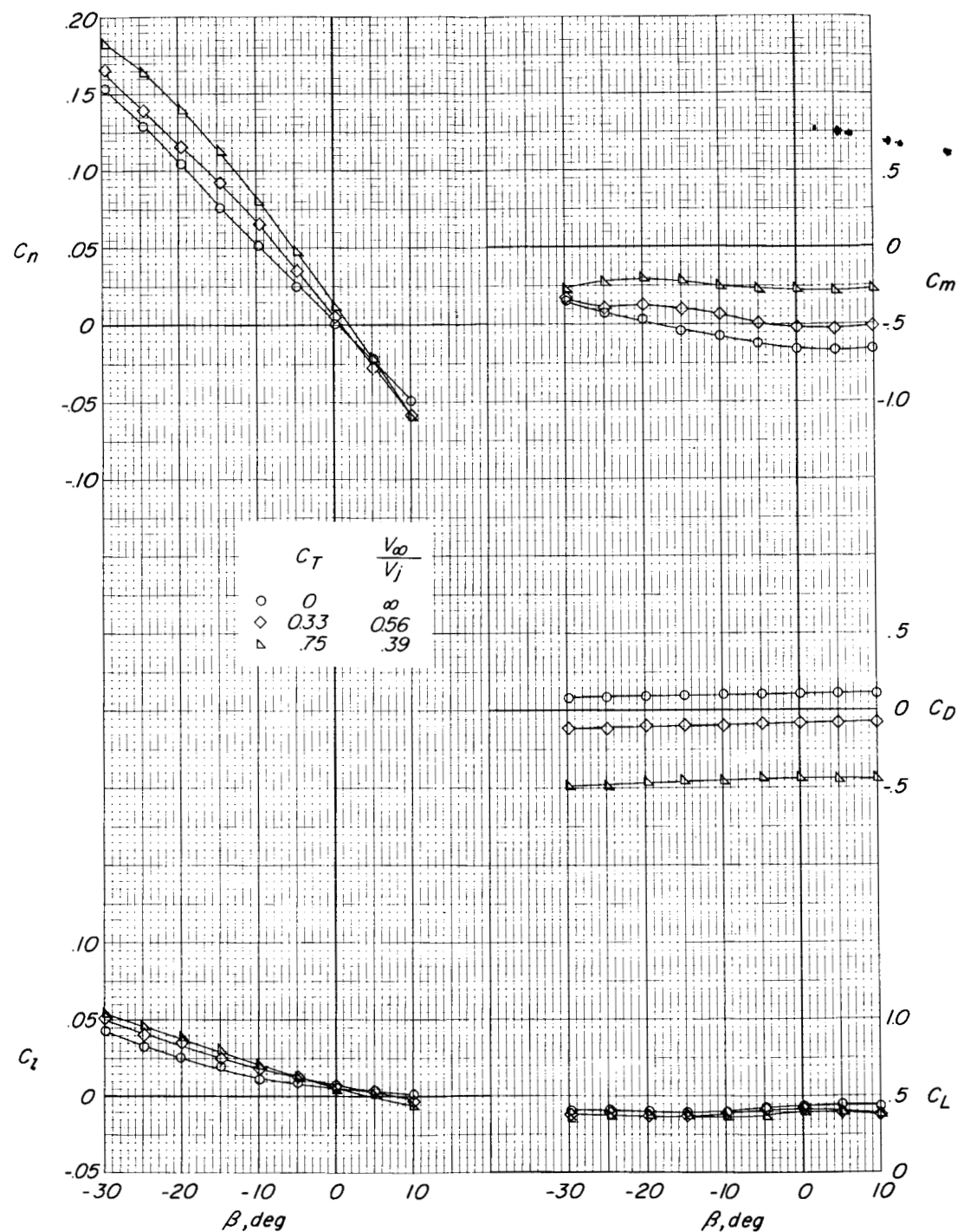
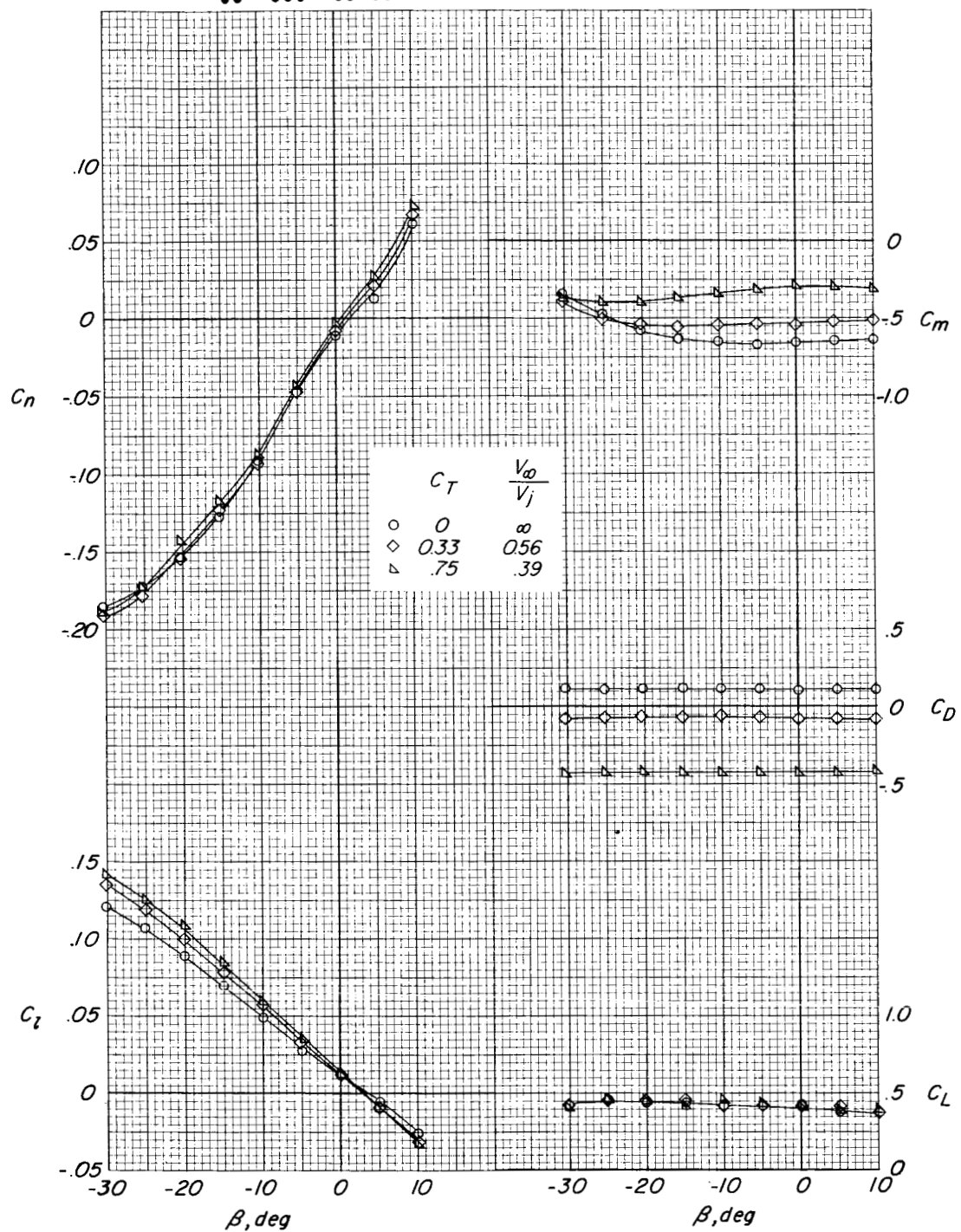


Figure 17.- Lateral characteristics of the basic model with the vertical tail off.  
 $\delta_j = 4^\circ$ ;  $\delta_f = 0^\circ$ ;  $\delta_e = 10^\circ$ ;  $\alpha = 0^\circ$ ;  $\Lambda = 15^\circ$ .

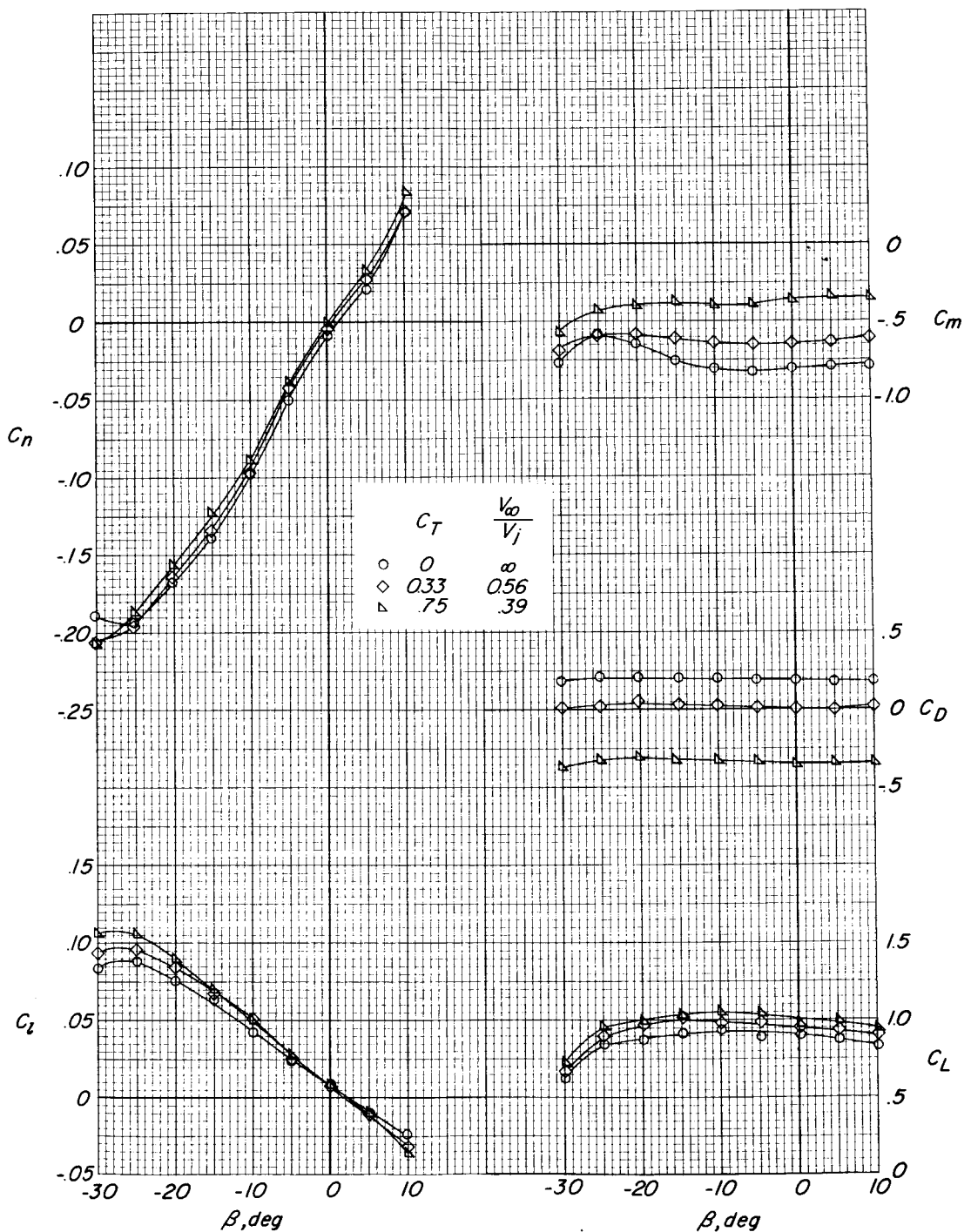
# DECODIFIED



(a)  $\delta_j = 4^\circ$ ;  $\alpha = 0^\circ$ .

Figure 18.- Lateral characteristics of the basic model with the vertical tail on.  
 $\delta_f = 0^\circ$ ;  $\delta_e = 10^\circ$ ;  $\Lambda = 15^\circ$ .

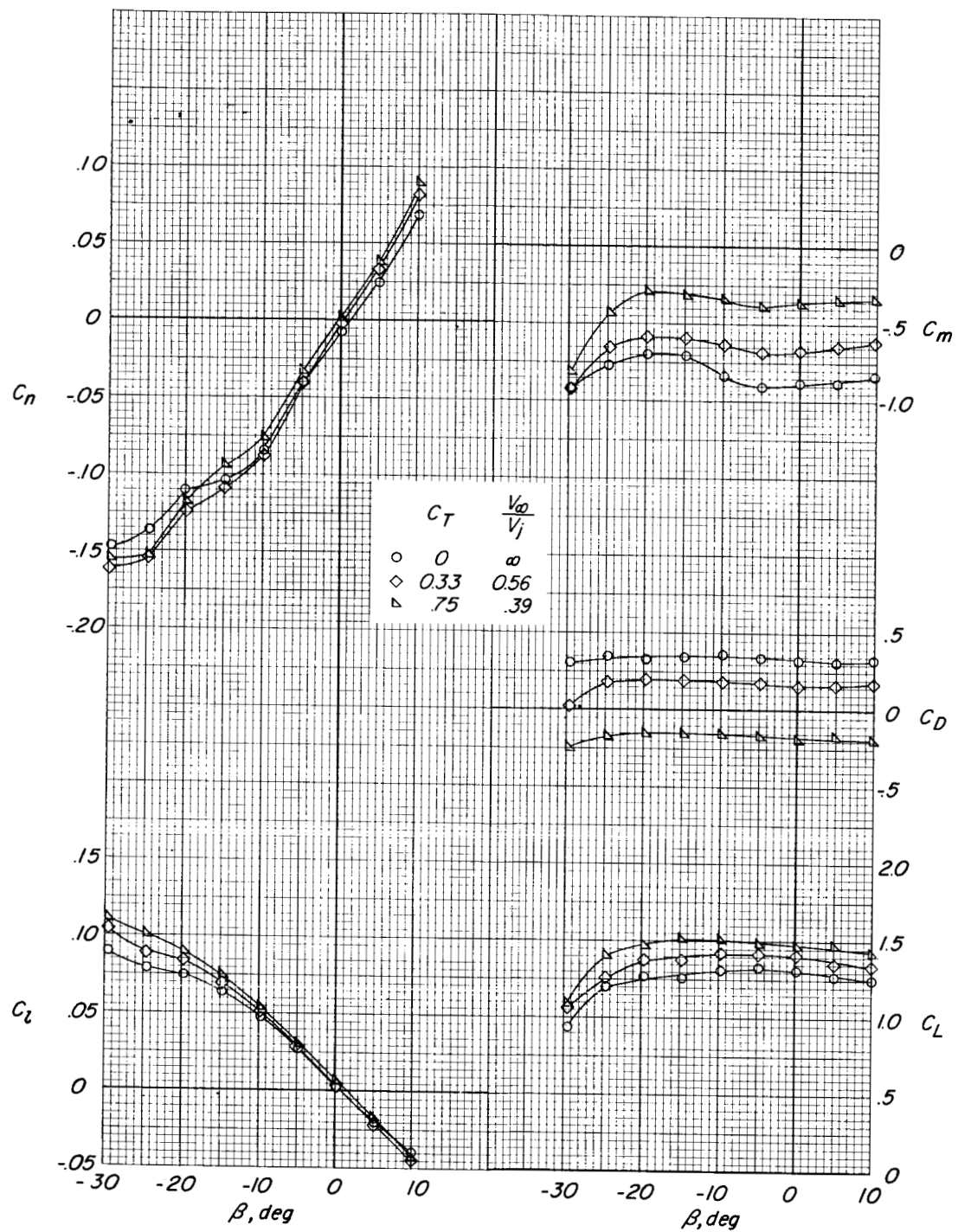
031702A1030



$$(b) \quad \delta_j = 4^\circ; \quad \alpha = 5^\circ.$$

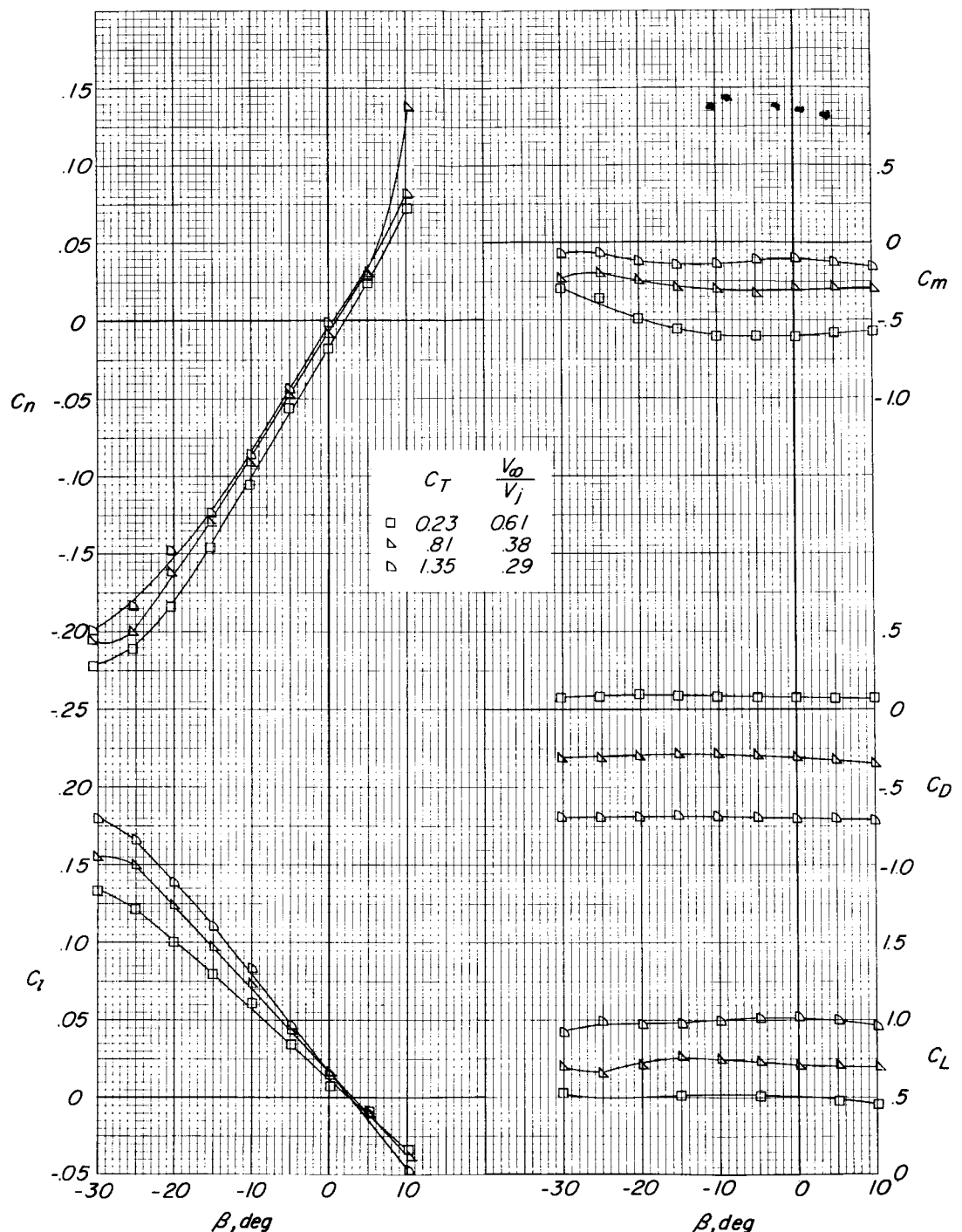
Figure 18.- Continued.

DECLASSIFIED



(c)  $\delta_j = 4^\circ$ ;  $\alpha = 10^\circ$ .

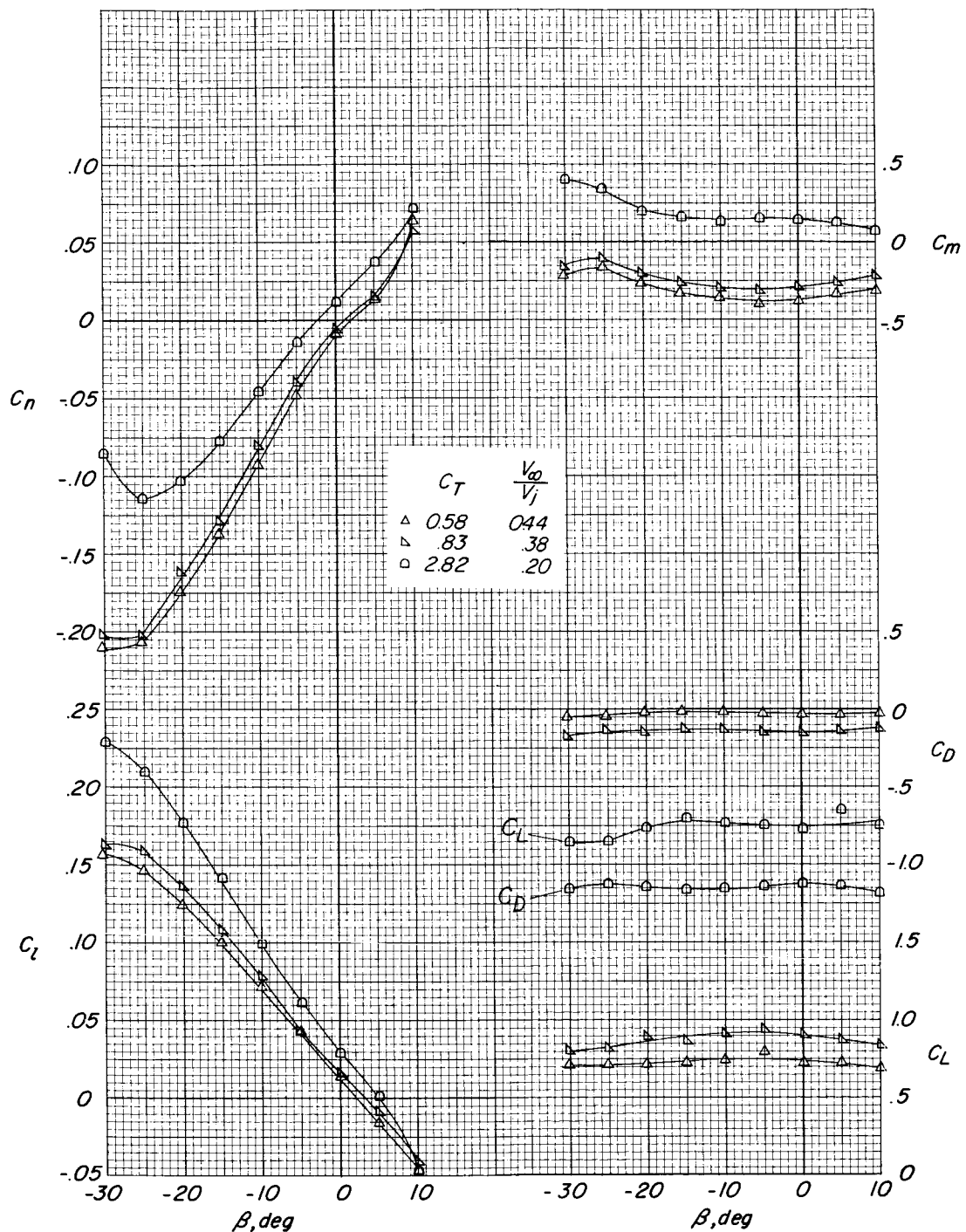
Figure 18.- Continued.



(d)  $\delta_j = 31^\circ$ ;  $\alpha = 0^\circ$ .

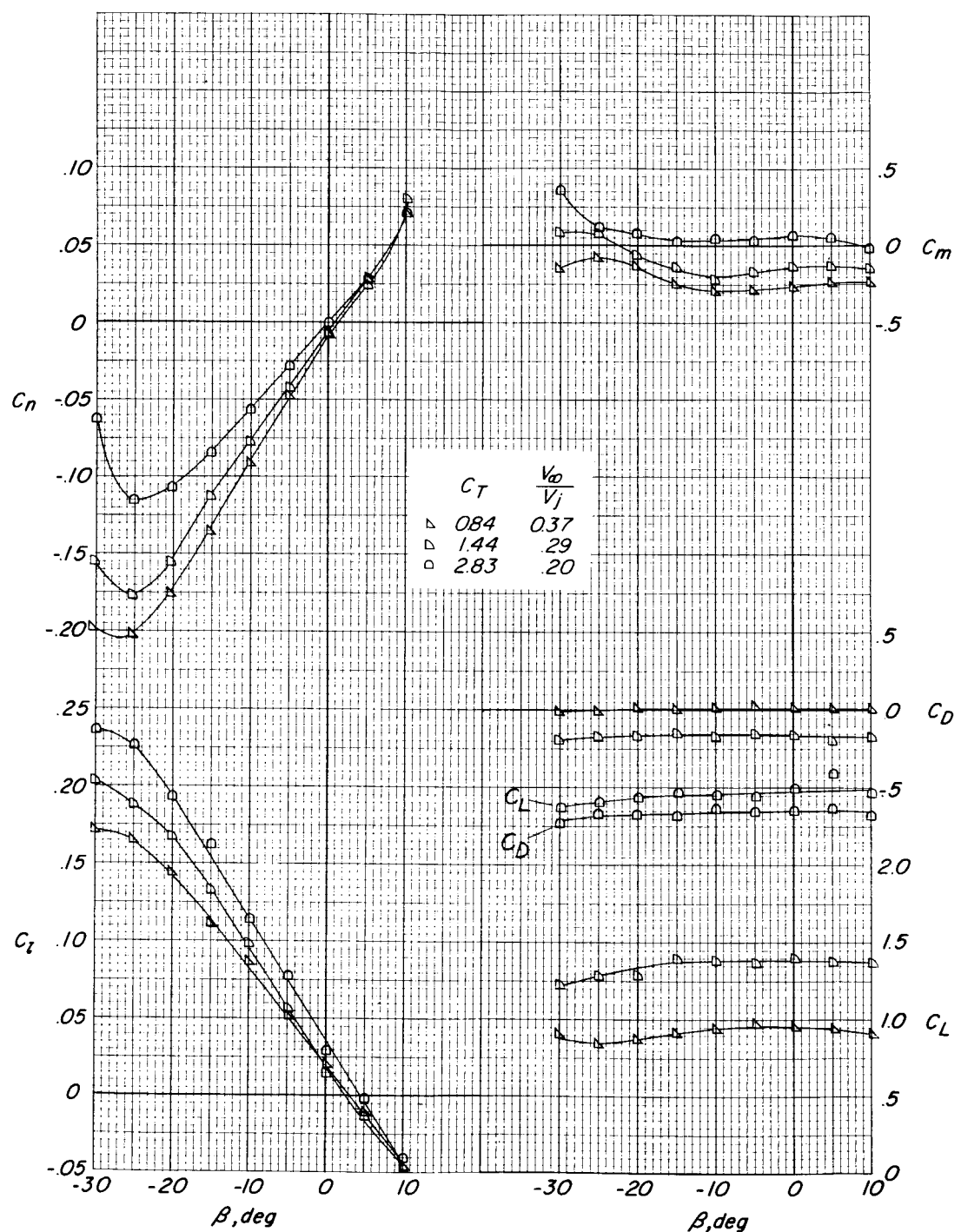
Figure 18.- Continued.

# DECLASSIFIED



(e)  $\delta_j = 49^\circ$ ;  $\alpha = 0^\circ$ .

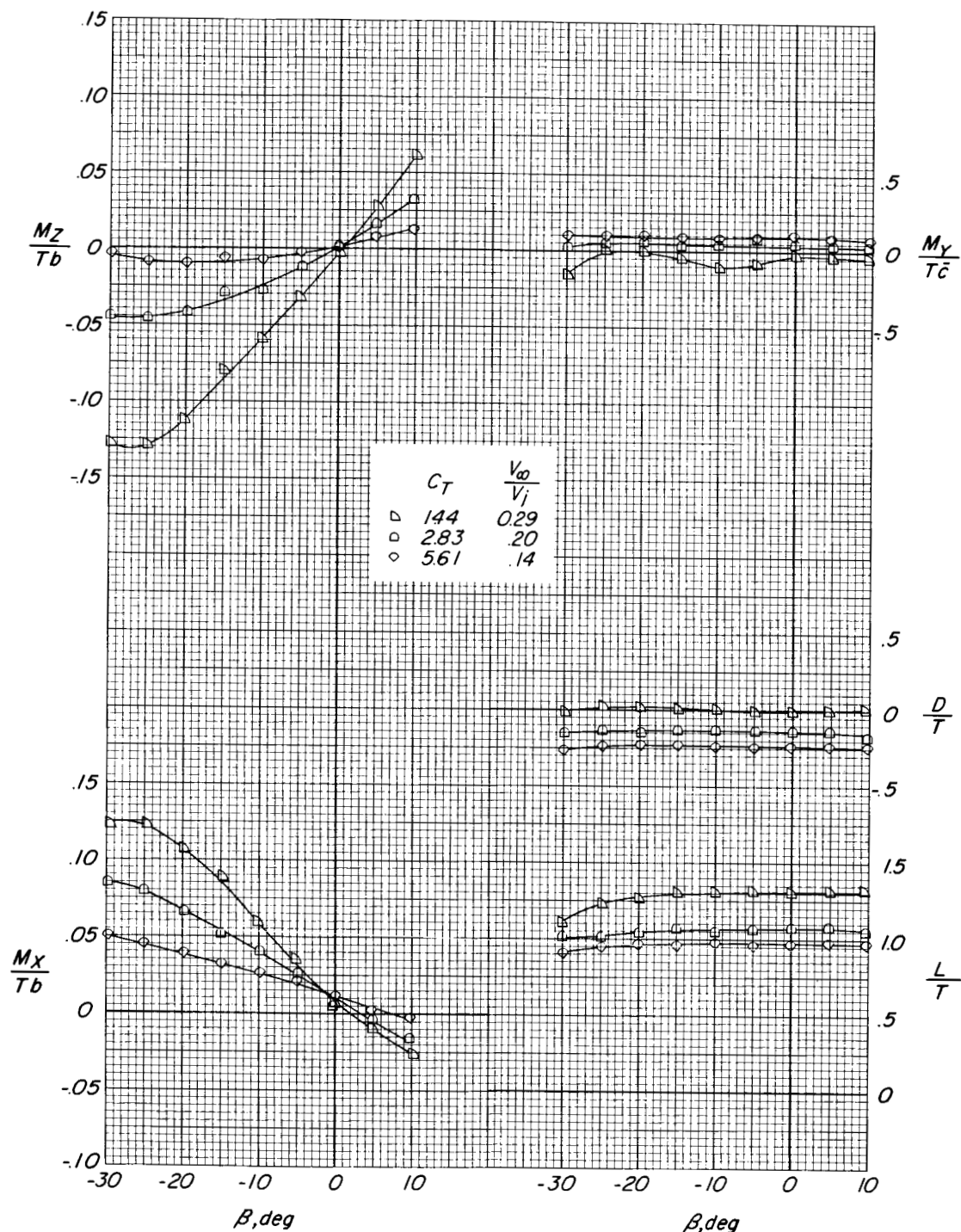
Figure 18.- Continued.



(f)  $\delta_j = 60^\circ; \alpha = 0^\circ.$

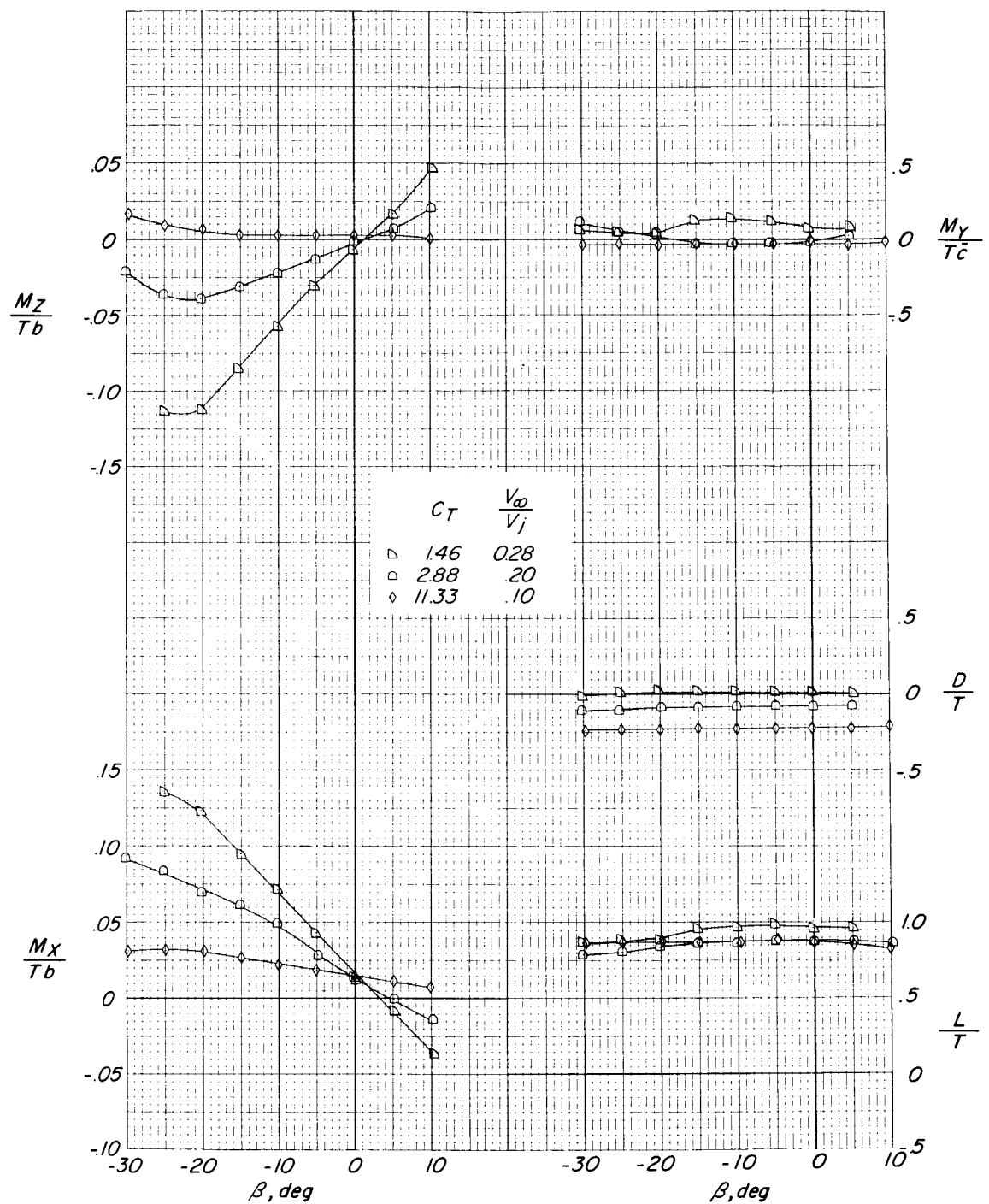
Figure 18.- Continued.

# DECCELERATED



(g)  $\delta_j = 60^\circ$ ;  $\alpha = 5^\circ$ .

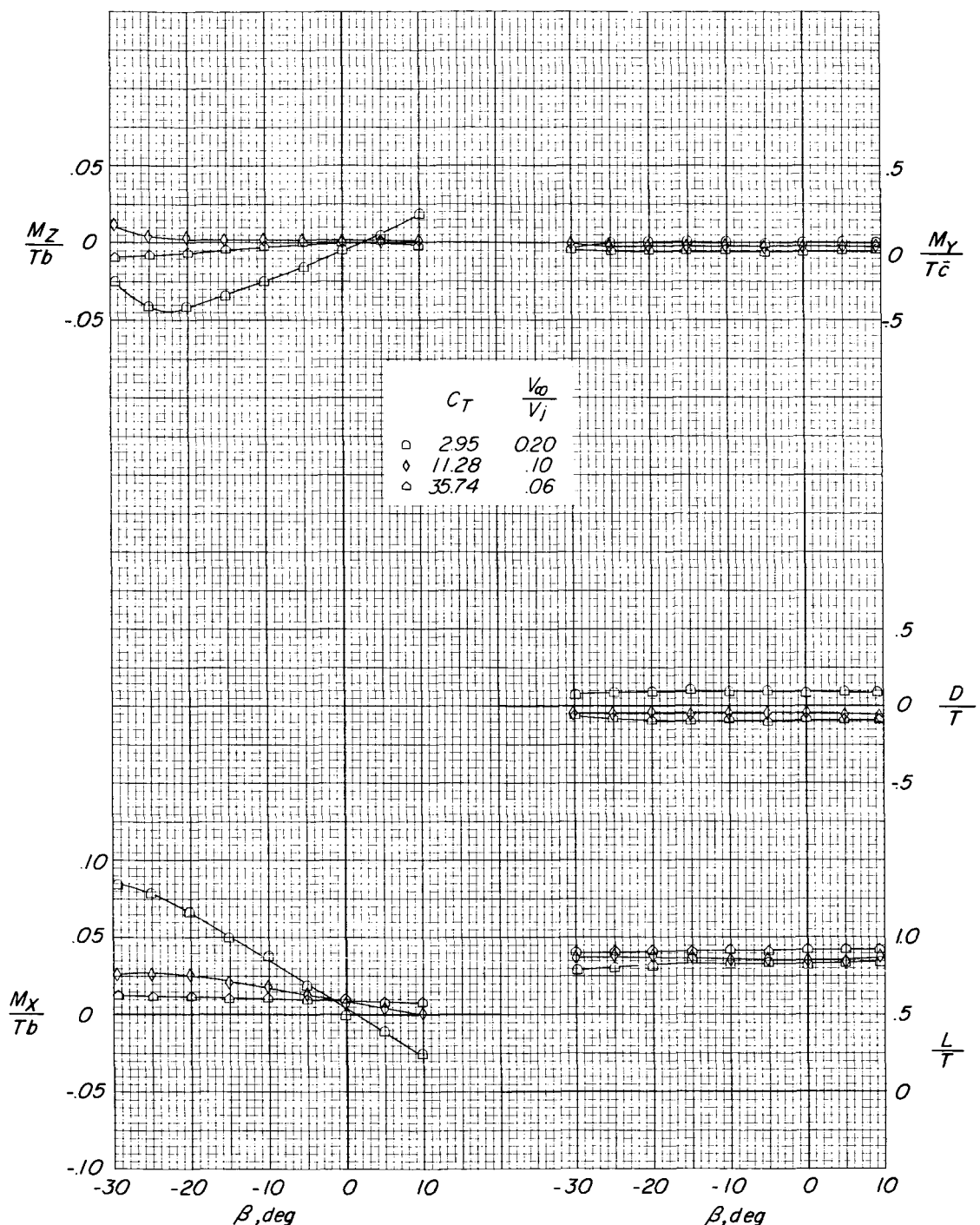
Figure 18.- Continued.



(h)  $\delta_j = 68^\circ$ ;  $\alpha = 0^\circ$ .

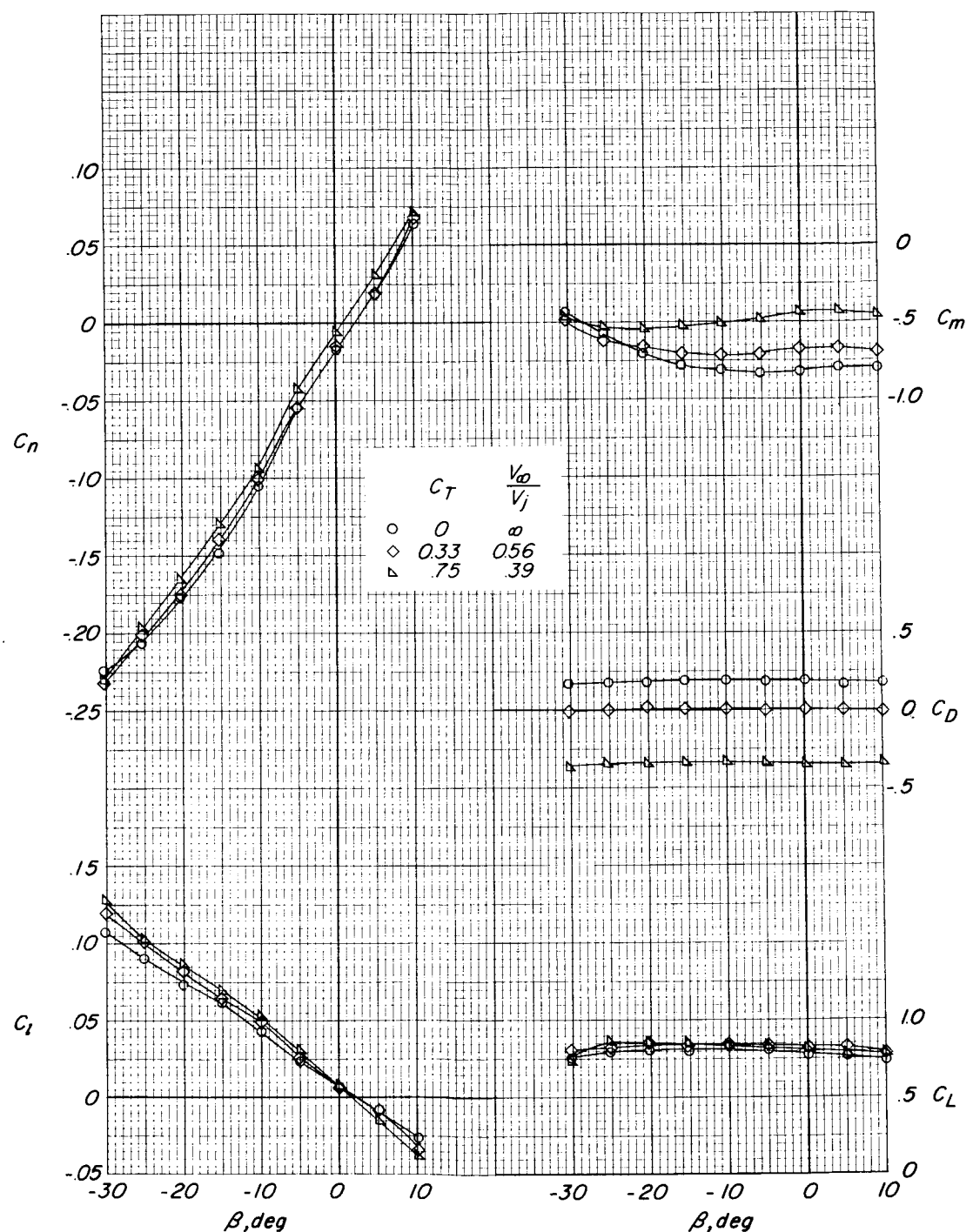
Figure 18.- Continued.

DECLASSIFIED



(i)  $\delta_j = 78^\circ$ ;  $\alpha = 0^\circ$ .

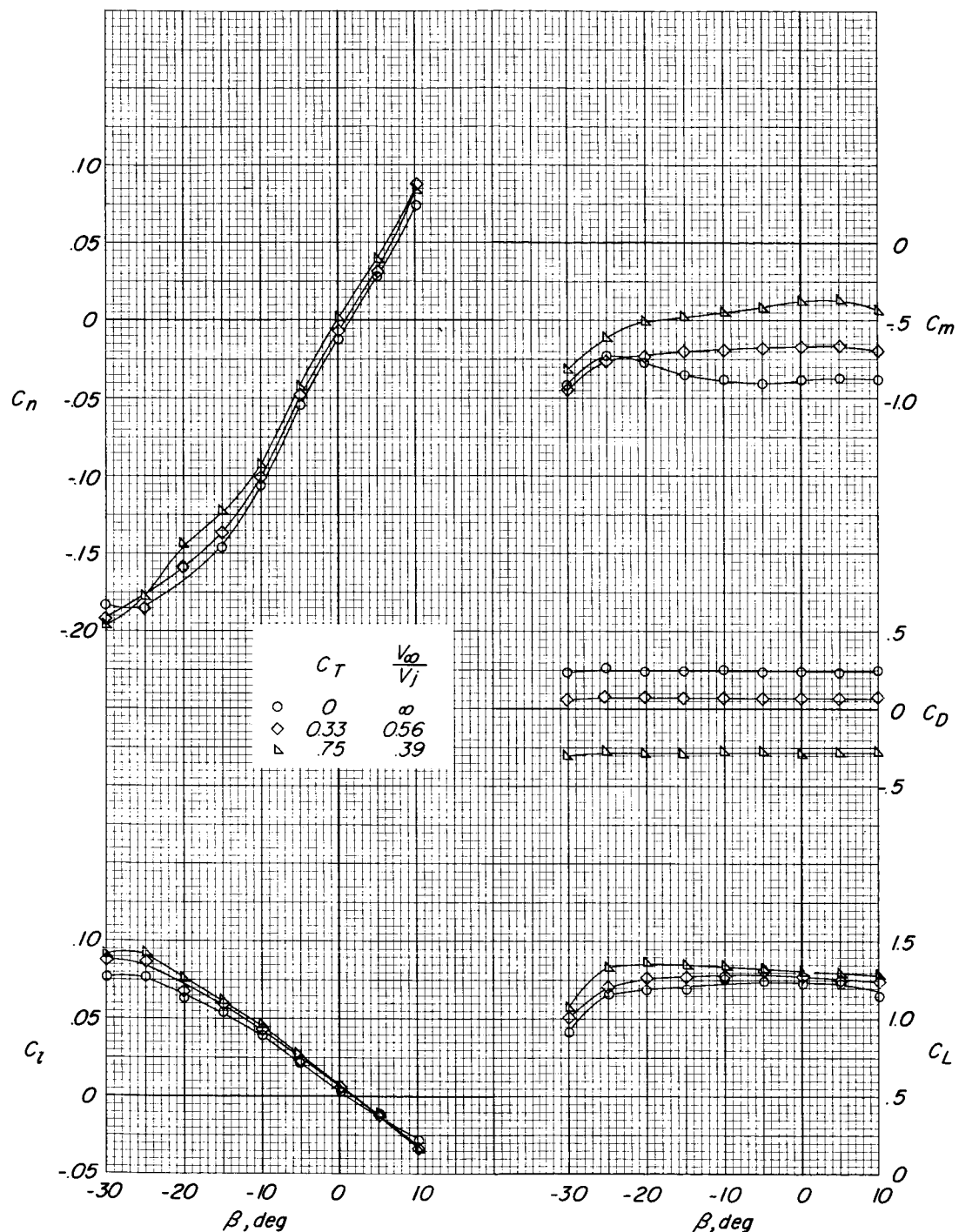
Figure 18.- Concluded.



(a)  $\delta_j = 4^\circ; \alpha = 0^\circ.$

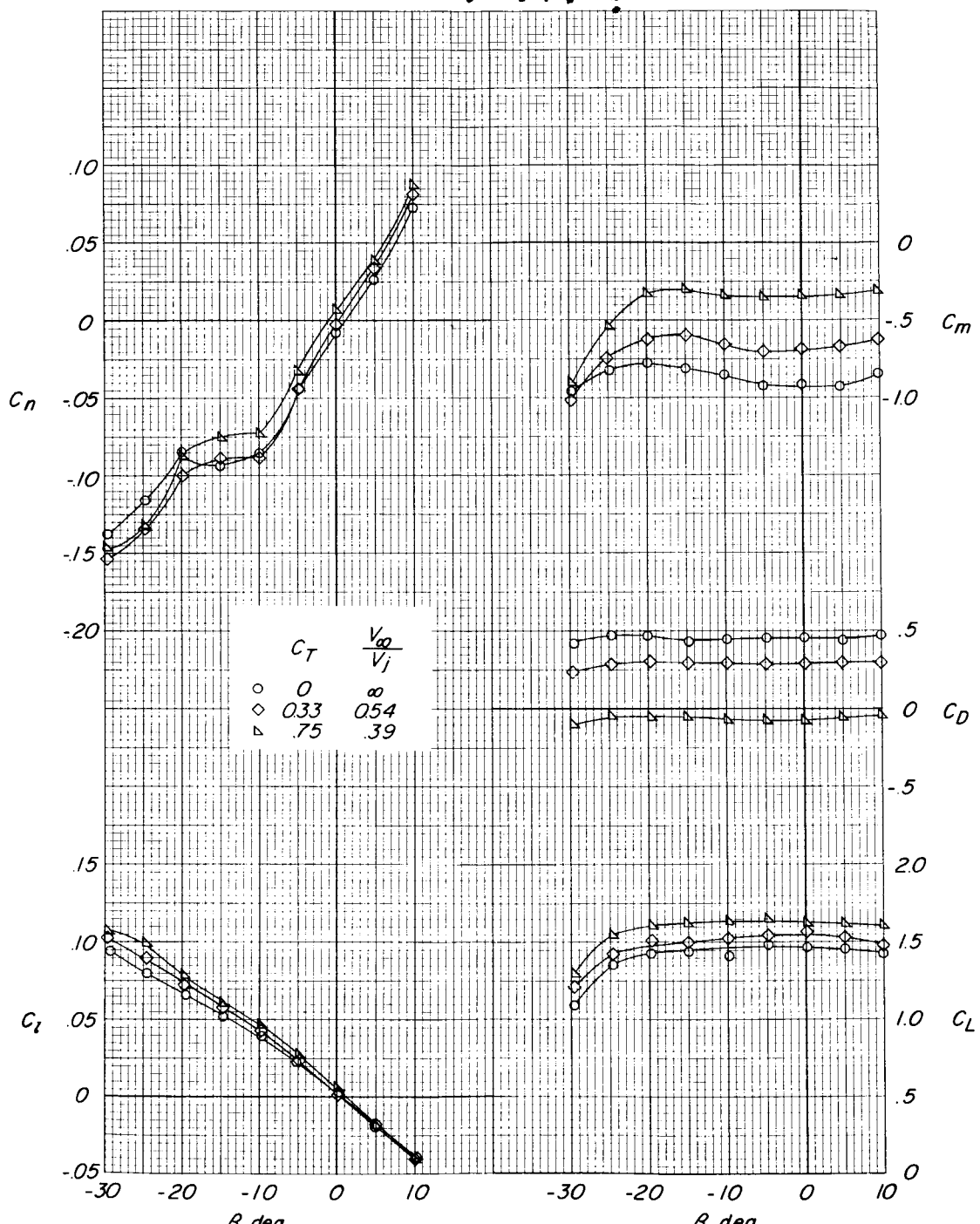
Figure 19.- Lateral characteristics of the basic model with the vertical tail on and flaps deflected  $40^\circ$ .  $\delta_e = 10^\circ; \Lambda = 15^\circ$ .

DECLASSIFIED



$$(b) \quad \delta_j = 4^\circ; \quad \alpha = 5^\circ.$$

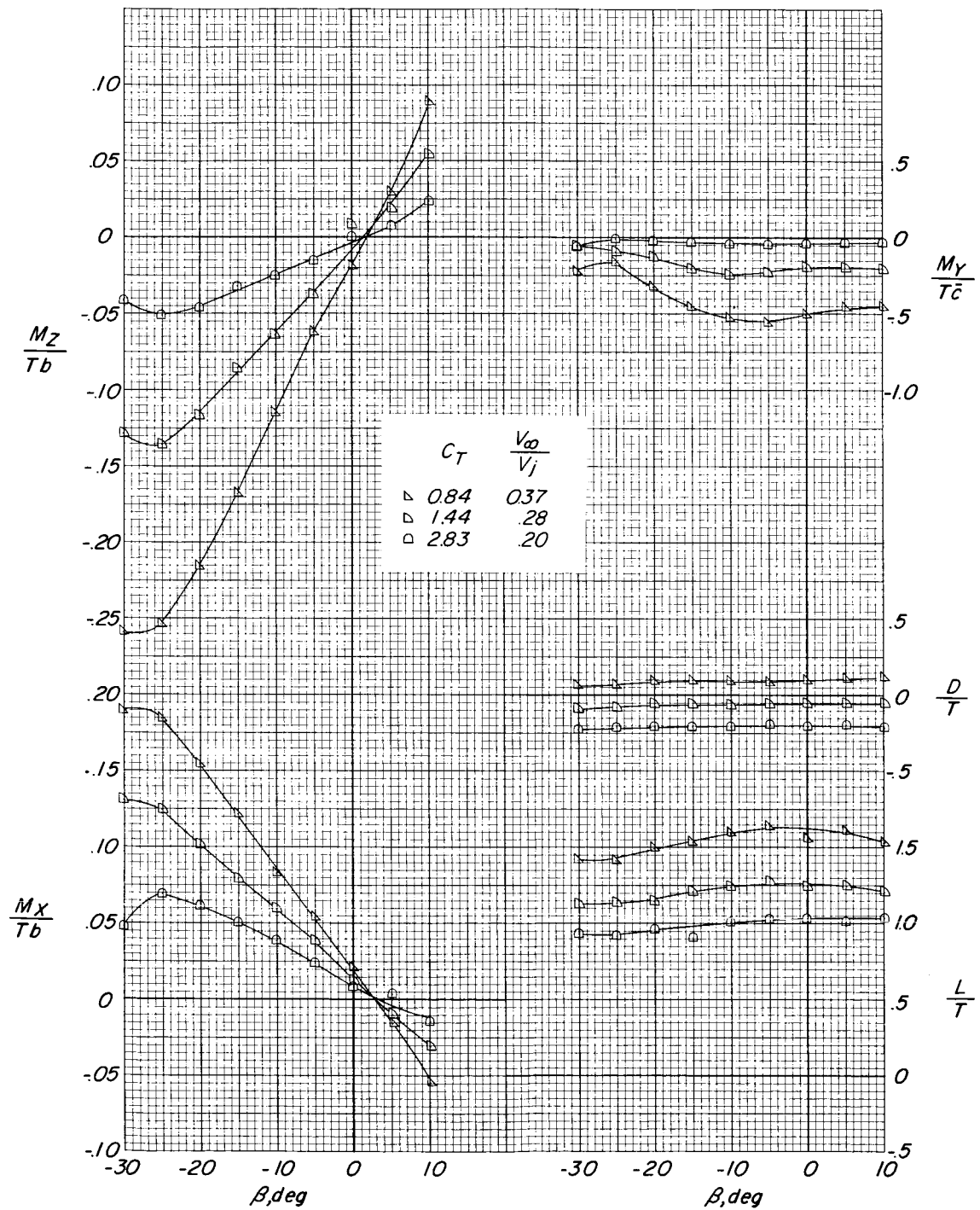
Figure 19.- Continued.



(c)  $\delta_j = 4^\circ$ ;  $\alpha = 10^\circ$ .

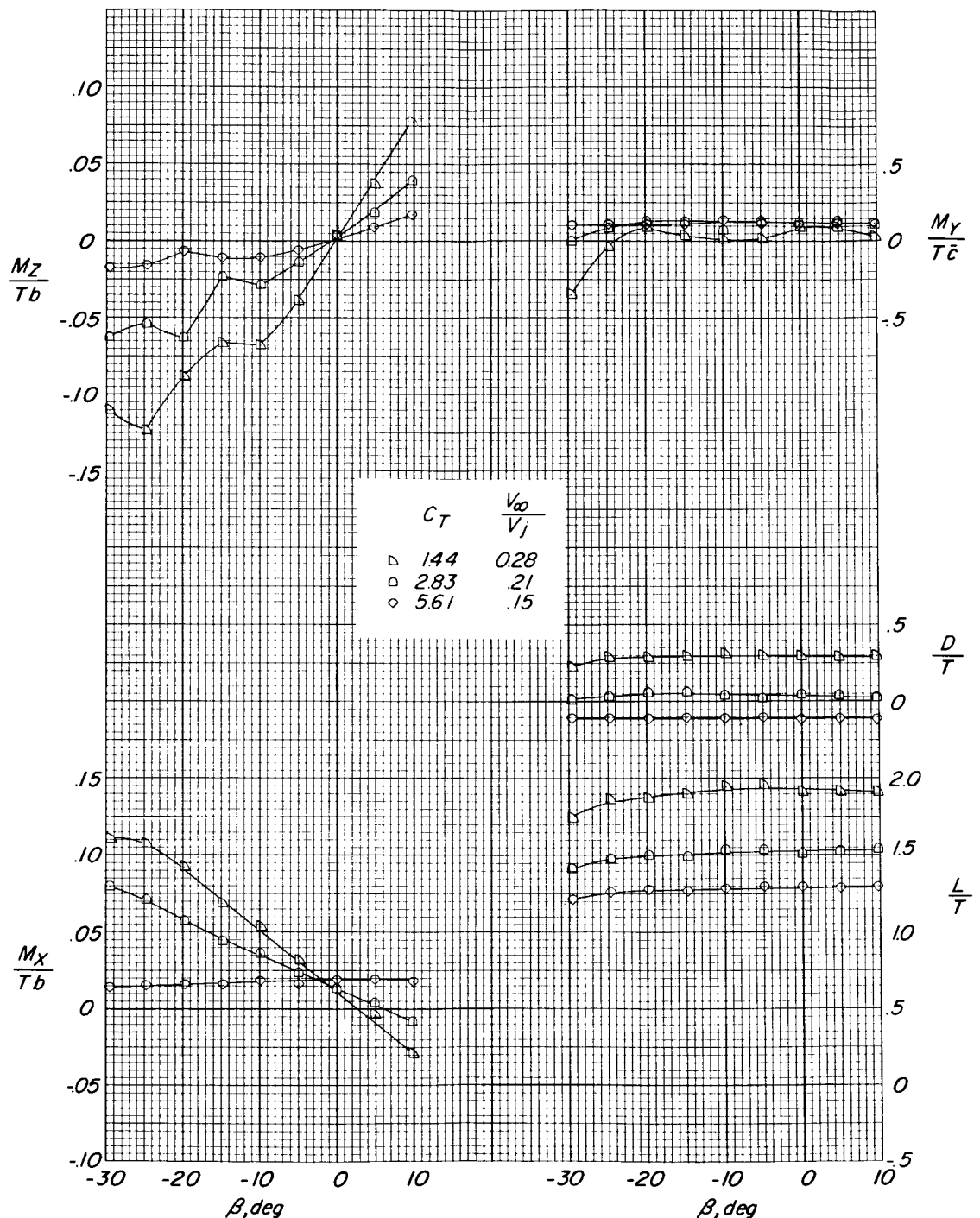
Figure 19.- Continued.

# DECOMPOSED



(d)  $\delta_j = 60^\circ$ ;  $\alpha = 0^\circ$ .

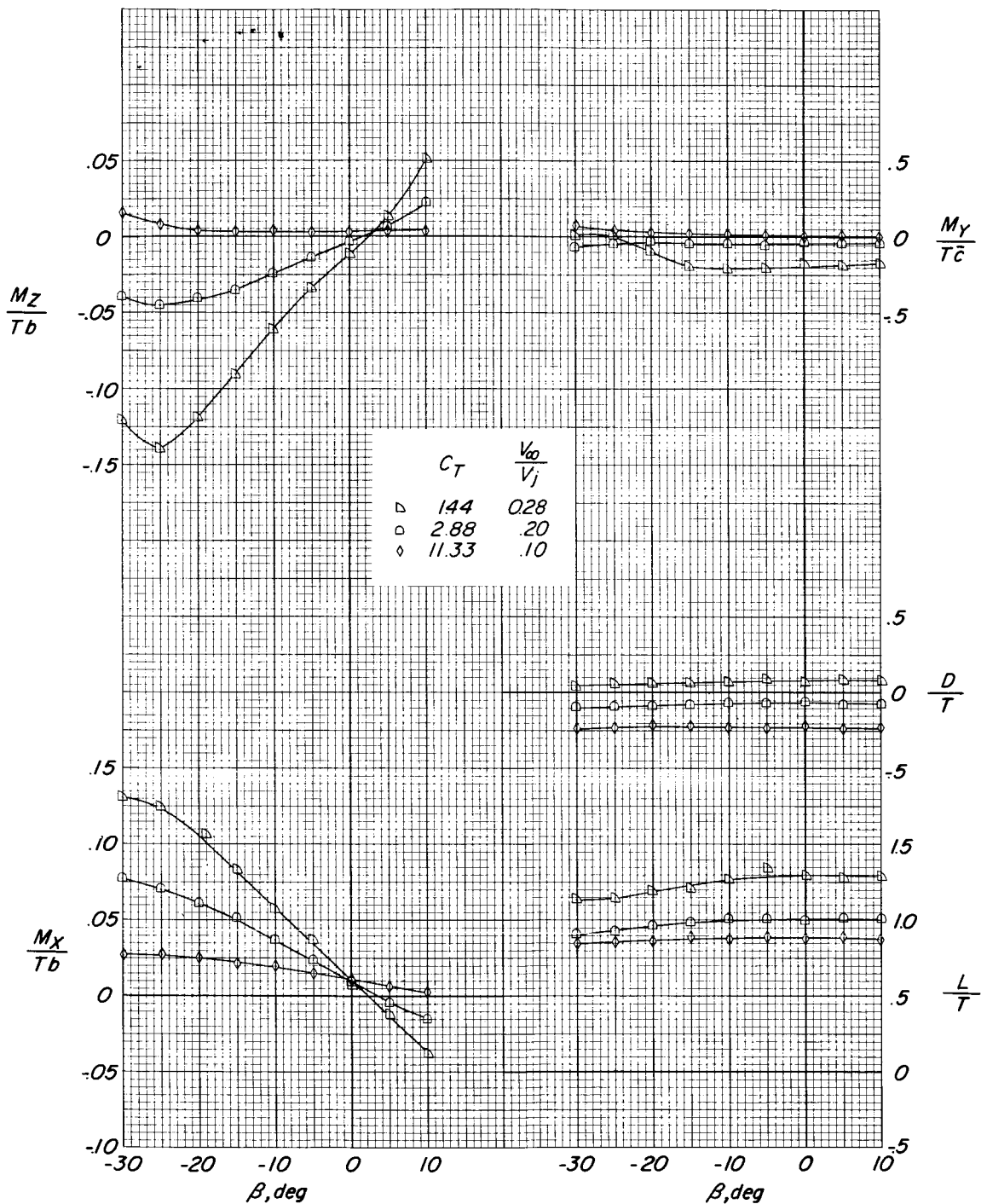
Figure 19.- Continued.



(e)  $\delta_j = 60^\circ; \alpha = 10^\circ.$

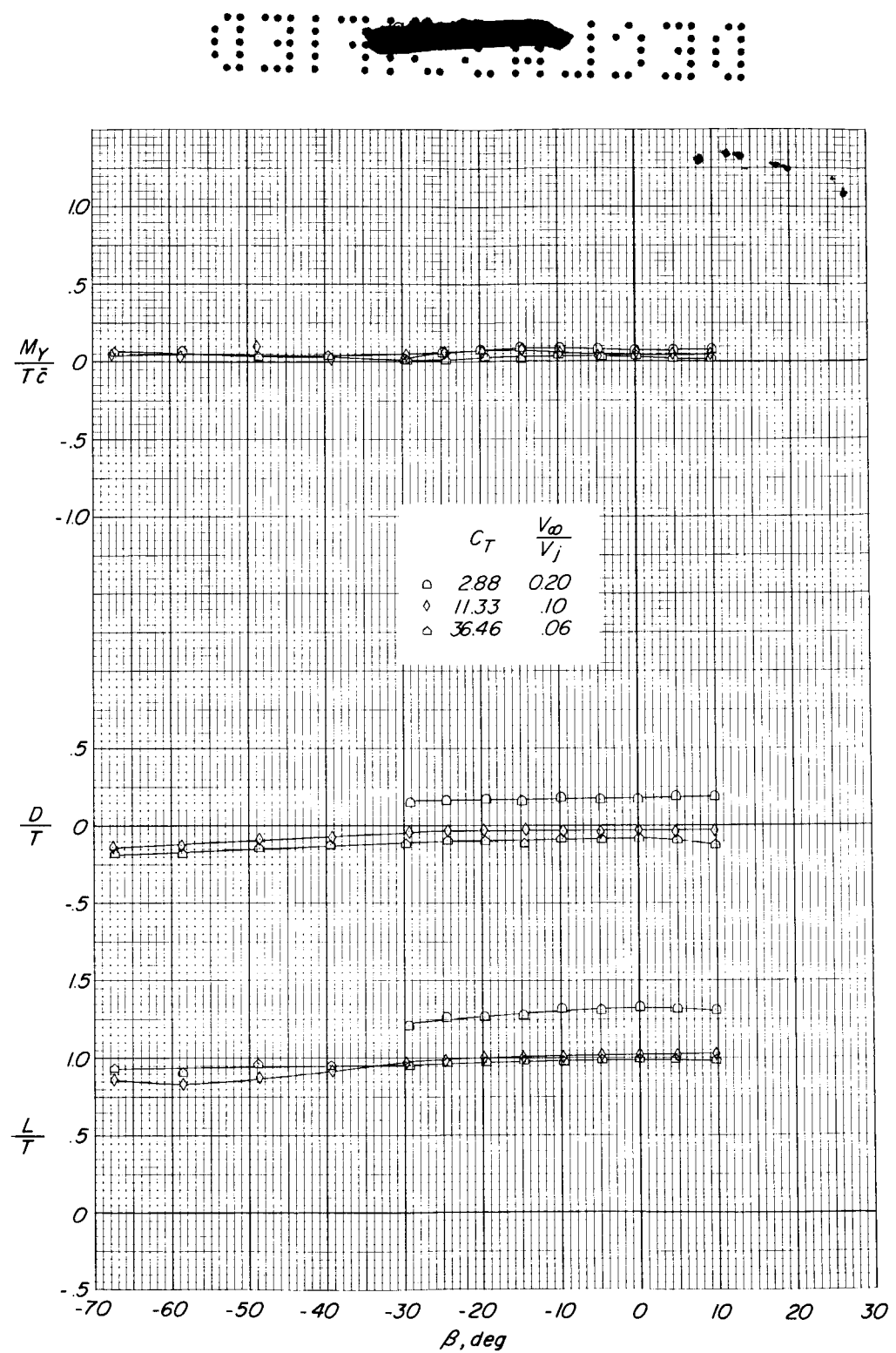
Figure 19.- Continued.

# DECLASSIFIED



(f)  $\delta_j = 68^\circ$ ;  $\alpha = 0^\circ$ .

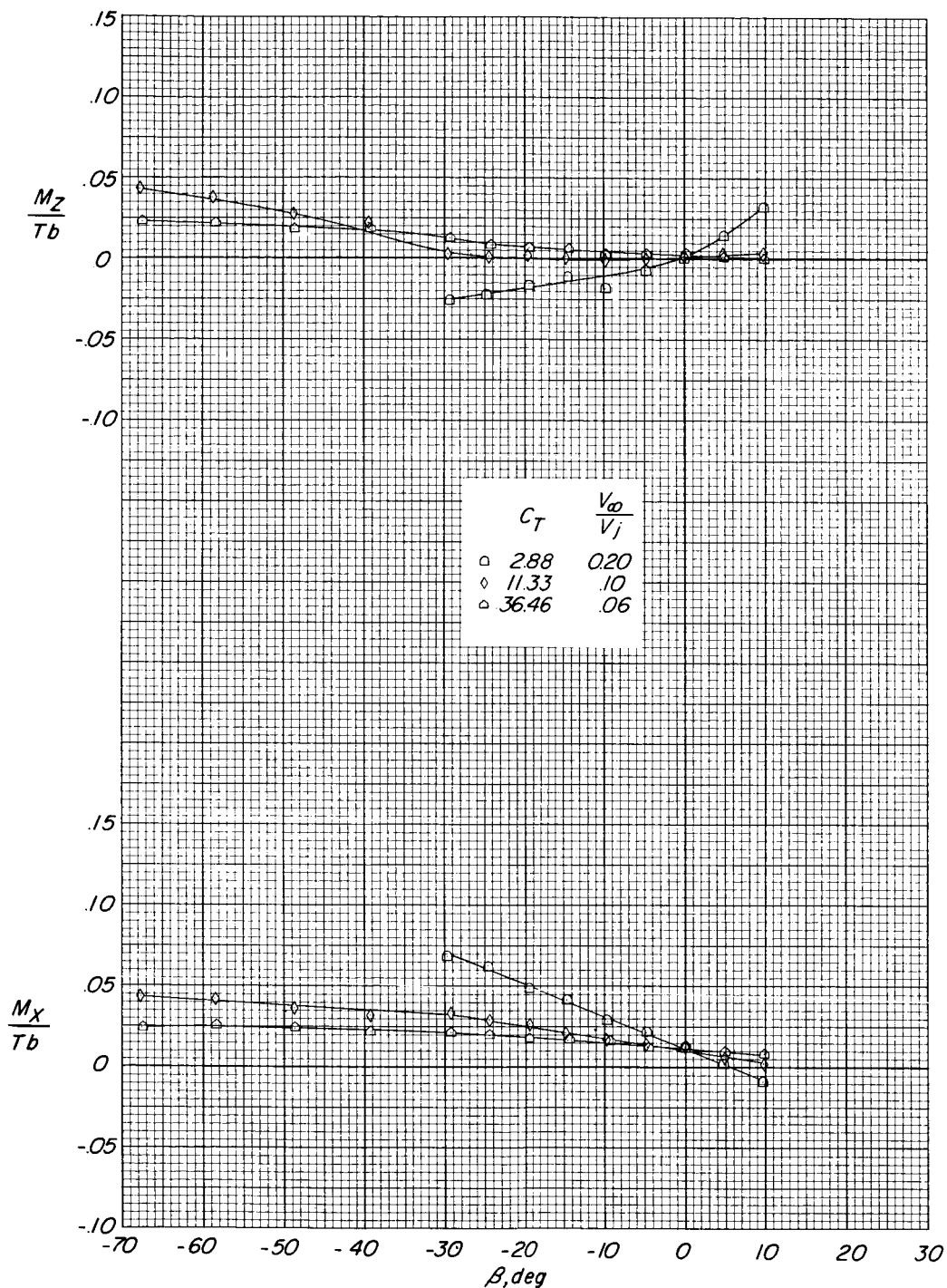
Figure 19.- Continued.



(g)  $\delta_j = 68^\circ; \alpha = 10^\circ.$

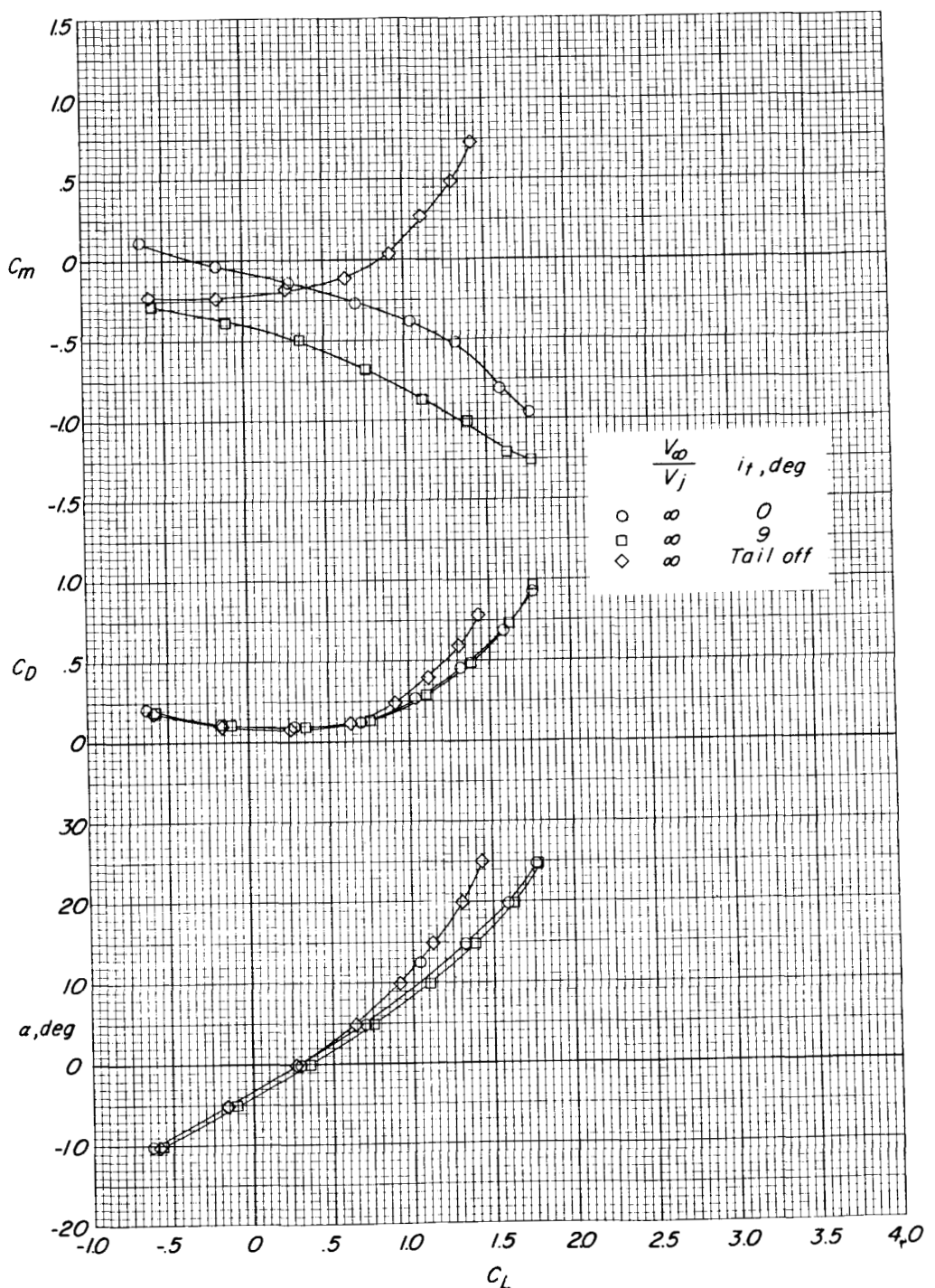
Figure 19.- Continued.

~~DECLASSIFIED~~



(g)  $\delta_j = 68^\circ$ ;  $\alpha = 10^\circ$ . Concluded.

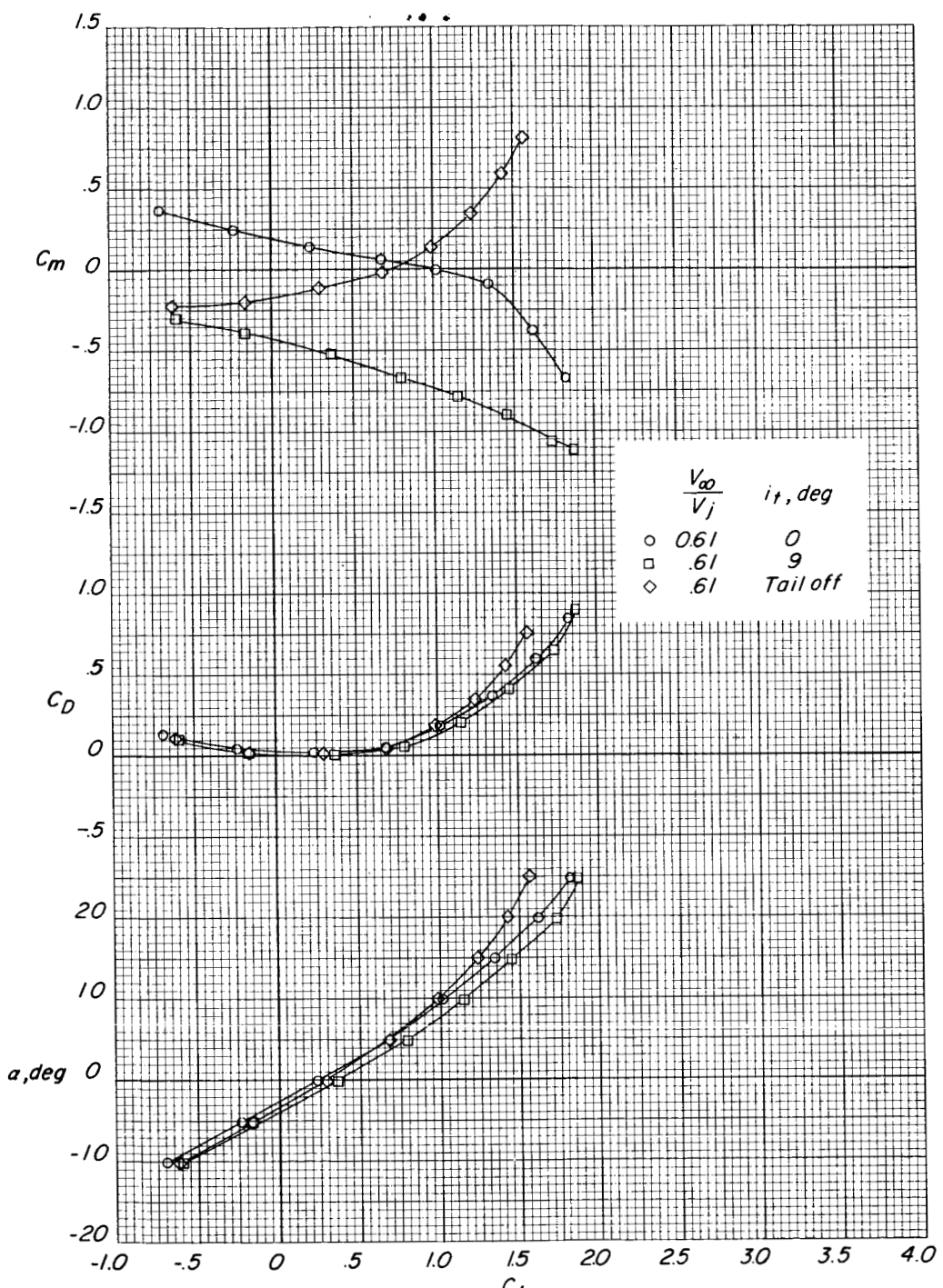
Figure 19.- Concluded.



(a)  $C_T \approx 0$ .

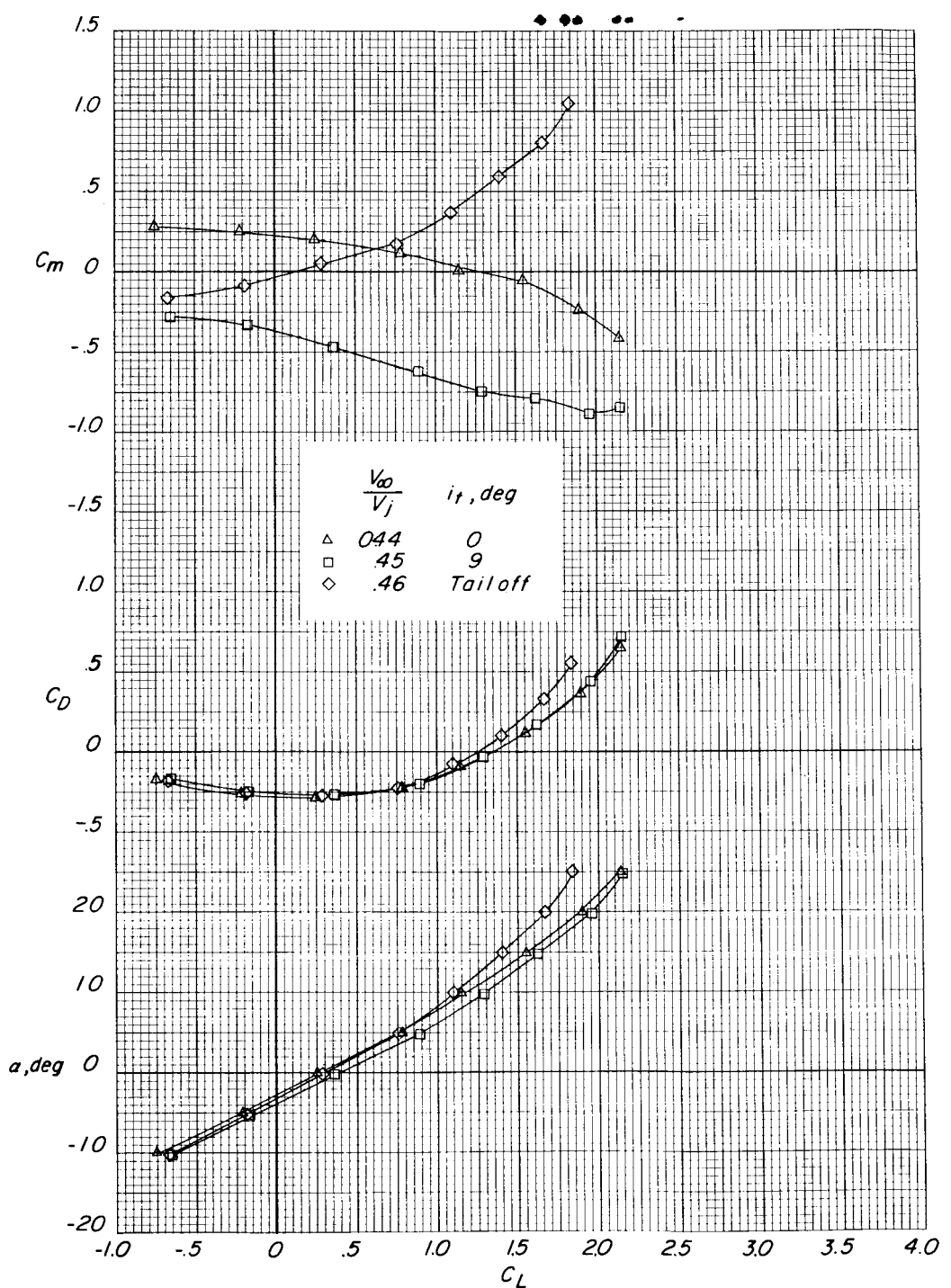
Figure 20.- Horizontal-tail effectiveness at various power settings of the modified model with flaps undeflected.  $\delta_j = 4^\circ$ ;  $\Lambda = 15^\circ$ .

~~DECLASSIFIED~~



(b)  $C_T \approx 0.21$ .

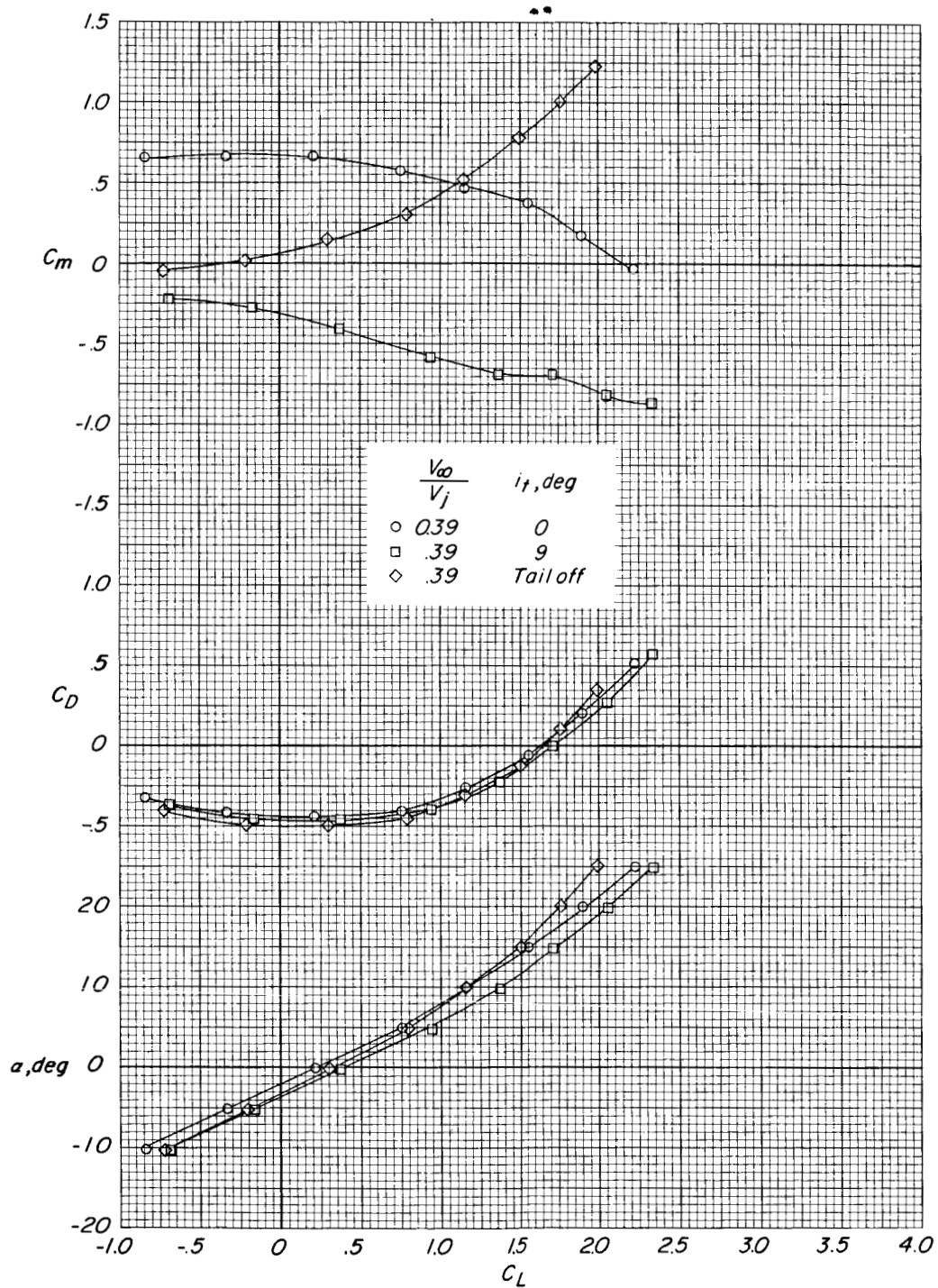
Figure 20.- Continued.



(c)  $C_T \approx 0.51$ .

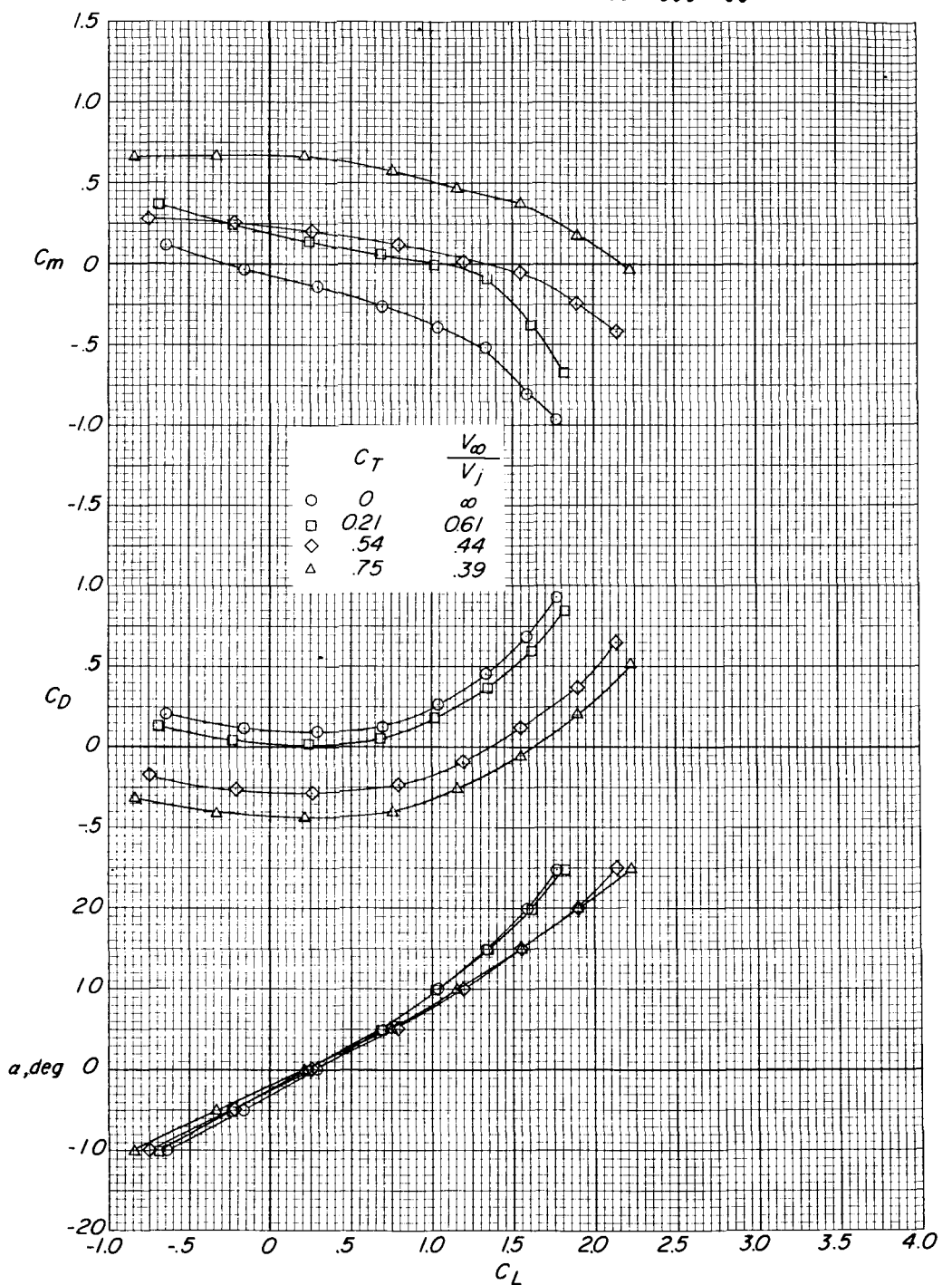
Figure 20.- Continued.

~~DECLASSIFIED~~



(a)  $C_T \approx 0.75$ .

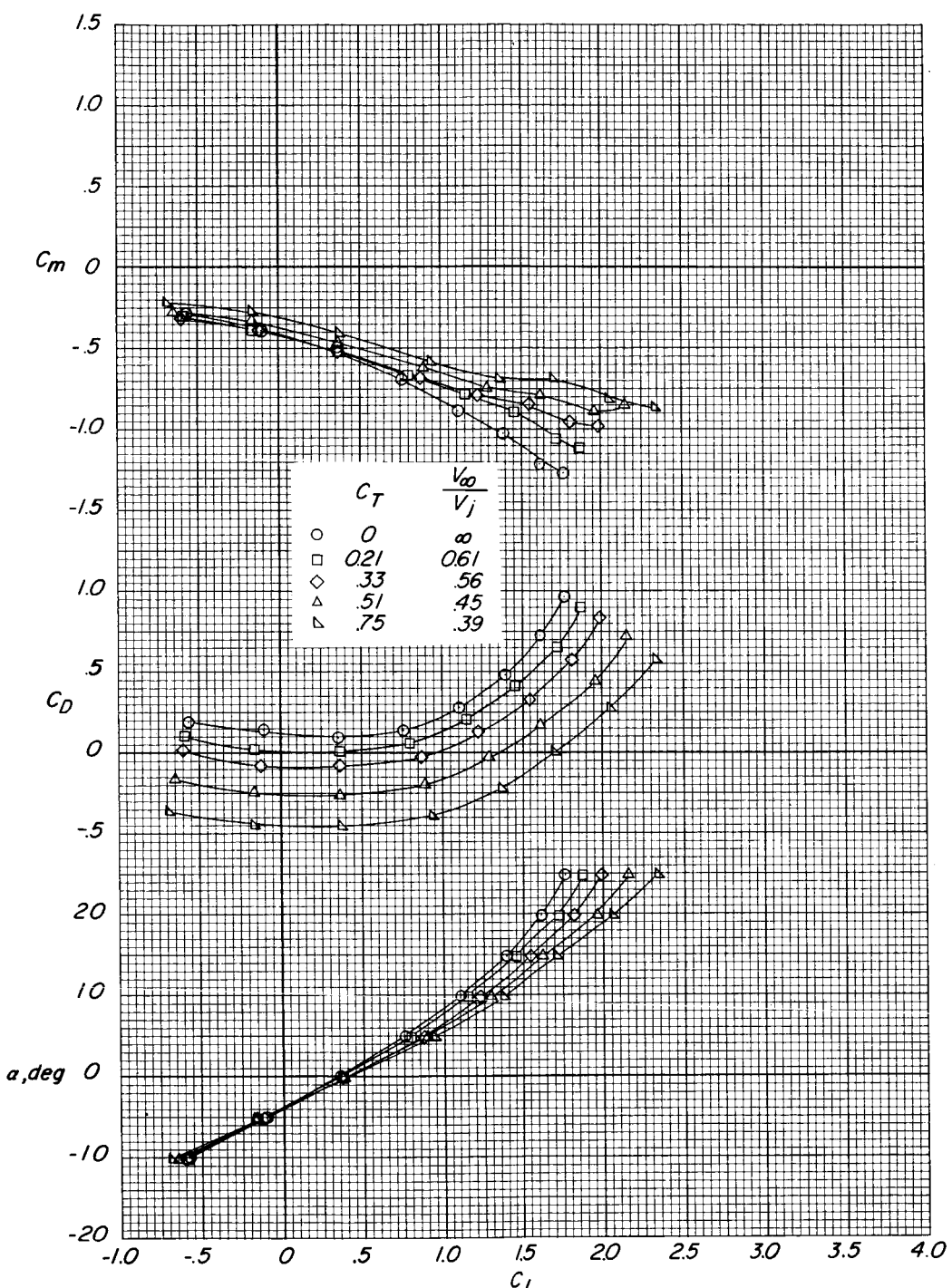
Figure 20.- Concluded.



(a)  $i_t = 0^\circ$ .

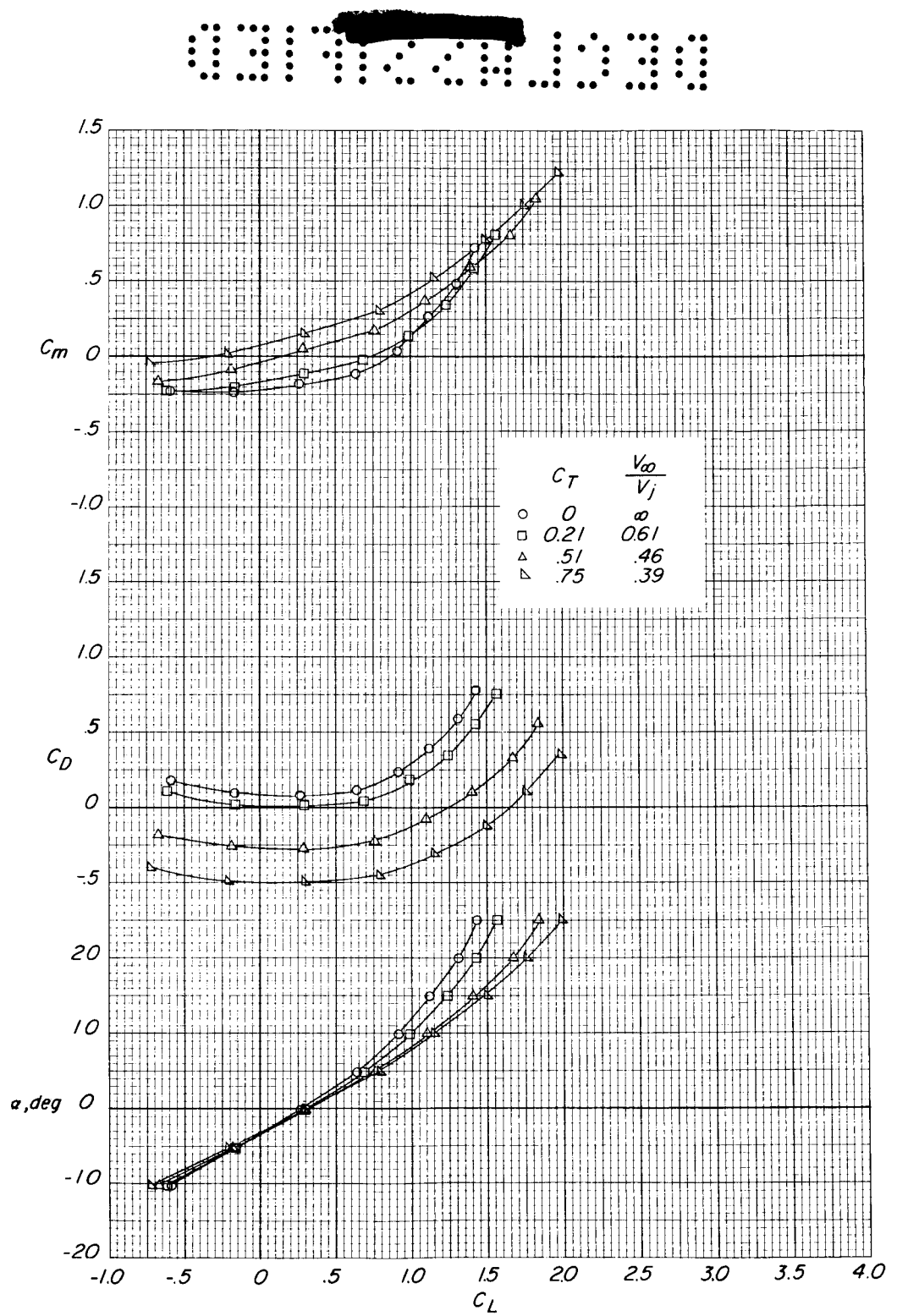
Figure 21.- Effect of power on the longitudinal aerodynamic characteristics of the modified model. Flaps undeflected;  $\delta_j = 4^\circ$ ;  $\Lambda = 15^\circ$ .

~~DECLASSIFIED~~



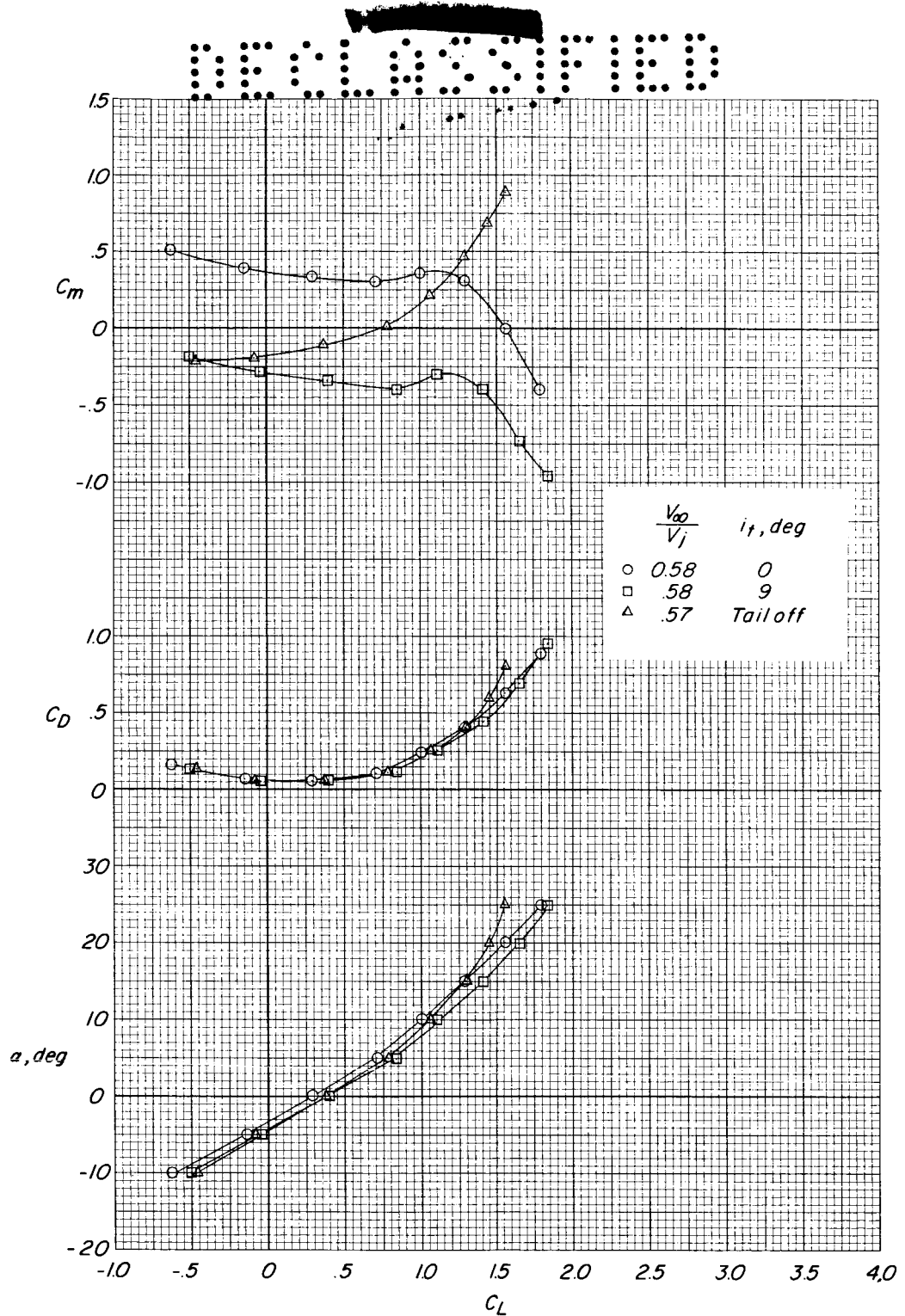
(b)  $i_t = 9^\circ$ .

Figure 21.- Continued.



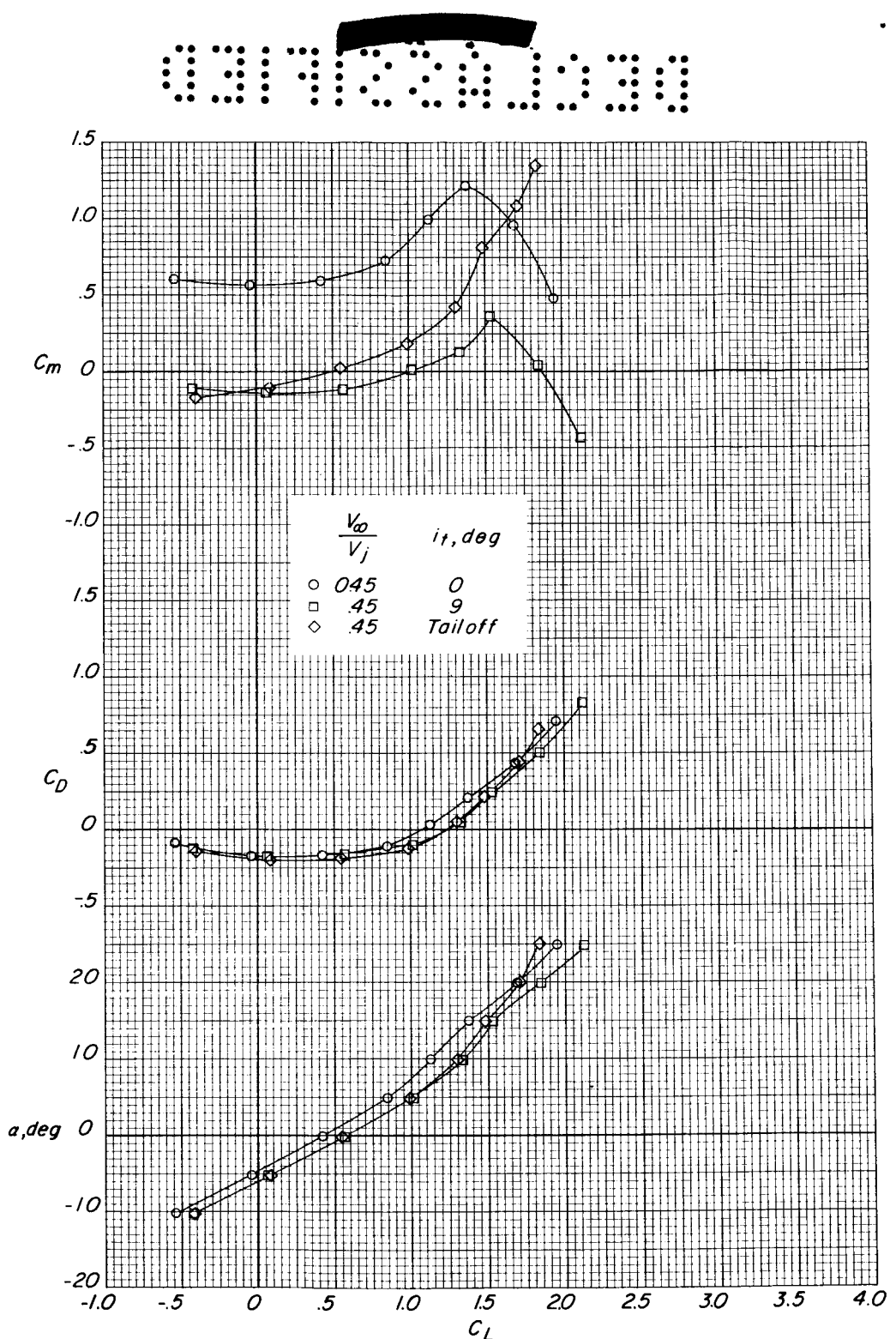
(c) Tail off.

Figure 21.- Concluded.



(a)  $C_T \approx 0.23$ .

Figure 22.- Horizontal-tail effectiveness at various power settings of the modified model with flaps undeflected.  $\delta_j = 31^\circ$ ;  $\Lambda = 15^\circ$ .

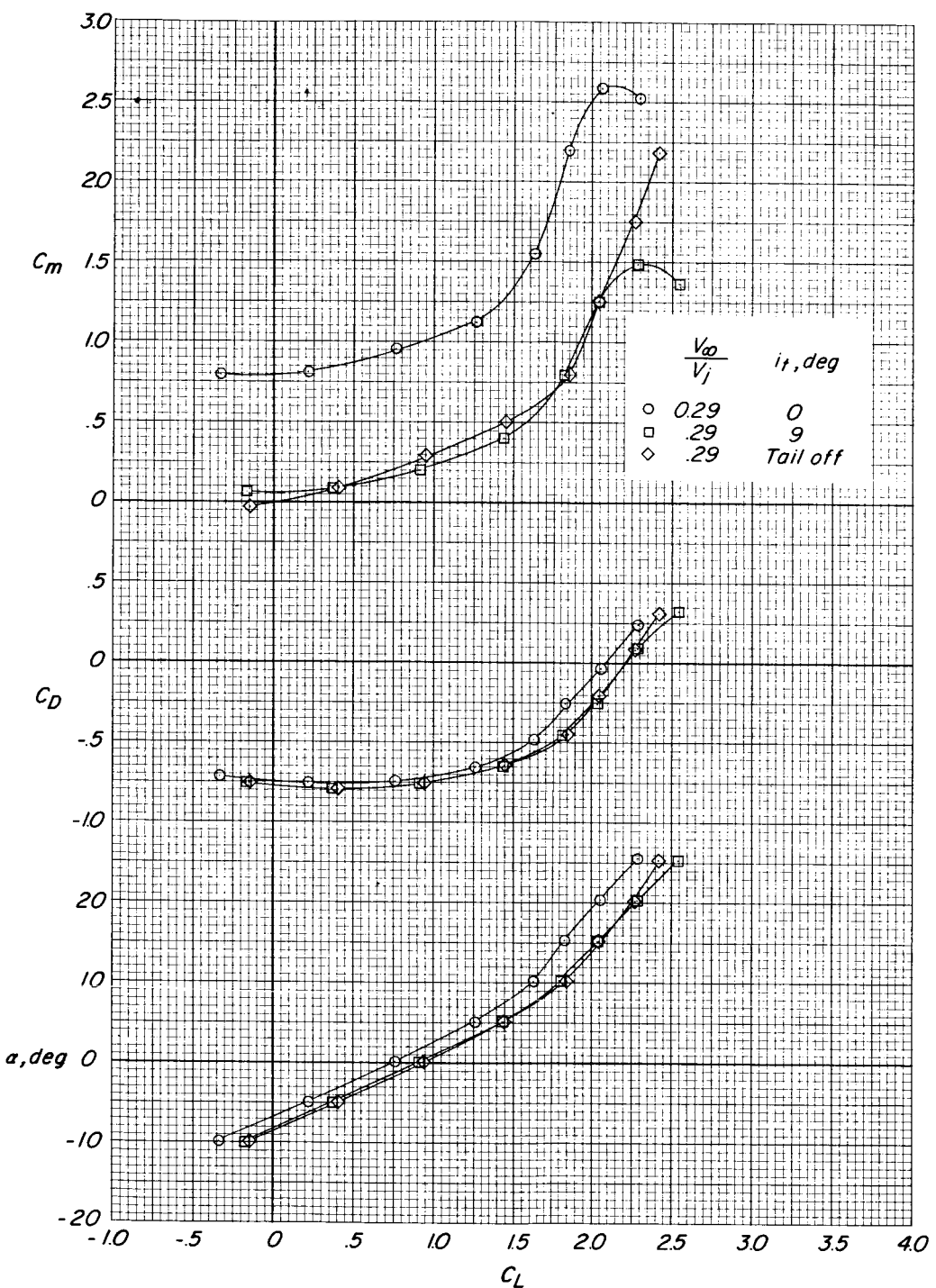


(b)  $C_T \approx 0.54$ .

Figure 22.- Continued.

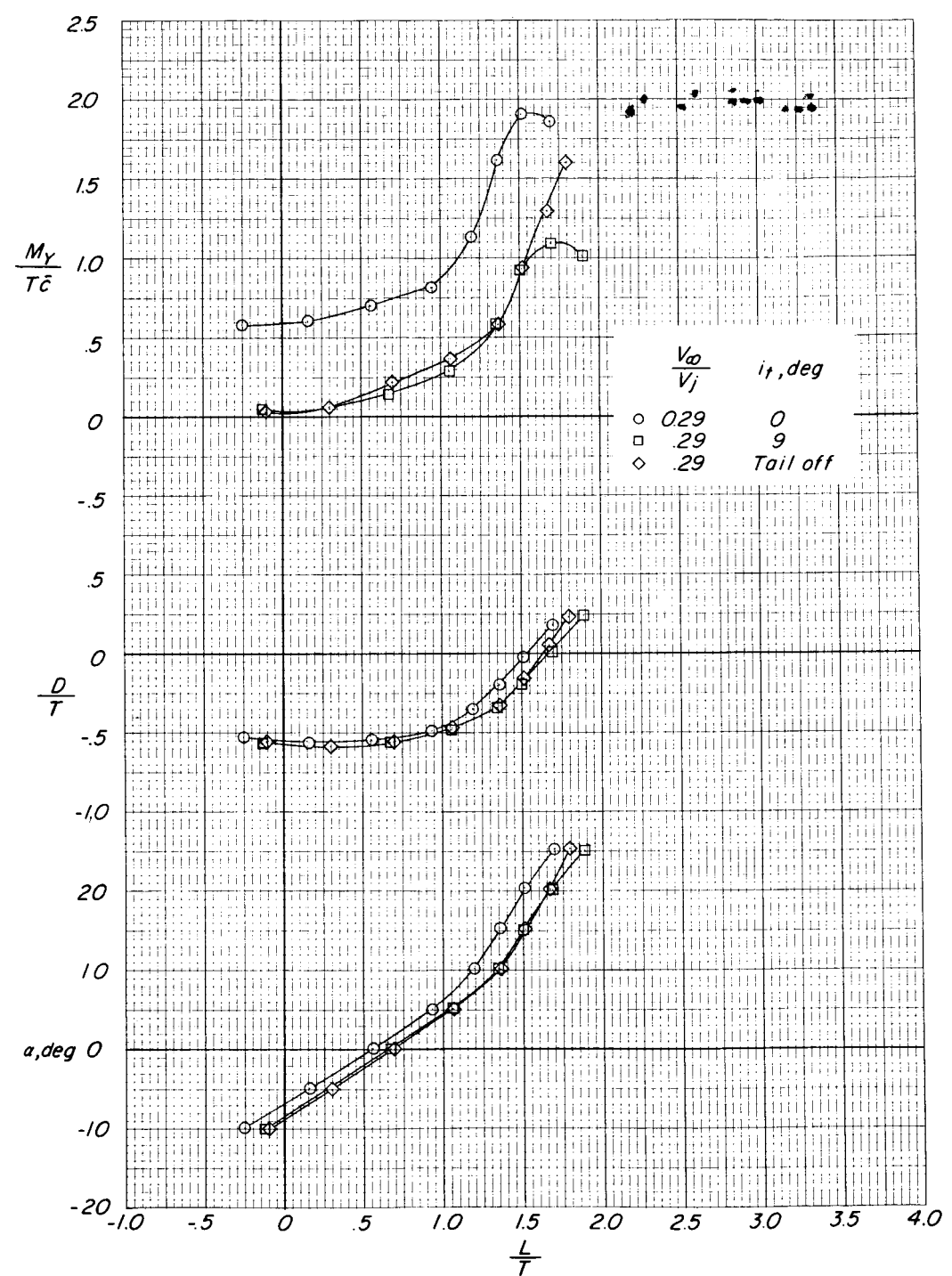
~~SECRET~~

DECLASSIFIED



(c)  $C_T \approx 1.35$ .

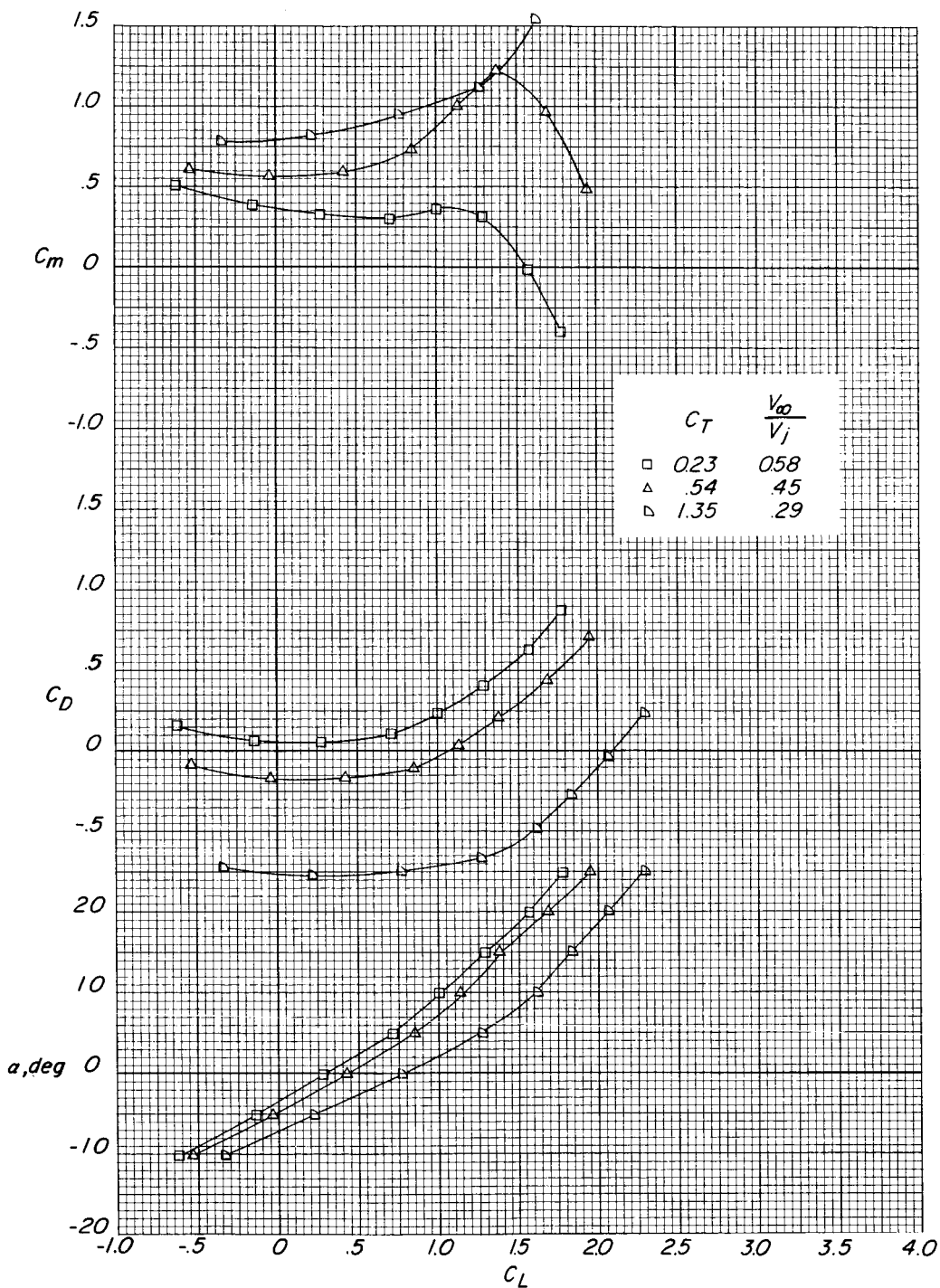
Figure 22.- Continued.



(c)  $C_T \approx 1.35$ . Concluded.

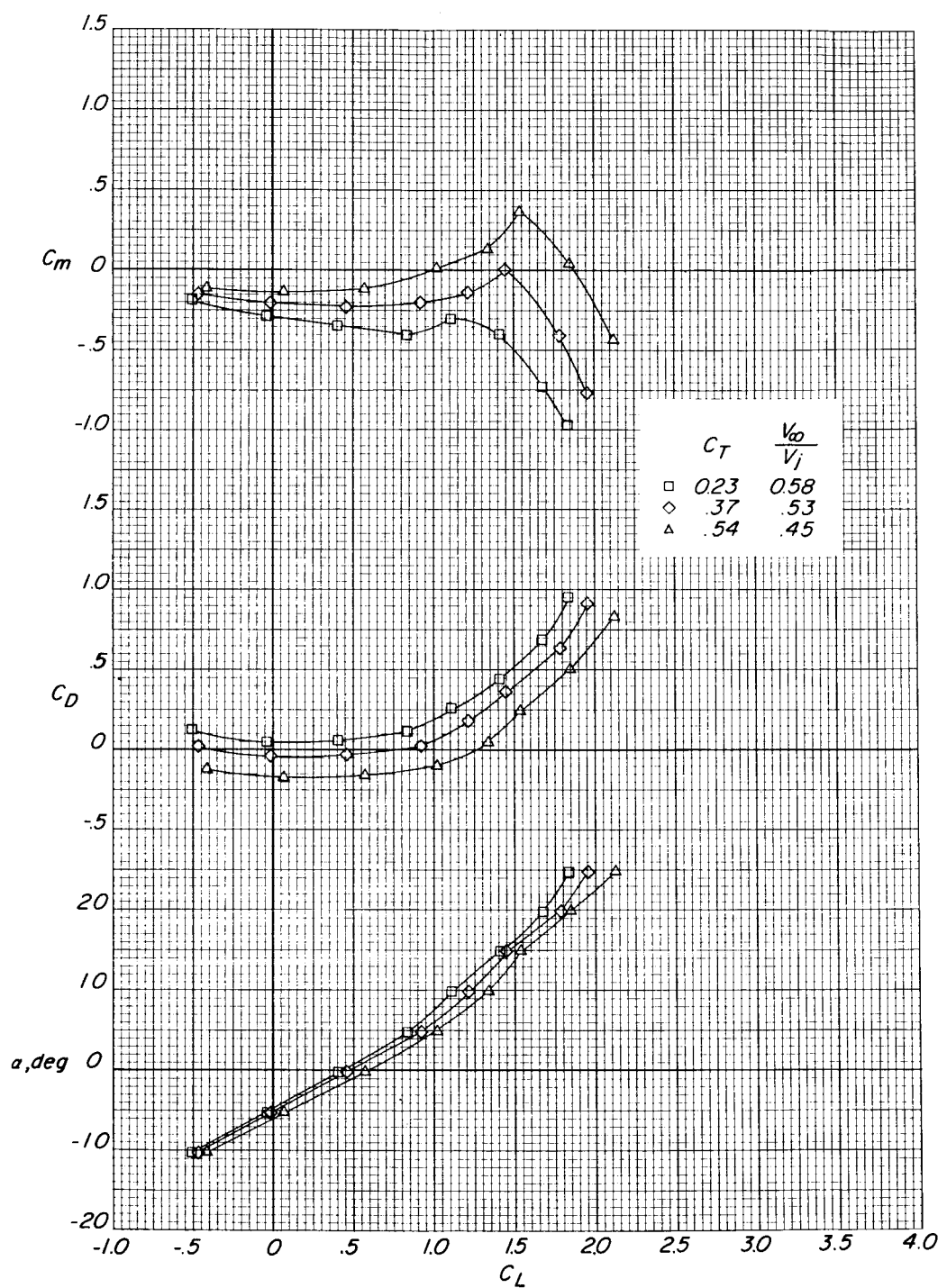
Figure 22.- Concluded.

# DECOMPOSED FIELD



(a)  $i_t = 0^\circ$ .

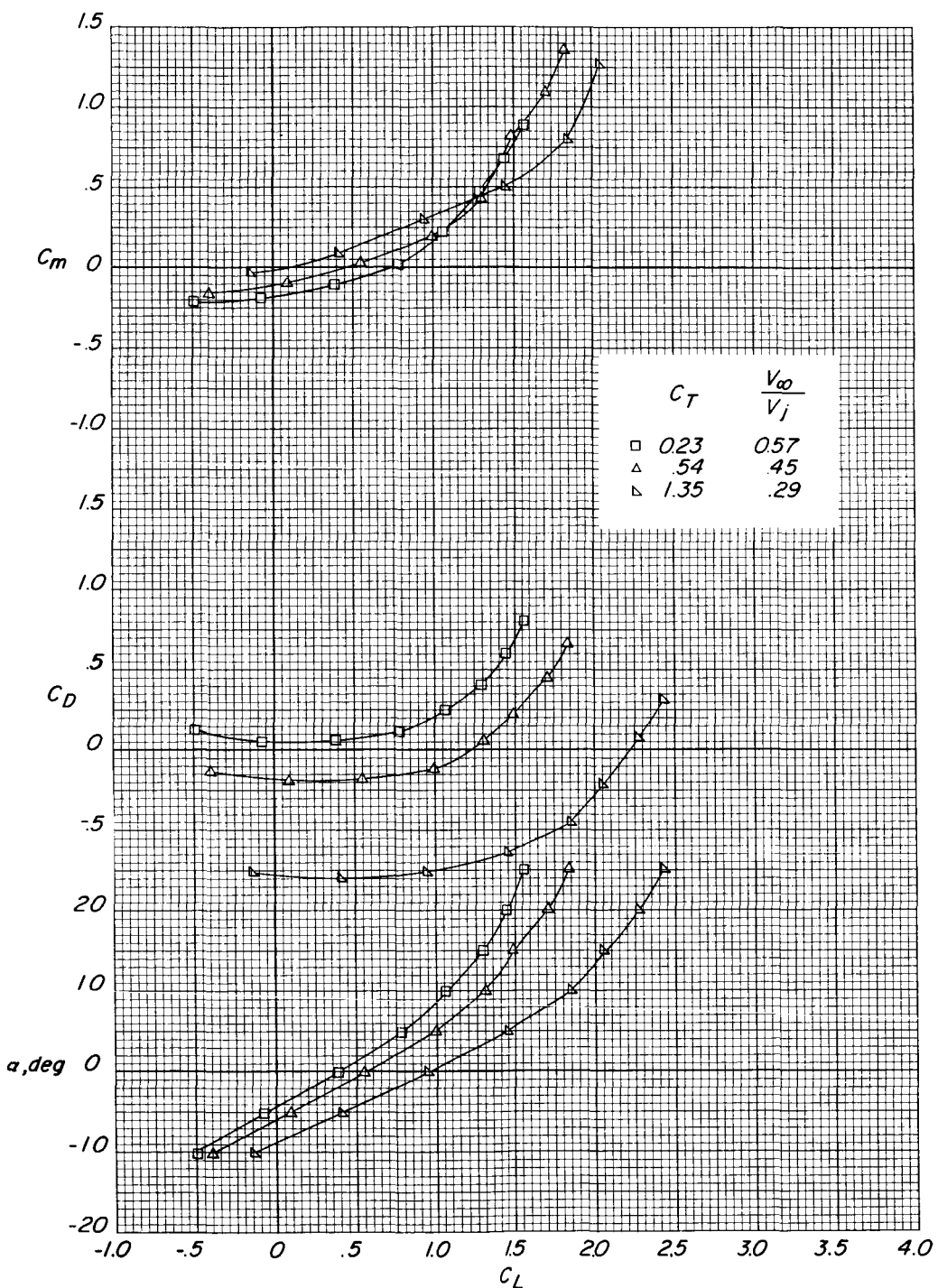
Figure 23.- Effect of power on the longitudinal aerodynamic characteristics of the modified model. Flaps undeflected;  $\delta_j = 31^\circ$ ;  $\Lambda = 15^\circ$ .



(b)  $i_t = 90^\circ$ .

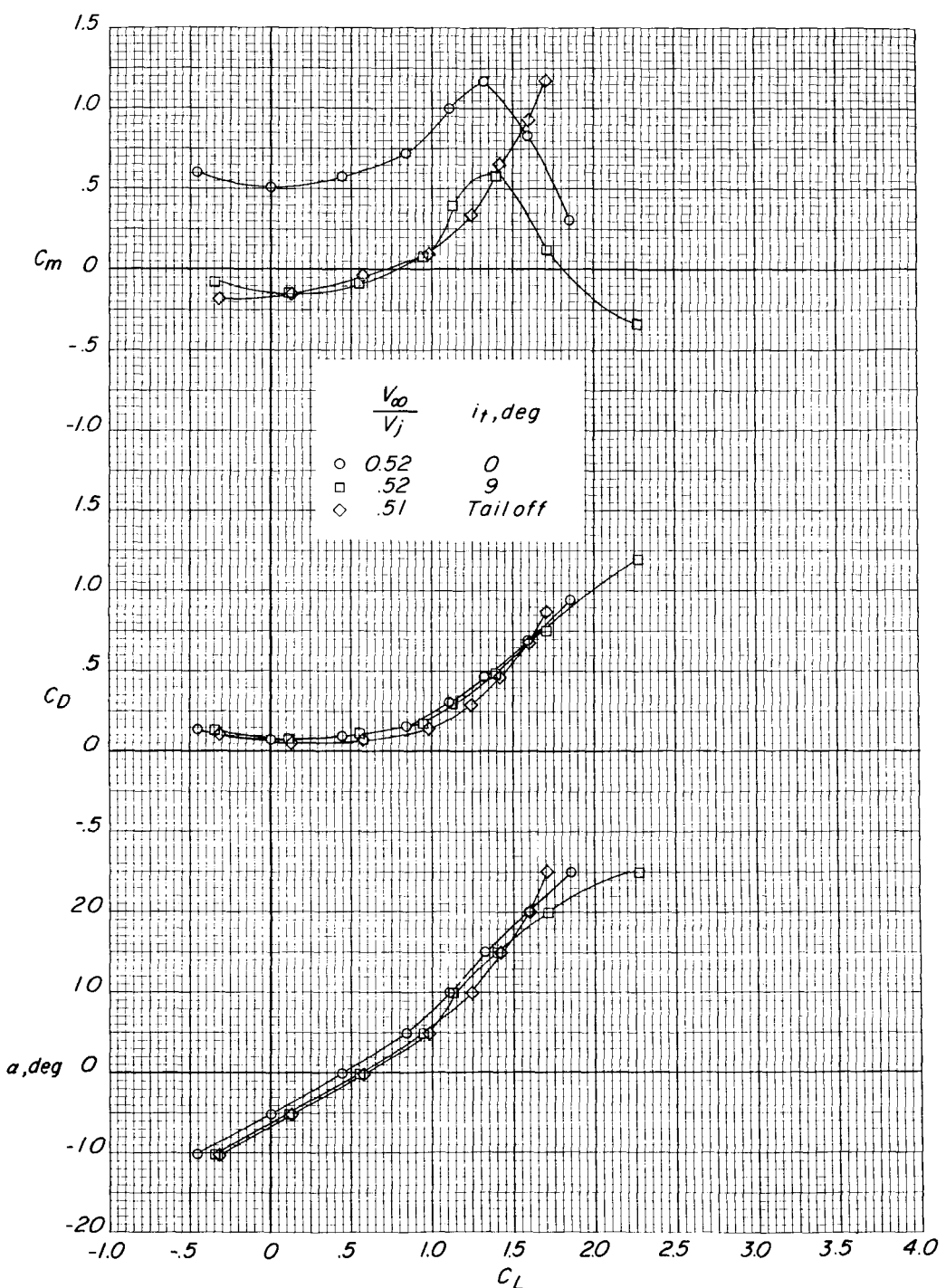
Figure 23.- Continued.

~~DECLASSIFIED~~



(c) Tail off.

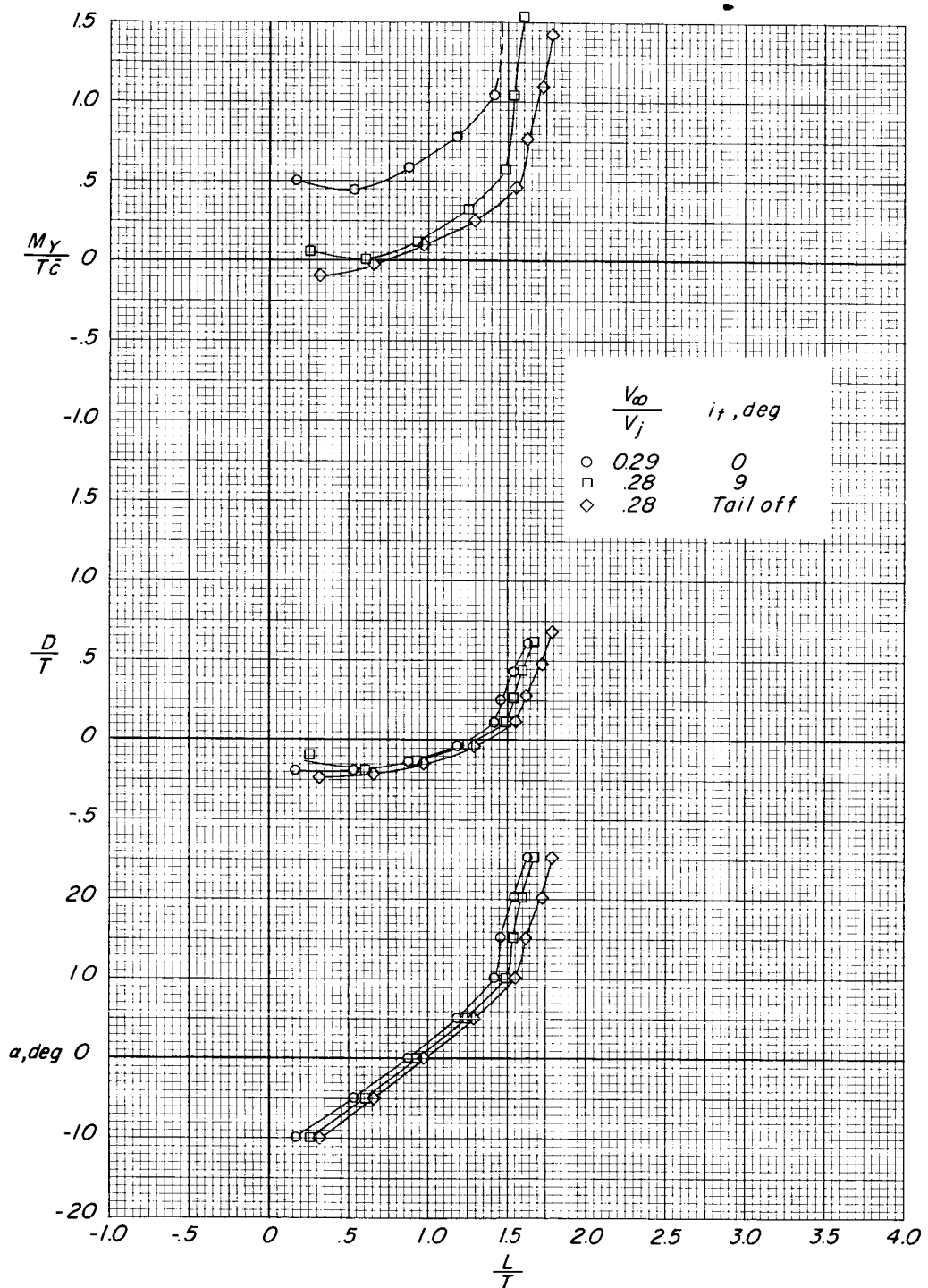
Figure 23.- Concluded.



(a)  $C_T \approx 0.38$ .

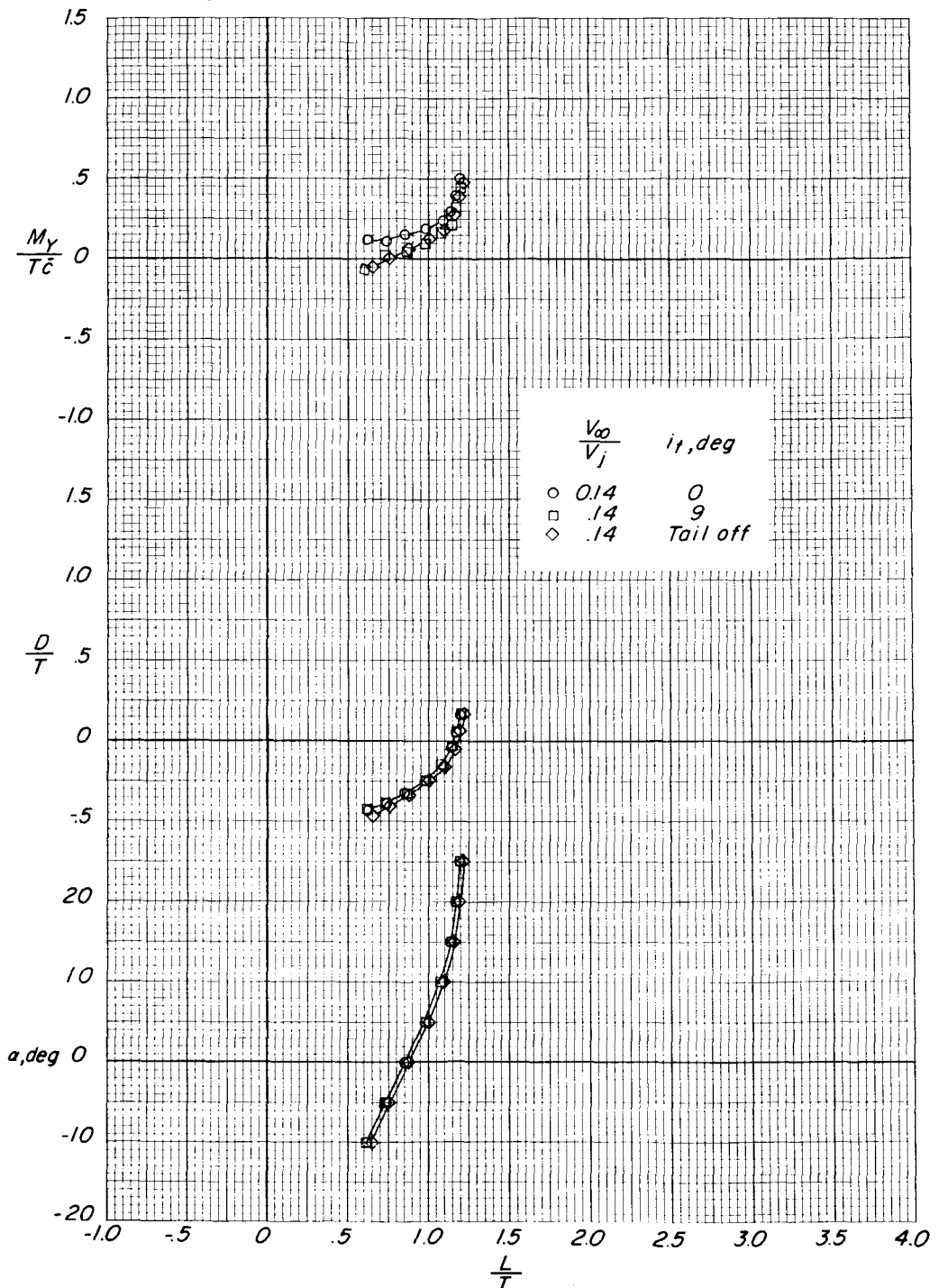
Figure 24.- Horizontal-tail effectiveness at various power settings of the modified model with flaps undeflected.  $\delta_j = 60^\circ$ ;  $\Lambda = 15^\circ$ .

# DECCELERATION



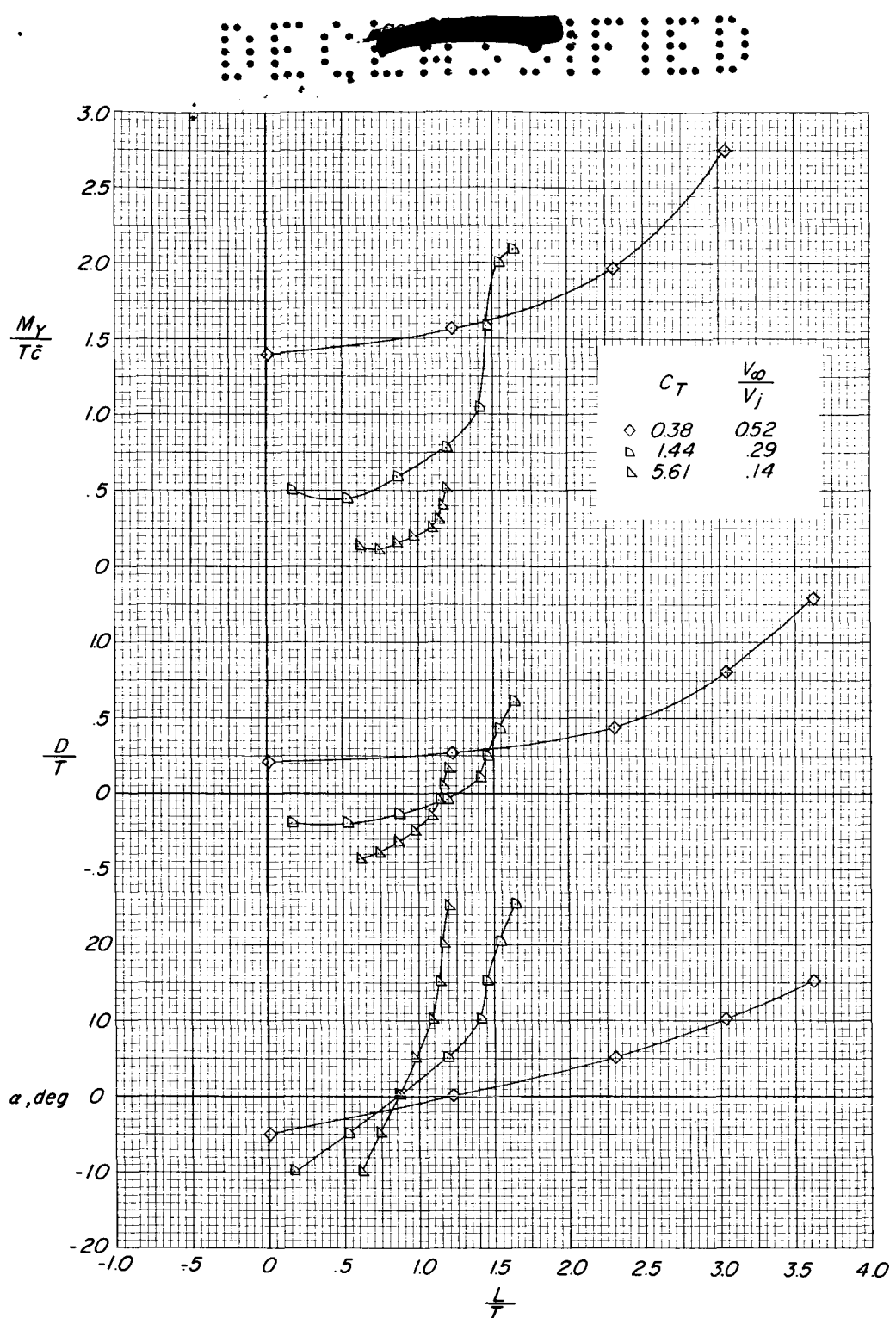
(b)  $C_T \approx 1.44$ .

Figure 24.- Continued.



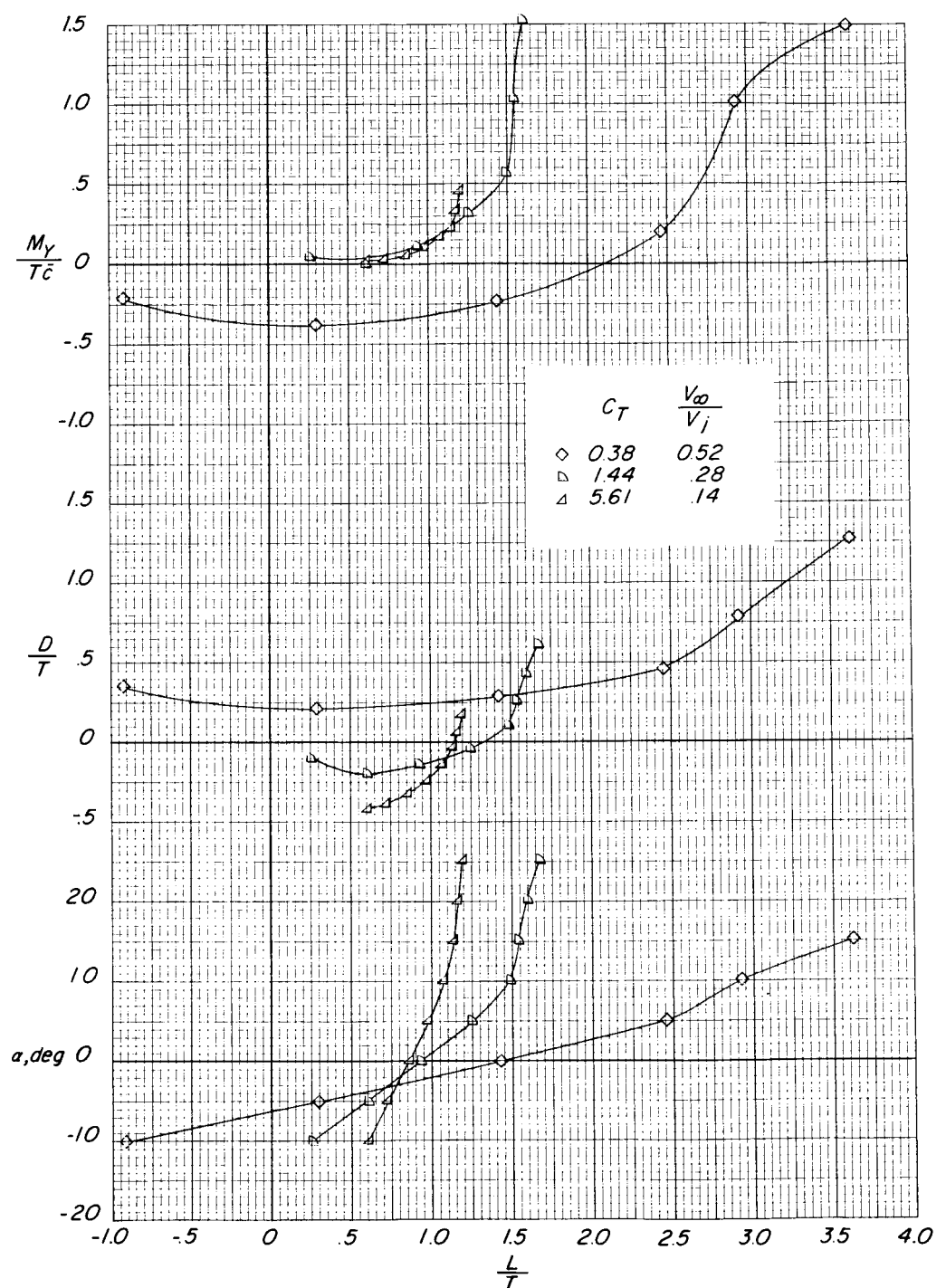
(c)  $C_T \approx 5.61$ .

Figure 24.- Concluded.



(a)  $i_t \approx 0^\circ$ .

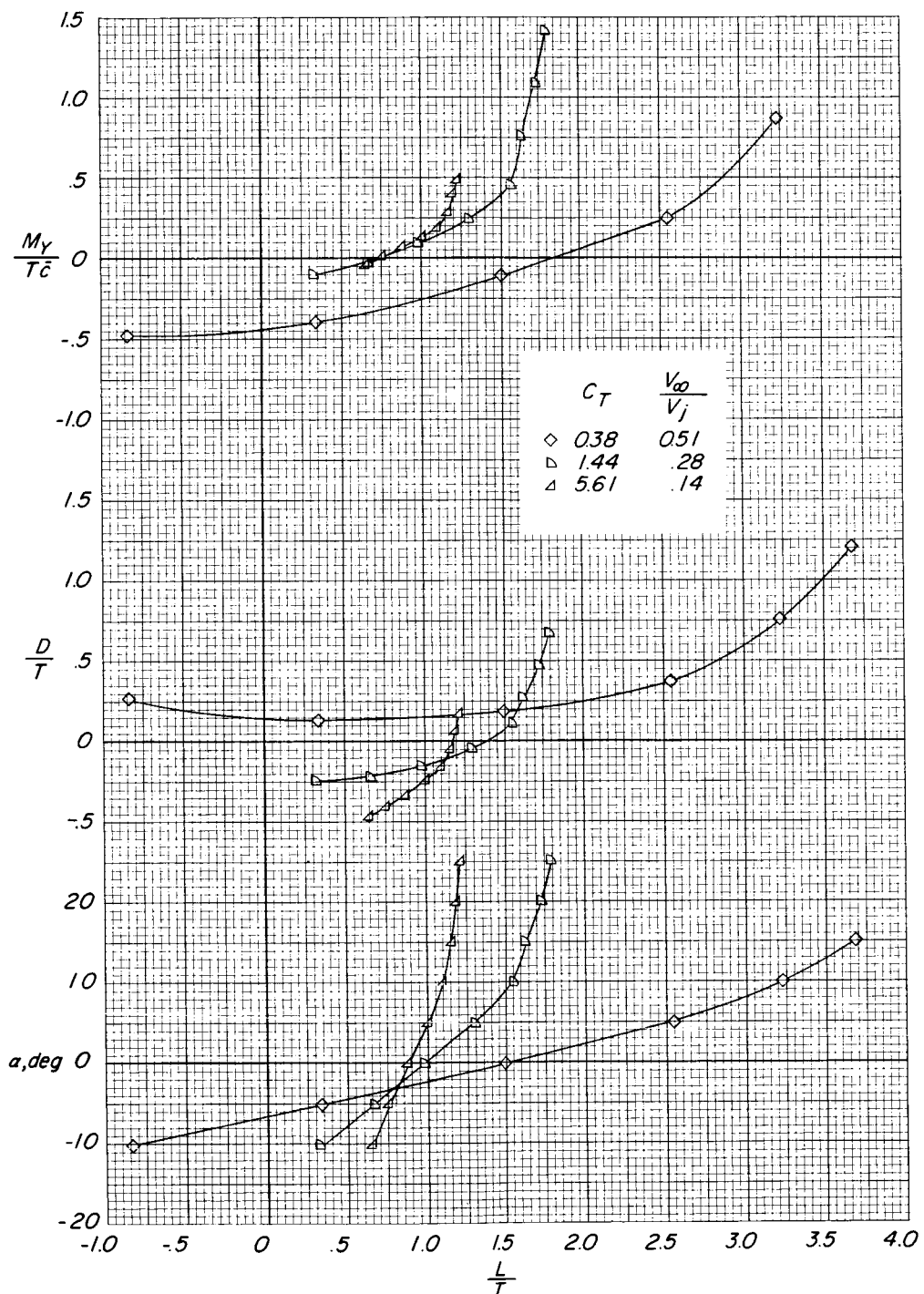
Figure 25.- Effect of power on the longitudinal aerodynamic characteristics of the modified model. Flaps undeflected;  $\delta_j = 60^\circ$ ;  $\Lambda = 15^\circ$ .



(b)  $i_t = 9^\circ$ .

Figure 25.- Continued.

~~SECRET~~



(c) Tail off.

Figure 25.- Concluded.

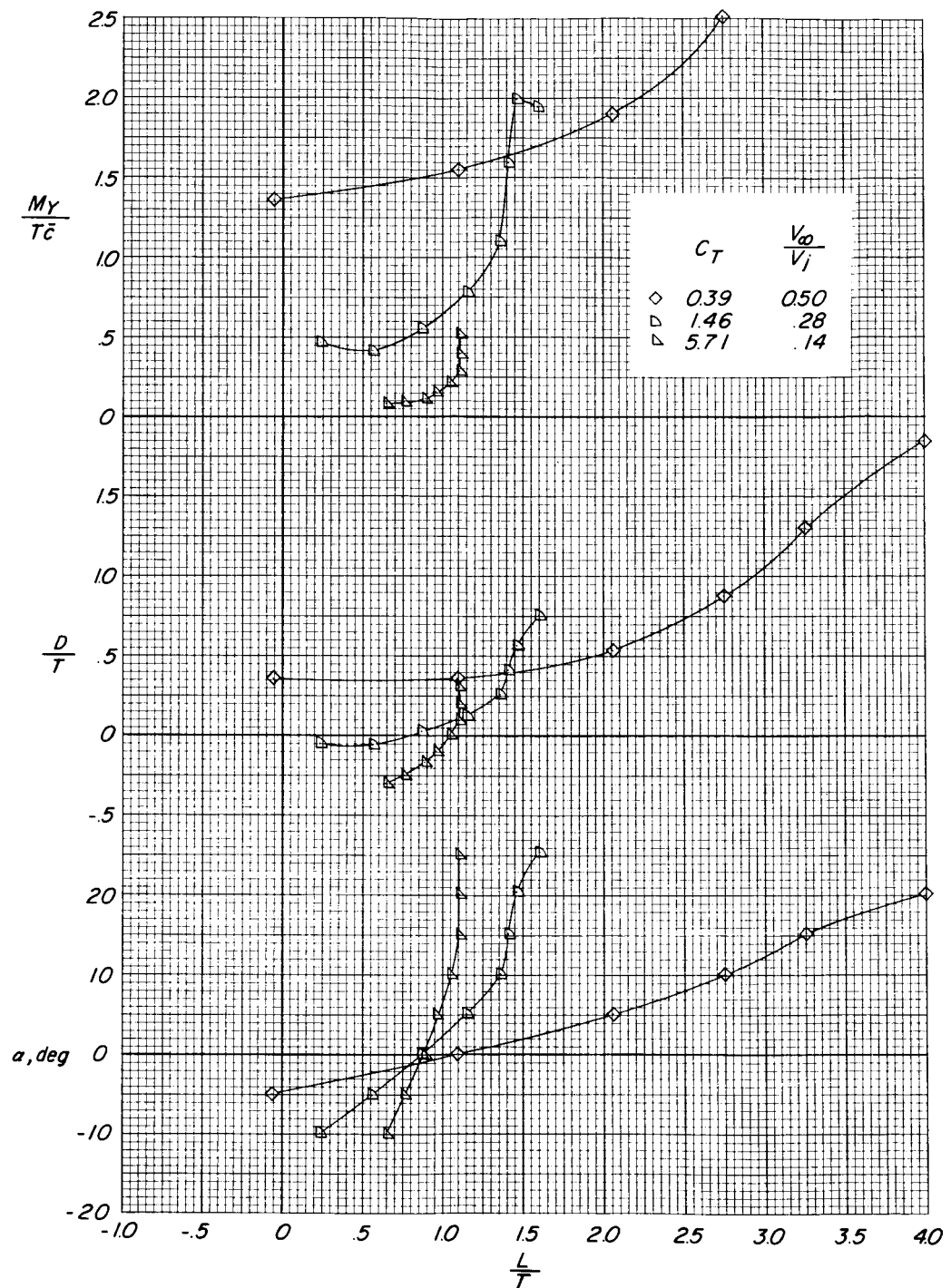


Figure 26.- Effect of power on the longitudinal aerodynamic characteristics of the modified model. Flaps undeflected;  $\delta_j = 68^\circ$ ;  $i_t = 0^\circ$ ;  $\Lambda = 15^\circ$ .

DECLASSIFIED

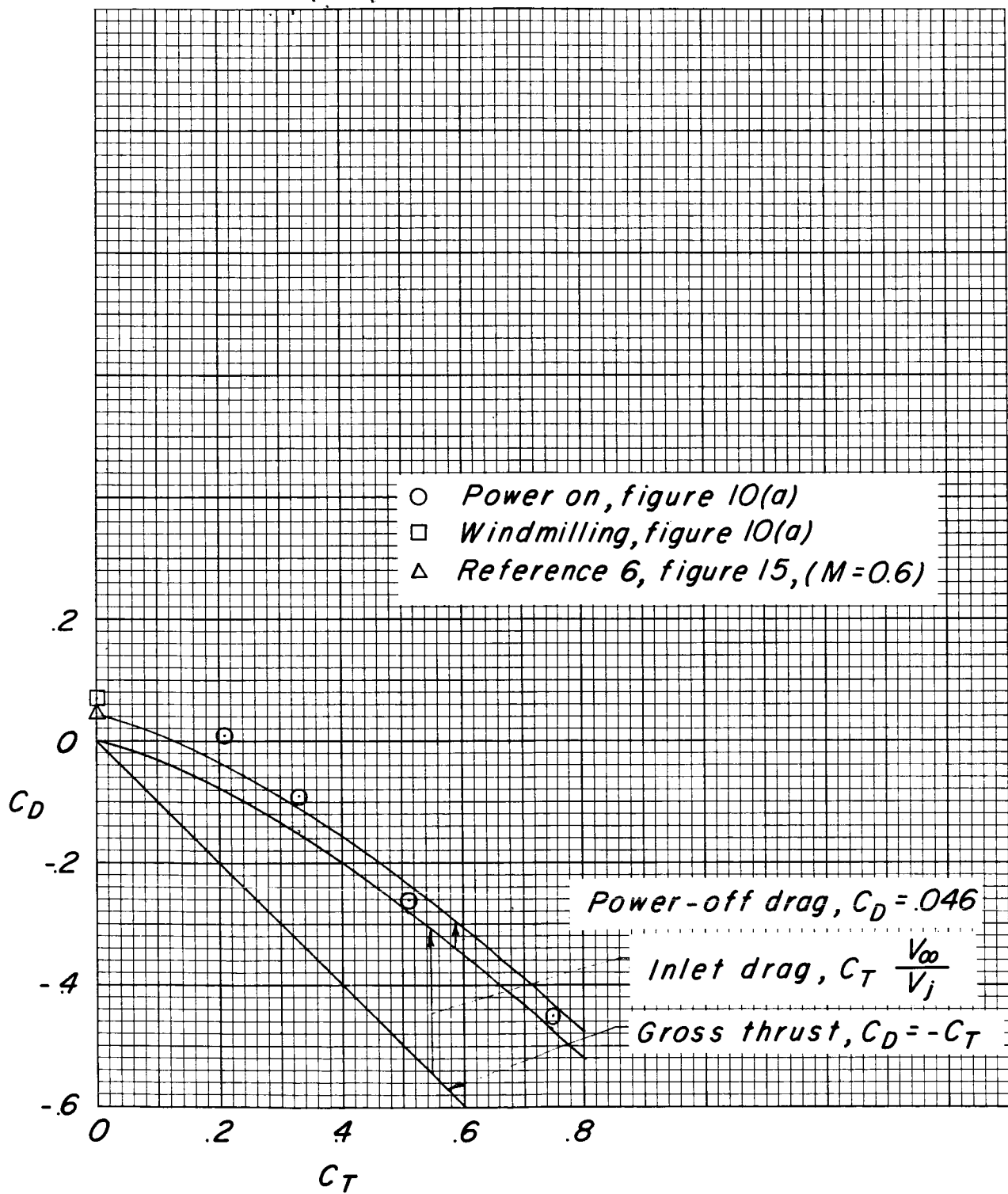


Figure 27.- Breakdown of the drag-thrust relationship.

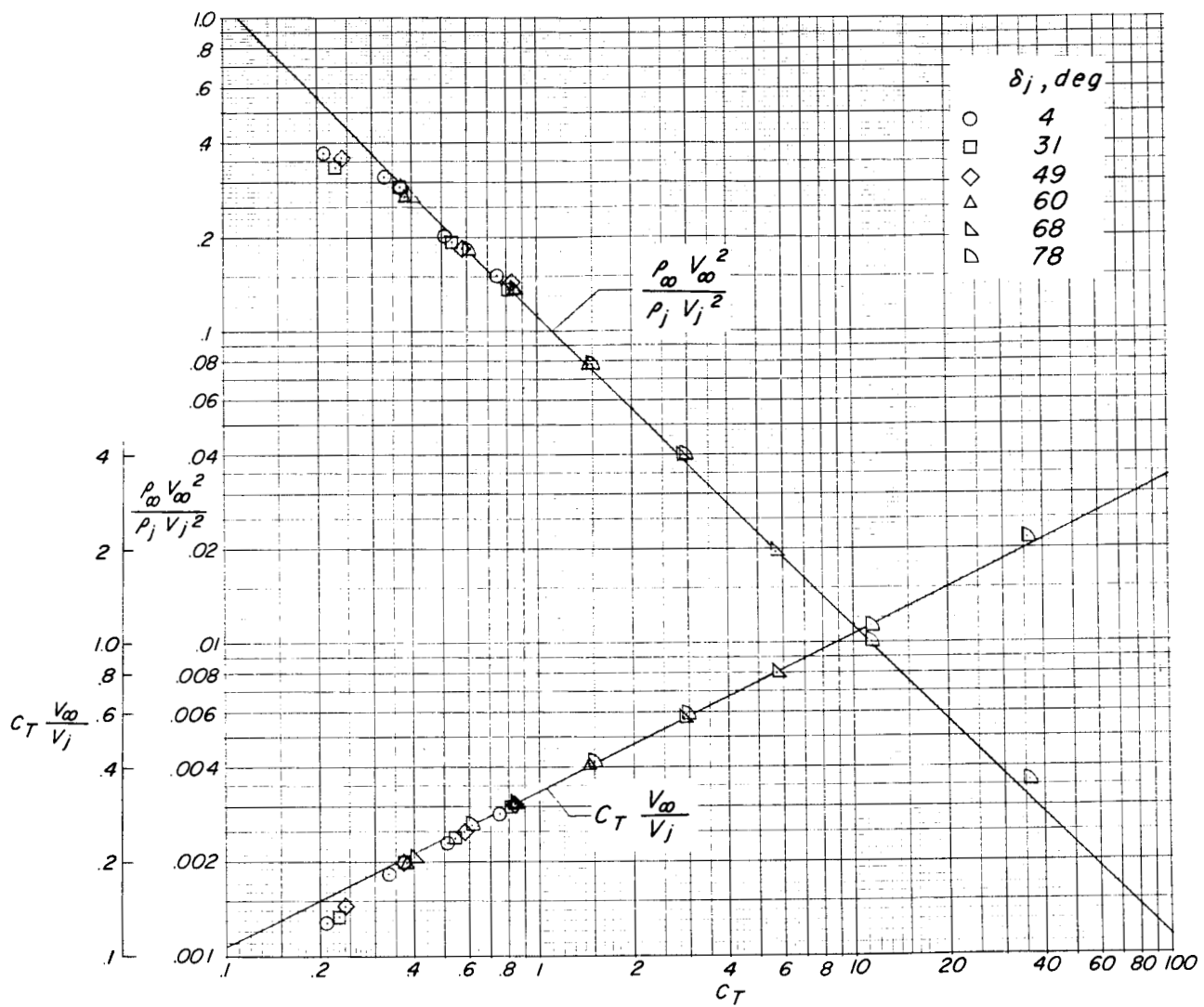
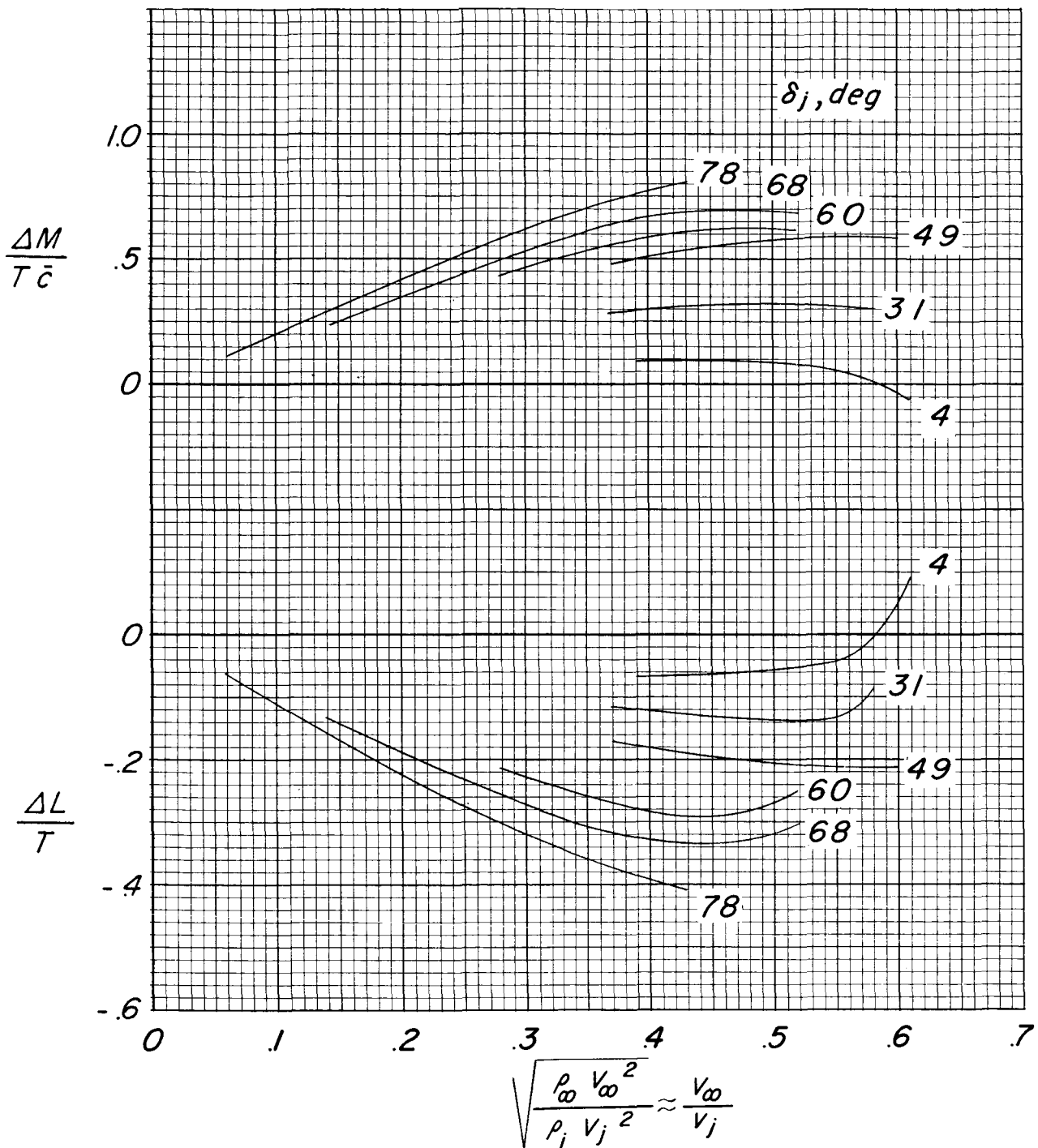


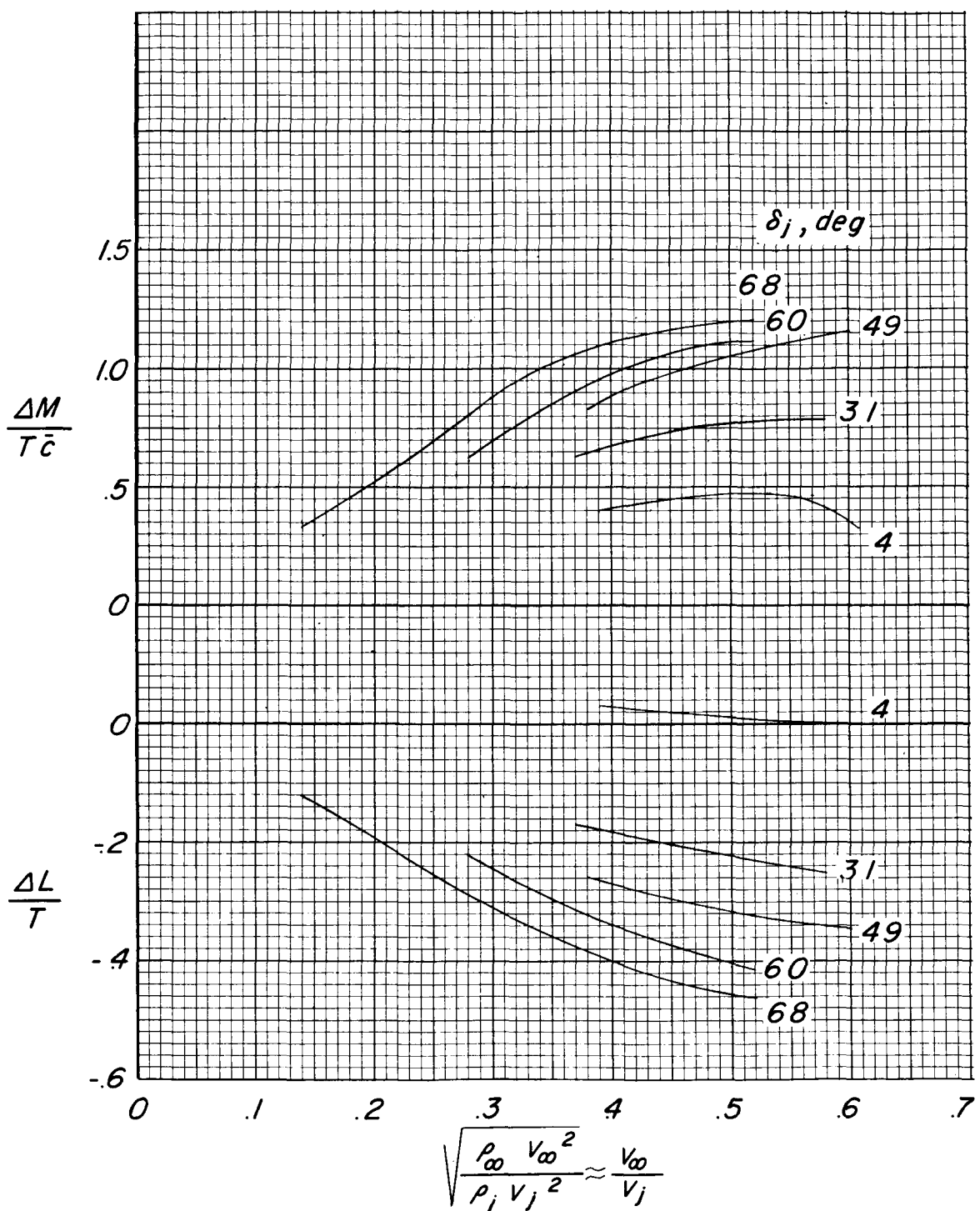
Figure 28.- Relationship between velocity ratios and thrust coefficient.

DECLASSIFIED



(a)  $\alpha = 0^\circ$ ;  $\delta_f = 0^\circ$ .

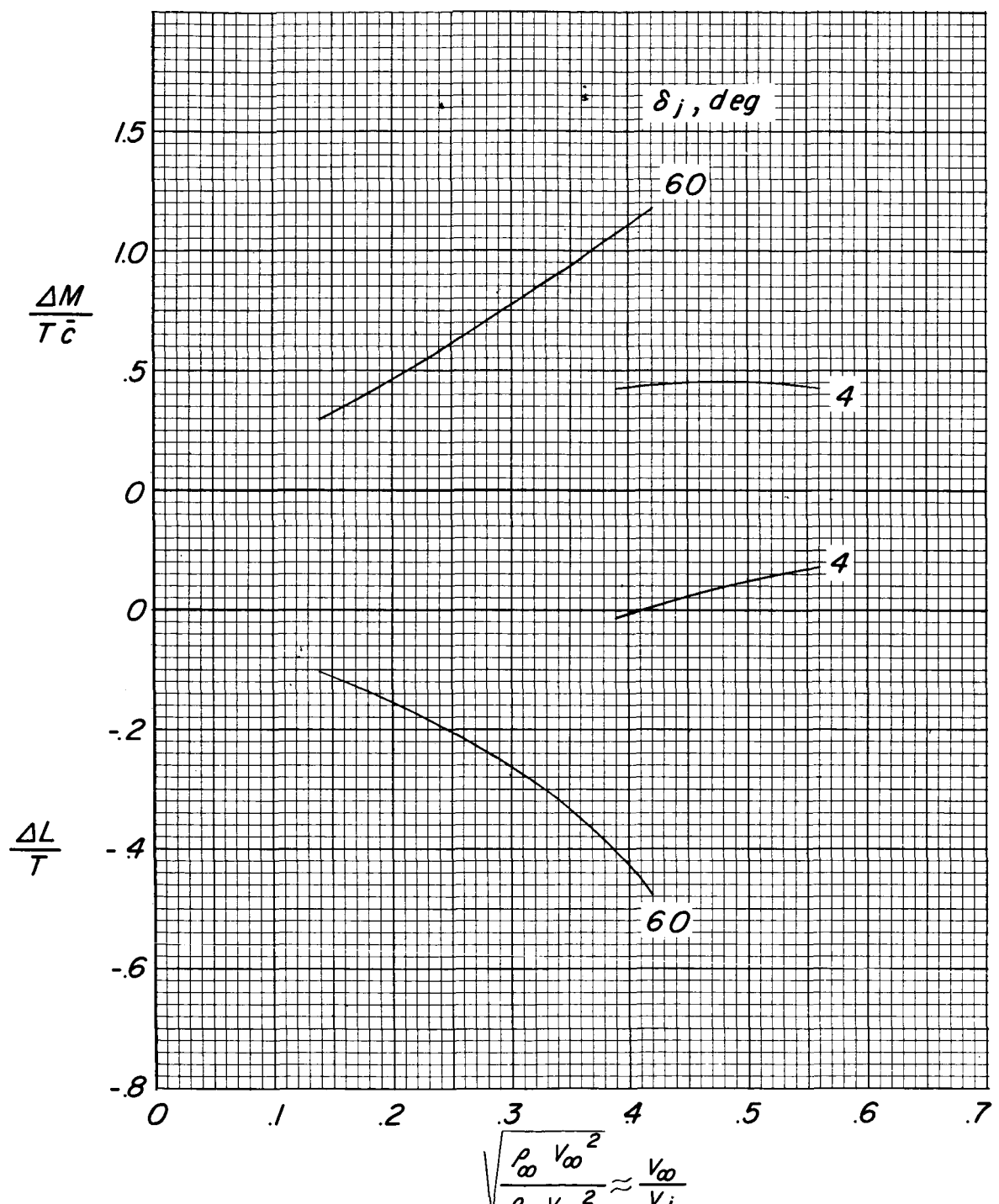
Figure 29.- Effect of jet deflection and velocity ratio on the lift and pitching-moment interference increments of the basic model.



(b)  $\alpha = 10^\circ; \delta_f = 0^\circ.$

Figure 29.- Continued.

DECLASSIFIED



(c)  $\alpha = 10^\circ$ ;  $\delta_f = 40^\circ$ .

Figure 29.- Concluded.

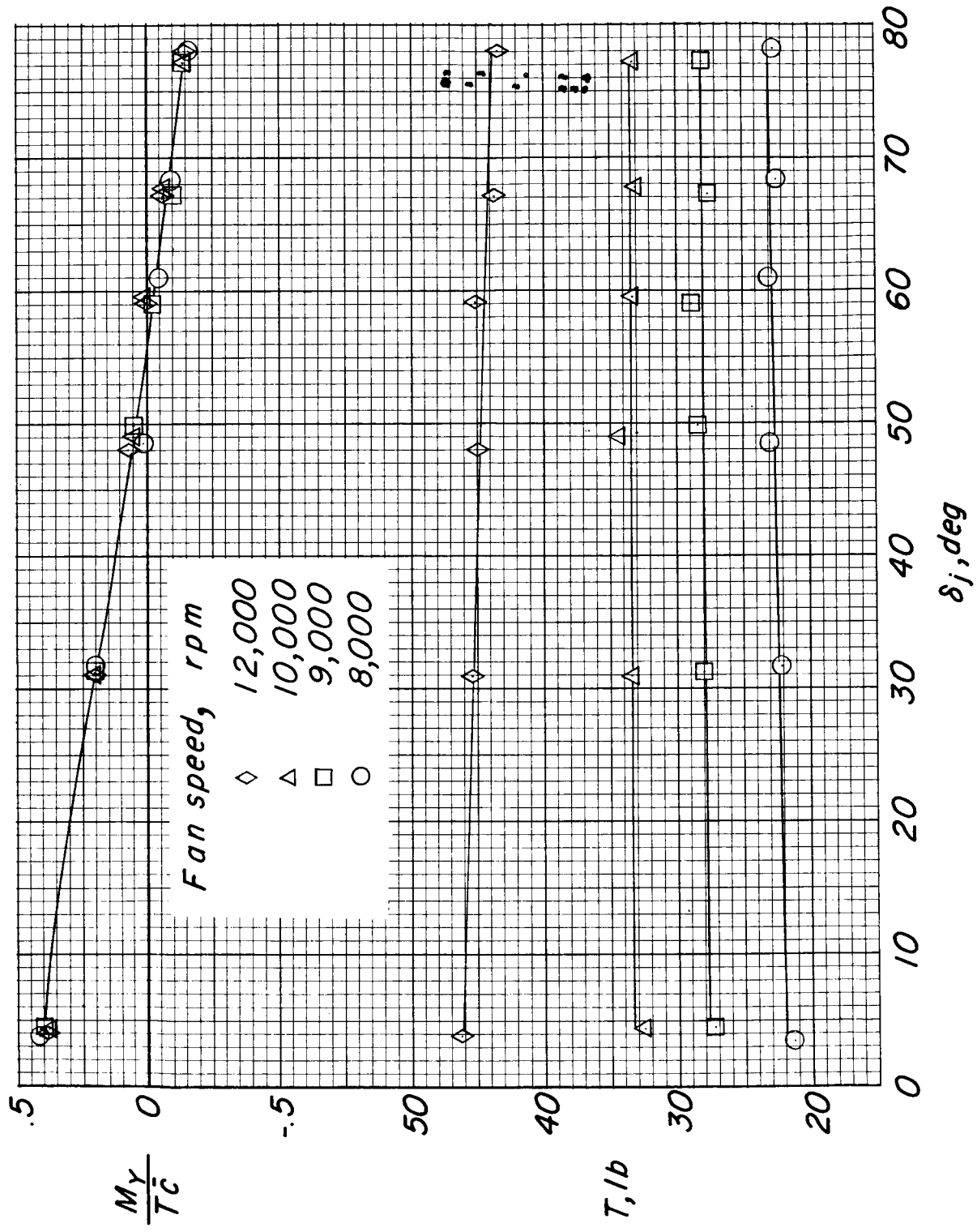
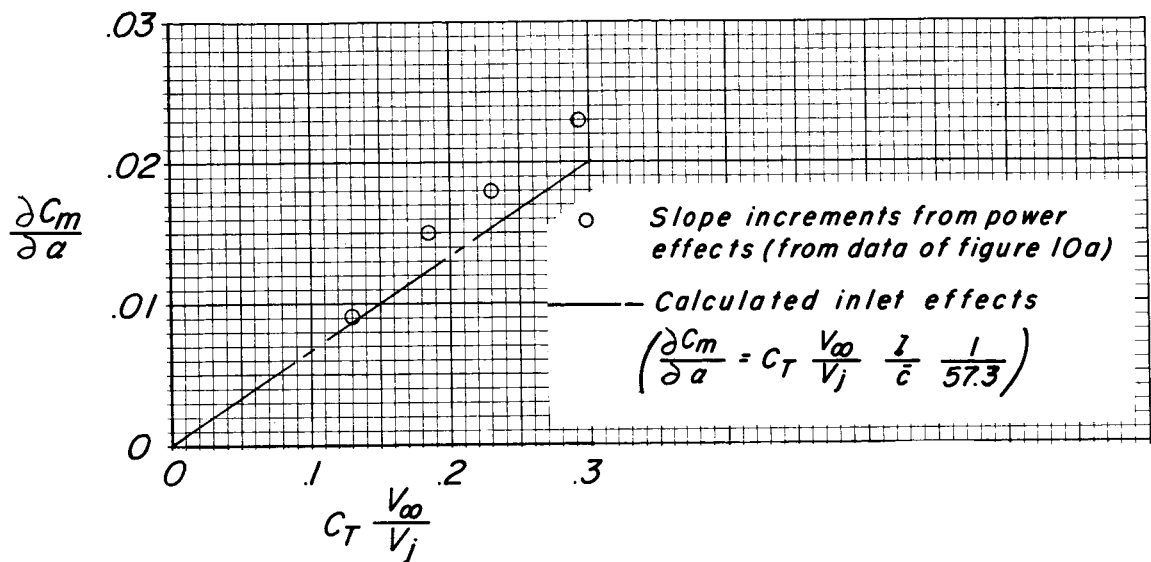
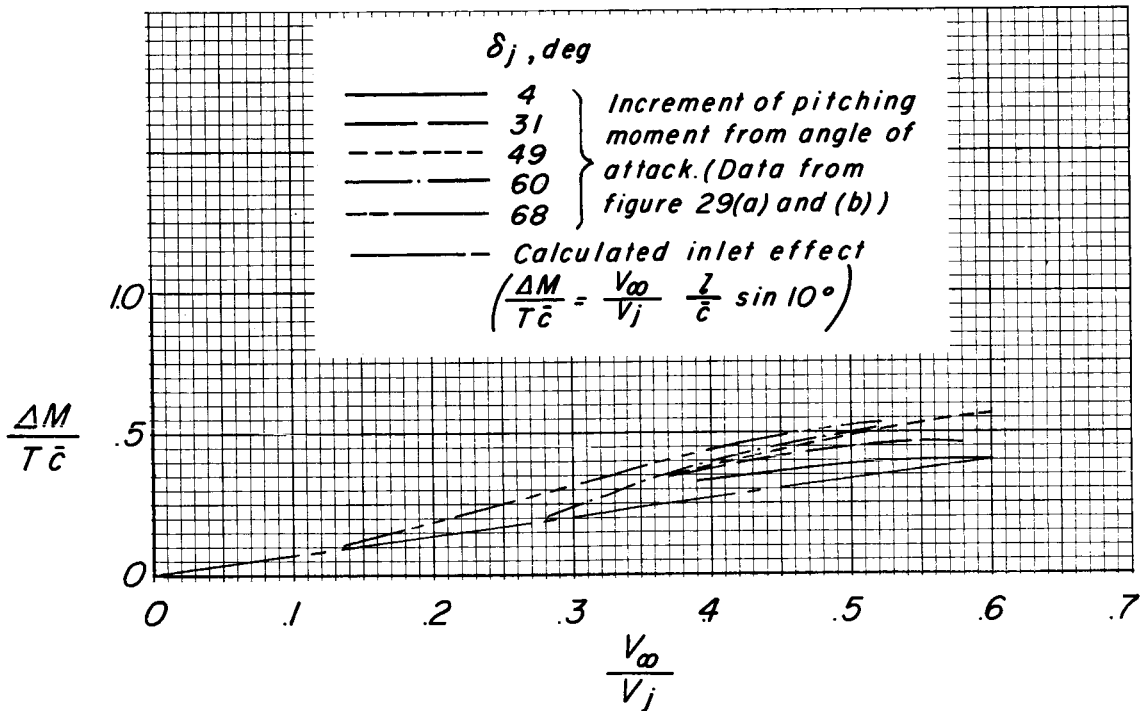


Figure 30.- Static thrust and pitching moment at various fan speeds and jet angles for the modified model with the wing and horizontal tail removed.

~~DEC CLASSIFIED~~



(a) Power effect.



(b) Angle-of-attack effect.

Figure 31.- Measured incremental effects and calculated inlet effects of power and angle of attack on the stability and pitching moments of the basic model.

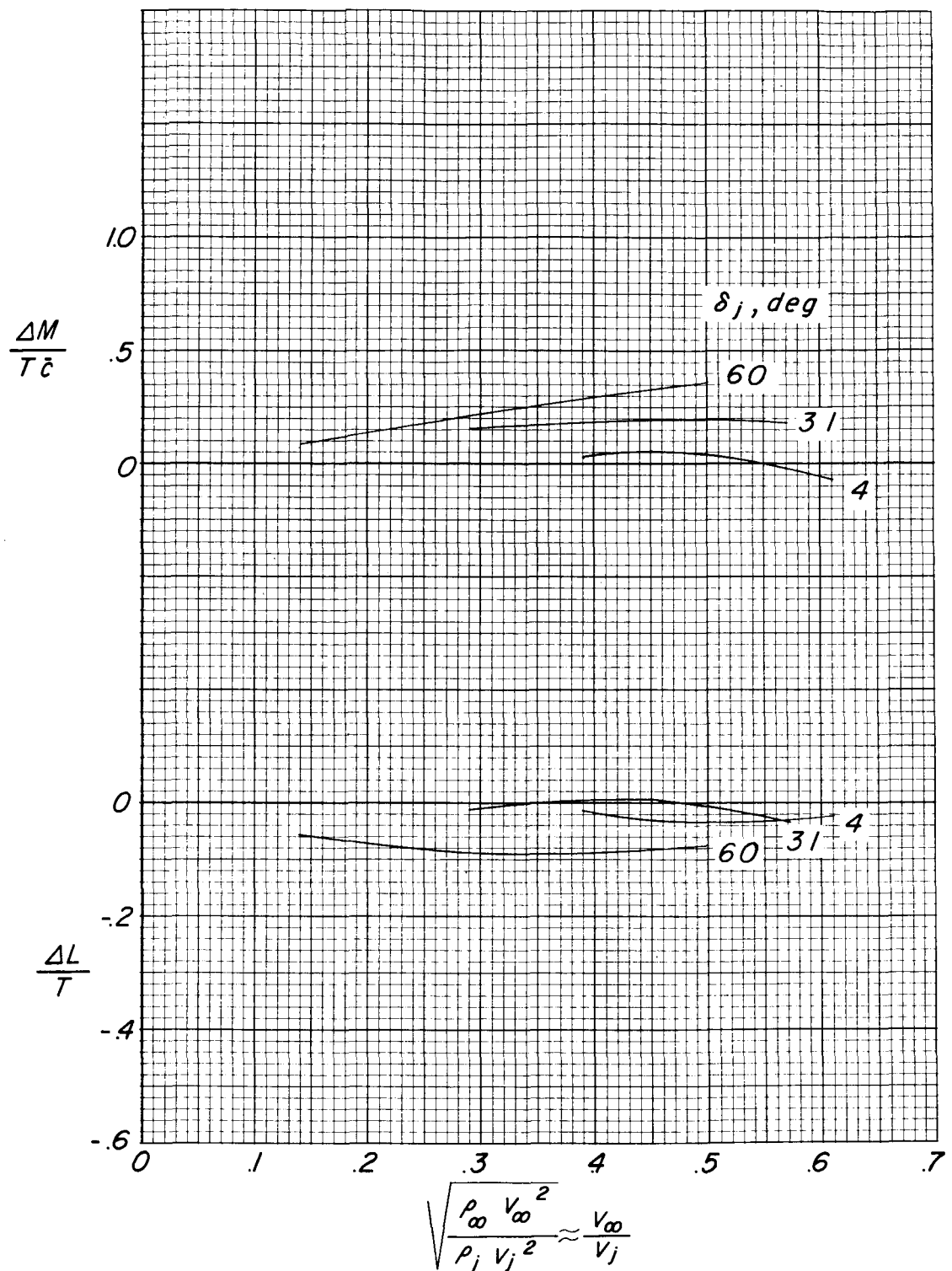
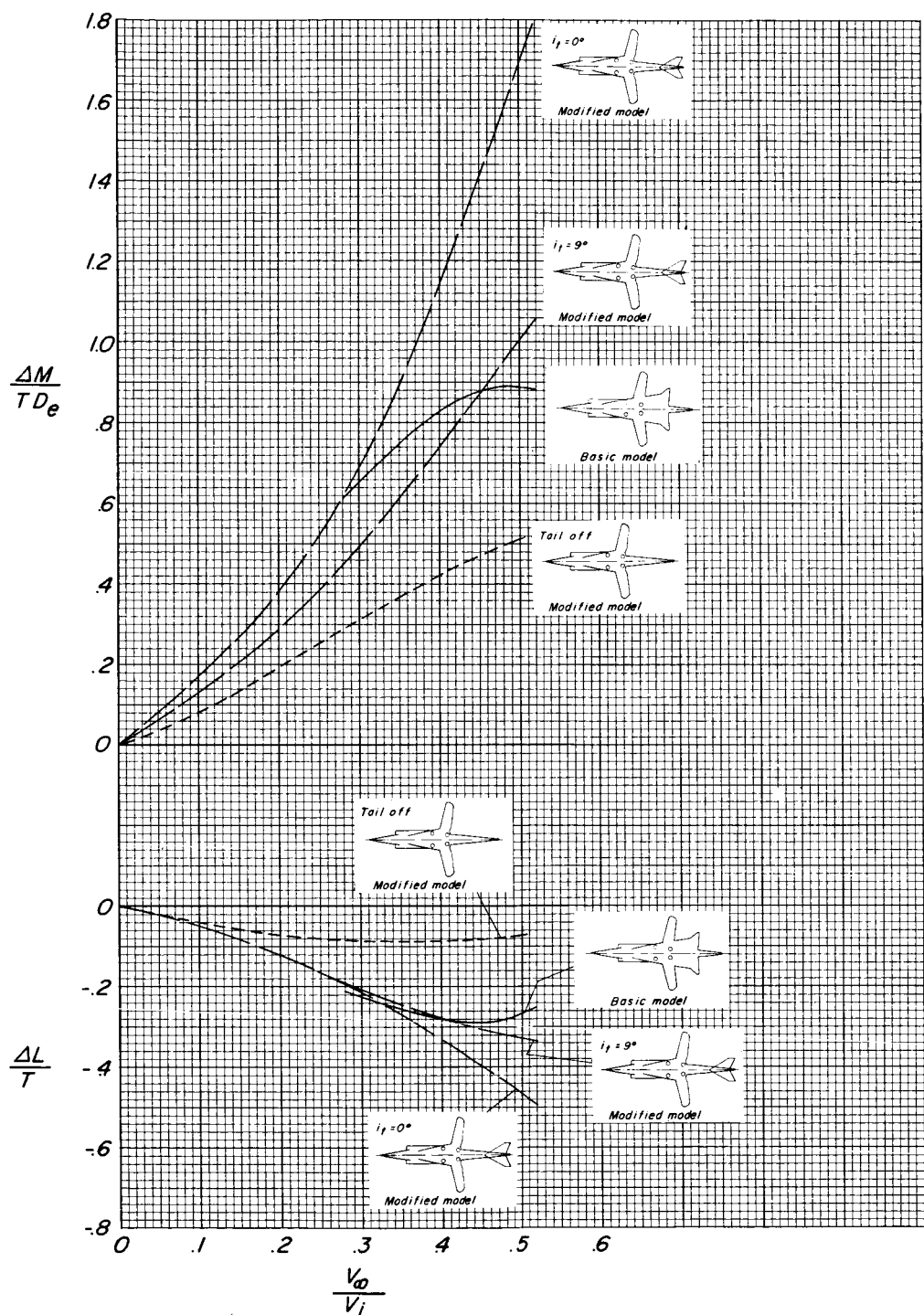


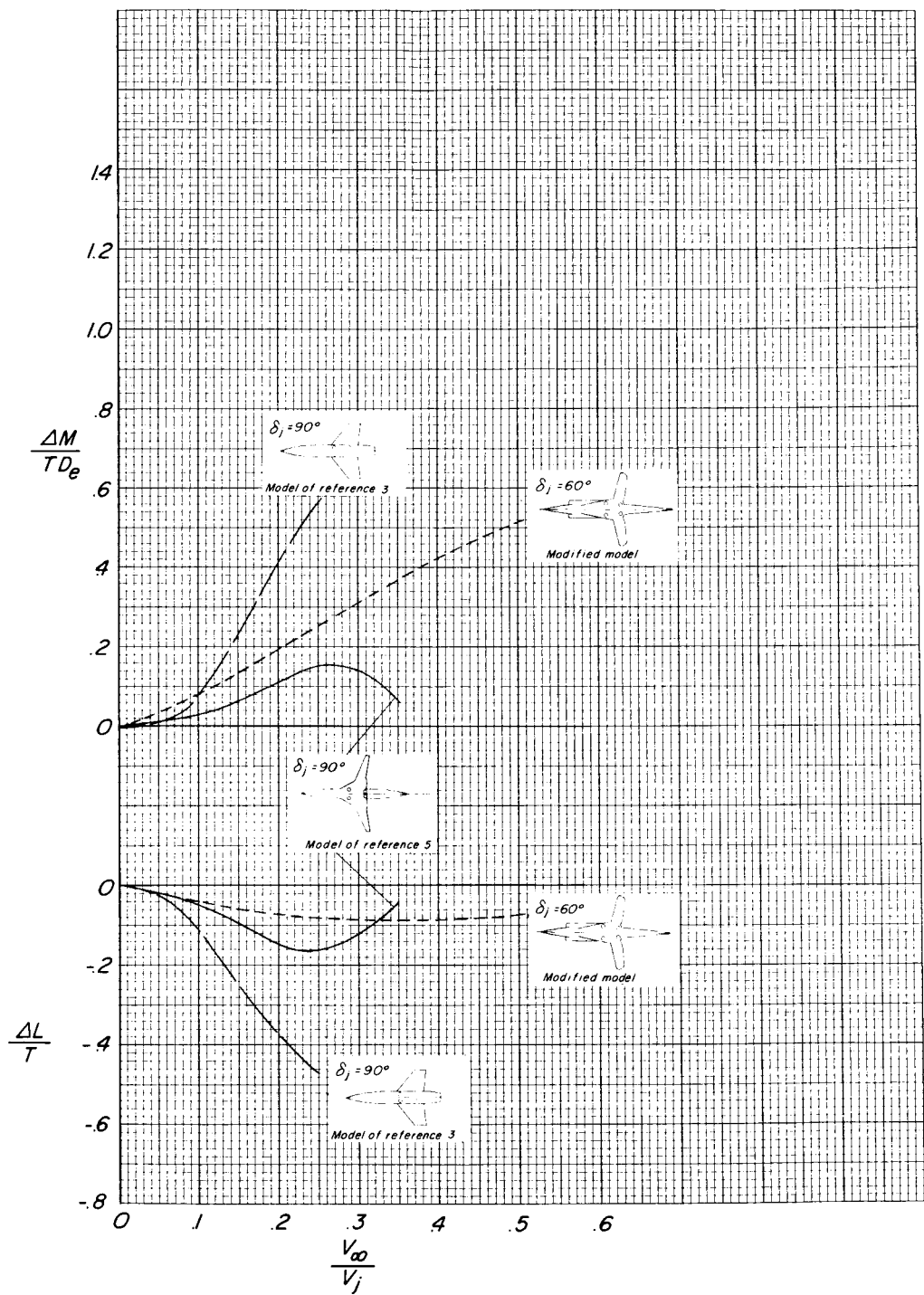
Figure 32.- Effect of jet deflection and velocity ratio on the lift and pitching-moment interference increments of the modified model. Tail off;  $\alpha = 0^\circ$ .

DECLASSIFIED



(a) Basic and modified models;  $\delta_j = 60^\circ$ .

Figure 33.- Comparison of the interference increments of VTOL models.  $\alpha = 0^\circ$ .



(b) Tail-off modified model and models of references 3 and 5.

Figure 33.- Concluded.

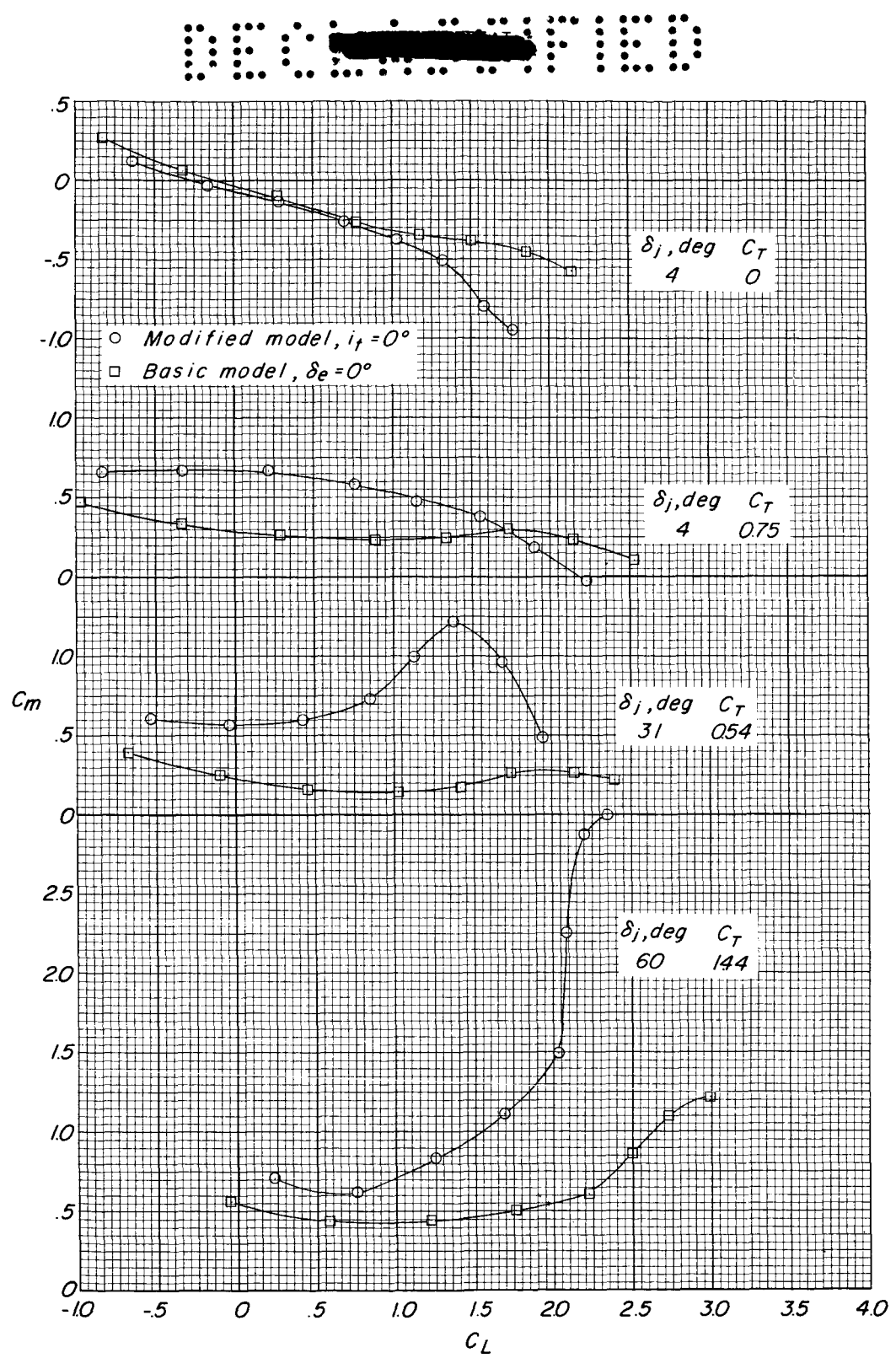


Figure 34.- Comparison of the longitudinal stability characteristics of the two models for various jet deflections and power conditions.

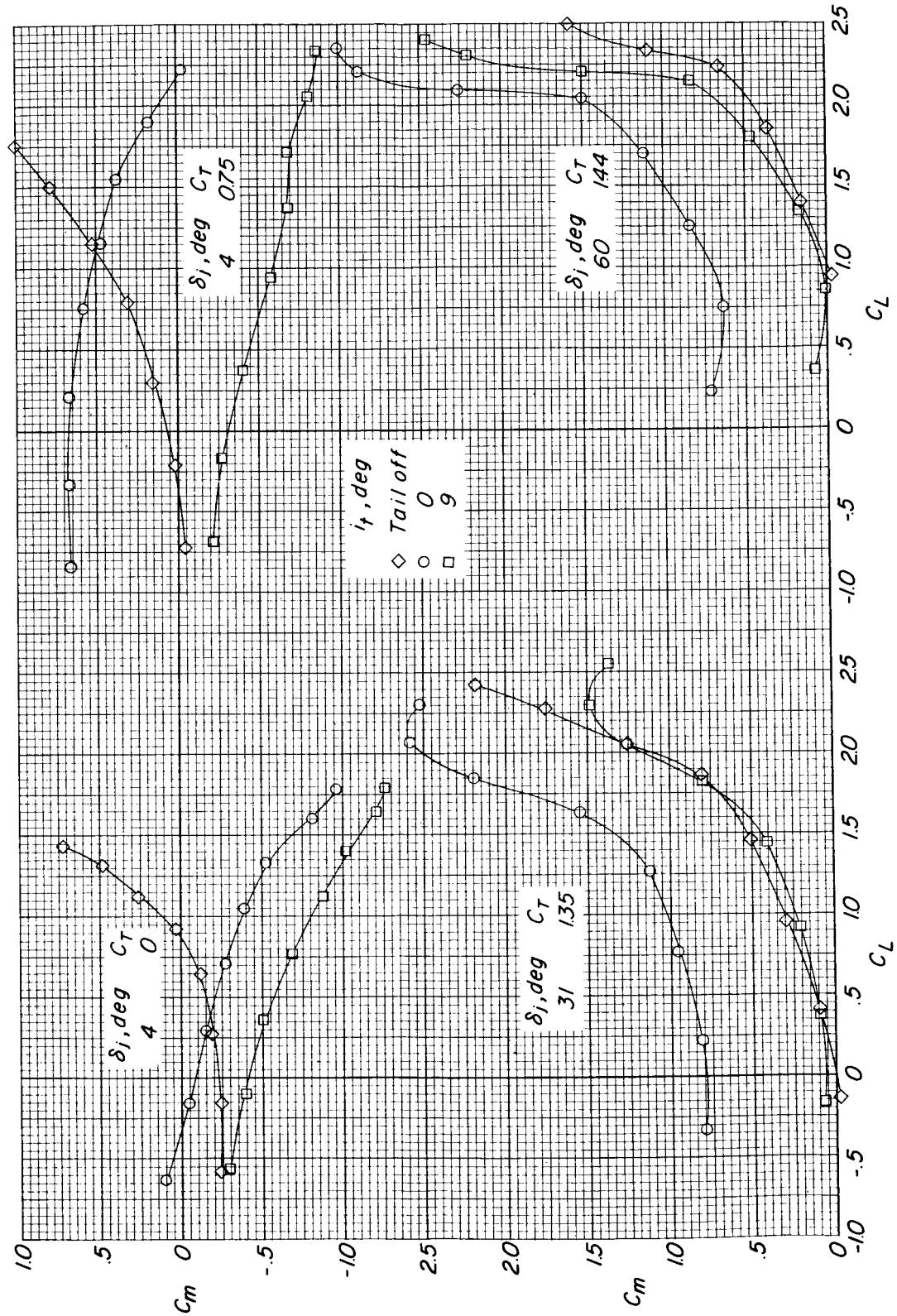


Figure 35.- Effect of power and jet deflection on the longitudinal stability characteristics of the modified model.

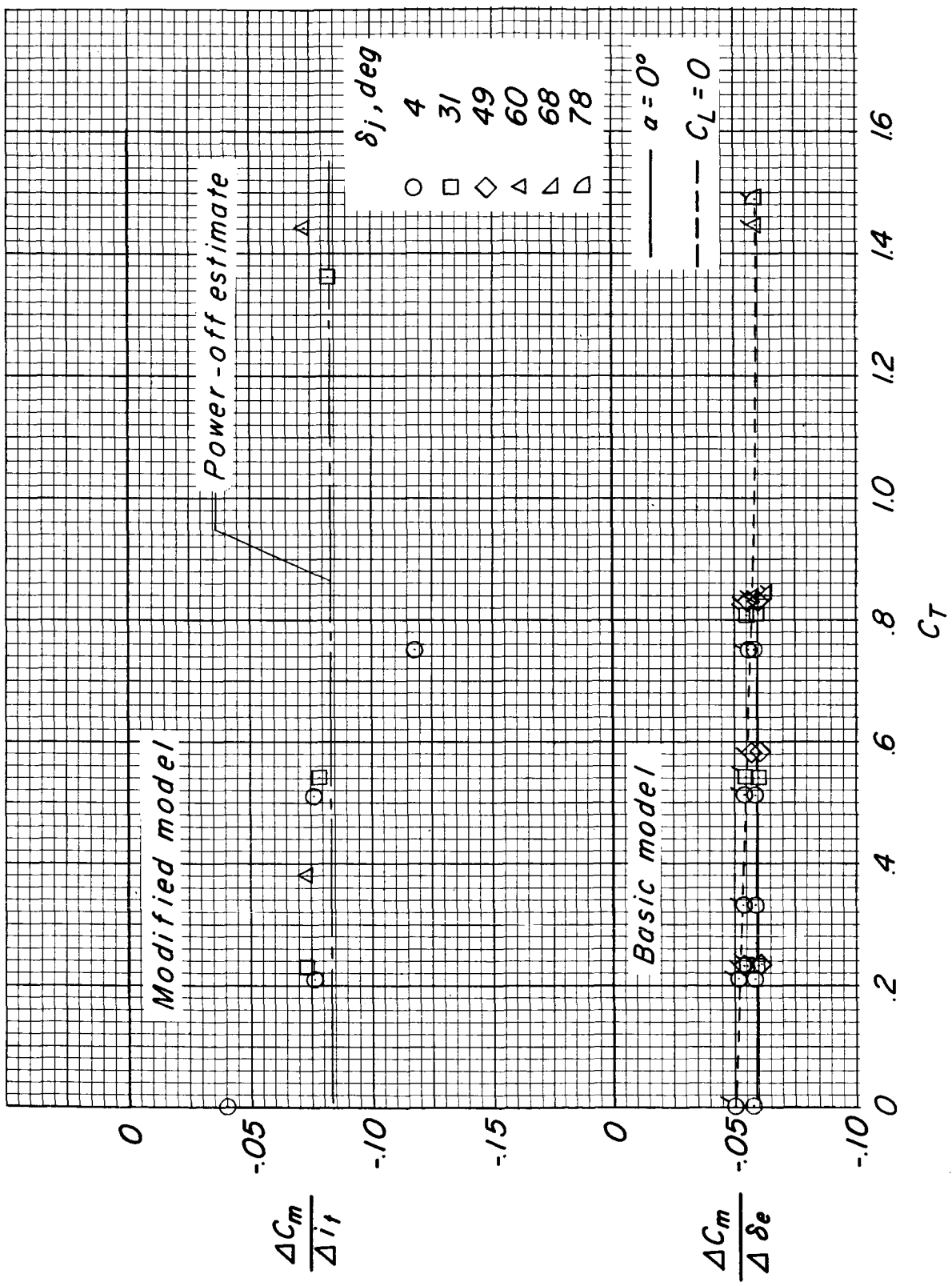


Figure 36. - Horizontal-tail and elevator control effectiveness for various jet deflections through a thrust range.

0317 [REDACTED] 030

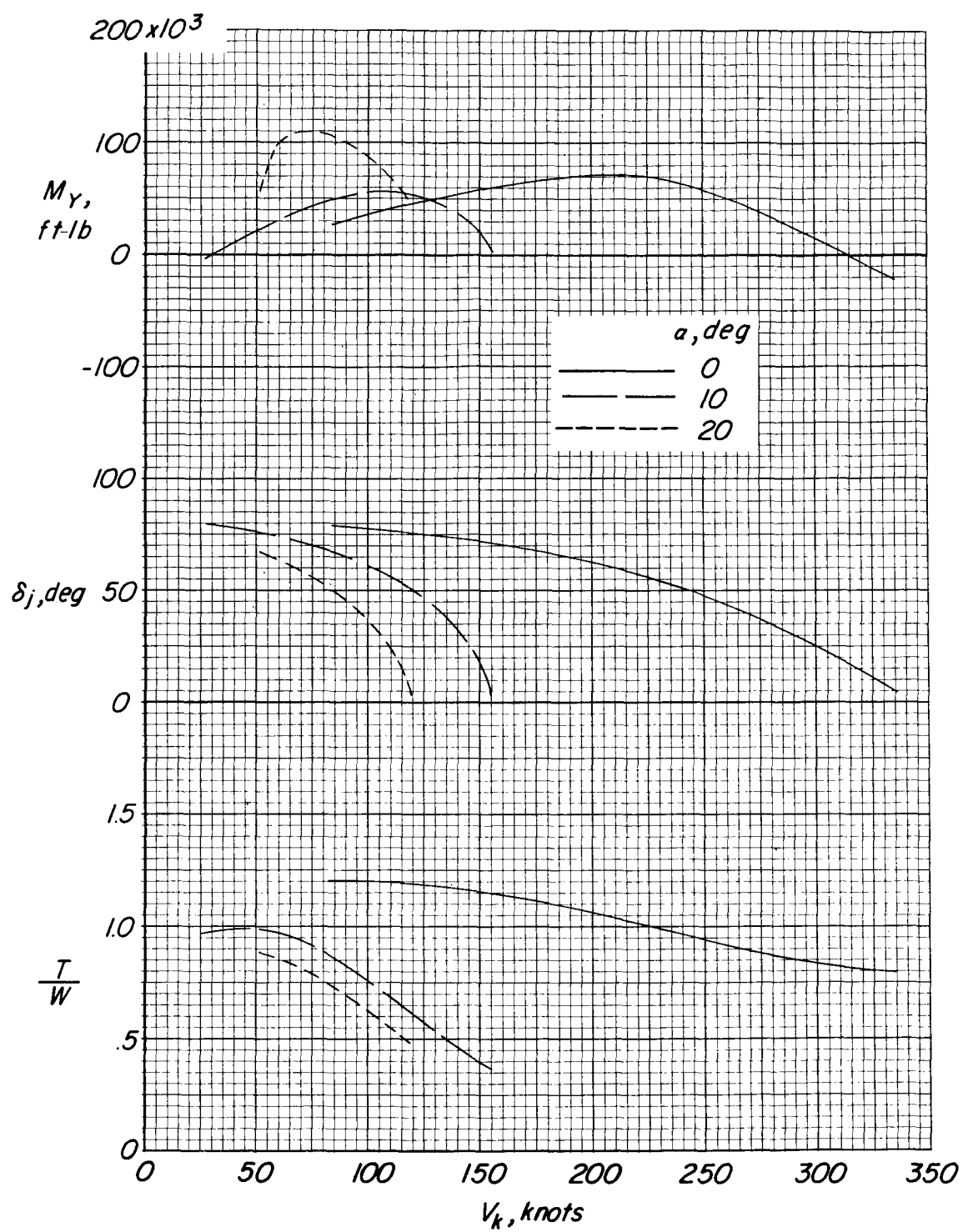


Figure 37.- Characteristics of an assumed 30,000-pound airplane of the basic configuration in transition from hovering to normal flight.  $\delta_e = 0^\circ$ ;  $\delta_f = 0^\circ$ .

DECLASSIFIED

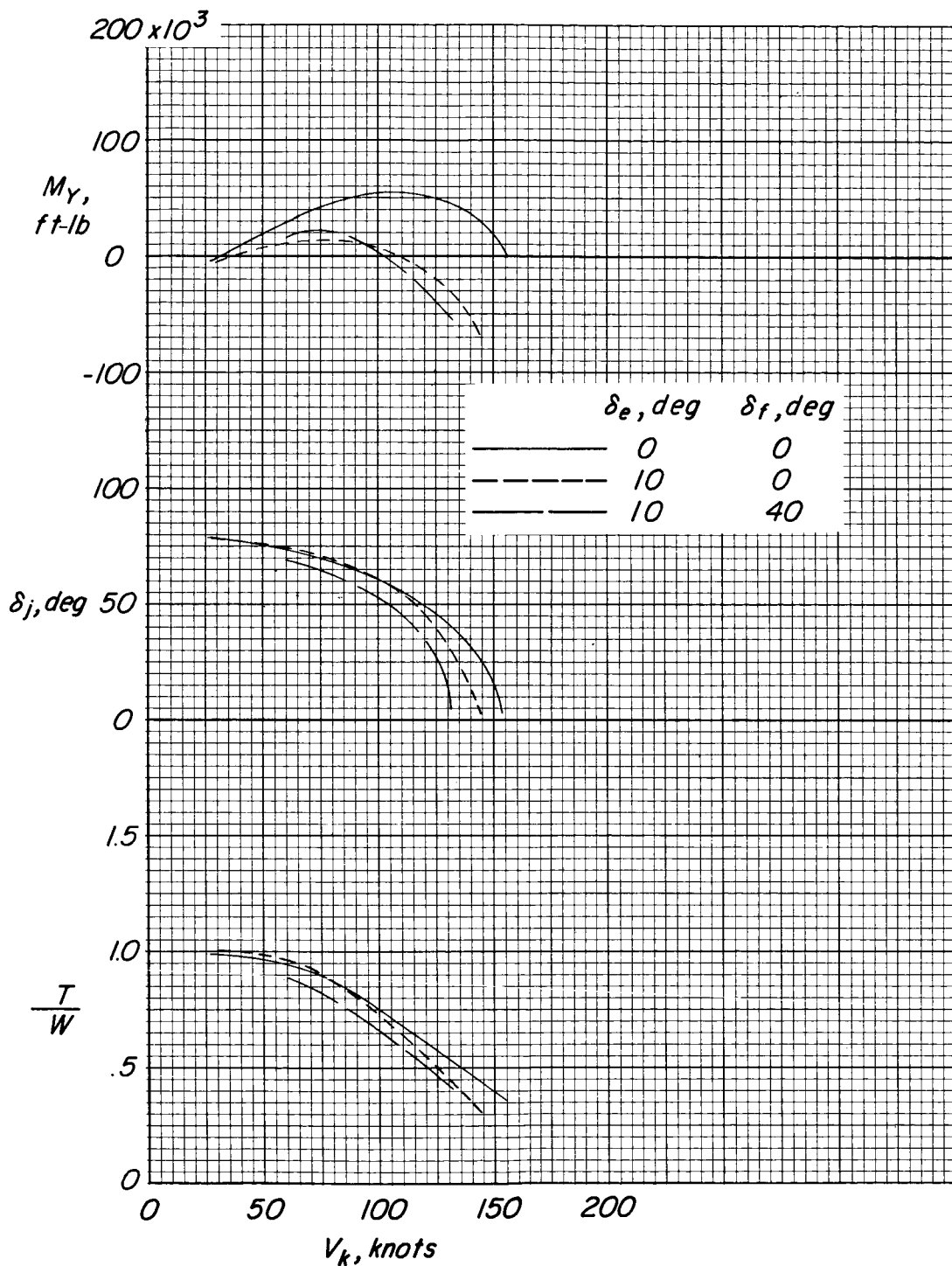


Figure 38.- Effect of flap and elevator on the characteristics of an assumed 30,000-pound airplane of the basic configuration in transition from hovering to normal flight.  $\alpha = 10^\circ$ .

0317030 1030

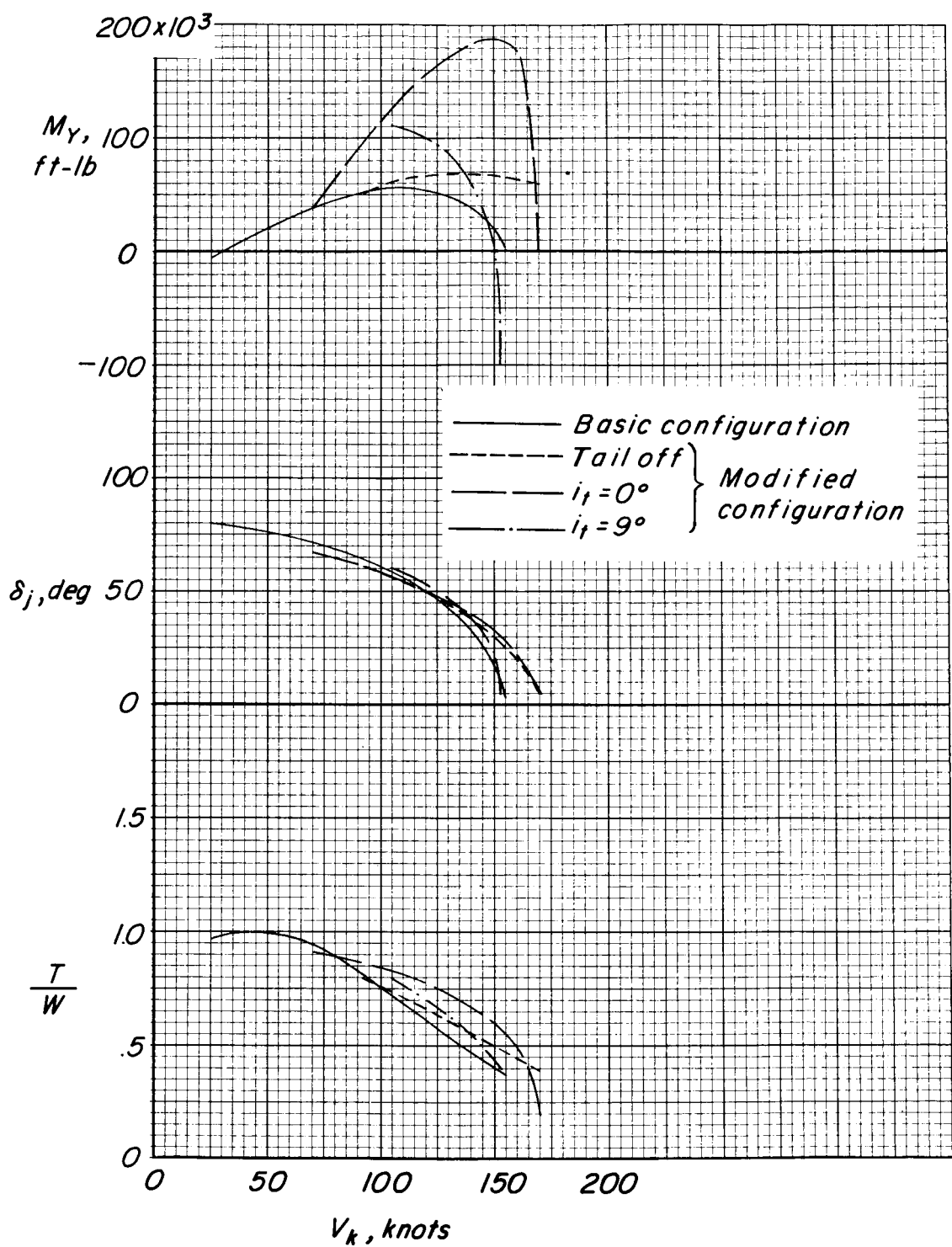


Figure 39.- Comparison of the transition characteristics of the basic and modified 30,000-pound airplanes.  $\alpha = 10^\circ$ ;  $\delta_f = 0^\circ$ .

DECLASSIFIED

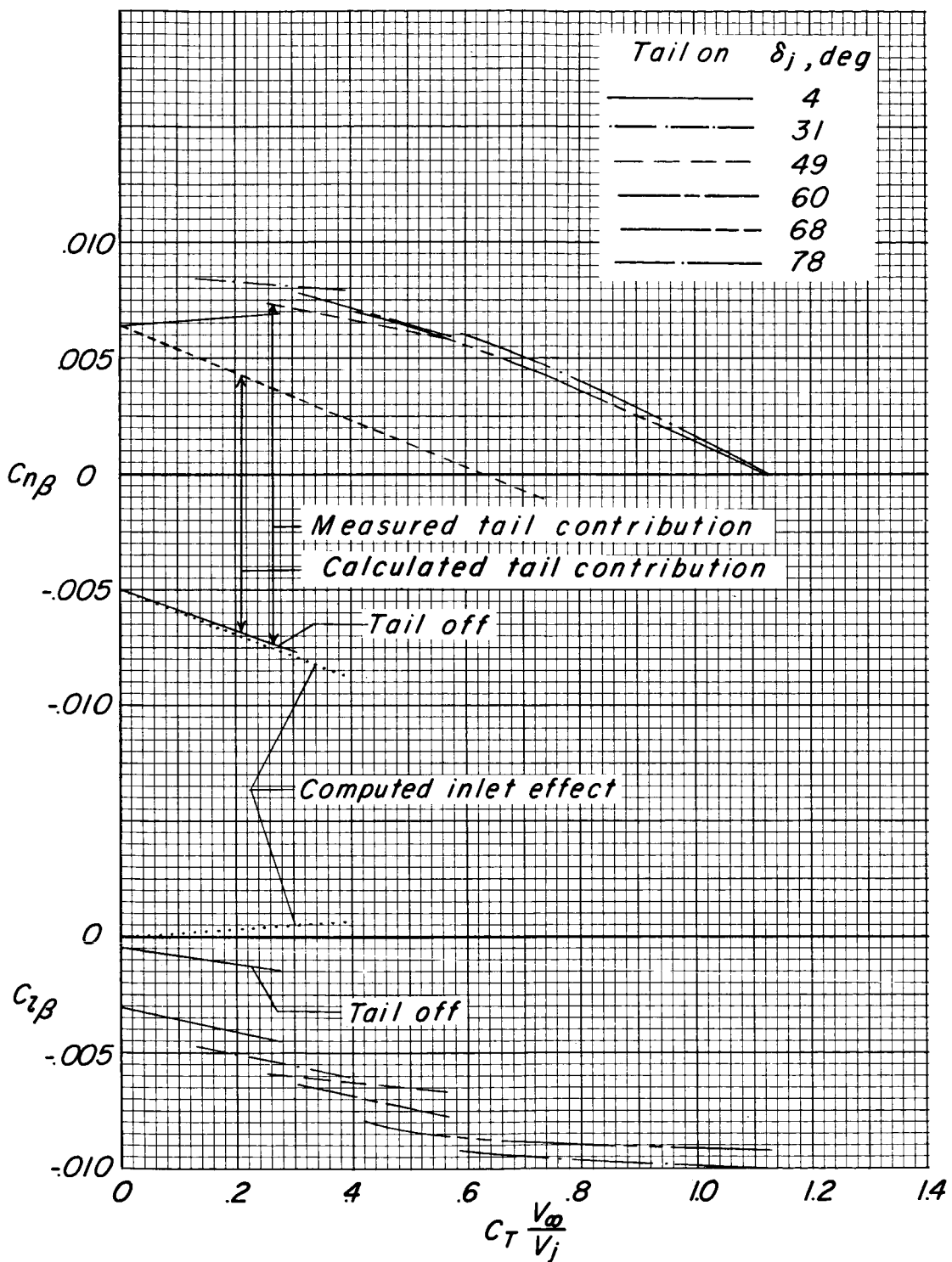


Figure 40.- Effect of vertical tail, inlet, and jet deflection on the sideslip derivatives of the basic model.  $\alpha = 0^\circ$ ;  $\delta_f = 0^\circ$ .

03191226 1030

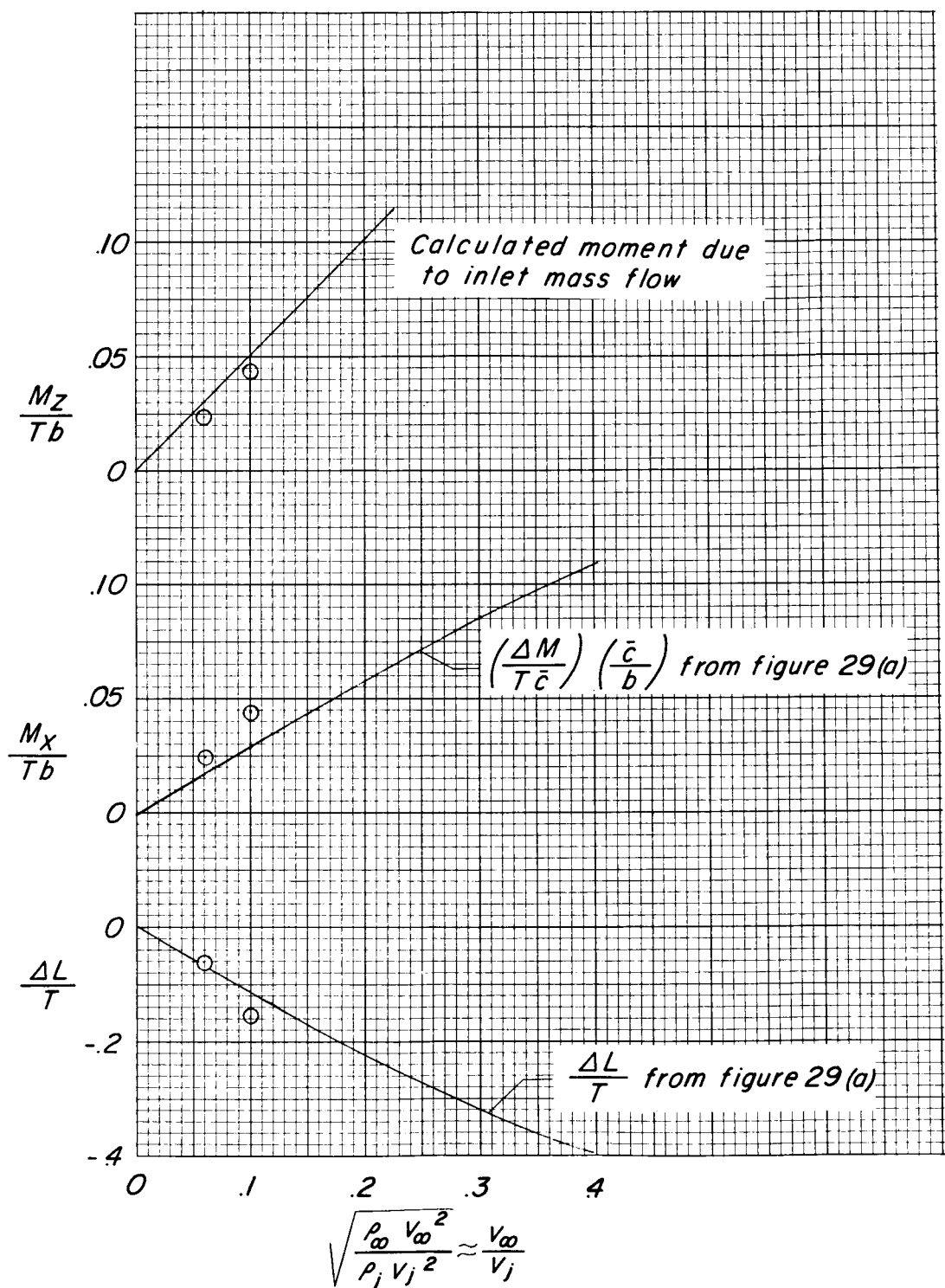


Figure 41.- Inlet and exit interference effects on the lateral characteristics of the basic model at sideslip angles of  $-70^\circ$  and  $\delta_j = 78^\circ$ .

DECLASSIFIED

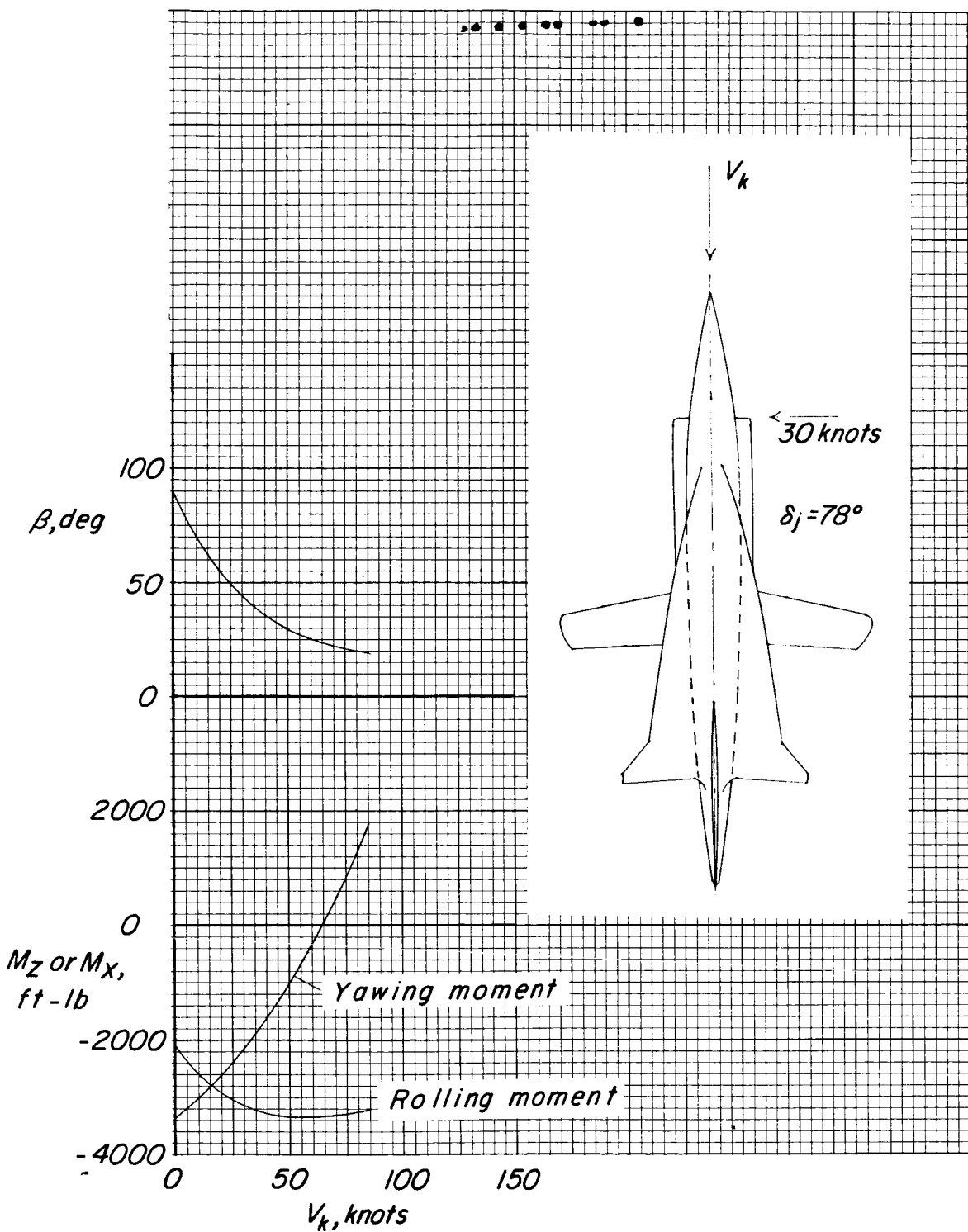


Figure 42.- Effect of a 30-knot cross wind on the rolling and yawing moments of the basic airplane for an assumed weight of 30,000 pounds.